Synthesis and Characterization of Thiophene-Based Copolymers: Effects of Comonomer Design and Doping Method on Solubility, Morphology, and Conductivity

A Dissertation Presented for the

Doctor of Philosophy

Degree

The University of Tennessee, Knoxville

Abigail N. Linhart

December 2025

Acknowledgements

First, thank you to my advisor, Prof. S. Michael Kilbey II, for all his support and guidance during my time in his group. Every time we talked about my work, he challenged me to think more deeply, understand things more fully, and communicate more clearly. I truly can't thank him enough for helping me grow into the scientist I am today. I'm also grateful for how much he emphasized that life outside the lab matters, especially when it comes to family and the Packers.

I would also like to thank my committee members—Prof. Brian Long, Prof. Johnathan Brantley, and Prof. Gila Stein—for their advice, feedback, and encouragement throughout my time at UT. Every meeting with them pushed me to improve and made a real difference in my scientific development.

My dissertation research was financially supported by a research grant from the U.S. National Science Foundation (award #2204396) as well as through a National Defense Science and Engineering Graduate Fellowship that was sponsored by the Office of Naval Research. These have facilitated my progress and provided valuable opportunities to me.

I'm incredibly grateful to all my peers here at UT who helped me along the way. First, I would like to thank my group members: Elizabeth O'Connell, Will Ledford, Dani Chun, Nia Parker, Bishal Upadhyay, Candice Halbert, Evan Holt, KJ Bell, Manvendra Singh, and Taylor Kearbey. They were there through every research update, practice talk, and rough draft and their feedback and support made a huge difference. And I can't forget Christy Witcher Barker, Brooke Smith, and Susan Kenny. I couldn't have asked for a better

group of people to go through this wild ride with. Their friendship and encouragement kept me going, and I'll always be thankful for that.

I extend my greatest thanks to my parents, Tim and Vickie Linhart. Their continued support, not only through these last four years, but throughout my entire life has been amazing. I would not be the person that I am today without them, and am so proud to call them my parents. Also, I can never truly express how thankful I am for the constant support and unwavering confidence in me that I received from my siblings, Samantha and Timmy. And I also thank my sister-in-law, Ashley, who has supported me as if she has been my sister my entire life. And my final thanks goes to my nephew and niece, Bodie and Charlotte. Their love of life, silliness, and growth has brought much joy to me throughout this journey.

I thank you all for being a part of my life and helping shape me into the scientist and person I am today!

Abstract

Conjugated polymers are promising materials for organic electronic devices due to their low cost, light weight and flexible nature, and use of naturally abundant elements. However, achieving metal-like conductivities requires chemical doping. This dissertation investigates the complex relationship between repeat unit design and polymer properties, such as solubility, morphology, and conductivity, with a particular focus on doping methods. A series of expanded core thiophene-based copolymers were synthesized to examine how reduced steric demand along the polymer backbone, relative to the benchmark poly(3-hexylthiophene), influences solubility, polymer-dopant interactions, and conductivity. The dopant 2,3,5,6-tetrafluoro-7,7,8,8-tetracyanoquinodimethane (F4TCNQ) was used to evaluate three doping approaches: solution doping, sequential doping, and serial doping, which is a two-step method that successively utilizes both solution and sequential doping. This work demonstrates that increasing the core size of these copolymers enhances doping efficiency and conductivity. Consistent with prior reports, sequential doping outperforms solution doping by achieving higher conductivity at lower dopant concentrations; however, this efficiency strongly depends on the choice of dopant solvent. A key contribution of this research is the development of a predictive framework for solvent selection to optimize conductivity based on the polymer–solvent interaction energies that is universally shared by polymers of different structure and chemical type. In addition, serial doping is shown to further enhance thin-film conductivity by inducing crystallite formation, offering a strategy to improve the performance of otherwise amorphous conjugated polymers. Altogether, the systematic studies presented

herein offer new insights into design-structure-property relationships of conjugated polymers and support the development of broadly applicable doping strategies that maximize conductivity across a wide range of polymer designs.

Table of Contents

Chapter 1. Introduction 1

1.1. Conjugated Polymers 1

1.2. Chemical Doping 3

1.2.1. Methods of Dopant Integration 4

1.3. Spacing Units in Repeat Unit Designs of Conjugated Polymers 9

1.4. Synthesis and Characterization of Conjugated Polymers 12

1.4.1. Copolymer Synthesis via Direct Arylation Polymerization (DArP) 12

1.4.2. Quantifying Solubility of Conjugated Polymers 16

1.4.3. Thin Film Morphology 18

1.4.4. Electrical Conductivity 20

1.5. Motivation and Research Objectives 22

Chapter 2. Universality in Solvent-Dependent Conductivity of Conjugated Thiophene-Based Copolymers with Expanded Core Monomer Designs 25

2.1. Abstract 26

2.2. Introduction 27

2.3. Materials and Methods 31

2.3.1. Materials 31

2.3.2. Synthesis of Core Expanded Monomers and Polymerization Method 31

2.3.3. Macromolecular Characterization 37

2.3.4. Thin Film Preparations 37

2.3.5. AFM Measurements 38

2.3.6. Conductivity Measurements 39
2.3.7. Absorbance Measurements 39
2.3.8. Determination of Hansen Solubility Parameters 40
2.4. Results and Discussion 40
2.4.1. Comonomer Synthesis and Characterization 40
2.4.2. Copolymer Synthesis and Characterization 44
2.4.3. Solution Doping of Thiophene-Based Copolymers 52
2.4.4. Sequential Doping of Thiophene-Based Copolymers 64
2.4.5. Comparison of Solution and Sequential Doping 73
2.4.6. Core Expansion using Dithienothiophene 75
2.5. Conclusions 80
Chapter 3. Enhancing Thin Film Morphology and Conductivity Through Serial Doping of Conjugated Thiophene-Based Copolymers 82
3.1. Abstract 83
3.2. Introduction 84
3.3. Materials and Methods 88
3.3.1. Materials 88
3.3.2. Synthesis of Comonomers and Copolymers Procedures 89
3.3.3. Polymer Characterization 89
3.3.4. DSC Measurements 89
3.3.5. Thin Film Preparations 90
3.3.6. Conductivity Measurements 91

3.3.7. Thin Film UV-Vis-NIR Measurements 91
3.3.8. GIWAXS Measurements 92
3.4. Results and Discussion 92
3.4.1. Copolymer Synthesis and Characterization. 92
3.4.2. Electrical Conductivity of Doped Copolymer Thin Films 96
3.4.3. UV-Vis-NIR Analysis of Doped Copolymer Thin Films 100
3.4.4. GIWAXS Measurements of Doped Copolymer Thin Films 105
3.5. Conclusions 112
Chapter 4. Impact of Analysis Method on Accuracy of Gel Permeation Chromatography Measurements of Thiophene-Based Conjugated Polymers 114
4.1. Abstract 115
4.2. Introduction 116
4.3. Materials and Methods 119
4.3.1. Materials 119
4.3.2. Synthesis of Expanded Core Copolymers 119
4.3.3. Measurement of d*n*/d*c* 120
4.3.4. GPC Measurements 120
4.4. Results and Discussion 121
4.4.1. GPC Characterization of Expanded Core Copolymers 121
4.4.2. Absolute M_n and M_w Characterization of P3HT 132
4.4.3. Proposed Alternative for Absolute M_n and M_w Characterization 136
4.5. Conclusions 138

Chapter 5. Solvent-Dependent Conductivity of Sequentially-Doped Conjugated Polymers: Universal Relationship Between Solvent-Polymer Interaction Energy and Conductivity 140

5.1. Abstract 141

5.2. Introduction 142

5.3. Materials and Methods 144

5.3.1. Materials 144

5.3.2. Synthesis of P3HT and the Copolymers 144

5.3.3. Polymer Characterization 146

5.3.4. Hansen Solubility Parameter Determination 147

5.3.5. Thin Film Preparation 147

5.3.6. AFM Film Thickness Measurements 148

5.3.7. Conductivity Measurements 148

5.3.8. Thin Film UV-Vis Measurements 148

5.3.9. GIWAXS Measurements 149

5.4. Results and Discussion 149

5.5. Conclusions 166

Chapter 6. Conclusions and Future Work 168

6.1. Conclusions 168

6.2. Future Work 171

6.2.1. Impact of Regioregularity on Conductivity and Morphology 171

6.2.2. Additives to Induce Crystallinity 172

6.2.3. Extensions into Donor-Acceptor Copolymers 174
References 176
Appendices 194
Appendix A. Supplementary Information for Chapter 2 194
A.1. ^{1}H and ^{13}C NMR of Comonomers 194
A.2. ^{1}H NMR Spectra of Synthesized Polymers and Copolymers 199
A.3. Polymer and Copolymer Characterizations 202
A.4. AFM Characterization of Solution-Doped Thin Films 205
A.5. UV-Vis-NIR Characterization of Solution-Doped Thin Films 208
A.6. AFM Characterization of Sequentially-Doped Thin Films 211
A.7. UV-Vis-NIR Characterization of Sequentially-Doped Thin Films 215
Appendix B. Supplementary Information for Chapter 3 218
B.1. ^{1}H NMR Spectra of P3HT and Expanded Core Copolymers 218
B.2. GPC Characterization of P3HT and Expanded Core Copolymers 220
B.3. AFM Film Thickness Measurements 220
B.4. DSC Thermograms of P3HT and Expanded Core Copolymers 222
Appendix C. Supplementary Information for Chapter 4 225
C.1. GPC Traces of PS, P3HT, and Expanded Core Copolymers 225
C.2. Mark-Houwink Plots 228
Appendix D. Supplementary Information for Chapter 5 231
D.1. ^{1}H NMR of P3HT and Copolymers 231
D.2. Molecular Weight Characterization of P3HT and Copolymers 234

D.3. Film Thickness of As-Cast and Sequentially-Doped Thin Films 234

D.4. Thin Film UV-Vis Measurements 235

Vita..... 237

List of Tables

Table 2.1. Optical characteristics of thiophene-based comonomers. 43

Table 2.2. Macromolecular characteristics of thiophene-based copolymers and P3HTs. 47

Table 2.3. Hansen solubility parameters (HSPs) of the thiophene-based polymers. 51

Table 2.4. Surface roughness of solution-doped thin films at various doping levels determined from AFM measurements. 54

Table 2.5. Calculated solubility parameter distance, R_a, of each polymer-solvent pair... 66

Table 2.6. Surface roughnesses of sequentially-doped thin films as a function of the solvent used for doping. 66

Table 3.1. T_g, T_c, and T_m for P3HT and the expanded core copolymers. 95

Table 3.2. Out-of-plane *d*-spacing of as-cast and doped thin films. 109

Table 4.1. Experimentally determined d*n*/d*c* values for PS, **P3HT**, and each of the expanded core copolymer (**P3**-**P6)**. 124

Table 4.2. Weight-average molecular weight (M_w) and dispersity (Đ) of PS, **P3HT**, and each of the expanded core copolymers (**P3**-**P6**) determined via triple detection. .. 126

Table 4.3. Mark-Houwink parameters, *K* and *a*, for PS, **P3HT**, and each of the expanded core copolymer (**P3**-**P6**)..... 128

Table 4.4. Number-average molecular weight and dispersity of **P3HT** and each core expanded copolymer (**P3**-**P6**) measured via universal calibration and triple detection. 133

Table 4.5. M_n and Đ of **P3HT-PhOMe** determined via GPC and NMR measurements. 137

Table 5.1. Hansen solubility parameters (HSPs), radius of solubility sphere (R_o), and quality of data fit for **P3HT**, **P(EDOT-co-ProDOT)**, and **P(DHPP-co-DPP)**. 152

Table 5.2. Summary of R_a values for each polymer-solvent pair based on their respective HSPs..... 154

Table 5.3. Summary of *d*-values for each polymer-solvent pair based on the respective HSPs of the polymer, solvent, and dopant. 154

Table 5.4. Summary of *d*-spacing values obtained from the (100) diffraction peaks of the out-of-plane 1D GIWAXS profiles..... 164

Table A.1. Observed solubility of each polymer or copolymer in various solvents at a concentration of 1 mg/mL. A score of 0 indicates not soluble while a score of 1 indicates soluble. 204

Table A.2. Film thicknesses of solution-doped thin films as a function of doping level, as determined from AFM scratch tests. 208

Table A.3. Film thicknesses of sequentially-doped thin films obtained from AFM scratch tests. 214

Table B.1. Molecular weight characterization of each copolymer based on universal analysis. 220

Table B.2. Film thickness of as-cast films and those created using solution, sequential, and serial doping, as determined by AFM measurements. 221

Table D.1. Molecular weight characterization of **P3HT**, **P(EDOT-*co*-ProDOT)**, and **P(DHPP-*co*-DPP)**. 234

Table D.2. Film thickness of as-cast and doped thin films for each polymer-solvent pair as determined by AFM measurements. 234

List of Figures

Figure 1.1. Illustration of HOMO and LUMO energy gaps for insulating, semi-conducting, and conducting materials along with examples of each material. 2

Figure 1.2. Energy diagram schematic of p-type doping between P3HT and F4TCNQ. The subsequent formation of the charged species, cationic P3HT (or polaron) and anionic F4TCNQ ($F4TCNQ^{-}$) by charge transfer, is depicted on the right..... 5

Figure 1.3. Illustration of the method used to prepare solution-doped thin films..... 5

Figure 1.4. Illustration of the method used to prepare sequentially-doped thin films. 7

Figure 1.5. Generic depiction of polymer-dopant interactions with and without the use of a spacing unit. 11

Figure 1.6. Illustration of DArP for (a) an AB type polymerization and (b) an AA+BB type polymerization. 13

Figure 1.7. Proposed catalytic cycle for DArP using 2-bromo-3-hexylthiophene, an AB type monomer, as an example..... 15

Figure 1.8. Circuit diagram of Van der Pauw measurements to obtain resistance in the vertical (R_V) and horizontal (R_H) direction. Note that the subscripts of each measured resistance identifies the orientation in which the measurement was performed. The first two numbers indicate the contact points that have the voltage applied to them while the last two numbers identify the contact points that are used to measure the current. 21

Figure 2.1. Absorbance spectra of thiophene-based comonomers (**M3**-**M6**) in $CHCl_3$ (<1 mg/mL). Spectra are normalized by the absorbance measured at λ_{max} for each monomer. A red-shift is observed as the core size increases, which increases the spacing length between alkyl side chains. 43

Figure 2.2. Optical bandgap of thiophene-based copolymers determined from Tauc analysis as a function of number of thiophene units per chain. For **P4**, thienothiophene was counted as a single unit. The behavior indicates that the bandgap is constant above ~20 thiophene rings per chain. Horizontal error bars represent the uncertainty of the M_n determined by GPC using universal analysis. 47

Figure 2.3. Representative AFM images of solution-doped thin films at 0 mol% (a-f) and 23 mol% (g-l) doping for each copolymer. The surface roughness remains low (< 4 nm) for all films at all doping levels except for solution-doped films of **P4**, **P5**, and **P6** at 23 mol%, where dramatic increases in roughness are evident. 54

Figure 2.4. Conductivity of solution-doped copolymer thin films as a function of doping level. Doping level is determined as a mol% of F4TCNQ relative to relative to the moles of thiophene in the polymer solution. Conductivity measurements were performed on samples spin cast on 1 in × 1 in glass slides with film thicknesses ranging from 10-25 nm. 56

Figure 2.5. FT-IR spectra (left) of powder F4TCNQ and powder $F4TCNQ^-$ and their respective key peak positions (right). Assignments were made based on a report from Watts et al.[65] The shifts observed for the vibrational modes validate the successful conversion of F4TCNQ to $F4TCNQ^-$. 59

Figure 2.6. UV-Vis spectra of F4TCNQ and $F4TCNQ^-$, normalized by the peak absorbances recorded at 387 nm and 411 nm, respectively. Each sample was prepared in acetonitrile at 1.5 mg/mL. 59

Figure 2.7. Normalized UV-Vis-NIR spectra of F4TCNQ thin films created by drop casting from a methanol solution at 1.5 mg/mL. The local maximum at 868 nm is used for $F4TCNQ^-$ quantification in subsequent thin film measurements. 60

Figure 2.8. UV-Vis-NIR spectra of thin films created by solution doping of **P6**. The absorbance spectra measured at each doping level was normalized by film thickness, which ranged from 10-13 nm for these **P6** films. Regions highlighted in blue correspond to the mode associated with neutral F4TCNQ, while regions shaded in red correspond to the anionic form, $F4TCNQ^-$..... 62

Figure 2.9. Comparison of conductivity and $F4TCNQ^-$ absorbance in solution-doped thin films of (a) **P3HT (AA+BB)**, (b) **P3HT (AB)**, (c) **P3**, (d) **P4**, (e) **P5**, and (f) **P6** as a function of doping level. The $F4TCNQ^-$ absorbance is taken as the local maximum at 868 nm obtained from UV-Vis-NIR measurements and is normalized by film thickness. As a result, the normalized absorbance is proportional to $F4TCNQ^-$ concentration. 63

Figure 2.10. Representative AFM height images of **P3HT (AB)** thin films sequentially-doped with F4TCNQ at 1 mg/mL in acetone. Images correspond to (a) an as-cast film and (b) the film after a methanol rinse. Each image was obtained in tapping mode over an area of 20 μm × 20 μm. This comparison indicates that the F4TCNQ aggregates

appearing in (a) are washed away by methanol and that the underlying film is smooth and homogeneous..... 68

Figure 2.11. Conductivity of sequentially-doped thin films as a function of the solubility parameter distance between the polymer and solvent used for sequential doping. (a) **P3HT (AB)** and **P3HT (AA+BB)** and (b) the expanded thiophene-based copolymers. Doping was performed with six different solvents (THF, DCM, 50:50 acetone:DCM, 75:25 acetone:DCM, acetone, and DMF) at 1 mg/mL. Films were spin cast and doped on 1 in × 1 in glass slides and have film thicknesses ranging from 10-30 nm. 70

Figure 2.12. Comparison of measured conductivity and $F4TCNQ^-$ absorbance in sequentially-doped thin films of (a) **P3HT (AA+BB)**, (b) **P3HT (AB)**, (c) **P3**, (d) **P4**, (e) **P5**, and (f) **P6** as a function of solubility parameter distance, R_a. The $F4TCNQ^-$ absorbance is taken as the local maximum at 868 nm obtained from UV-Vis-NIR measurement and is normalized by film thickness. This normalized absorbance is proportional to $F4TCNQ^-$ concentration. 72

Figure 2.13. Comparison of $F4TCNQ^-$ absorbance and conductivity for solution and sequentially-doped thin films of (a) **P3HT (AA+BB)**, (b) **P3HT (AB)**, (c) **P3**, (d) **P4**, (e) **P5**, and (f) **P6**. The $F4TCNQ^-$ absorbance is taken as the local maximum at 868 nm obtained from UV-Vis-NIR measurement and is normalized by film thickness. This normalized absorbance is proportional to $F4TCNQ^-$ concentration. For the expanded designs (**P3**, **P4**, **P5**, **P6**), it is clear that higher conductivities are reached at lower $F4TCNQ^-$ concentrations..... 74

Figure 2.14. ^{1}H NMR spectrum of 2,6-bis(3-hexylthiophen-2-yl)di-thieno[3,2-*b*:2',3'-*d*]-thiophene (**M7**) in $CDCl_3$ with the inset highlighting the aromatic region. 76

Figure 2.15. ^{1}H NMR spectrum of poly(2-(4,4'-dihexyl-[2,2'-bithiophen]-5-yl)-6-(3-hexyl-thiophen-2-yl)dithieno[3,2-b:2',3'-d]thiophene) (**P7**) in $C_2D_2Cl_4$..... 77

Figure 2.16. ^{1}H NMR of 3',4,4"-trihexyl-2,2':5',2"-terthiophene (**M7-R2**) in $CDCl_3$. 79

Figure 3.1. Structures of **P3HT** and the expanded core copolymers containing spacing units of thiophene (**P3**), thieno[3:2,*b*]thiophene (**P4**), 2,2'-bithiophene (**P5**), and 2,2':5',2"-terthiophene (**P6**). 93

Figure 3.2. Schematic drawings illustrate (a) solution, (b) sequential, and (c) serial doping methods. Solution-doped thin films are cast from a solution made by mixing separate solutions of 30 mg/mL polymer and 1 mol% F4TCNQ in chlorobenzene at 70 °C. For sequential doping, a 30 mg/mL polymer solution in chlorobenzene at 70 °C is used to cast a pristine polymer film and then the film is submerged in a 1 mg/mL F4TCNQ solution in acetone for 30 s. Serial doping involves first creating the solution-doped thin film, followed by a second doping step in which the solution-doped thin film is submerged in a 1 mg/mL F4TCNQ solution in acetone for 30 s. 97

Figure 3.3. Conductivity of solution-, sequential-, and serial-doped thin films of **P3HT** and each expanded core copolymer (**P3**-**P6**). The inset shows the solution-doped thin film measurements on a log scale to visualize the data effectively. For solution doping, films were cast from a polymer solution having 1 mol% F4TCNQ. With sequential doping, the polymer thin films were submerged in an acetone solution containing 1

mg/mL F4TCNQ solution for 30 s. Serial doping used a two-step process in which a solution-doped film was made and then submerged in a 1 mg/mL F4TCNQ acetone solution in acetone for 30 s. Clearly, the increase in conductivity resulting from serial doping exceeds what would be expected from a purely additive result. 99

Figure 3.4. UV-Vis-NIR spectra of (a) **P3HT**, (b) **P3**, (c) **P4**, (d) **P5**, and (e) **P6** as-cast films and films doped via solution, sequential, and serial doping methods. The spectra are normalized by film thickness which makes the absorbance signal proportional to concentration. The black circles indicate the λ_{max} of each polymer, while the orange star indicates the peak attributed to $F4TCNQ^-$ (868 nm) that is used for analysis. The broad absorbance appearing at $\lambda > 1200$ nm signifies polaron formation. 102

Figure 3.5. Comparison of conductivity and $F4TCNQ^-$:polymer absorbance ratio for thin films created by each doping method: (a) **P3HT**, (b) **P3**, (c) **P4**, (d) **P5**, and (e) **P6**. The ratio of $F4TCNQ^-$: polymer was calculated using the absorbance at 868 nm for $F4TCNQ^-$ and the absorbance at the λ_{max} for each of the respective polymers. Common axis scales are used to enable comparisons. The lack of correlation between conductivity and relative level of effective charge transfer expressed by the absorbance ratio indicates that the changes in conductivity are not solely driven by the amount of $F4TCNQ^-$ generated. 104

Figure 3.6. Out-of-plane 1D GIWAXS profiles of (a) as-cast and (b) solution-doped thin films. The y-axis is offset on a logarithmic scale to facilitate comparison. These out-of-plane profiles provide insight into the prevalence of edge-on crystallites in the films. 106

Figure 3.7. 2D GIWAXS images acquired from as-cast thin films of each polymer. ... 107

Figure 3.8. 2D GIWAXS images acquired from solution-doped (1 mol% F4TCNQ) thin films of each polymer. 107

Figure 3.9. Out-of-plane 1D GIWAXS profiles of (a) sequential- and (b) serial-doped thin films. The y-axis is offset on a logarithmic scale to facilitate comparison..... 109

Figure 3.10. 2D GIWAXS images acquired from sequentially-doped thin films of each polymer. 110

Figure 3.11. 2D GIWAXS images acquired from serial-doped thin films of each polymer. 110

Figure 4.1. Structures of the reference polymer (polystyrene, PS), the benchmark thiophene-based conjugated polymer (poly-3-hexythiophene, **P3HT**), and the expanded core copolymers (**P3**, **P4**, **P5**, and **P6**). 122

Figure 4.2. Change in refractive index (dRI) as a function of concentration for PS, **P3HT**, and each of the expanded core polymers (**P3**-**P6**). The slope of each line is the d*n*/d*c* of that polymer. 124

Figure 4.3. Comparison of M_w determined via conventional calibration analysis (y-axis) and triple detection (x-axis). The x=y line is a visual guide for what is expected if the M_w value of conventional analysis matches that of the M_w determined from triple detection. 126

Figure 4.4. Relationship between the Mark-Houwink parameter, *a*, and the percent deviation in the M_w obtained from conventional calibration from the M_w obtained from triple detection. 128

Figure 4.5. Comparison of M_w measured via triple detection to M_w measured via universal calibration (a) assuming 100% mass recovery and (b) using the measured d*n*/d*c* values. This shows that assuming 100% mass recovery leads to large deviations in M_w from triple detection in some cases; however, when using the measured d*n*/d*c* the M_w values obtained from universal calibration match closely with M_w determined from triple detection. 131

Figure 4.6. (a) Relationship of mass recovery and percent deviation in the estimated d*n*/d*c* when 100% mass recovery is assumed from the measured d*n*/d*c*. (b) Relationship of the percent deviation of d*n*/d*c* and the percent deviation of molecular weights obtained from universal calibration when 100% mass recovery is assumed and universal calibration when the measured d*n*/d*c* is used. This shows that lower mass recoveries result in higher deviations in the estimated d*n*/d*c* and measured M_w, therefore, the assumption of 100% mass recovery can lead to inaccuracies in molecular weight measurements. 131

Figure 4.7. ^{1}H NMR of **P3HT-PhOMe**. The peak at 3.86 ppm associated with the methoxy end group is normalized to 3 protons, which results in a X_n of 198 based on the integration of the β-proton of the thiophene (a). This X_n is also consistent with the integrations of b and c aliphatic protons. 135

Figure 5.1. Structures of **P3HT**, **P(EDOT-*co*-ProDOT),** and **P(DHPP-*co*-DPP)**..... 150

Figure 5.2. Conductivity measurements of **P3HT**, **P(EDOT-*co*-ProDOT)**, and **P(DHPP-*co*-DPP)** thin films doped via sequential doping as a function of R_a values. R_a was calculated for each polymer-solvent pair and the solvents used are DCM, THF, acetone, DMF, DMSO, and 50:50 acetone:THF. Each polymer shows a clear R_a-dependent conductivity in which moderate R_a values yield the highest conductivity. 155

Figure 5.3. Absorbance ratio of $F4TCNQ^-$:Polymer as a function of R_a value for sequentially doped thin films made from (a) **P3HT**, (b) **P(EDOT-*co*-ProDOT)**, and (c) **P(DHPP-*co*-DPP)**. The absorbance ratio shows the same R_a-dependence as conductivity, indicating that the solvent-polymer interaction energy influences dopant integration and formation of $F4TCNQ^-$, which largely regulates thin film conductivity..... 158

Figure 5.4. Out-of-plane 1D GIWAXS profiles of sequentially doped (a) **P3HT**, (b) **P(EDOT-*co*-ProDOT)**, and (c) **P(DHPP-*co*-DPP)** thin films with various solvents. The color of each profile corresponds to the dopant solvent used (e.g., blue is THF) and the respective R_a values for the solvent-polymer pair are given (in parentheses). For each polymer, the traces are ordered, from the bottom to the top, from good solvent (low R_a) to poor solvent (high R_a). 160

Figure 5.5. 2D GIWAXS images of as-cast and doped thin films made from **P3HT**. Images are arranged (left to right, row by row) in order of decreasing solvent quality (R_a value)..... 160

Figure 5.6. 2D GIWAXS images of as-cast and doped thin films made from **P(EDOT-*co*-ProDOT)**. Images are arranged (left to right, row by row) in order of decreasing solvent quality (R_a value). 161

Figure 5.7. 2D GIWAXS images of as-cast and doped thin films made from **P(DHPP-*co*-DPP)**. Images are arranged (left to right, row by row) in order of decreasing solvent quality (R_a value). 162

Figure 6.1. Proposed structures of regioregular (top) and regio-irregular (bottom) expanded core polymers, which can be used to examine the impact of regioregularity on film structure and properties. 173

Figure A.1. ^{1}H NMR spectrum of 3,3”-dihexyl-2,2’:5’,2”-terthiophene (M3) in $CDCl_3$ with the inset highlighting. the aromatic region. 194

Figure A.2. ^{13}C NMR spectrum of 3,3"-dihexyl-2,2':5',2"-terthiophene (M3) in $CDCl_3$. 194

Figure A.3. ^{1}H NMR spectrum of 2,5-bis(3-hexylthiophen-2-yl)thieno[3,2-*b*]thiophene (**M4**) in $CDCl_3$ with the inset highlighting the aromatic region. 195

Figure A.4. ^{13}C NMR spectrum of 2,5-bis(3-hexylthiophen-2-yl)thieno[3,2-b]thiophene (**M4**) in $CDCl_3$. 195

Figure A.5. ^{1}H NMR spectra of 3,3'''-dihexyl-2,2':5',2":5",2'''-quaterthiophene (**M5**) in $CDCl_3$ with the inset highlighting the aromatic region. 196

Figure A.6. ^{13}C NMR spectrum of 3,3'''-dihexyl-2,2':5',2":5",2'''-quaterthiophene (**M5**) in $CDCl_3$. 196

Figure A.7. ^{1}H NMR spectrum of 3,3""-dihexyl-2,2':5',2":5",2"':5"',2""-quinquethiophene (**M6**) in $CDCl_3$ with the inset highlighting the aromatic region. 197

Figure A.8. ^{13}C NMR spectrum of 3,3""-dihexyl-2,2':5',2":5",2"':5"',2""-quinquethiophene (**M6**) in $CDCl_3$. 197

Figure A.9. ^{1}H NMR spectrum of 2,5-dibromo-3-hexylthiophene in $CDCl_3$. 198

Figure A.10. ^{13}C NMR spectrum of 2,5-dibromo-3-hexylthiophene in $CDCl_3$..... 198

Figure A.11. ^{1}H NMR spectrum of poly(3,3",4"'-trihexyl-2,2':5',2":5",2"'-quaterthiophene) (**P3**) in $CDCl_3$..... 199

Figure A.12. ^{1}H NMR spectrum of poly(2-(4,4'-dihexyl-[2,2'-bithiophen]-5-yl)-5-(3-hexyl-thiophen-2-yl)thieno[3,2-*b*]thiophene) (**P4**) in $C_2D_2Cl_4$..... 200

Figure A.13. ^{1}H NMR spectrum of poly(3,3"',4""-trihexyl-2,2':5',2":5",2"':5"',2"" quinque-thiophene) (**P5**) in $CDCl_3$..... 200

Figure A.14. ^{1}H NMR spectrum of poly(3,3"",4""'-trihexyl-2,2':5',2":5",2"':5"',2"":5"",2""'-sexi-thiophene) (**P6**) in $CDCl_3$. Note the high integration for the aromatic peak is attributed to the regio-irregularity of the polymer as described by Qu et al.[130]..... 201

Figure A.15. ^{1}H NMR spectrum of poly(3-hexylthiophene) (AB) (**P3HT (AB)**) in $CDCl_3$. Peaks at 2.8 ppm (labeled b) and 2.6 ppm (labeled b') are used to compute the regioregularity, which is found to be 93%..... 201

Figure A.16. ^{1}H NMR spectrum of poly(3-hexylthiophene) (AA+BB) (**P3HT (AA+BB)**) in $CDCl_3$. Peaks at 2.8 ppm (labeled b) and 2.6 ppm (labeled b') are used to compute the regioregularity, which is found to be 57%. Note the high integration for the

aromatic peak is attributed to the regio-irregularity of the polymer as described by Qu et al.[130] 202

Figure A.17. GPC traces of **P3HT (AA+BB)**, **P3HT (AB)**, **P3**, **P4**, **P5**, and **P6** acquired using THF as the mobile phase at a flow rate of 1 mL/min. 202

Figure A.18. Absorbance spectra of **P3HT (AA+BB)**, **P3HT (AB)**, **P3**, **P4**, **P5**, and **P6** in $CHCl_3$ (<1 mg/mL). Spectra are normalized by the absorbance measured at λ_{max} for each polymer/copolymer. A red-shift is observed as the spacing length of the expanded core increases. 203

Figure A.19. Absorbance spectra of **P3HT (AA+BB)**, **P3HT (AB)**, **P3**, **P4**, **P5**, and **P6** thin films. Spectra are normalized by the absorbance measured at λ_{max}. Thin films were made by spin casting from chlorobenzene (at 2 mg/mL), and thicknesses range from 10-16 nm. A red-shift is observed compared to solution measurements and red-shifts are also observed as the spacing length increases. 203

Figure A.20. Representative AFM height images of **P3** thin films solution-doped at a) 0 mol%, b) 6 mol%, c) 10 mol%, d) 17 mol%, and e) 23 mol% F4TCNQ. Each image was obtained in tapping mode over an area of 20 μm × 20 μm. 205

Figure A.21. Representative AFM height images of **P4** thin films solution-doped at a) 0 mol%, b) 6 mol%, c) 10 mol%, d) 17 mol%, and e) 23 mol% F4TCNQ. Each image was obtained in tapping mode over an area of 20 μm × 20 μm. 205

Figure A.22. Representative AFM height images of **P5** thin films solution-doped at a) 0 mol%, b) 6 mol%, c) 10 mol%, d) 17 mol%, and e) 23 mol% F4TCNQ. Each image was obtained in tapping mode over an area of 20 μm × 20 μm. 206

Figure A.23. Representative AFM height images of **P6** thin films solution-doped at a) 0 mol%, b) 6 mol%, c) 10 mol%, d) 17 mol%, and e) 23 mol% F4TCNQ. Each image was obtained in tapping mode over an area of 20 μm × 20 μm. 206

Figure A.24. Representative AFM height images of **P3HT (AB)** thin films solution-doped at a) 0 mol%, b) 6 mol%, c) 10 mol%, d) 17 mol%, and e) 23 mol% F4TCNQ. Each image was obtained in tapping mode over an area of 20 μm × 20 μm. 207

Figure A.25. Representative AFM height images of **P3HT (AA+BB)** thin films solution-doped at a) 0 mol%, b) 6 mol%, c) 10 mol%, d) 17 mol%, and e) 23 mol% F4TCNQ. Each image was obtained in tapping mode over an area of 20 μm × 20 μm. 207

Figure A.26. UV-Vis-NIR spectra of solution-doped **P3HT (AB)** thin films. The absorbance is normalized by film thickness, and thicknesses range from 11 to 20 nm. 208

Figure A.27. UV-Vis-NIR spectra of solution-doped **P3HT (AA+BB)** thin films. The absorbance is normalized by film thickness, and thicknesses range from 9 to 16 nm. 209

Figure A.28. UV-Vis-NIR spectra of solution-doped **P3** thin films. The absorbance is normalized by film thickness, and thicknesses range from 14 to 21 nm. 209

Figure A.29. UV-Vis-NIR spectra of solution-doped **P4** thin films. The absorbance is normalized by film thickness, and thicknesses range from 10 to 16 nm. 210

Figure A.30. UV-Vis-NIR spectra of solution-doped **P5** thin films. The absorbance is normalized by film thickness, and thicknesses range from 11 to 24 nm. 210

Figure A.31. Representative AFM height images of **P3** thin films sequentially-doped with F4TCNQ dissolved at 1 mg/mL in a) THF, b) DCM, c) 50:50 acetone:DCM, d) 75:25 acetone:DCM, e) acetone and f) DMF. Each image was obtained in tapping mode over an area of 20 μm × 20 μm. 211

Figure A.32. Representative AFM height images of **P4** thin films sequentially-doped with F4TCNQ dissolved at 1 mg/mL in a) THF, b) DCM, c) 50:50 acetone:DCM, d) 75:25 acetone:DCM, e) acetone and f) DMF. Each image was obtained in tapping mode over an area of 20 μm × 20 μm. 211

Figure A.33. Representative AFM height images of **P5** thin films sequentially-doped with F4TCNQ dissolved at 1 mg/mL in a) THF, b) DCM, c) 50:50 acetone:DCM, d) 75:25 acetone:DCM, e) acetone and f) DMF. Each image was obtained in tapping mode over area of 20 μm × 20 μm. 212

Figure A.34. Representative AFM height images of **P6** thin films sequentially-doped with F4TCNQ dissolved at 1 mg/mL in a) THF, b) DCM, c) 50:50 acetone:DCM, d) 75:25 acetone:DCM, e) acetone and f) DMF. Each image was obtained in tapping mode over an area of 20 × 20 μm. 212

Figure A.35. Representative AFM height images of **P3HT (AB)** thin films sequentially-doped with F4TCNQ dissolved at 1 mg/mL in a) THF, b) DCM, c) 50:50 acetone:DCM, d) 75:25 acetone:DCM, e) acetone and f) DMF. Each image was obtained in tapping mode over an area of 20 μm × 20 μm. 213

Figure A.36. Representative AFM height images of **P3HT (AA+BB)** thin films sequentially-doped with F4TCNQ dissolved at 1 mg/mL in a) THF, b) DCM, c) 50:50 acetone:DCM, d) 75:25 acetone:DCM, e) acetone and f) DMF. Each image was obtained in tapping mode over an area of 20 μm × 20 μm. 213

Figure A.37. UV-Vis-NIR spectra of sequentially-doped **P3HT (AB)** thin films. The absorbance is normalized by film thickness, and thicknesses range from 10 to 17 nm. All films were doped using solutions at 1 mg F4TCNQ /mL. 215

Figure A.38. UV-Vis-NIR spectra of sequentially-doped **P3HT (AA+BB)** thin films. The absorbance is normalized by film thickness, and thicknesses range from 10 to 24 nm. All films were doped using solutions at 1 mg F4TCNQ /mL. 215

Figure A.39. UV-Vis-NIR spectra of sequentially-doped **P3** thin films. The absorbance is normalized by film thickness, and thicknesses range from 14 to 28 nm. All films were doped using solutions at 1 mg F4TCNQ /mL 216

Figure A.40. UV-Vis-NIR spectra of sequentially-doped **P4** thin films. The absorbance is normalized by film thickness, and thicknesses range from 9 to 19 nm. All films were doped using solutions at 1 mg F4TCNQ /mL. 216

Figure A.41. UV-Vis-NIR spectra of sequentially-doped **P5** thin films. The absorbance is normalized by film thickness, and thicknesses range from 8 to 22 nm. All films were doped using solutions at 1 mg F4TCNQ /mL. 217

Figure A.42. UV-Vis-NIR spectra of sequentially-doped **P6** thin films. The absorbance is normalized by film thickness, and thicknesses range from 14 to 29 nm. All films were doped using solutions at 1 mg F4TCNQ /mL. 217

Figure B.1. ^{1}H NMR spectra of poly(3-hexylthiophene) (**P3HT**) in $CDCl_3$. Peaks at 2.8 ppm and 2.6 ppm were used to calculate the regioregularity of 93%. 218

Figure B.2. ^{1}H NMR spectrum of poly(3,3"',4"'-trihexyl-2,2':5',2":5",2"'-quaterthiophene) (**P3**) in $CDCl_3$ 218

Figure B.3. ^{1}H NMR spectrum of poly(2-(4,4'-dihexyl-[2,2'-bithiophen]-5-yl)-5-(3-hexyl-thiophen-2-yl)thieno[3,2-*b*]thiophene) (**P4**) in $C_2D_2Cl_4$. 219

Figure B.4. ^{1}H NMR spectrum of poly(3,3"',4""-trihexyl-2,2':5',2":5",2"':5"',2""-quinque-thiophene) (**P5**) in $CDCl_3$ 219

Figure B.5. ^{1}H NMR spectrum of poly(3,3"",4"""-trihexyl-2,2':5',2":5",2"':5"',2"":5"",2"""-sexi-thiophene) (**P6**) in $CDCl_3$. 219

Figure B.6. GPC traces of (a) differential refractive index and (b) differential pressure (viscosity detector) for each copolymer, which were used to determine molecular weight based on universal analysis. 220

Figure B.7. DSC thermogram of **P3HT**. Measurement was performed from −50-300 °C at a rate of 10 °C/min and the 2nd cycle, shown here, was used for analysis. 222

Figure B.8. DSC thermogram of **P3**. Measurement was performed from −50-300 °C at a rate of 10 °C/min and the 2nd cycle, shown here, was used for analysis. 223

Figure B.9. DSC thermogram of **P4**. Measurement was performed from −50-300 °C at a rate of 10 °C/min and the 2nd cycle, shown here, was used for analysis. 223

Figure B.10. DSC thermogram of **P5**. Measurement was performed from −50-300 °C at a rate of 10 °C/min and the 2nd cycle, shown here, was used for analysis. 224

Figure B.11. DSC thermogram of **P6**. Measurement was performed from −50-300 °C at a rate of 10 °C/min and the 2nd cycle, shown here, was used for analysis. 224

Figure C.1. GPC traces of PS corresponding to the light scattering (LS) signal, refractive index (dRI) signal, and differential pressure (DP) signal. 225

Figure C.2. GPC traces of **P3HT** corresponding to the light scattering (LS) signal, refractive index (dRI) signal, and differential pressure (DP) signal. 225

Figure C.3. GPC traces of **P3** corresponding to the light scattering (LS) signal, refractive index (dRI) signal, and differential pressure (DP) signal. 226

Figure C.4. GPC traces of **P4** corresponding to the light scattering (LS) signal, refractive index (dRI) signal, and differential pressure (DP) signal. 226

Figure C.5. GPC traces of **P5** corresponding to the light scattering (LS) signal, refractive index (dRI) signal, and differential pressure (DP) signal. 227

Figure C.6. GPC traces of **P6** corresponding to the light scattering (LS) signal, refractive index (dRI) signal, and differential pressure (DP) signal. 227

Figure C.7. Mark-Houwink plot of PS. Calibration standards of different molecular weights were used to obtain the plot. 228

Figure C.8. Mark-Houwink plot of **P3HT** 228

Figure C.9. Mark-Houwink plot of **P3**. 229

Figure C.10. Mark-Houwink plot of **P4**. 229

Figure C.11. Mark-Houwink plot of **P5**. 230

Figure C.12. Mark-Houwink plot of **P6**. 230

Figure D.1. ^{1}H NMR spectra of **P3HT** obtained in $C_2D_2Cl_4$. Peaks at 2.8 ppm and 2.6 ppm were used to calculate the regioregularity of 93%. 231

Figure D.2. ^{1}H NMR spectrum **P(EDOT-*co*-ProDOT)**. 231

Figure D.3. ^{1}H NMR spectrum of **P(DHPP-*co*-DPP)**. 232

Figure D.4. Hansen solubility spheres of F4TCNQ and **P3HT**. The overlap volume is 145.1 $(MPa^{1/2})^3$ 232

Figure D.5. Hansen solubility spheres of F4TCNQ and **P(EDOT-*co*-ProDOT)**. The overlap volume is 275.8 $(MPa^{1/2})^3$. 233

Figure D.6. Hansen solubility spheres of F4TCNQ and **P(DHPP-*co*-DPP)**. The overlap volume is 0 $(MPa^{1/2})^3$. 233

Figure D.7. UV-Vis spectra of as-cast and doped thin films made from **P3HT**. The spectra are normalized by film thickness. The λ_{max} obtained from the as-cast spectrum is 521 nm. 235

Figure D.8. UV-Vis spectra of as-cast and doped thin films made from **P(EDOT-*co*-ProDOT)**. The spectra are normalized by film thickness. The λ_{max} obtained from the as-cast spectrum is 563 nm. 235

Figure D.9. UV-Vis spectra of as-cast and doped thin films made from **P(DHPP-*co*-DPP)**. The spectra are normalized by film thickness. The λ_{max} obtained from the as-cast spectrum is 693 nm. 236

List of Schemes

Scheme 2.1. Synthesis of thiophene-based comonomers (**M3**-**M6**) via (a) Stille and (b) Suzuki-Miyaura cross-couplings. 42

Scheme 2.2. Synthesis of thiophene-based copolymers (**P3-P6**) via DArP. 45

Scheme 2.3. Synthesis of 2,6-bis(3-hexylthiophen-2-yl)di-thieno[3,2-*b*:2',3'-*d*]thiophene (**M7**) via Suzuki-Miyaura cross-coupling. 76

Scheme 2.4. Synthesis of poly(2-(4,4'-dihexyl-[2,2'-bithiophen]-5-yl)-6-(3-hexyl-thiophen-2-yl)-dithieno[3,2-b:2',3'-d]thiophene) (**P7**) via DArP. 77

Scheme 2.5. Synthesis of (a) 3',4,4"-trihexyl-2,2':5',2"-terthiophene (**M7-R2**) via Stille cross-coupling and (b) copolymerization to form **P7** via DArP. 79

Scheme 4.1. Post-polymerization end group modification of **P3HT**. 135

Scheme 4.2. Proposed synthetic route for a fluorene-thiophene containing copolymer for molecular weight analysis. 137

Chapter 1. Introduction

1.1. Conjugated Polymers

Polymers are widely valued for their low cost, light weight and flexible nature, and their versatility, as well as for their use of naturally abundant elements.[1-3] However, conventional polymers like polystyrene and polyethylene are inherently insulating, which significantly limits their use in electrical or optoelectronic devices. The discovery of the conductive polymer polyacetylene in the 1970s sparked considerable interest in conjugated polymers, which paved the way for polymer materials to be used in organic electronic devices.[3-5]

The semiconducting behavior of conjugated polymers arises from delocalization of electrons along their fully π-conjugated backbone.[3,6-8] This extended π-conjugation reduces the energy gap between the highest occupied molecular orbital (HOMO) and the lowest unoccupied molecular orbital (LUMO), referred to as the bandgap (E_{gap}), compared to insulating polymers.[3,6,8] In contrast, conducting materials like copper exhibit a complete overlap of the HOMO and LUMO levels, as illustrated in Figure 1.1. Overall, the E_{gap} gives insight into the inherent electrical conductivity of a material.[9] Insulators possess a large E_{gap}, making it highly unlikely for electrons to be excited from the HOMO to the LUMO (which also is synonymously referred to as the conduction band) and, as a result, they lack conductive properties.[9] Semiconductors, which have a smaller E_{gap}, allow more electrons to be excited into the LUMO, enabling moderate levels of conductivity. With conductors, the HOMO and LUMO completely overlap, which enables electrons to move freely, resulting in high electrical conductivities.

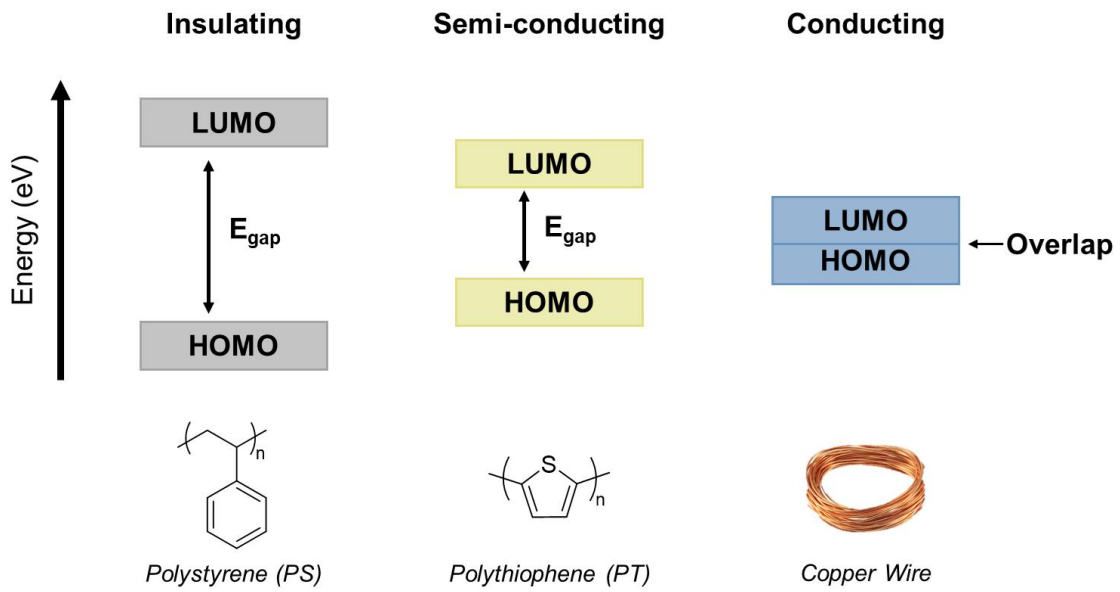

Figure 1.1. Illustration of HOMO and LUMO energy gaps for insulating, semi-conducting, and conducting materials along with examples of each material.

As a result, a significant number of efforts have been directed toward altering copolymer design and leveraging chemical dopants to modify the E_{gap} of conjugated polymers to enhance their electrical conductivity. Within those studies focused on the doping of conjugated polymers, particular emphasis has been devoted to dopant molecule selection, copolymer design modifications, and the doping process itself.[10-14] Despite various advances, there remains a wide range of outcomes from doping and there is no universally-accepted doping method that is suitable for all conjugated polymers. Therefore, deeper investigation into the chemical doping process is necessary to build the body of scientific knowledge and support the development of standardized approaches across all conjugated polymers.

1.2. Chemical Doping

Molecular dopants interact with conjugated polymers to create charged species by inducing charge transfer across the conjugated backbone by either n- or p-type doping. P-doping is an oxidative method in which electrons are transferred from the HOMO of the conjugated polymer to the LUMO of the dopant.[3,15,16] On the other hand, n-doping is reductive, transferring an electron from the HOMO of the dopant to the LUMO of the polymer.[3,17,18] Recent research has found that n-doping is not as effective due to its limited ability to lower the LUMO of conjugated polymers and poor miscibility of conjugated polymers and n-type dopants. Thus, p-doping has been more heavily used and studied.[15,17] The most commonly used p-type dopant is 2,3,5,6-tetrafluoro-7,7,8,8-tetracyano-quinodimethane (F4TCNQ) due to its deep LUMO level (-5.24 eV), which aligns well with the HOMO level of many conjugated polymers.[16,19] This is particularly true for poly(3-

hexylthiophene) (P3HT), which is viewed by the field as the benchmark conjugated polymer. P3HT has a HOMO of -5.2 eV.[13,15] Upon electron transfer from P3HT to F4TCNQ, a charged complex of $P3HT^+$ and $F4TCNQ^-$ is formed, as depicted in Figure 1.2. The unpaired electron and quinoidal structure observed in $P3HT^+$ is referred to as a polaron.[20,21] The presence of a polaron creates new allowed optical transitions that arise from half-filled states moving into the band gap, thus effectively lowering the E_{gap}.[9,20,21] These new transitions can be observed in the mid-IR and near-IR energy range for P3HT and most conjugated polymers. The delocalization of electrons across the polaron ultimately results in electrical conductivity.[22]

1.2.1. Methods of Dopant Integration

The most facile method of dopant integration is solution doping. This doping process consists of mixing separately prepared polymer and dopant solutions and then (typically) spin casting the combined solution to create doped polymer thin films, as illustrated in Figure 1.3.[13,15] The films usually display significant increases in conductivity as the amount of dopant added increases, however, there is a "saturation" limit.[13,16,23] Duong et al. showed that for F4TCNQ-doped P3HT films made by this method, the in-plane conductivity of P3HT increases by about four orders of magnitude until a concentration of 17 molecules of F4TCNQ per 83 monomer units of P3HT, which corresponds to roughly 20 mol%, is reached.[16] Increasing the concentration of the dopant beyond this point was found to decrease the conductivity.[16] Untilova et al. also demonstrated that in thin films of P3HT/F4TCNQ, despite an expected maximum doping

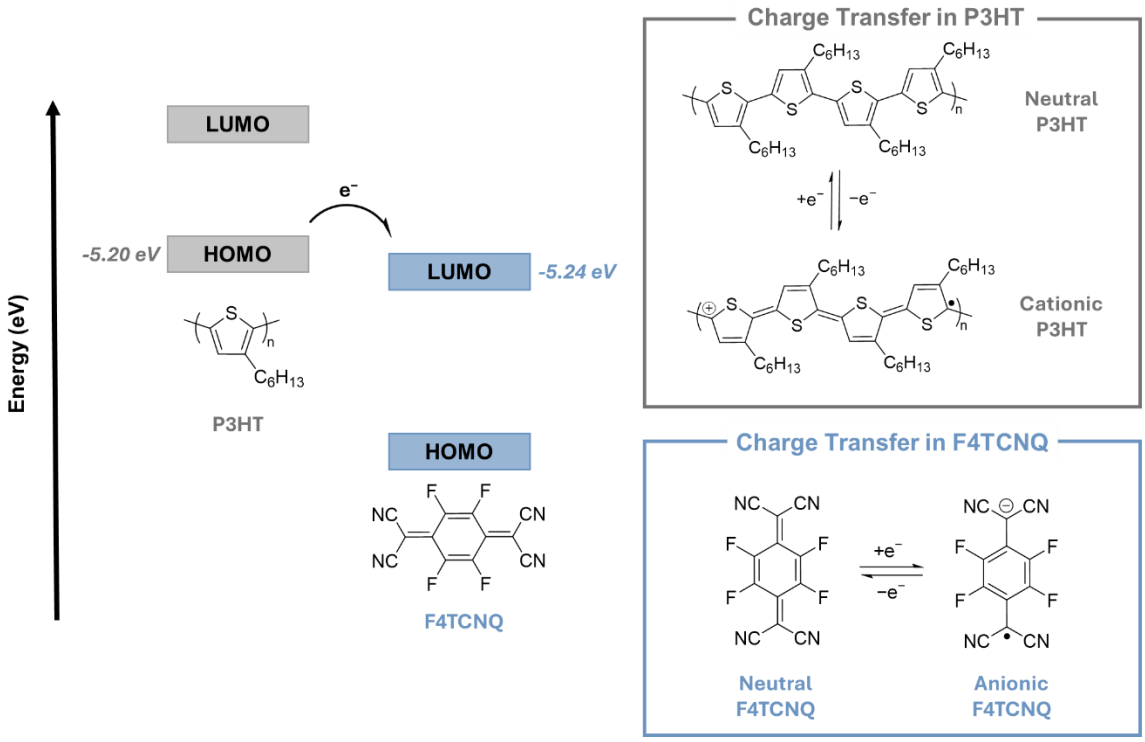

Figure 1.2. Energy diagram schematic of p-type doping between P3HT and F4TCNQ. The subsequent formation of the charged species, cationic P3HT (or polaron) and anionic F4TCNQ (F4TCNQ⁻) by charge transfer, is depicted on the right.

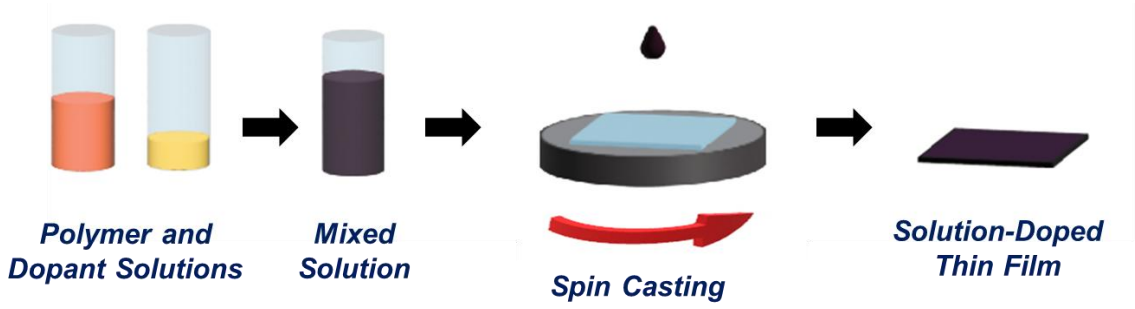

Figure 1.3. Illustration of the method used to prepare solution-doped thin films.

concentration of 25 mol%, the apparent doping level determined experimentally is only ~14 mol%.[23] These results, along with others, indicate that the saturation limit is 20-25 mol% F4TCNQ. Thereafter, the addition of more dopant is detrimental because the excess dopant no longer participates in electron transfer–rather, it acts as insulating material.[16,23,24]

Another disadvantage of using large amounts of dopant during the solution doping process is the propensity for aggregates to form. Upon electron transfer, for example, from P3HT to F4TCNQ, a charged complex is formed. These complexes are inherently insoluble in the organic solvents that are required to dissolve the conjugated polymers.[13,25,26] Thus, the charge complexes aggregate and/or precipitate from solution and because the thin films take on the characteristics of their parent casting solution, these aggregates are also present in the thin films. In addition to the presence of ill-defined aggregate structures, charge carriers are usually confined to these aggregates, which restricts their mobility and decreases film conductivity.[27,28] Therefore, alternative doping approaches in which aggregation is minimized have become prominent.

The most widely accepted alternative doping method is sequential doping. With sequential doping, a pristine polymer film is cast first and then the dopant is added in a secondary doping step, as depicted in Figure 1.4.[13,25,26,29] Most studies that utilize P3HT as the conjugated polymer state that solution doping is absolutely inferior to sequential doping because the process of sequential doping prevents the formation of aggregates and minimizes disruption of the microscale organization of the pristine polymer film.[13,26] For example, Scholes et al. showed that P3HT films sequentially-doped with F4TCNQ had the same size and orientation of crystallites in comparison to as-cast P3HT films.[26]

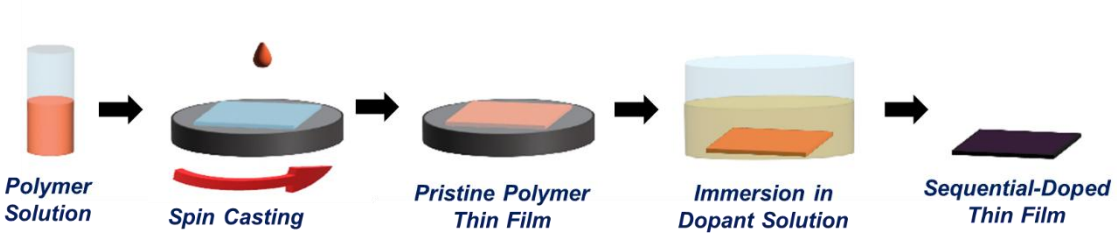

Figure 1.4. Illustration of the method used to prepare sequentially-doped thin films.

Although sequential doping effectively prevents aggregation, it relies heavily on finding an optimal dopant solvent.[30-32] The dopant solvent must swell the polymer chains to allow for effective dopant integration without dissolving the underlying polymer film. Yoon et al. showed that with sequentially-doped films of P3HT, the degree of solubility of the conjugated polymer with respect to the dopant solvent significantly impacted the resulting electrical conductivity.[30] Specifically, a higher density of charge carriers were generated when dopant solvents that had moderate solubility for the polymer and good wettability with the polymer film were used.[30]

Other doping methods that enhance the efficiency of doping and increase the resultant conductivity have also been reported. For example, Fontana et al. demonstrated that evaporation-based sequential doping of P3HT with F4TCNQ yields electrical conductivities and degrees of doping that are similar to those realized by solution-based sequential doping.[25] However, while the evaporation-based doping is more advantageous for large-area films, solution-based sequential doping is better for films with micrometer scale thicknesses.[25] A method called "Sequential-Twice-Doping" was developed by Chai et al. in which P3HT was solution-doped with F4TCNQ (at 7 mol%) and the resulting film was then sequentially-doped through immersion of the solution-doped film in an iron chloride ($FeCl_3$) solution.[33] Their assessments of morphology showed that the solution doping step doped the amorphous regions while the sequential doping step improved doping efficiency while maintaining the size of crystalline domains.[33] Additionally, the films doped via Twice-Sequential-Doping exhibited enhanced conductivity compared to the solution- and sequential-doped counterparts.[33] Similarly, Yoon et al. used what they

called a “hybrid doping” approach in which P3HT was doped in solution with F4TCNQ at various levels (5-20 wt%), cast into a thin film, and then sequentially-doped by immersion in an F4TCNQ solution.[34] This hybrid doping method resulted in higher film conductivity compared to solution doping or sequential doping alone and also maximized the thermoelectric power factor.[34]

These studies of various doping processes provide valuable insights into the key factors required to enhance doping efficiency and conductivity. However, many of these efforts focus exclusively on the polymer/dopant pair of P3HT/F4TCNQ, which calls into question whether these methods are broadly applicable to other conjugated polymers. Moreover, careful reading reveals a lack of standardized doping procedures (i.e., concentrations, solvents, film thicknesses, etc.), which hinders meaningful comparison between different studies. Therefore, systematic studies are essential to deepen our understanding of doping across a variety of conjugated polymers.

1.3. Spacing Units in Repeat Unit Designs of Conjugated Polymers

The efficiency of chemical doping relies on the ability of the dopant to non-covalently interact with the conjugated backbone of the polymer chain; however, these interactions are commonly disrupted or hindered by the presence of side chains along the chain. Typically, long alkyl side chains are used to disrupt intermolecular π-stacking interactions of the polymer chains to allow for greater solubility in organic solvents; however, the presence of these chains can also sterically hinder polymer-dopant interactions.[35-37] Thus, a few studies have focused on altering the density of side chains along the conjugated backbone to improve conductivity.[14,38,39] One such strategy is to

introduce spacing units into the repeat unit design. These spacing units are aryl units without side chains to provide free space (reduce steric demand) for the dopant to interact with the conjugated backbone. Figure 1.5 shows a schematic example of how the presence of a spacing unit that reduces the steric barrier along the backbone enhances accessibility of dopant molecules to the polymer backbone. It is known that in the case of P3HT, which is a semicrystalline polymer, doping is most effective when the F4TCNQ resides in the lamellae and is in close proximity to the backbone.[40,41] Thus, when no spacing unit is present, the side chains can hinder this proximity. However, with the introduction of a spacer units along the chain, the steric barrier for the dopant to approach and reside at/near the backbone is reduced, which allows interaction between the dopant and the polymer backbone, thereby efficiently facilitating electron transfer. An example of this strategy of altering sterics along the backbone comes from Li et al., who showed that the incorporation of fused-ring thienothiophene spacer units into poly(quaterthiophene) enhanced doping efficiency by reducing the steric demand along the backbone, which ultimately led to higher conductivity in sequentially-doped thin films.[14] Similarly, Nam et al. designed diketopyrrolopyrrole (DPP)-copolymers with cyclopentadithiophenes and cyclopentadithiophenyl thiophene donor groups to create sparse designs in terms of intramolecular alkyl chain spacing compared to traditional DPP-copolymers. They demonstrated that these structural changes resulted in enhanced doping efficiency.[38]

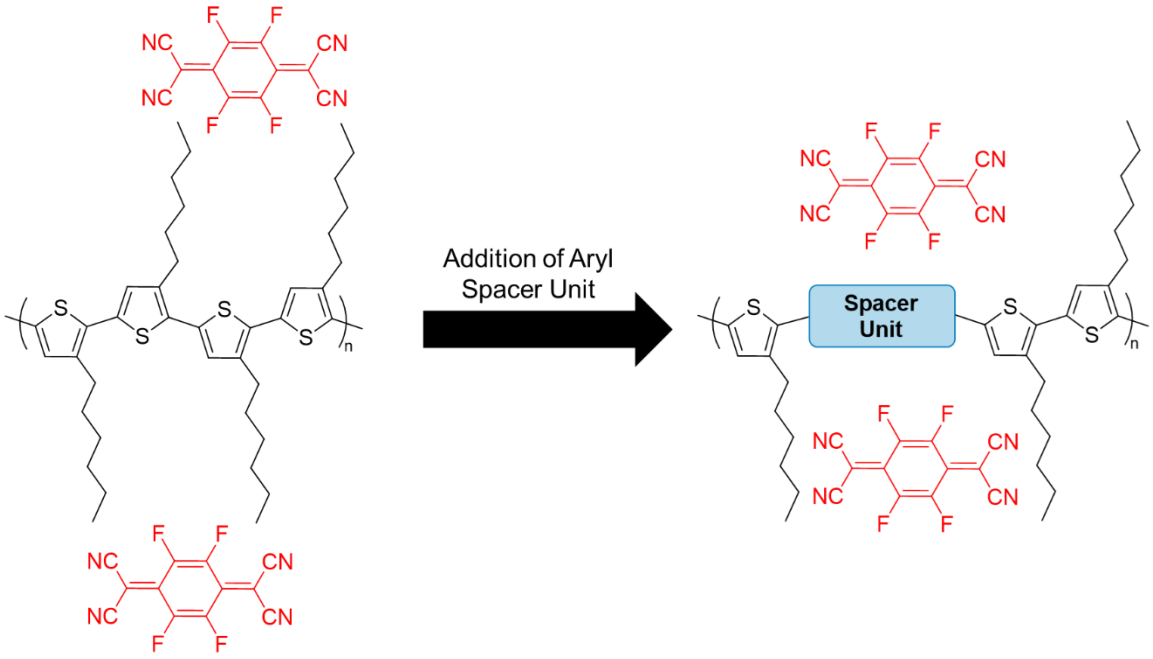

Figure 1.5. Generic depiction of polymer-dopant interactions with and without the use of a spacing unit.

1.4. Synthesis and Characterization of Conjugated Polymers

In this dissertation, I will describe the synthesis and characterization of a series of thiophene-based copolymers. The synthesis of these copolymers will focus on the incorporation of spacing units to enhance polymer-dopant interactions and ultimately increase the electrical conductivity of thin films. However, film conductivity is impacted by a complex interplay between polymer design, solubility, and morphology. Therefore, studies aimed to unravel these relationships will be of significant importance and focus.

1.4.1. Copolymer Synthesis via Direct Arylation Polymerization (DArP)

Direct arylation polymerization (DArP) has emerged as a widely used method for synthesizing conjugated polymers due to its environmentally friendly nature, atom efficiency, and cost-effectiveness compared to traditional palladium cross-coupling reactions (i.e., Stille and Suzuki cross-couplings) that are typically used in conjugated polymer synthesis.[42-45] For the research described in this dissertation, DArP is particularly useful because its known to be highly effective with thiophene-based monomers.[42]

DArP is a step-growth polymerization method that relies on C−H activation to couple arenes and haloarenes.[42,46] Polymers made via DArP can be synthesized from either AB type monomers in which monofunctional haloarenes are used or AA+BB type comonomers in which a dihaloarene monomer is coupled with an arene.[42,46] These two processes are depicted in Figure 1.6. With AB type polymerizations, the resultant polymer is regioregular and has known end groups of −H and −X (typically X = Cl or Br). On the other hand, AA+BB type polymerizations will only produce a regioregular polymer if both

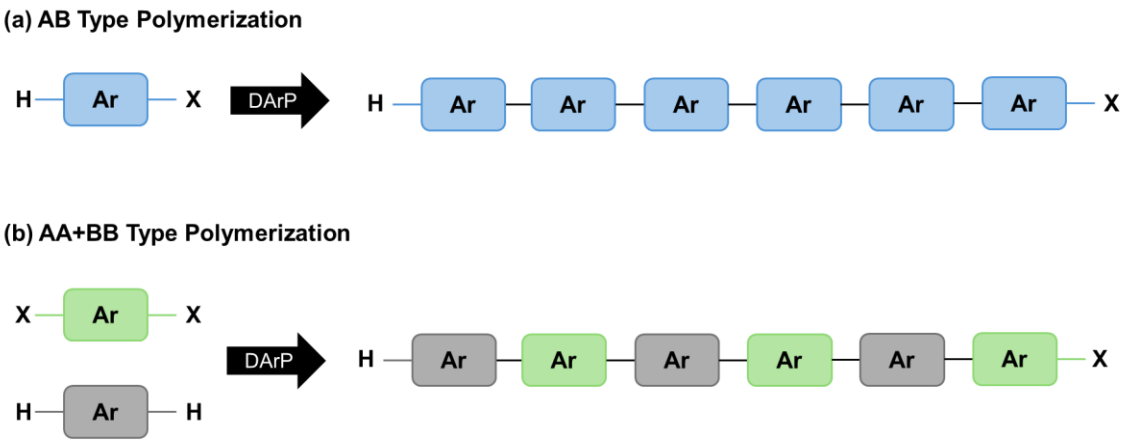

Figure 1.6. Illustration of DArP for (a) an AB type polymerization and (b) an AA+BB type polymerization.

the AA and BB monomers are symmetric; otherwise a regio-irregular polymer will be made. Also, due to the nature of the AA+BB type polymerization, the end groups are essentially unknown because the chain ends could be either −H/−H, −H/−X, or −X/−X.

Figure 1.7 shows the proposed catalytic cycle of DArP using the AB monomer, 2-bromo-3-hexythiophene, as the example.[42,43,46] Fundamentally, the process relies on palladium catalyst-directed activation of an aromatic C-H bond through a concerted metalation-deprotonation pathway. The catalytic cycle begins with the oxidative addition of the haloarene to the Pd(0) catalyst. Next, a carboxylic acid, serving as a proton shuttle, is deprotonated by a base to facilitate ligand exchange with the halide. This is followed by a concerted metalation-deprotonation step, during which a six-membered transition state is formed, where the α-proton of the arene (here, from the haloarene) undergoes deprotonation by the proton shuttle while the palladium-carbon bond is formed. Finally, reductive elimination yields the coupled product.

With this cross-coupling catalytic cycle there are undesired byproducts that can form, with the most notable being homocoupling and β-coupling.[42,43] Homocoupling occurs when the haloarene couples to itself via activations of two C-X bonds. Homocouplings are detrimental to the polymerization because it can terminate the polymerization and/or alter the stoichiometric balance while also changing the regioisomerism of the polymer.[42,43] These homocoupling defects can usually be avoided by removing residual oxygen and other oxidative impurities that can convert Pd(0) to Pd(II) and by lowering the catalyst loading levels.[42,43] On the other hand, β-coupling occurs when

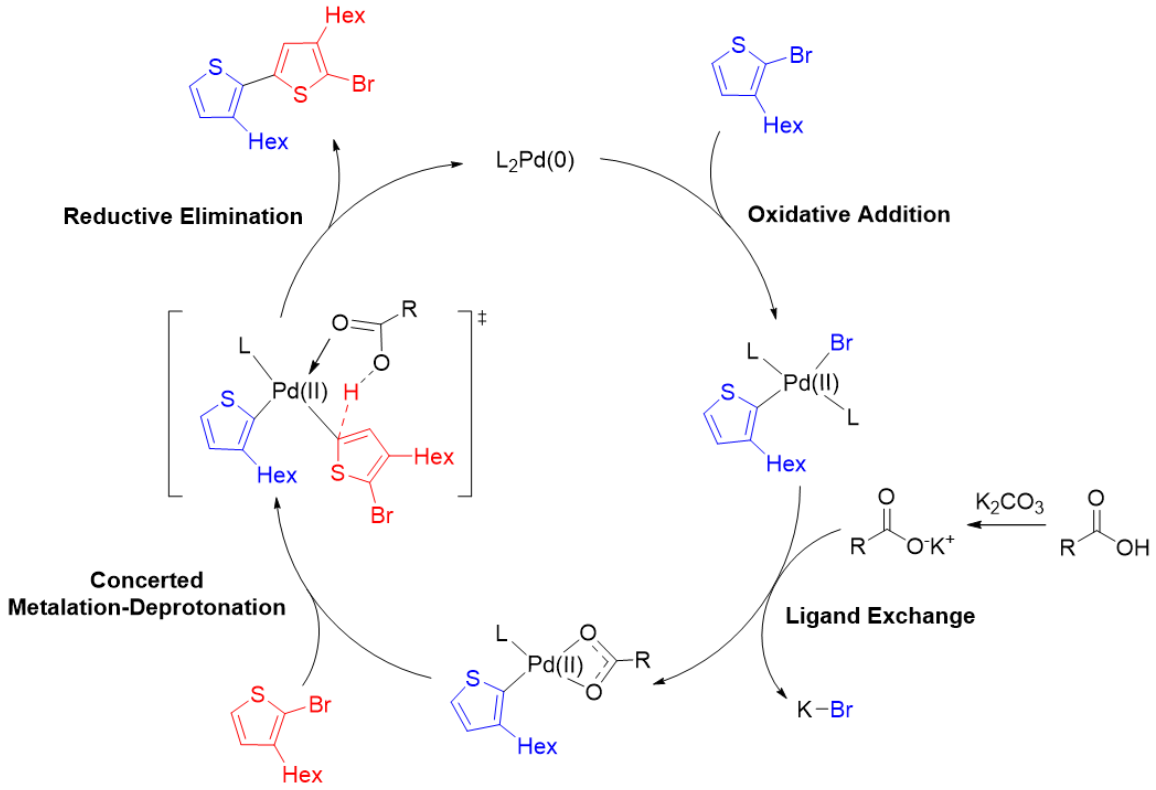

Figure 1.7. Proposed catalytic cycle for DArP using 2-bromo-3-hexylthiophene, an AB type monomer, as an example.

a vicinal proton (e.g., the β-proton of 3-substitued thiophene) is activated rather than the α-proton.[42,43] This defect can be minimized by using lower temperatures and bulkier proton shuttles that sterically hinder the β-position.[42,43]

1.4.2. Quantifying Solubility of Conjugated Polymers

The relationship between Gibbs free energy, enthalpy, and entropy, which is shown in Equation 1.1, is commonly used to describe any non-reactive process at constant temperature and pressure, including dissolution of a solute in a solvent.[47] Therefore, examining entropic and enthalpic contributions can provide valuable information on the solubility of polymers in a solvent.

$$\Delta G = \Delta H - T\Delta S \qquad \text{(Eq. 1.1)}$$

The conformational mobility of polymer chains and number of different accessible states of equal energy dictates that the change in entropy associated with making a solution, ΔS, would be positive.[47] Therefore, it can be concluded that the magnitude of enthalpy change, ΔH, dictates the sign of ΔG, making ΔH the most important contribution that determines solubility. For all systems, $\Delta G < 0$ signifies a spontaneous process and a negative ΔG would describe a polymer that dissolves spontaneously in a specific solvent. Given that dissolution is marked by $\Delta S > 0$, a small ΔH is required to achieve dissolution.[47]

Dissolution can be thought of as a mixing of two pure compounds (polymer and solvent), thus the enthalpy change can be described by the heat of mixing (ΔH_{mix}). Hildebrand and Scott proposed that the ΔH_{mix} can be calculated based on the energy of vaporization (per volume) of both the solute (1) and the solvent (2) as illustrated in Equation 1.2.[47] In this expression, V_{mix} is the volume of the mixture, V_1 and V_2 are the molar

volumes of the two components, Φ_1 and Φ_2 are their respective volume fractions, and ΔE_1 and ΔE_2 are the energies of vaporization of each component.

$$\Delta H_{mix} = V_{mix}\left[\left(\frac{\Delta E_1}{V_1}\right)^{1/2} - \left(\frac{\Delta E_2}{V_2}\right)^{1/2}\right]^2 \Phi_1 \Phi_2 \qquad \text{(Eq. 1.2)}$$

Additionally, $\Delta E/V$ is defined as the cohesive energy density, which describes the amount of energy needed to remove one unit volume of molecules from their neighbors.[47] Thus, a higher cohesive energy density indicates stronger intermolecular interactions that make it more difficult to vaporize (remove to the gaseous state) molecules from a substance. The term $(\Delta E/V)^{1/2}$ is typically represented by δ, which is known as the solubility parameter, thus resulting in Equation 1.3.[47]

$$\Delta H_{mix} = V_{mix}\,(\delta_1 - \delta_2)^2 \Phi_1 \Phi_2 \qquad \text{(Eq. 1.3)}$$

As previously mentioned, ΔG must be negative for a polymer to dissolve; therefore, ΔH must be small to ensure solubility. This indicates that δ_1 and δ_2 must be close or equal.[47] Thus, predictions of solubility can be made based on the respective solubility parameters of the polymer and solvent forming the mixture. However, this parameter, which is considered the Hildebrand solubility parameter, is limited in its applicability. The Hildebrand model is useful for amorphous, nonpolar polymers, but breaks down when describing semicrystalline and/or polar polymers.[48] More specifically, because nonpolar polymers do not have significant polar and/or hydrogen-bonding interactions, the cohesive energy adequately captures the attractive intermolecular interactions that govern solubility. However, with more polar polymers, hydrogen bonding and dipole interactions are more prevalent, making predictions of solubility based only on the cohesive energy more problematic.[48] To account for polar interactions of polymers, the Hansen model was

developed. This model utilizes three parameters defined as δ_D, δ_P, and δ_H to characterize dispersive, polar, and hydrogen-bonding contributions, respectively.[48,49] With these Hansen solubility parameters (HSPs), the character of a solvent, whether it is "good" or "poor" for a polymer, is described by the solubility parameter distance, R_a, which is expressed through differences between the polymer and solvent interaction energies. This parameter is calculated using Equation 1.4, where the subscripts p and s on the HSPs corresponds to the polymer or to the solvent, respectively.[49] A low R_a value indicates a good solvent for the polymer while a high R_a value indicates a poor solvent for the polymer.[49]

$$R_a = (4(\delta_{Dp} - \delta_{Ds})^2 + (\delta_{Pp} - \delta_{Ps})^2 + (\delta_{Hp} - \delta_{Hs})^2)^{1/2} \qquad \text{(Eq. 1.4)}$$

In this dissertation, I will assess the HSPs of each copolymer to quantify polymer-solvent interaction energies, thereby providing insight into how a particular solvent used for doping impacts conductive properties of the film.

1.4.3. Thin Film Morphology

As discussed previously, thin film conductivity is significantly influenced by the morphology of doped films. Grazing incidence wide angle x-ray scattering (GIWAXS) is commonly used to probe thin film crystallinity of conjugated polymer thin films in their pre- and post-doped states.[14,25,26,50,51] GIWAXS is specifically used instead of other scattering techniques (i.e., grazing incidence small angle x-ray scattering) as it probes length scales associated with molecular packing, such as lamellar spacing and π-stacking distances.[50] This method relies on x-rays incident on a surface at a low incident angle (α_i) and once the x-rays interact with the atoms/molecules of the film, scattering occurs.[50,52]

The scattering vector, q, describes the spatial frequency of the features that give rise to scattering in a material, and it is defined in Equation 1.5, where λ is the x-ray wavelength and θ is the scattering angle.[50,53]

$$q = \frac{4\pi}{\lambda}\sin(\theta) \quad \text{(Eq. 1.5)}$$

The scattering occurs in both the out-of-place (q_z) and in-plane (q_x) direction and offers information about crystal orientation and inter-layer spacing.[50] Specifically, when scattering is observed mainly in the out-of-plane direction, the polymer crystallites prefer an edge-on orientation while a face-on orientation is preferred when scattering is observed primarily in the in-plane direction.[50,52] The *d*-spacing (d) of the planes of polymer chains can be determined from q using the relationship shown in Equation 1.6.[52]

$$q = \frac{2\pi}{d} \quad \text{(Eq. 1.6)}$$

Significant work has focused on characterizing P3HT and F4TCNQ-doped P3HT thin films using GIWAXS. Therefore, it is known that P3HT is semi-crystalline and prefers an edge-on orientation relative to the substrate.[26,40,50] F4TCNQ predominantly resides in the lamellae of P3HT, as evidenced by increases in the *d*-spacing in the out-of-plane direction.[26,40] Additionally, it has often been reported that the crystallinity in the out-of-plane direction is advantageous for achieving high in-plane conductivities because charge transport does not occur across the lamellae, but rather, charge carriers move intramolecularly, along the polymer backbone, and/or intermolecularly through the π-π stacked assemblies of chains.[22,54,55] Therefore, in this research, particular emphasis will be

placed on scattering in the out-of-plane direction, as this contributes directly to in-plane conductivity measurements.

1.4.4. Electrical Conductivity

A main method used to characterize the performance of chemically doped conjugated polymer films is electrical conductivity. The measurement technique used in this dissertation research is based on the method developed by Leo J. Van der Pauw.[56] Hence it is commonly known as the Van der Pauw method. The Van der Pauw method is used to measure the in-plane conductivity of thin films, regardless of the shape or size.[57-59] This is done by first adding conductive contacts to the edges of the sample area and then a voltage is applied along one edge while the current is measured along on the opposite edge.[57-59] A circuit diagram for a measurement in the vertical direction is depicted in Figure 1.8. Specifically, the diagram here shows the voltage being applied across contact points 1 and 2 while the current is measured across contact points 3 and 4. It should be noted that this measurement can be performed by applying a fixed voltage or by using an I-V sweep in which the voltage is steadily ramped at set increments to obtain measurements across a range of voltages. With either method, Ohm's Law, $V = IR$, is then used to calculate the resistance for the configuration, which in Figure 1.8 is identified as R_{1324}, indicating that voltage is applied across contacts 1 and 3 with the current measured across contacts 2 and 4. The measurements are then repeated until the resistance is obtained along each edge to determine R_V (vertical) and R_H (horizontal).[57-59] However, because resistance is an extrinsic property, it is dependent on the geometry of the material, which makes it difficult

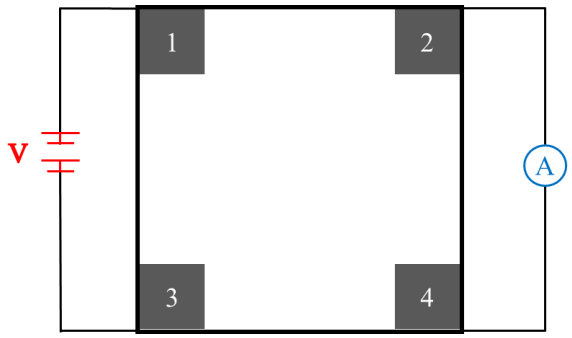

$$R_V = \frac{R_{1324} + R_{2413}}{2}$$

$$R_H = \frac{R_{1234} + R_{3412}}{2}$$

Figure 1.8. Circuit diagram of Van der Pauw measurements to obtain resistance in the vertical (R_V) and horizontal (R_H) direction. Note that the subscripts of each measured resistance identifies the orientation in which the measurement was performed. The first two numbers indicate the contact points that have the voltage applied to them while the last two numbers identify the contact points that are used to measure the current.

to compare samples to each other. Therefore, the Van der Pauw equation, shown in Equation 1.7, is used to determine the sheet resistance of the sample.[57-59]

$$e^{-((\pi R_V)/R_S)} + e^{-((\pi R_H)/R_S)} = 1 \qquad \text{(Eq. 1.7)}$$

However, the Van der Pauw equation can be simplified considerably with the assumption that $R_H \approx R_V$, which is true in the case of an isotropic sample with uniform thickness, resulting in Equation 1.8.[57-59]

$$R_s = \frac{\pi}{\ln(2)} R_{V,H} \qquad \text{(Eq. 1.8)}$$

Then using the film thickness, t, the resistivity, ρ, which is an intrinsic property can be calculated: $\rho = tR_s$. Finally, the inverse of resistivity is conductivity, σ: $\sigma = 1/\rho$. The calculation of conductivity allows for thin film measurements of different geometries, sizes, and thicknesses to be directly compared.

1.5. Motivation and Research Objectives

The central theme of my dissertation work is to elucidate design-structure-property relationships of thiophene-based conjugated copolymers featuring expanded cores. Within this, a key aspect of my research is to gain insight into how solubility and film morphology impact electrical conductivity with an emphasis on the doping method used. To achieve this, a series of thiophene-based copolymers with various spacing units were synthesized to enable a systematic study of how increasing the length of the spacing unit impacts solubility, morphology, and conductivity. With this in mind the specific goals of my research are as follows:

1. Evaluate how the incorporation of spacing units in thiophene-based copolymers impacts their solubility, thin film morphology, and conductivity.

2. Investigate how various doping methods, namely solution-, sequential-, and serial-doping, impact thin film morphology and conductivity.
3. Examine the impact of polymer-solvent interaction energy on dopant integration and thin film conductivity.

In *Chapter 2*, I describe a set of expanded core thiophene-based copolymers having various spacing units that were synthesized and characterized. These copolymers were then doped via solution and sequential doping methods. The topography and conductivity of the doped thin films were measured, as well as doping efficiency. Recognizing that the structure of the polymers affected their solubility, sequential doping was performed with various solvents to explore the impact that solvent-polymer interaction energy has on conductivity. This revealed a universal solvent quality dependence across all of the thiophene-based copolymers. In *Chapter 3*, the phenomenon of chemical doping was further explored by utilizing a two-step doping method, referred to here as serial doping, which consists of successive use of both solution doping and sequential doping steps. Films that were doped by serial doping exhibited an increase in conductivity relative to films doped with only solution doping or sequential doping. This enhancement in conductivity is attributed to an increase in crystallite formation, despite the amorphous character of the pristine polymer film. The research presented in *Chapter 4* investigates differences between conjugated polymer molecular weights obtained by gel permeation chromatography (GPC) using different analysis methods. Specifically, I explore how molecular weights obtained using conventional and universal calibration analyses compare to those determined using triple detection and relate those differences to the Mark-

Houwink parameters and d*n*/d*c* of the polymers. *Chapter 5* extends the idea and proof for the concept of universality in solvent-quality dependent conductivity that was observed in the work described in *Chapter 2.* This is accomplished by examining more complex copolymers consisting of dioxythiophene and dihydropyrrolopyrrole moieties. The same universality seen for thiophene-based polymers is observed for these copolymers; however, slight differences are seen based on the solubility and polarity of the copolymer (as evidenced by HSPs). Lastly, *Chapter 6* summarizes the major findings and insights from my dissertation research and ideas for future directions are presented and discussed.

Chapter 2. Universality in Solvent-Dependent Conductivity of Conjugated Thiophene-Based Copolymers with Expanded Core Monomer Designs

This chapter describes in part the work published in *Chemistry of Materials*, 2025, 37(4), 1667-1680. I synthesized all monomers and polymers described in this work and performed all the structural characterizations. I also performed all characterization including solubility parameter determination, absorbance measurements, and conductivity measurements. Coauthors include Sina Sabury and C. Elizabeth O'Connell, who designed and developed the synthetic procedures for the monomers and polymers, and Prof. S. Michael Kilbey II, who advised this work. This research was supported in part by the National Science Foundation (award #2204396).

2.1. Abstract

Conjugated polymers are promising materials for organic electronic devices; however, to achieve metal-like electrical properties, these materials need to be chemically doped. In this chapter, a series of structurally tailored thiophene-based copolymers are studied to elucidate relationships between copolymer design, doping method, solubility, and electrical conductivity. Results show that increasing the distance between side chains along the conjugated backbone increases thin film conductivity, with conductivities eclipsing that of P3HT by several orders-of-magnitude for solution and sequential doping with F4TCNQ. In addition, conductivities of films subjected to sequential doping show a dependence on polymer-solvent interaction energy that appears universal for this series of thiophene-based copolymers, which offers a potentially predictive basis for choosing an optimal solvent for doping. These studies also show that sequential doping provides higher thin film conductivity at lower concentrations of anionic F4TCNQ. This indicates that sequential doping is superior in that less dopant is necessary to achieve the same, if not

greater, electrical performance for these thiophene-based copolymers. Overall, this work provides fundamental insight into how copolymer design, doping method, and strength of polymer-solvent interaction energy impacts electrical performance, paving the way for printed electronics, sensors, and other applications for chemically-doped conjugated polymers.

2.2. Introduction

Conjugated polymers are promising materials for thermoelectric devices, sensors, and printed electronics due to their electrical and mechanical properties.[3,60-62] However, conjugated polymers are typically semiconducting or insulating in nature and must be doped to attain useful electrical conductivities. Therefore, molecular dopants are used to either oxidize (p-doping) or reduce (n-doping) conjugated polymers to generate charged carriers, resulting in greater conductivity.[3,15,63] P-type doping is more prevalent in organic semiconductors due to the greater stability of p-type dopants in ambient conditions and electron-donating π-systems of common conjugated polymers.

One of the most extensively studied p-type systems is that of P3HT and F4TCNQ. F4TCNQ is particularly well suited for p-doping due to its deep LUMO level (-5.24 eV), which aligns well with the HOMO level of P3HT (-5.2 eV).[13,15] This energy level alignment allows for facile electron transfer from the polymer to the dopant, resulting in the formation of a charged complex. However, the regioregularity of P3HT significantly impacts the doping process and resultant conductivity. Hynynen et al. showed that P3HT with a regioregularity of 28% had a very low degree of doping (as evidenced by the lack of anionic F4TCNQ formation) while P3HT samples with regioregularity above 84% could

be readily doped with F4TCNQ.[40] Guchait et al. found that charge conductivity in regioregular P3HT was roughly 50 times higher than that of regiorandom P3HT due to the increased doping level associated with regioregular P3HT.[29] The change in electrical performance with higher degrees of regioregularity is not only due to the increased doping levels, but also to enhanced microstructural organization. For instance, Noriega et al. studied doping of blends of regiorandom P3HT with regioregular P3HT nanofibrils and determined that within the heterogenous microstructure adopted by the blends, charge carriers were confined to the ordered nanofiber regions due to energetic offsets at order/disorder interfaces.[27] Additionally, Pingel et al. found that with P3HT, the macroscopic charge mobility was two orders-of-magnitude lower than the local mobility due to heterogeneity in the microscale organization.[28] The macroscopic mobility was reduced (compared to the local mobility) due to the disordered regions in the system.[28] These studies highlight that regioregular P3HT is superior compared to regiorandom P3HT in that higher doping levels, greater microstructural organization, and higher electrical performance can be achieved.

To improve their solubility, conjugated polymers are typically decorated with aliphatic side chains; however, these side chains may inhibit polymer-dopant interactions due to increased steric demand. Therefore, it has become conceptually attractive to alter polymer design to increase the "spacing length" between alkyl chains in the backbone of conjugated polymers to allow for increased polymer-dopant interactions. For example, Li et al. studied the incorporation of a thienothiophene spacer unit in a quaterthiophene-based polymer and found that separating the side chains along the backbone improved dopant

integration.[14] This in turn improved ordering and π-stacking while also increasing doping efficiency and conductivity.[14] Similarly, Nam et al. showed that introducing thiophene spacing units in diketopyrrolopyrrole (DPP) copolymers enhanced intercalation of the dopant into the lamellae, thereby enhancing doping efficiency.[38] These works highlight how polymer design can be strategically tuned to improve doping efficiency and enhance conductivity, though it should be appreciated that decreasing the number density of side chains alters solubility.

In addition to altering polymer design, the method of dopant integration is known to have a significant impact on doping efficiency and, therefore, conductivity. Specifically, solution and sequential doping have been extensively studied, especially with the polymer-dopant system of P3HT and F4TCNQ. In the case of solution doping, polymer and dopant solutions are directly mixed and then cast to form doped polymer thin films.[13,15] This approach typically results in a significant number of aggregates due to the formation of charged complexes that are too polar to be dissolved in the same solvent that is used to dissolve the neutral polymer.[13,25,26] These ill-defined aggregate structures result in heterogenous microstructures that restrict charge mobility and decrease film conductivity. For example, Jacobs et al. showed that once solutions containing aggregated assemblies generated via solution doping were cast into films, there were highly conductive crystalline domains; however, these domains were not connected, thus the conductivity of the film was diminished.[13] With sequential doping, the polymer film is created first by casting, and then the dopant is added by exposing the film to a dopant solution that uses a marginal solvent for the polymer that swells, but does not dissolve the polymer.[13,25] This method

avoids the formation of aggregates and minimizes disruption of the microscale organization of the pristine polymer film. For instance, Scholes et al. showed that with sequential doping of P3HT with F4TCNQ, the size and orientation of the crystallites were unchanged in comparison to the as-cast P3HT films.[26] Although the sequential doping method prevents aggregation of the copolymer, it relies heavily on finding an appropriate solvent.[30,31] Yoon et al. showed that the degree of solubility of the conjugated polymer with respect to the dopant solvent impacts resultant electrical conductivity in sequentially-doped films.[30] Specifically, greater charge carrier generation was seen with dopant solvents that offer moderate solubility for the polymer and good wettability, which enhanced dopant diffusion into the film.[30] Overall, most studies that focus on P3HT and F4TCNQ have defined a heuristic that solution doping is absolutely inferior to sequential doping, despite the convenience afforded by this method.[13,25,26]

Herein, we report the synthesis and characterization of thiophene-based copolymers in which the π-conjugated repeat unit is systematically altered to increase the spacing length between alkyl side chains. We examine the impact that copolymer design has on optoelectronic properties, solubility, and electrical performance (i.e., conductivity) as functions of doping level and method. We find that the heuristic defined for the benchmark P3HT/F4TCNQ system is not universal; however, the dependence on solvent quality with sequential doping appears to follow a consistent pattern of behavior across the spectrum of thiophene-based copolymers studied.

2.3. Materials and Methods

2.3.1. Materials

2,5-bis(trimethylstannyl)thiophene (97%, Sigma), 2,5-bis(trimethyl-stannyl)thieno-[3,2-*b*]thiophene (97%, Sigma), 5,5'-dibromo-2,2'-bithiophene (98%, TCI), 5,5"-dibromo-2,2':5',2"-terthiophene (97%, Sigma), 2-bromo-3-hexylthiophene (97%, Sigma), 3-hexylthiophene-2-boronic acid pinacol ester (95%, Sigma), 3-hexyl thiophene (99%, Sigma), tetrakis(triphenylphosphine)palladium(0) ($Pd(PPh_3)_4$, 99%, Sigma), palladium(II) acetate ($Pd(OAc)_2$, 98%, Sigma), potassium carbonate (99.7%, Fisher), neodecanoic acid (NDA, Sigma), magnesium sulfate ($MgSO_4$, 99.5%, Alfa Aesar), 2,3,5,6-tetrafluoro-7,7,8,8-tetracyanoquinodimethane (F4TCNQ, 99%, Ossila), lithium iodide (LiI, 99.999%, ultra dry, Alfa Aesar), toluene (99.85%, extra dry, Thermo Scientific), diethyl ether (anhydrous, Fisher), ethyl acetate (99%, Fisher), hexanes (98.5%, Fisher), dimethyl formamide (DMF, 99.8%, Thermo Scientific), N,N-dimethylacetamide (DMAc, 99.5%, extra dry, Thermo Scientific), methanol (99%, Fisher), acetone (99%, Fisher), chloroform (98%, Fisher), chlorobenzene (99.8%, anhydrous, Sigma), acetonitrile (99%, Fisher) and graphite conductive adhesive (aqueous based, Alfa Aesar) were used as received. N-bromosuccinimide (NBS, 99%, Sigma) was recrystallized in water and vacuum dried prior to use.

2.3.2. Synthesis of Core Expanded Monomers and Polymerization Method

Synthesis of 3,3''-dihexyl-2,2':5',2''-terthiophene (**M3**). 2,5-bis(trimethylstannyl)-thiophene (409 mg, 1 mmol, 1 equiv.) was added to a dry 100 mL 3-neck round bottom flask fitted with a condenser under positive argon pressure. 2-Bromo-3-hexylthiophene

(494 mg, 398 µL, 2 mmol, 2 equiv.), tetrakis(triphenylphosphine)-palladium(0) ($Pd(PPh_3)_4$, 69 mg, 0.06 mmol, 0.06 equiv.), and 50 mL dry toluene were added to the reaction flask under positive argon pressure. The remaining necks of the flask were sealed with rubber septa and the reaction mixture was stirred at reflux temperature for 24 h. After this time, the reaction was quenched by adding deionized (DI) water to the flask. The crude product mixture was extracted with 100 mL of diethyl ether and the aqueous phase was discarded. The organic phase was washed with brine (3×) and then dried over $MgSO_4$. The $MgSO_4$ was removed by filtration and the crude product mixture was concentrated via rotary evaporation. The crude product was then isolated via silica gel column chromatography using a 98:2 hexanes:ethyl acetate mixture as the mobile phase. The purified product was subsequently concentrated via rotary evaporation and isolated as a colorless oil at an overall yield of 92%. ^{1}H NMR (500 MHz, $CDCl_3$) δ (ppm): 7.19 (d, J = 5.1 Hz, 2H), 7.09 (s, 2H), 6.97 (d, J = 5.2 Hz, 2H), 2.85 – 2.80 (m, 4H), 1.73 – 1.65 (m, 4H), 1.46 – 1.31 (m, 12H), 0.96 – 0.90 (m, 6H). ^{13}C NMR (500 MHz, $CDCl_3$) δ (ppm): 139.71, 136.10, 130.45, 130.07, 126.07, 123.76, 31.73, 30.77, 29.34, 29.29, 22.68, 14.14.

Synthesis of 2,5-bis(3-hexylthiophen-2-yl)thieno[3,2-b]thiophene (**M4**). 2,5-bis(trimethyl-stannyl)thieno[3,2-*b*]thiophene (465 mg, 1 mmol, 1 equiv.) was added to a dry 100 mL 3-neck round bottom flask fitted with a condenser under positive argon pressure. 2-Bromo-3-hexylthiophene (494 mg, 398 µL, 2 mmol, 2 equiv.), $Pd(PPh_3)_4$ (69 mg, 0.06 mmol, 0.06 equiv.), and 50 mL dry toluene were added to the reaction flask under positive argon pressure. The remaining two necks of the flask were sealed with rubber septa and the reaction mixture was stirred at reflux temperature for 24 h. After this time, the

reaction was quenched by adding DI water to the flask. The crude product mixture was extracted with 100 mL of diethyl ether and the aqueous phase was discarded. The organic phase was washed with brine (3×) and then dried over $MgSO_4$. The $MgSO_4$ was removed by filtration and the crude product mixture was concentrated via rotary evaporation. The crude product was then isolated via silica gel column chromatography using a 98:2 hexanes:ethyl acetate mixture as the mobile phase. The purified product was subsequently concentrated via rotary evaporation and isolated as a yellow powder at an overall yield of 49%. ^{1}H NMR (500 MHz, $CDCl_3$) δ (ppm): 7.27 (s, 2H), 7.23 (d, J = 5.2 Hz, 2H), 6.99 (d, J = 5.2 Hz, 2H), 2.87 – 2.80 (m, 4H), 1.74 – 1.65 (m, 4H), 1.46 – 1.29 (m, 12H), 0.98 – 0.86 (m, 6H). ^{13}C NMR (500 MHz, $CDCl_3$) δ (ppm): 140.27, 139.18, 137.66, 130.78, 130.07, 124.35, 118.05, 31.74, 31.73, 30.83, 29.30, 22.69, 14.14.

Synthesis of 3,3‴-dihexyl-2,2′:5′,2″:5″,2‴-quaterthiophene (**M5**). 5,5'-dibromo-2,2'-bithiophene (324 mg, 1 mmol, 1 equiv.) was added to a dry 100 mL 3-neck round bottom flask fitted with a condenser under positive argon pressure. 3-Hexylthiophene-2-boronic acid pinacol ester (647 mg, 658 µL, 2.2 mmol, 2.2 equiv.), $Pd(PPh_3)_4$ (92 mg, 0.08 mmol, 0.08 equiv.), and 40 mL dry toluene were added to the reaction flask while maintaining a positive pressure of argon. Then, 10 mL of a previously prepared 2 M potassium carbonate solution was added to the flask. The remaining two necks of the flask were sealed with rubber septa and the reaction mixture was stirred at reflux temperature for 48 h. After this time, the reaction was quenched by adding DI water to the flask. The crude product mixture was extracted with 100 mL of diethyl ether and the aqueous phase was discarded. The organic phase was washed with brine (3×) and then dried over $MgSO_4$.

The $MgSO_4$ was removed by filtration and the crude product mixture was concentrated via rotary evaporation. The crude product was then isolated via silica gel column chromatography using a 98:2 hexanes:ethyl acetate mixture as the mobile phase. The purified product was subsequently concentrated via rotary evaporation and isolated as a yellow-orange oil at an overall yield of 74%. ^{1}H NMR (500 MHz, $CDCl_3$) δ (ppm): 7.22 (d, *J* = 5.2 Hz, 2H), 7.19 (d, *J* = 3.7 Hz, 2H), 7.10 (s, 2H), 7.00 (d, *J* = 5.2 Hz, 2H), 2.90 – 2.84 (m, 4H), 1.79 – 1.69 (m, 4H), 1.53 – 1.37 (m, 12H), 1.04 – 0.95 (m, 6H). ^{13}C NMR (500 MHz, $CDCl_3$) δ (ppm): 139.87, 136.80, 135.34, 130.34, 130.09, 126.52, 123.85, 123.83, 31.70, 30.66, 29.31, 29.24, 22.65, 14.13.

Synthesis of 3,3''''-dihexyl-2,2':5',2'':5'',2''':5''',2''''-quinquethiophene (**M6**). 5,5''-dibromo-2,2':5',2''-terthiophene (406 mg, 1 mmol, 1 equiv.) was added to a dry 100 mL 3-neck round bottom flask fitted with a condenser under positive argon pressure. 3-Hexylthiophene-2-boronic acid pinacol ester (647 mg, 658 µL, 2.2 mmol, 2.2 equiv.), $Pd(PPh_3)_4$ (92 mg, 0.08 mmol, 0.08 equiv.), and 40 mL dry toluene were added to the reaction flask while maintaining a positive pressure of argon. Then, 10 mL of a previously prepared 2 M potassium carbonate solution was added to the flask. The remaining two necks of the flask were sealed with rubber septa and the reaction mixture was stirred at reflux temperature for 48 h. After this time, the reaction was quenched by adding DI water to the flask. The crude product mixture was extracted with 100 mL of diethyl ether and the aqueous phase was discarded. The organic phase was washed with brine (3×) and then dried over $MgSO_4$. The $MgSO_4$ was removed by filtration and the crude product mixture was concentrated via rotary evaporation. The crude product was then isolated via silica gel

column chromatography using a 98:2 hexanes:ethyl acetate mixture as the mobile phase. The purified product was subsequently concentrated via rotary evaporation and isolated as a yellow crystalline powder at an overall yield of 68%. ^{1}H NMR (500 MHz, $CDCl_3$) δ (ppm): 7.19 (d, *J* = 5.2 Hz, 2H), 7.13 (d, *J* = 3.8 Hz, 2H), 7.10 (s, 2H), 7.03 (d, *J* = 3.8 Hz, 2H), 6.95 (d, *J* = 5.2 Hz, 2H), 2.83 – 2.76 (m, 4H), 1.72 – 1.62 (m, 4H), 1.45 – 1.28 (m, 12H), 0.96 – 0.86 (m, 6H). ^{13}C NMR (500 MHz, CDCl3) δ (ppm): 139.90, 136.69, 135.99, 135.45, 130.30, 130.11, 126.53, 124.23, 123.92, 123.89, 31.69, 30.65, 29.32, 29.24, 22.65, 14.13.

Synthesis of 2,5-dibromo-3-hexylthiophene. N-bromosuccimide (NBS) was first recrystallized in DI water and vacuum dried. The recrystallized NBS (2.2 g, 12.4 mmol, 2.2 eq.) was added to a dry 250 mL round bottom flask while maintaining positive argon pressure. The flask was sealed with a rubber septum. Dry and degassed DMF (32 mL) was added to the flask via cannula and stirred until the NBS was completely dissolved. The reaction mixture was then cooled to 0 ºC in an ice bath. Then, 3-hexylthiophene (1.02 mL, 5.7 mmol, 1 eq.) was added dropwise via syringe under positive argon pressure. The reaction flask was then covered with aluminum foil and stirred at room temperature for 18 h. The reaction was quenched with the addition of DI water (100 mL) and extracted with ethyl acetate. The organic phase was washed with brine (3×) and then dried over $MgSO_4$. The $MgSO_4$ was removed by filtration and the crude product mixture was concentrated via rotary evaporation. The crude product was then purified via silica gel column chromatography using hexanes as the mobile phase. The purified product was subsequently concentrated via rotary evaporation and isolated as a colorless oil at an overall yield of

78%. ^{1}H NMR (500 MHz, $CDCl_3$) δ 6.77 (s, 1H), 2.55 – 2.46 (m, 2H), 1.60 – 1.49 (m, 2H), 1.38 – 1.25 (m, 6H), 0.98 – 0.78 (m, 3H). ^{13}C NMR (500 MHz, $CDCl_3$) δ 142.99, 130.95, 110.28, 107.91, 31.55, 29.54, 29.47, 28.77, 22.56, 14.06.

General Procedure for DArP of Expanded Core Copolymers. The dibrominated monomer (1 equiv.) and H/H comonomer (1 equiv.) were added to a dry 100 mL round bottom flask while under positive argon pressure. Neodecanoic acid (NDA, 0.3 equiv.), K_2CO_3 (2.4 equiv.), and palladium(II) acetate ($Pd(OAc)_2$, 0.02 equiv.) were added to the mixture while maintaining positive argon pressure. The flask was sealed with a rubber septum. Then, 5 mL of dry and degassed dimethylacetamide (DMAc) was transferred to the flask via cannula. The reaction mixture was stirred at 90 °C for 24 h. After this time, the reaction mixture was precipitated into cold methanol and recovered in a cellulose Soxhlet thimble. A series of Soxhlet extractions using methanol, acetone, and hexanes (each for 48 h) was used to wash and purify the (co)polymer. After these Soxhlet extractions, a final extraction with chloroform was done to collect the (co)polymer in solution. The resultant (co)polymer solution was concentrated via rotary evaporation to obtain the final product. P3HT was synthesized using the same procedure; however, 2-bromo-3-hexylthiophene was used as the sole monomer.

Synthesis of F4TCNQ Anion. To identify particular modes in UV-Vis spectra associated with doping (charge transfer), it was necessary to produce a spectrum of F4TCNQ anion. Following a procedure similar to that described in Kiefer et al.,[64] F4TCNQ was converted to its anionic form, $F4TCNQ^{-}$. In brief, F4TCNQ (52 mg) and LiI (39.8 mg) were added into two separate Schlenk flasks that were sealed with a rubber septum. Each

flask was evacuated and then backfilled with argon. This procedure was repeated a total of 4 times. Sparged acetonitrile (3 mL) was added to each flask via cannula under argon, and the contents were then cooled to 0 ºC in an ice bath. The LiI solution was then added to the F4TCNQ solution via cannula. The reaction was stirred for 30 min at 0 ºC under argon. The resultant reaction mixture was centrifuged and the dark blue/purple solid, $F4TCNQ^{-}$, was collected and dried under argon. The formation of $F4TCNQ^{-}$ was confirmed using FT-IR and UV-Vis spectroscopies.[64,65]

2.3.3. Macromolecular Characterization

^{1}H and ^{13}C NMR spectra of each monomer and the ^{1}H NMR spectrum of each copolymer were acquired using a Varian VNMRS 500 MHz NMR. Gel permeation chromatography (GPC) was used to determine the number-average molecular weight (M_n) and dispersity (Đ) of each copolymer based on universal analysis. An Agilent 1260 Infinity II system was used for these measurements with a mobile phase of THF at 25 °C and a flow rate of 1 mL/min. Solutions for GPC measurements were made at a concentration of 3-5 mg/mL in THF and filtered through a 0.2 μm PTFE filter prior to injection.

2.3.4. Thin Film Preparations

Solution Doping. Solutions of 0, 6, 10, 17, and 23 mol% F4TCNQ (relative to the total number of moles of thiophene repeat units) were made by mixing premade solutions of the copolymer and F4TCNQ in chlorobenzene. These solutions were prepared so that after mixing the final copolymer concentration was 2.0 mg/mL. The resultant polymer/dopant solution was heated to 70 °C prior to film deposition. Glass slides (1 in × 1 in) were cleaned with KimWipes™, then washed with acetone and methanol, and dried

with a stream of dry N_2 gas. Two layers of polymer/dopant were spin-cast onto the cleaned glass substrate. First, 200 μL of the polymer/dopant solution were deposited statically and then spun at 1000 rpm for 40 s. Immediately after, 200 μL of the same polymer/dopant solution was added dynamically under the same conditions. The resultant polymer film was allowed to dry for at least 10 minutes.

Sequential Doping. For sequential doping, the copolymer was dissolved in chlorobenzene (2.0 mg/mL) at 70 °C while F4TCNQ was dissolved in the indicated dopant solvent (1.0 mg/mL) at room temperature. Clean glass slides were prepared as described above. A copolymer thin film was created on the glass substrate by spin casting. 200 μL of the polymer solution were deposited statically and then spun at 1000 rpm for 40s. Then, another 200 μL were deposited dynamically at the same conditions (1000 rpm for 40 s). Immediately after film deposition, the dopant was spin cast onto the polymer thin film following the same two-step procedure. The resulting doped copolymer films were allowed to dry for at least 10 minutes.

2.3.5. AFM Measurements

An Asylum Atomic Force Microscope was used in tapping mode to probe the topography of thin films. AC200TS tips with a spring constant of 9 N/m and resonance frequency of 150 kHz were used to acquire images of 20 μm × 20 μm. To measure the thickness of each film, a scratch test was performed. A razor was used to scratch the film, thereby displacing the polymer film and exposing the glass substrate. Images were then acquired at the scratch interface, and film thickness was taken as the height difference between the polymer film and glass substrate.

2.3.6. Conductivity Measurements

Conductive graphite adhesive was used to add contact points at each corner of the solution-doped and sequentially-doped thin films. A Keithley 2450 Sourcemeter was used to perform current-voltage (I-V) sweeps from 0 to 10 V. Voltage was applied at the contact points across one edge and the current was measured along the contact points on the opposite edge. This was repeated along each of the four edges of the film in accordance with the van der Pauw method[57-59] and a total of 3 replicate samples were measured for each reported conductivity value. The sheet resistance, R_s, was calculated using the slope of the I-V curve in the initial linear region (0-2 V). R_s, along with the film thicknesses, t, obtained from AFM measurements, were used to calculate the film resistivity, ρ. Subsequently, conductivity, σ, was calculated using: $\sigma = \rho^{-1}$.

2.3.7. Absorbance Measurements

Thin Film Measurements. UV-Vis-NIR spectra were acquired for as-cast and doped thin films using a Cary 5000 UV-Vis-NIR Spectrophotometer in the wavelength range of 350 to 2000 nm. A clean glass slide was used as the background spectrum to baseline correct the spectra acquired for thin films. Each spectrum was then normalized by film thickness, as practiced by Li et al.[14]

Solution Measurements. To determine the effective conjugation length (ECL) of each copolymer, samples of different molecular weight were collected. This was done by recovering the copolymers resulting from Soxhlet extractions that used acetone and hexanes in the overall process of purifying each copolymer. The solids obtained from these fractions were dried and the degree of polymerization (X_n) and number of thiophenes per

chain was calculated from the M_n determined via GPC using universal calibration analysis. The UV-Vis spectra were acquired for these samples in chloroform across a wavelength range of 300-600 nm using a Thermo Scientific Evolution 300 spectrophotometer. The optical band gap was calculated using Tauc plot analysis.[66] The optical band gap of the monomers and purified copolymers were measured in the same manner.

2.3.8. Determination of Hansen Solubility Parameters

The Hansen solubility parameters (HSPs) of each polymer were determined as described by Díaz de los Ríos and Ramos.[49] In brief, 1 mg of the polymer was added to 1 mL of a particular solvent (or solvent blend). Twenty-three (23) different solvents were used, and the homogeneity of the solution was evaluated based on visual observations. Each solution was given a score of 1 (soluble) or 0 (not soluble) and entered in the Excel spreadsheet accessible from Díaz del los Ríos and Ramos' work.[49] For those solutions deemed partially soluble at room temperature, the sample was heated gently. If the copolymer subsequently dissolved and the solution remained homogenous for more than 1 h, it was considered to be soluble and given a score of 1. Using the embedded formulae and data solver in Excel, the HSPs of each copolymer were calculated based on these observations.

2.4. Results and Discussion

2.4.1. Comonomer Synthesis and Characterization

A series of thiophene-based copolymers were used to investigate how repeat unit design alters key properties, such as solubility and conductivity of chemically-doped thin films. Thiophene comonomers were synthesized via Stille (**M3**, **M4**) and Suzuki-Miyaura

(**M5**, **M6**) cross-couplings, as depicted in Scheme 2.1. The structure of each comonomer was verified via ^{1}H NMR and ^{13}C NMR spectroscopies, as seen in *Appendix A* (Figure A.1-A.8). It should be noted that each comonomer is flanked with a hexyl thiophene at each end to improve solubility of the monomer and the resultant copolymer.[67] Thiophene (**M3**), 2,2'-bithiophene (**M5**), and 2,2':5',2"-terthiophene (**M6**) were chosen as "cores" to compare how decreasing the steric demand along the backbone by increasing the spacing between alkyl side chains impacts copolymer solubility, dopant integration, and film conductivity. The fused ring core of thieno[3:2,*b*]thiophene (**M4**) was selected to provide insight into how increasing monomer rigidity and planarity affects solubility and conductivity. To first evaluate how comonomer design impacts optoelectronic properties, the absorbance spectrum of each comonomer was measured, as shown in Figure 2.1, and the corresponding optical band gap was calculated via Tauc plot analysis.[66] Table 2.1 summarizes the absorbance maximum, λ_{max}, and optical band gap, E_{gap}^{opt}, of each of the thiophene-based comonomers in solution. The λ_{max} values, which correspond to the π-π^* transition, range from 339-405 nm and show a red-shift as the core size of the comonomer increases. This red-shift is indicative of increased electron-richness in the comonomer with the addition of more thiophene units. Additionally, the band gap decreases as the core size increases due to increased conjugation. These two trends are seen most clearly across the series of **M3** to **M5** to **M6**. On the other hand, when the core is changed from thiophene (**M3**) to thieno[3:2,*b*]thiophene (**M4**), the changes are less pronounced, as the red-shift is only 9 nm and E_{gap}^{opt} decreases by only 0.07 eV. These comparisons suggest that adding a

Scheme 2.1. Synthesis of thiophene-based comonomers (**M3**-**M6**) via (a) Stille and (b) Suzuki-Miyaura cross-couplings.

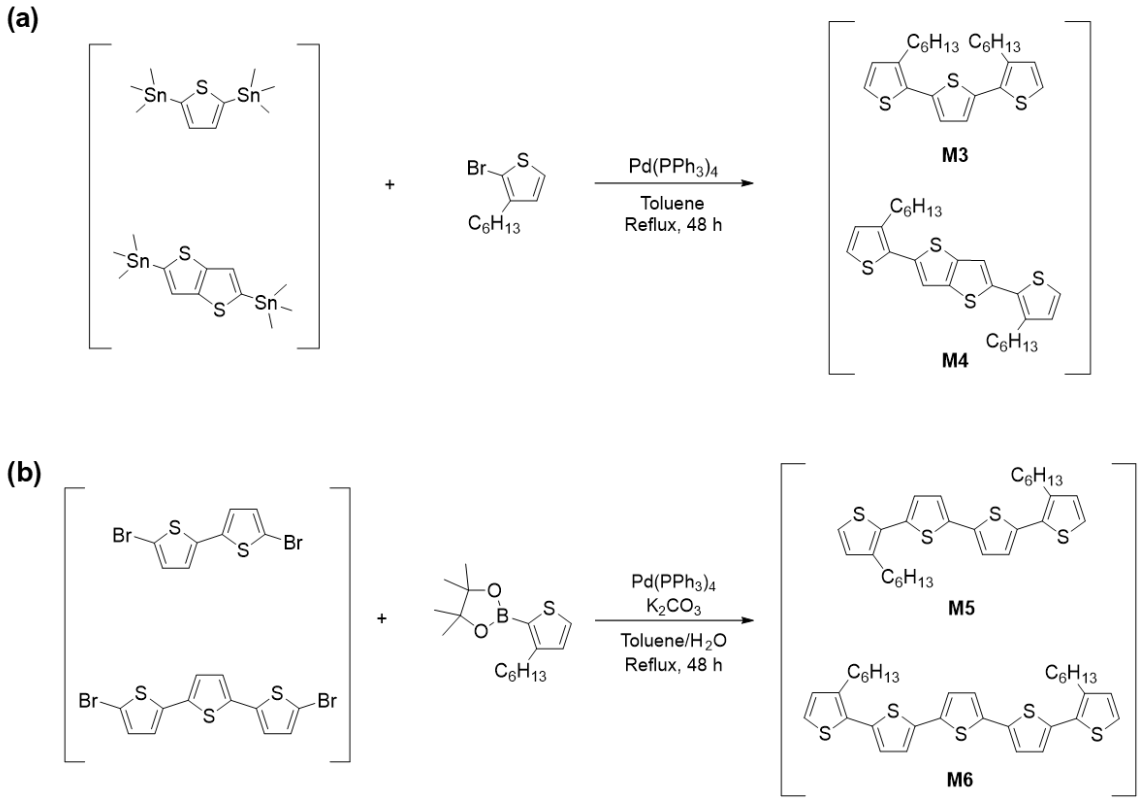

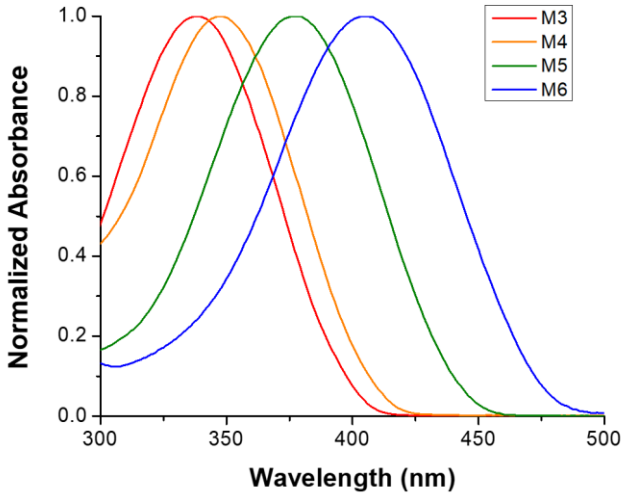

Figure 2.1. Absorbance spectra of thiophene-based comonomers (**M3**-**M6**) in $CHCl_3$ (<1 mg/mL). Spectra are normalized by the absorbance measured at λ_{max} for each monomer. A red-shift is observed as the core size increases, which increases the spacing length between alkyl side chains.

Table 2.1. Optical characteristics of thiophene-based comonomers.

Comonomer	**Absorbance λ_{max} (nm)**[a]	**E_{gap}^{opt} (eV)**[b]
M3	339	3.25
M4	348	3.18
M5	378	2.93
M6	405	2.72

[a]*UV-Vis spectra acquired in chloroform.*
[b]*Determined via Tauc plot analysis.*

few thiophene units produces a greater impact on optoelectronic properties than increasing the planarity/rigidity through the introduction of a fused-ring structure in the backbone. However, as described later, the addition of thiophene rings to the core decreases the solubility of the resulting copolymer.

2.4.2. Copolymer Synthesis and Characterization

As shown in Scheme 2.2, each of the comonomers **M3-M6** were copolymerized with 2,5-dibromo-3-hexylthiophene (^{1}H and ^{13}C NMR shown in Figure A.9 and A.10) via direct arylation polymerization (DArP) using conditions typically reported for thiophene-based conjugated polymers.[42,43,46,68] The AA+BB nature of this step-growth polymerization along with the lack of symmetry in 2,5-dibromo-3-hexylthiophene results in regio-irregular copolymers; however, due to the symmetry of comonomers **M3**-**M6**, the regioregularity of each copolymer (**P3**-**P6**) can be assumed to be 50%. The structures of the thiophene-based copolymers were confirmed via ^{1}H NMR, as shown in Figure A.11-A.14. For comparisons to the thiophene-based copolymers **P3-P6**, DArP was used to synthesize P3HT via AB and AA+BB type step-growth polymerizations. **P3HT (AB)** was chosen because it is a benchmark for thiophene-based polymers and **P3HT (AA+BB)** was used for comparison due to the regio-irregularity of the core-expanded copolymers. From ^{1}H NMR it was determined that the P3HT synthesized by an AB polymerization was 93% regioregular while the P3HT synthesized via the AA+BB copolymerization was 57% regioregular. (^{1}H NMR spectra are shown in Figure A.15-A.16.)

The molecular weight of each polymer was determined by GPC and the traces are

Scheme 2.2. Synthesis of thiophene-based copolymers (**P3-P6**) via DArP.

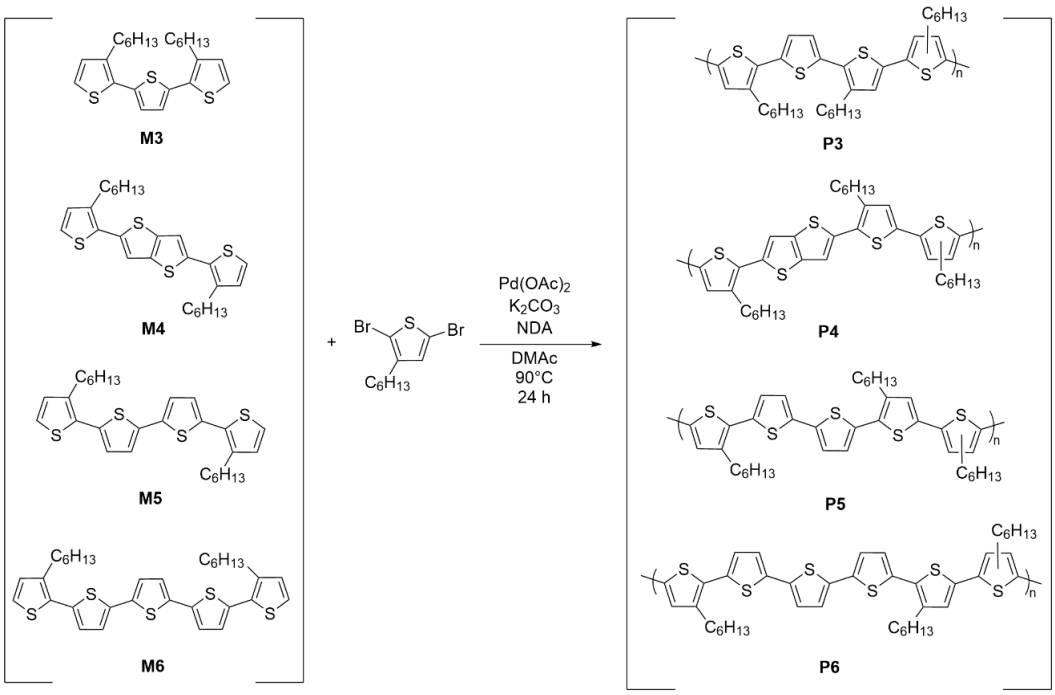

shown in Figure A.17. As shown in Table 2.2, the number-average molecular weight (M_n) of the copolymers, as determined via universal calibration analysis, range from 5.0-11.2 kg/mol. Therefore, to enable comparisons between copolymers of different designs, the effective conjugation length (ECL) of each of the thiophene-based copolymers was assessed. The ECL, which is identified as the chain size at which the addition of repeat units no longer alters optoelectronic properties,[69] was determined based on the number of thiophene units per chain, rather than the degree of polymerization (X_n) because the copolymers studied here have different repeat unit structures. For example, while the M_n of **P3** (11.2 kg/mol) equates to a X_n of 19 based on repeat unit structure, this copolymer has 76 thienyl rings per chain on average. Also, for this analysis, the thieno[3:2,*b*]thiophene subunit in **P4** is counted as one thiophene unit, as it is one conjugated unit. UV-Vis measurements presented in Figure 2.2 show that the optical band gap of each polymer becomes independent of chain size above ~20 thiophene units per chain, which sets the ECL at 20 thiophene units. This result is in agreement with characterization of the ECL of P3HT and other polythiophene derivatives by de Oliveira et al.[70] and Nakanishi et al.[71] Therefore, we posit that any differences in optoelectronic and/or conductive properties observed in the subsequent studies are attributed to structural design, rather than a function of molecular weight differences, as each polymer contains more than 20 thiophene units per chain. The absorbance maxima and optical band gaps of the copolymers in solution ($CHCl_3$) and thin film form were determined from UV-Vis measurements, and the results are summarized in Table 2.2. The solution and thin film spectra are shown in Figure A.18

Table 2.2. Macromolecular characteristics of thiophene-based copolymers and P3HTs.

Polymer	M_n (kg/mol)[a]	Đ	X_n	Thiophene units[b]	Solution λ_{max} (nm)[c]	Solution E_{gap}^{opt} (eV)[d]	Thin Film λ_{max} (nm)[c]	Thin Film E_{gap}^{opt} (eV)[d]
P3	11.2	2.2	19	76	459	2.38	542	1.99
P4	8.4	2.4	13	52	453	2.40	516	2.03
P5	5.0	1.8	8	40	465	2.36	545	1.94
P6	7.5	1.9	10	60	471	2.33	533	2.02
P3HT (AB)	9.0	2.2	54	54	435	2.45	506	2.07
P3HT (AA+BB)	9.7	2.3	58	58	425	2.54	436	2.45

[a] *M_n based universal calibration analysis.*
[b] *Number of thiophene units per chain calculated from X_n and the number of conjugated thiophene units in the repeat unit.*
[c] *λ_{max} values determined from UV-Vis measurements using $CHCl_3$ solutions (< 1 mg/mL) and thin films cast from chlorobenzene (at 2 mg/mL).*
[d] *E_{gap}^{opt} values were determined from Tauc plot analyses of UV-Vis spectra measured from solutions and thin films.*

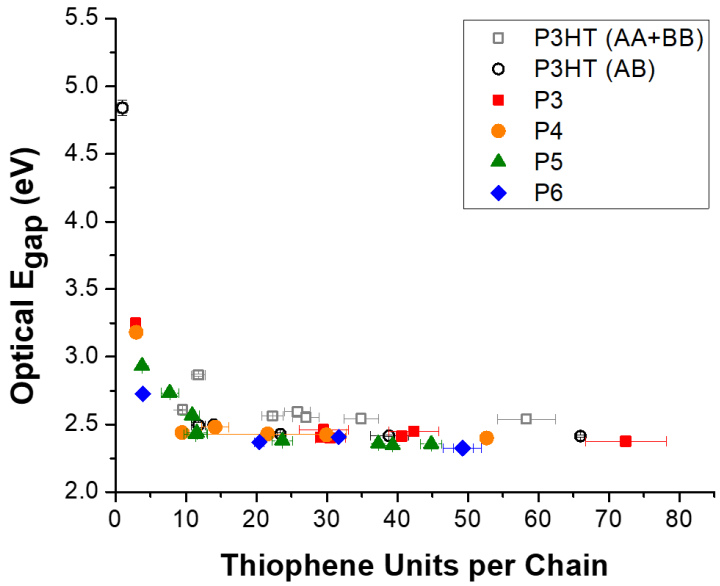

Figure 2.2. Optical bandgap of thiophene-based copolymers determined from Tauc analysis as a function of number of thiophene units per chain. For **P4**, thienothiophene was counted as a single unit. The behavior indicates that the bandgap is constant above ~20 thiophene rings per chain. Horizontal error bars represent the uncertainty of the M_n determined by GPC using universal analysis.

and A.19, respectively. Results are consistent with well-known behaviors in that a red-shift in λ_{max} and a corresponding decrease in E_{gap}^{opt} is observed from solution to solid-state due to the organization in the solid-state brought on by π-stacking interactions. More specific behaviors can be attributed to chain microstructure and monomer design. For example, when comparing the photophysical characteristics of **P3HT (AA+BB)** to **P3HT (AB)** measured in solution, there is a significant increase in the E_{gap}^{opt} (+0.11 eV) and a blueshift in the λ_{max} of 10 nm. These differences in optoelectronic properties are related to the degree of regioregularity of the two P3HTs. The lower degree of regioregularity of **P3HT (AA+BB)** leads to greater rotational freedom along the backbone, thereby decreasing the persistence length and increasing the resultant E_{gap}^{opt}.[72] In addition, the decrease in E_{gap}^{opt} for the thin film compared to the solution of **P3HT (AA+BB)** is not as significant as that seen with **P3HT (AB)**. This smaller change in E_{gap}^{opt} is attributed to poor ordering in the film due to more rotational degrees of freedom caused by the regio-irregularity of **P3HT (AA+BB)**.

Despite the regio-irregularity inherent in the series of "core expanded" copolymers that arises from the synthetic design (symmetrical + asymmetrical monomer), there is no obvious detrimental impact seen in the solution or thin film measurements like those observed for **P3HT (AA+BB)**. Therefore, it is believed that the spacing units minimize the impact regio-irregularity has on ordering and π-stacking interactions. Furthermore, within the series of copolymers, a slight red-shift and decrease in E_{gap}^{opt} is observed in solution as thiophenyl moieties are added to the repeat unit design (**P3** to **P5** to **P6**) and side chain densities are reduced. These changes are attributed to decreasing the steric demand along the backbone with the incorporation of the spacing units, thereby allowing for more π-π

interactions. However, measurements of **P4** in solution reveal a small blue-shift and an increase in E_{gap}^{opt} compared to **P3**, **P5**, and **P6**. According to Danielsen et al., monomers that impart a non-zero deflection angle along the backbone decrease the persistence length of conjugated polymers.[73] Thus, despite the planarity of the fused ring structure, it is believed that that the persistence length of **P4** is reduced compared to the other copolymers due to the introduction of the thieno[3:2,*b*]thiophene core, which alters the deflection angle compared to P3HTs and the other copolymers. This decrease in persistence length would cause a subsequent increase in the E_{gap}^{opt} of **P4** compared to the other copolymers. It is also noted that for **P6**, the decrease in E_{gap}^{opt} from solution to solid-state is not as pronounced as it is with the other copolymers (**P3**-**P5**) and **P3HT (AB)**. The smaller change in E_{gap}^{opt} is attributed to poor ordering in the film, which may be due to aggregation or increased rotational freedom resulting from the increased spacing length between alkyl side chains (by using terthiophene as the central core). Furthermore, it is observed that in the solid state, E_{gap}^{opt} is higher and λ_{max} is lower for **P6** in comparison to **P5**. These findings suggest that there may be a limit on the size of the spacing unit before it is no longer advantageous for use in thin films and indicate that there are complex trade-offs involving spacing length, conformational flexibility, and solubility that impact properties and performance of the copolymers.

To gain insight into how spacing length between side chains and planarity impacts polymer solubility, the Hansen solubility parameters (HSPs) of each copolymer were evaluated following the method described by Díaz de los Ríos and Ramos.[49] This method relies on assessing the solubility of the polymer in various solvents for which values of the

dispersive, polar, and hydrogen-bonding contributions, δ_D, δ_P, δ_H, respectively, are known. The HSPs determined for the thiophene-based copolymers are summarized in Table 2.3, and the underlying assessments of their solubility in 23 different solvents/solvent blends are listed in Table A.1. The tabulated results show that for the two P3HTs and all of the copolymers, the main contributor to the solubility is dispersive interactions (δ_D), since the polymers are non-polar. We also note that the HSPs defined for **P3HT (AB)** are in agreement with those reported by Yoon et al.[30] and Machui et al.[74] There are clear differences in the HSPs between **P3HT (AB)** and **P3HT (AA+BB)**, reflecting the fact that regioregularity impacts solubility. Specifically, **P3HT (AA+BB)**, which is 57% regioregular, has lower HSP energies, and the values are consistent with those reported by King et al.[75] This difference can be attributed to **P3HT (AB)** having stronger interchain π-stacking interactions due to its higher regioregularity, which increases the cohesive energy density of the polymer. Table 2.3 also shows that the values of δ_D, δ_P, and δ_H increase with an increase in the spacing length from one (**P3**) to two (**P5**) to three (**P6**) thiophene units, although the changes are very small from **P3** to **P5**. We posit that the increased spacing length that results from expanding the comonomer core facilitates interchain π-stacking interactions, thus increasing the dispersive energy, δ_D. The small increases in δ_P and δ_H, which reflect an increase in polarity and hydrogen bonding capacity, are most likely the result of the decreased density of alkyl side chains along the backbone. Finally, we note that the increase in HSPs of the copolymers compared to **P3HT (AB)** is more drastic with the addition of thieno[3:2,*b*]thiophene (**P4**) than with thiophene (**P3**) or bithiophene (**P5**).

Table 2.3. Hansen solubility parameters (HSPs) of the thiophene-based polymers.

Polymer	δ_D (MPa$^{1/2}$)	δ_P (MPa$^{1/2}$)	δ_H (MPa$^{1/2}$)
P3	18.3	1.4	6.2
P4	18.8	1.2	5.6
P5	18.4	1.5	6.6
P6	19.4	2.0	6.8
P3HT (AB)	18.3	2.8	3.8
P3HT (AA+BB)	17.5	3.2	2.2

This pattern of behavior indicates that the fused ring core alters the solubility more significantly than its non-fused ring counterparts. Although the HSPs of each copolymer offer significant information on polymer-solvent interaction energies, it does not directly indicate which polymer is considered more soluble than others. However, it can be inferred that the solubilities of **P3**, **P4**, **P5**, and **P6** are decreased compared to **P3HT (AB)**, as the solubility scores listed in Table A.1 show that these core expanded copolymers dissolve in fewer solvents (11, 9, 10, and 7 solvents, respectively) compared to **P3HT (AB)** (which dissolves in 13 solvents). This decrease in solubility is consistent with expectations, as increasing the number of thiophene units in the comonomer core reduces the density of alkyl side chain in the repeat unit, thereby reducing their effectiveness in promoting solubility of the conjugated polymer.

2.4.3. Solution Doping of Thiophene-Based Copolymers

In this study, F4TCNQ was used as the dopant due to its compatibility with thiophene-based polymers, especially P3HT.[23,26,41] In these solution doping studies, each of the copolymers was doped at levels ranging from 0 to 23 mol% F4TCNQ, which is based on the moles of thiophene in the polymer solution. Adopting this basis provides consistency across all copolymers despite differences in their repeat unit design. One drawback frequently noted with solution doping is the appearance of aggregates that form upon mixing due to the creation of charged complexes.[16] Therefore, because polymer thin films deposited from solution inherit structural characteristics from their parent solution, to assess the presence of aggregation in the solid-state, the solution-doped thin films were

imaged by atomic force microscopy (AFM). Figure 2.3 presents topographical images of thin films created from spin casting the solution-doped systems at 0 mol% and 23 mol % doping. Representative images for the other doping levels are shown in Figure A.20-A.25 and the surface roughnesses are summarized in Table 2.4. There are several salient points to highlight: First, there are significant differences in the film topography of **P3HT (AB)** and **P3HT (AA+BB)**. As documented in Table 2.4, **P3HT (AA+BB)** has a higher surface roughness compared to its regioregular counterpart, **P3HT (AB)**, at all doping levels. In addition, the large roughness measured for **P3HT (AA+BB)** at 0 mol% doping indicates that the regio-irregular nature of the chain microstructure disrupts the organization of the polymer film, thus decreasing the effectiveness of π-stacking interactions that drive interchain organization.[76,77] The **P3HT (AA+BB)** film cast from a solution of 6 mol% F4TCNQ also displays a high surface roughness, indicating the incorporation of F4TCNQ causes aggregation, even at low doping levels. Table 2.4 also shows that for all of the copolymers (**P3**-**P6**), the surface roughness remains relatively constant and low (generally ≤ 4 nm) at doping levels ranging from 0 to 17 mol%; however, at a doping level of 23 mol%, there is a significant increase in the topographical roughness, which likely indicates the prevalence of aggregates. The most substantial changes in roughness at high doping levels are seen for the expanded designs of **P4** (14.7 nm), **P5** (13.3 nm), and **P6** (25.1 nm). This is attributed to increased aggregation, which is likely exacerbated by the lower solubility, as reflected in the HSPs of these copolymers. Additionally, the increased prevalence of aggregates that are observable in the topological images, especially for **P5**

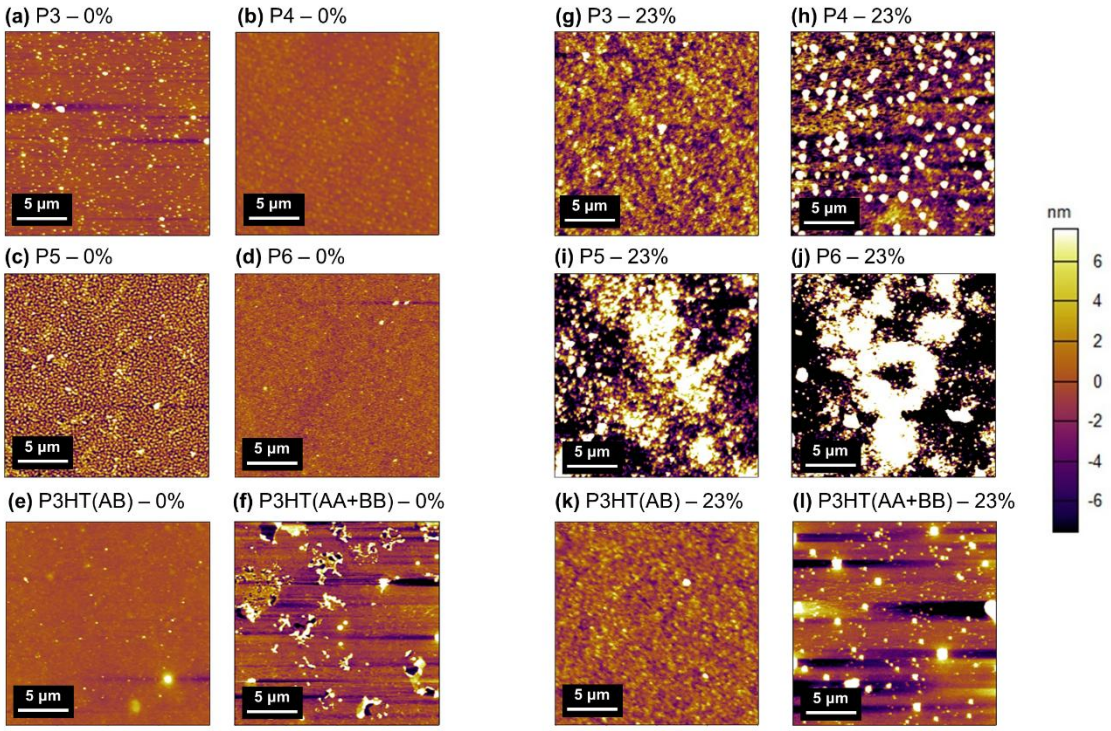

Figure 2.3. Representative AFM images of solution-doped thin films at 0 mol% (a-f) and 23 mol% (g-l) doping for each copolymer. The surface roughness remains low (< 4 nm) for all films at all doping levels except for solution-doped films of **P4**, **P5**, and **P6** at 23 mol%, where dramatic increases in roughness are evident.

Table 2.4. Surface roughness of solution-doped thin films at various doping levels determined from AFM measurements.

	Surface Roughness (nm)				
Polymer	**0 mol%**	**6 mol%**	**10 mol%**	**17 mol%**	**23 mol%**
P3	3.6 ± 1.5	1.8 ± 0.5	2.9 ± 1.1	2.6 ± 0.3	4.4 ± 0.8
P4	0.9 ± 0.7	1.4 ± 0.6	4.2 ± 2.1	3.0 ± 1.5	14.7 ± 7.9
P5	3.4 ± 1.8	3.3 ± 0.9	4.4 ± 1.4	7.6 ± 2.4	13.3 ± 5.2
P6	4.2 ± 1.4	1.3 ± 0.3	6.2 ± 2.6	2.9 ± 1.1	25.1 ± 11.9
P3HT (AB)	0.6 ± 0.3	1.0 ± 0.4	1.3 ± 0.4	1.9 ± 0.2	2.2 ± 0.6
P3HT (AA+BB)	6.4 ± 0.6	18.6 ± 6.6	5.5 ± 1.5	4.8 ± 0.8	6.0 ± 2.7

and **P6**, could be due to an increase in the amount or size of charged complexes formed during the solution doping process. This idea will be discussed later in more detail.

The influence of copolymer design and doping level on the electrical performance of solution-doped thin films was investigated by measuring the conductivity via the Van der Pauw method.[57,58] The sheet resistance, which was calculated from the measured I-V curves, was used along with the film thickness to calculate the conductivity. Film thicknesses measured via AFM scratch test are summarized in Table A.2. It should be appreciated that the conductivity values measured here are lower than some values reported for thiophene-based polymers (particularly for P3HTs[78,79]) due to the low film thicknesses (10-25 nm) and relatively large sample sizes (1 in × 1 in). As shown in Figure 2.4, there are drastic differences in thin film conductivity based on repeat unit structure. First, films made from **P3HT (AA+BB)** have very low conductivities at all doping levels. This is attributed to poor organization due to less efficient π-stacking that derives from the irregularity in regiochemistry, which reduces electron delocalization. On the other hand, **P3HT (AB)** has an appreciably higher conductivity due to its high regioregularity, which enhances inter-chain organization and facilitates electron delocalization. The regio-irregularity of copolymers **P3**-**P6** does not appear to impact the conductivity of their thin films, which again indicates that the spacing units allow the dopant to effectively access the copolymer backbone, which will be discussed in more detail later. For each copolymer (and **P3HT (AB)**) the conductivity increases by a few orders of magnitude as the doping level is increased. However, for **P3** and **P4** it appears that within experimental uncertainty,

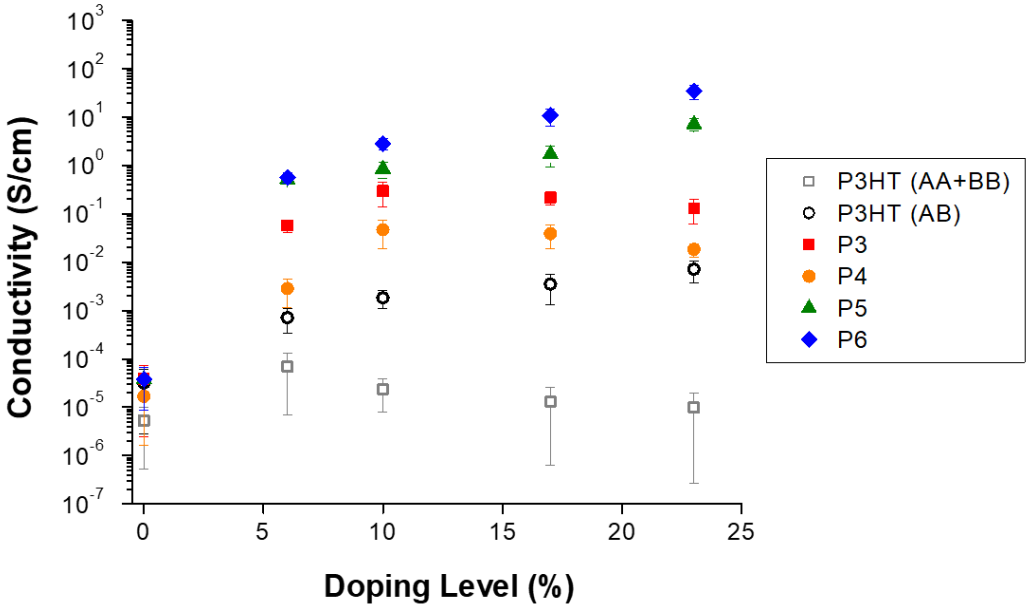

Figure 2.4. Conductivity of solution-doped copolymer thin films as a function of doping level. Doping level is determined as a mol% of F4TCNQ relative to relative to the moles of thiophene in the polymer solution. Conductivity measurements were performed on samples spin cast on 1 in × 1 in glass slides with film thicknesses ranging from 10-25 nm.

the conductivity plateaus after 10 mol%. This behavior is attributed to the formation of charged species and will be discussed later in more detail. Consistent with work by Li et al., who showed that decreasing the density of hexadecyl side chains through an alternating pattern of bithiophene and thienothiophene spacing units in the backbone enhanced the conductivity of polythiophene-based copolymers (relative to analogous copolymers without the spacing units),[14] an increase in conductivity is seen when a spacer unit is used. As the spacing length between alkyl chains in the repeat unit is increased from one (**P3**) to two (**P5**) to three (**P6**) thiophene units, the conductivity increases significantly, by orders-of-magnitude. The reason for this enhanced conductivity is inherent to the complex interplay between chain design, efficient doping, and structure at different length scales. To begin unraveling this behavior, it should be noted that the increase in conductivity for the copolymers follows the trend shown in Table 2.2 of decreasing E_{gap}^{opt} as spacing length is increased from **P3** (2.38 eV) to **P5** (2.36 eV) to **P6** (2.33 eV). Figure 2.4 also shows that **P4** has a lower conductivity than the other copolymers, which is consistent with it having the highest optical band gap (2.40 eV). This suggests that the incorporation of thieno[3:2,*b*]thiophene in **P4** results in a conformational change (i.e., non-zero deflection angle) that in turn decreases the persistence length compared to the other copolymers, which is known to decrease electron delocalization.[73] Therefore, a single characteristic property, such as E_{gap}^{opt}, cannot fully describe a macroscopic property such as electrical conductivity because it is also influenced by polymer structure and organization, efficient polymer-dopant interactions, and transport at multiple length scales.

As previously discussed, doping relies on electron transfer, which requires the dopant and the conjugated backbone to be in close proximity. Because the anionic form of F4TCNQ, $F4TCNQ^{-}$, is characteristic of efficient doping, it is useful to monitor this species to determine the relative extent of doping. To enable the identification of F4TCNQ and $F4TCNQ^{-}$ in a doped sample, a standard consisting of $F4TCNQ^{-}$ only was made via a LiI reduction.[64] FTIR and solution-based UV-Vis measurements were used to confirm the complete conversion of F4TCNQ to give the $F4TCNQ^{-}$ standard. As seen in Figure 2.5, there are clear frequency shifts in the vibrational modes of F4TCNQ after the LiI reduction; most significantly the shift of the v(C≡N) from 2226 cm^{-1} to 2195 cm^{-1} and the shift of v(C=C) ring from 1591 cm^{-1} to 1533 cm^{-1} indicate successful conversion.[65] Additionally, as seen by the solution absorbance spectra in Figure 2.6, upon reduction of F4TCNQ a red-shift from 387 nm to 411 nm is observed along with the significant increase in absorbance at 855 nm in the $F4TCNQ^{-}$ spectrum, thereby indicating successful conversion of F4TCNQ to $F4TCNQ^{-}$. Thin films of F4TCNQ and its anionic counterpart, $F4TCNQ^{-}$, were made by drop-casting, and characteristic peak positions were assessed by UV-Vis-NIR measurements. In the solid-state, F4TCNQ (neutral form) has a characteristic absorbance peak in the range of 348 – 444 nm while $F4TCNQ^{-}$ (anionic form) has one peak in the range of 475 – 570 nm and a second that appears at 728 – 955 nm, as shown in Figure 2.7. These peaks allow the amount of $F4TCNQ^{-}$ in doped thin films to be monitored as a function of doping level; however, because the $F4TCNQ^{-}$ peak from 475 – 570 nm overlaps with the π-π* peak of the copolymers, the local peak maximum at 868 nm associated with the second mode was used.

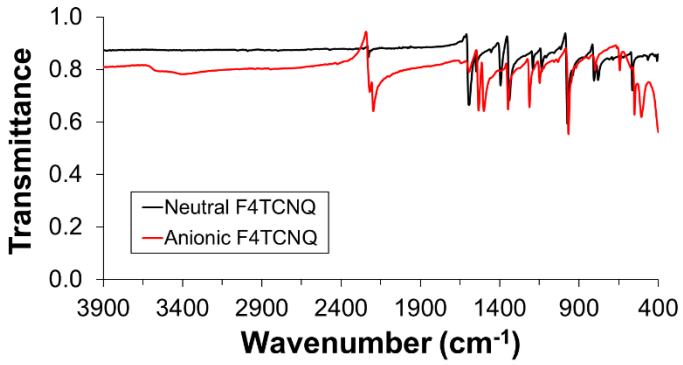

Assignment	Wavenumber (cm^{-1}) F4TCNQ	F4TCNQ$^-$
v(C≡N)	2226	2195
v(C=C)ring	1591	1533
v(C=C)exo	1547	1498
v(C-C) ring	1393	1346
v(C-CN) ring	1189	1212
v(ring)	1134	1148
v(C-F)	971	965

Figure 2.5. FT-IR spectra (left) of powder F4TCNQ and powder F4TCNQ$^-$ and their respective key peak positions (right). Assignments were made based on a report from Watts et al.[65] The shifts observed for the vibrational modes validate the successful conversion of F4TCNQ to F4TCNQ$^-$.

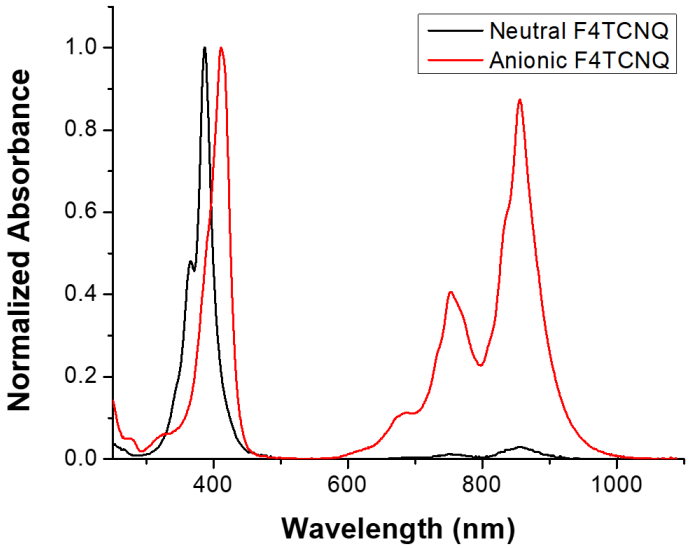

Figure 2.6. UV-Vis spectra of F4TCNQ and F4TCNQ$^-$, normalized by the peak absorbances recorded at 387 nm and 411 nm, respectively. Each sample was prepared in acetonitrile at 1.5 mg/mL.

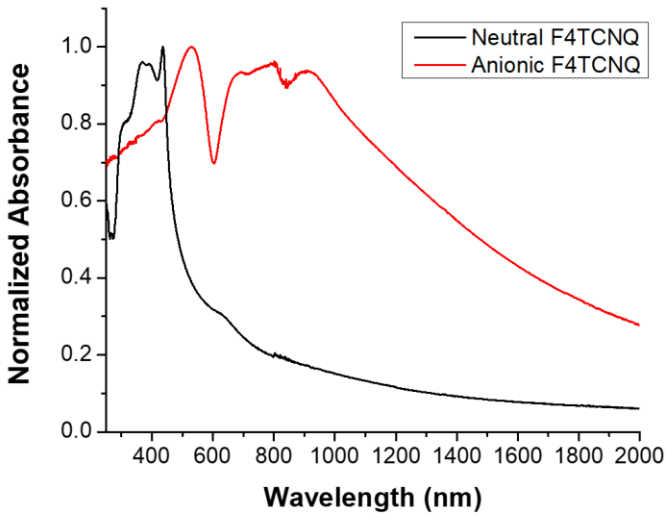

Figure 2.7. Normalized UV-Vis-NIR spectra of F4TCNQ thin films created by drop casting from a methanol solution at 1.5 mg/mL. The local maximum at 868 nm is used for $F4TCNQ^-$ quantification in subsequent thin film measurements.

As an example, the UV-Vis-NIR spectra of **P6** doped with F4TCNQ at various doping levels is shown in Figure 2.8. It should be noted that because the spectra are normalized by film thickness, the normalized absorbance directly correlates with concentration. Therefore, and as expected, there is a significant increase in the presence of $F4TCNQ^-$ with increasing doping levels, as evidenced by the increase in the absorbance band mode associated with neutral F4TCNQ while regions shaded in red correspond to the anionic form, $F4TCNQ^-$. at 728 – 955 nm. Additionally, with increasing doping levels, an increase in the vibrational mode assigned to the neutral form of F4TCNQ (observed from 348 to 444 nm) is also seen, which indicates that not all of the dopant is converted to its anionic form during the solution doping process. This saturation in doping is consistent with studies by Fontana et al.[25] and Duong et al.[16] on P3HT that was doped with F4TCNQ

Analogous UV-Vis-NIR measurements were performed on all thin films prepared by the solution doping method, and the spectra are shown in Figure A.26-A.30. From these results, the normalized absorbance (at 868 nm) of the anionic dopant is extracted and correlated with the measured conductivity of the doped thin films, as seen in Figure 2.9. As expected and shown in Figure 2.9a, there are low concentrations of $F4TCNQ^-$ in films made from **P3HT (AA+BB**) at all doping levels. Again, this is attributed to the irregular micro-organization which hinders effective doping, consistent with work by Hynynen et al.[40] The spectrum for **P3HT (AB)** (Figure 2.9b) and each of the copolymers (Figure 2.9c-2.9f) show that as the doping level increases, both the concentration of $F4TCNQ^-$ and the conductivity increase. Although the axes of each plot in Figure 2.9 were scaled consistently to facilitate comparison, the increase in normalized $F4TCNQ^-$ absorbance as a function of

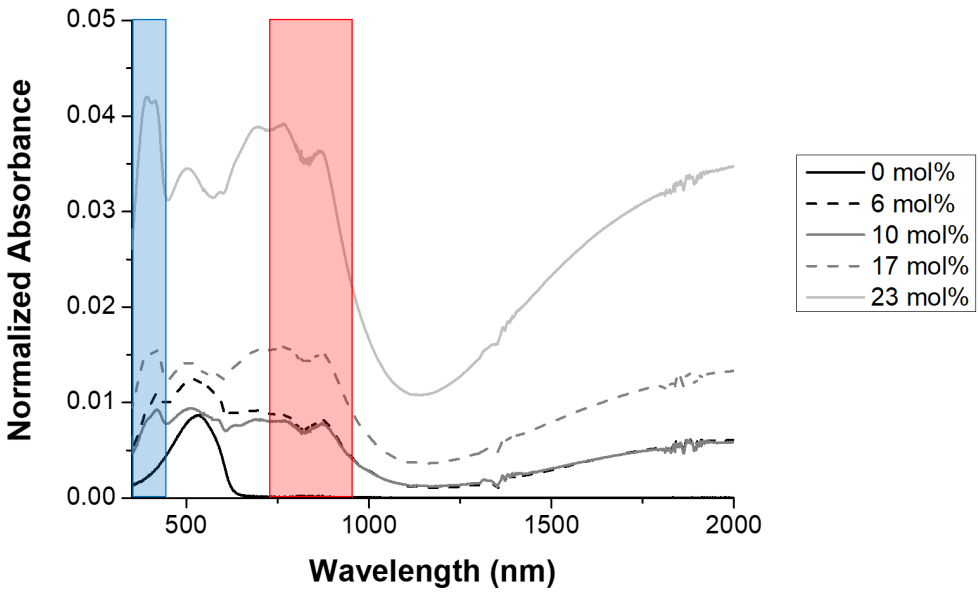

Figure 2.8. UV-Vis-NIR spectra of thin films created by solution doping of **P6**. The absorbance spectra measured at each doping level was normalized by film thickness, which ranged from 10-13 nm for these **P6** films. Regions highlighted in blue correspond to the mode associated with neutral F4TCNQ, while regions shaded in red correspond to the anionic form, $F4TCNQ^{-}$.

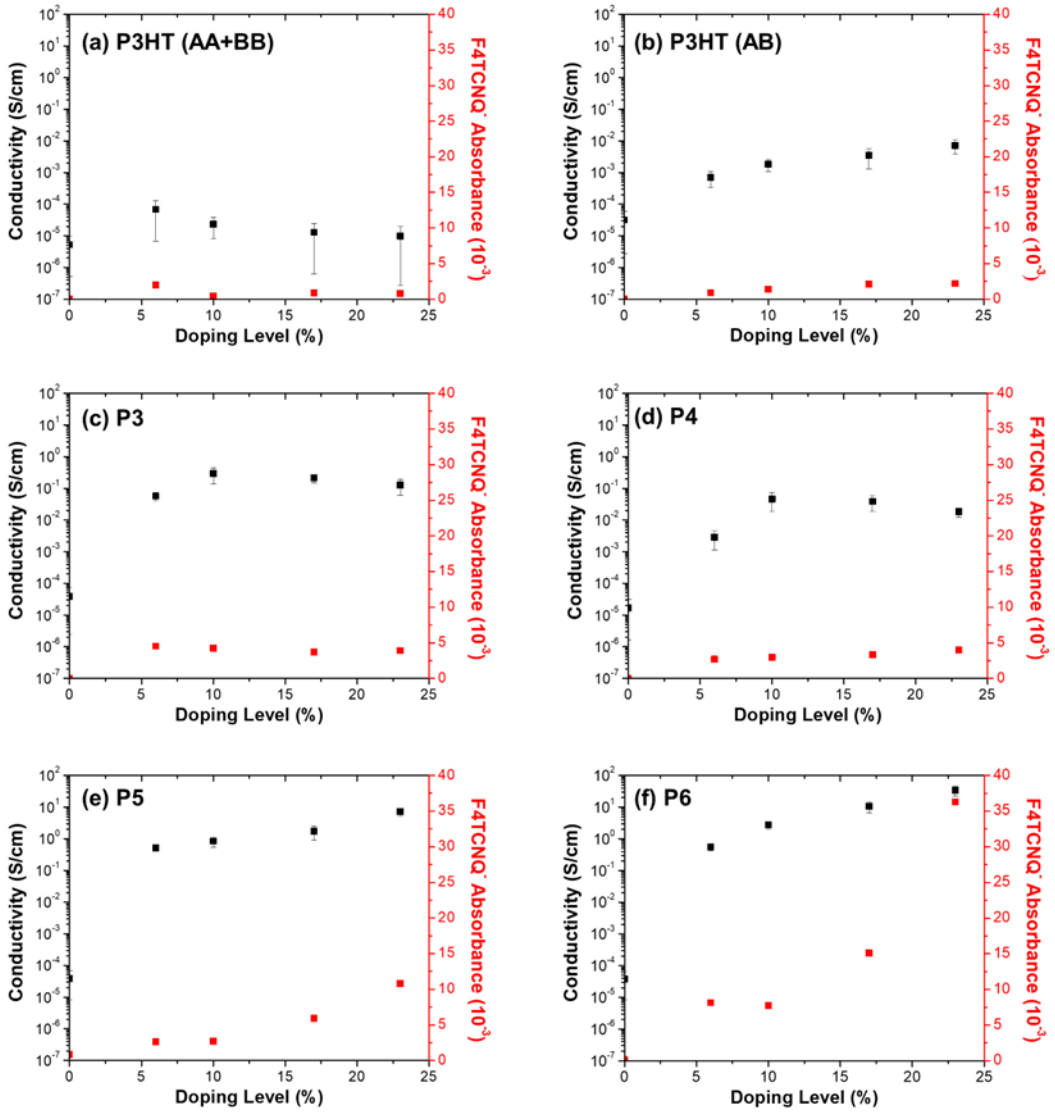

Figure 2.9. Comparison of conductivity and F4TCNQ⁻ absorbance in solution-doped thin films of (a) **P3HT (AA+BB)**, (b) **P3HT (AB)**, (c) **P3**, (d) **P4**, (e) **P5**, and (f) **P6** as a function of doping level. The F4TCNQ⁻ absorbance is taken as the local maximum at 868 nm obtained from UV-Vis-NIR measurements and is normalized by film thickness. As a result, the normalized absorbance is proportional to F4TCNQ⁻ concentration.

doping level is most apparent with the expanded designs of **P5** and **P6**. Nevertheless, the results obtained from the sets of solution-doped thin films show that there is a clear increase in the amount of $F4TCNQ^-$ as follows: **P4** ≤ **P3** < **P5** < **P6**. This trend generally correlates with the increase in spacing length between the alkyl side chains on the comonomer used to create each copolymer. Specifically, as the spacing length increases from one (**P3**) to two (**P5**) to three (**P6**) thiophene units, the steric demand is decreased, which allows F4TCNQ to access the polymeric backbone, enabling electron transfer (i.e., doping). In turn, this results in the formation of $F4TCNQ^-$, which enhances conductivity. It is also observed that the normalized absorbance of $F4TCNQ^-$ for **P4** is very similar to that of **P3**, despite the conductivity of solution-doped films of **P4** being approximately one order-of-magnitude lower than solution-doped films made from **P3**. This suggests that the difference in conductivity is significantly impacted by repeat unit design in addition to doping efficiency. As previously described, the fused ring thieno[3:2,*b*]thiophene in **P4** decreases the persistence length compared to **P3**, which is known to reduce electron delocalization and can lead to a reduction in film conductivity.[73] This result again shows the importance of efficient doping and structural organization on film conductivity. Lastly, with **P3** and **P4**, the absorbance of $F4TCNQ^-$ appears to remain relatively constant after 10 mol% doping, which indicates that the higher concentrations of dopant are not resulting in more doping events. This is consistent with the plateau in conductivity observed after 10 mol%.

2.4.4. Sequential Doping of Thiophene-Based Copolymers

Although it is a more complex process, sequential doping is viewed favorably because it circumvents issues of aggregation that are inherent to solution doping and

typically leads to enhanced levels of electrical conductivity.[13,26] Efficient sequential doping requires a solvent that is a good solvent for the dopant but a marginal solvent for the polymer – the solvent must swell, but not dissolve, the polymer film to allow for effective integration of the dissolved dopant molecule.[30] Therefore, an array of solvents and solvent blends were studied to determine the optimum solvent for sequential doping of the thiophene-based copolymers. Six specific solvents were selected based on their solubility parameter distance between the solvent and the corresponding copolymer, R_a. The R_a value for each solvent-copolymer pair was calculated using Equation 2.1, where the lowercase subscripts on the three HSPs correspond to either the polymer, *p*, or to the solvent, *s*.[48,49]

$$R_a = (4(\delta_{D_p} - \delta_{D_s})^2 + (\delta_{P_p} - \delta_{P_s})^2 + (\delta_{H_p} - \delta_{H_s})^2)^{1/2} \qquad \text{(Eq. 2.1)}$$

The corresponding R_a values for the six solvents used – THF, DCM, 50:50 acetone:DCM, 75:25 acetone:DCM, acetone, and DMF – and each copolymer are summarized in Table 2.5. With these solvents, R_a values range from approximately 5.45 to 14.00 $MPa^{1/2}$, with lower numbers indicating greater solubility of the polymer and higher numbers indicating poorer solubility. This range of solvent character enables insights into how polymer-solvent interaction energy impacts the resultant thin film conductivity. For all sequential doping studies, the concentration of F4TCNQ was fixed at 1 mg/mL.

As was done for solution-doped thin films, the surface roughness of sequentially-doped films was measured to assess film topology and potential aggregation. As summarized in Table 2.6, the surface roughness values are rather high and display a large sample-to-sample variation, especially compared to solution-doped thin films. These traits

Table 2.5. Calculated solubility parameter distance, R_a, of each polymer-solvent pair.

Polymer	R_a (MPa$^{1/2}$)					
	THF	DCM	50:50 Act:DCM	75:25 Act:DCM	Acetone (Act)	DMF
P3	5.48	6.45	8.39	9.47	10.57	13.38
P4	6.45	7.21	9.17	10.27	11.37	14.00
P5	5.45	6.45	8.43	9.52	10.63	13.19
P6	6.45	7.12	9.17	10.30	11.42	13.17
P3HT (AB)	5.92	6.17	7.90	8.92	9.97	13.38
P3HT (AA+BB)	6.45	6.45	7.73	8.59	9.50	13.89

Table 2.6. Surface roughnesses of sequentially-doped thin films as a function of the solvent used for doping.

Polymer	Surface Roughness (nm)					
	THF	DCM	50:50 Act:DCM	75:25 Act:DCM	Acetone (Act)	DMF
P3	16.1 ± 3.2	18.1 ± 6.7	21.3 ± 5.8	21.2 ± 7.6	36.7 ± 6.6	15.5 ± 5.1
P4	7.4 ± 3.5	34.1 ± 5.3	10.5 ± 6.8	15.2 ± 7.6	7.0 ± 3.6	2.0 ± 1.6
P5	21.6 ± 3.4	31.6 ± 16.0	22.9 ± 9.4	15.5 ± 1.8	8.6 ± 5.1	3.6 ± 0.7
P6	27.3 ± 15.8	32.2 ± 15.5	5.3 ± 1.1	28.1 ± 8.7	38.4 ± 6.8	10.2 ± 6.5
P3HT (AB)	20.1 ± 6.8	20.2 ± 8.9	26.5 ± 15.8	5.9 ± 1.0	19.1 ± 7.2	9.2 ± 7.0
P3HT (AA+BB)	17.9 ± 5.5	16.2 ± 9.0	28.2 ± 9.0	6.0 ± 2.7	15.4 ± 8.4	3.2 ± 0.8

are indicative of aggregation or non-uniformity in the film. The AFM images presented in Figure A.31-A.36 show the presence of aggregates across the film surfaces. These aggregate structures are believed to be excess dopant that did not integrate into the polymer film. This contention is supported by results from imaging **P3HT (AB)** films that were sequentially-doped with F4TCNQ using acetone as the dopant solvent and then rinsed with methanol, which dissolves F4TCNQ but does not dissolve or swell **P3HT (AB)** (R_a > 20 $MPa^{1/2}$). As shown in Figure 2.10, prior to rinsing, the surface was populated with large aggregates and had a measured roughness of 19.1 ± 7.2 nm. After rinsing with methanol, the surface was smooth and uniform with a roughness of 1.9 ± 1.4 nm. These results indicate that aggregates of excess F4TCNQ were the cause of the increased roughness and irregular topography observed for the sequentially-doped thin films. This finding is consistent with results from Jacobs et al., who reported phase segregated F4TCNQ domains on thin films when sequentially doping P3HT with F4TCNQ in acetonitrile at 1 mg/mL.[13] Due to the surface roughness being largely dominated by the presence of excess dopant, the images and surface roughness values do not offer much insight into the uniformity/topology of the underlying doped film. However, because the films are thin (< 30 nm) and to prevent removal of dopant from the upper region or from the entirety of the thin film, the methanol washing was not implemented as part of the process used to generate sequentially-doped thin films.

As with solution-doped thin films, after measuring the I-V curve of each sequentially-doped sample, film thicknesses were measured (Table A.3) and used to

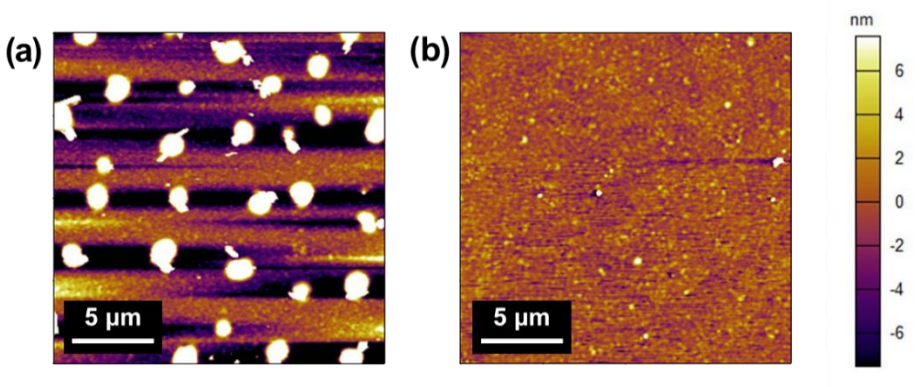

Figure 2.10. Representative AFM height images of **P3HT (AB)** thin films sequentially-doped with F4TCNQ at 1 mg/mL in acetone. Images correspond to (a) an as-cast film and (b) the film after a methanol rinse. Each image was obtained in tapping mode over an area of 20 µm × 20 µm. This comparison indicates that the F4TCNQ aggregates appearing in (a) are washed away by methanol and that the underlying film is smooth and homogeneous.

calculate the resultant conductivity. Figure 2.11 shows the conductivity of each sequentially-doped copolymer thin film as a function of the R_a value that characterizes the dopant solvent-copolymer pair. First and as seen in Figure 2.11a, **P3HT (AA+BB)** again shows low conductivity across the spectrum of solvents used for doping, which suggests that doping is inefficient in this regio-irregular polymer. In comparison, the conductivity of sequentially-doped **P3HT (AB)** thin films increases by ~3 orders of magnitude, depending on the dopant solvent used. This conductivity dependence on dopant solvent is consistent with work done by Yoon et al. with P3HT.[30] At low R_a values (5-8 $MPa^{1/2}$) and high R_a values (>12 $MPa^{1/2}$), the conductivity is low, while at moderate R_a values (8-12 $MPa^{1/2}$), the conductivity is much higher. This R_a-dependent conductivity is also seen for each copolymer film (Figure 2.11b), though the conductivity values are significantly higher than those measured for the P3HTs. In addition, the pattern of solvent-quality dependent behavior that is based on the thermodynamic interaction between the dopant solvent and polymer appears to be universally shared by all of these thiophene-based copolymers. Specifically, at low R_a values, the solvent can partially dissolve the film, which leads to inconsistent dopant integration. At high R_a values, the solvent is a poor solvent for the copolymer, which results in low levels of dopant integration beyond the polymer-solvent interface, resulting in the dramatic fall-off in conductivity. Lastly, with moderate R_a values, the solvent swells the copolymer chains, which allows for effective integration of the dopant, leading to higher conductivities.

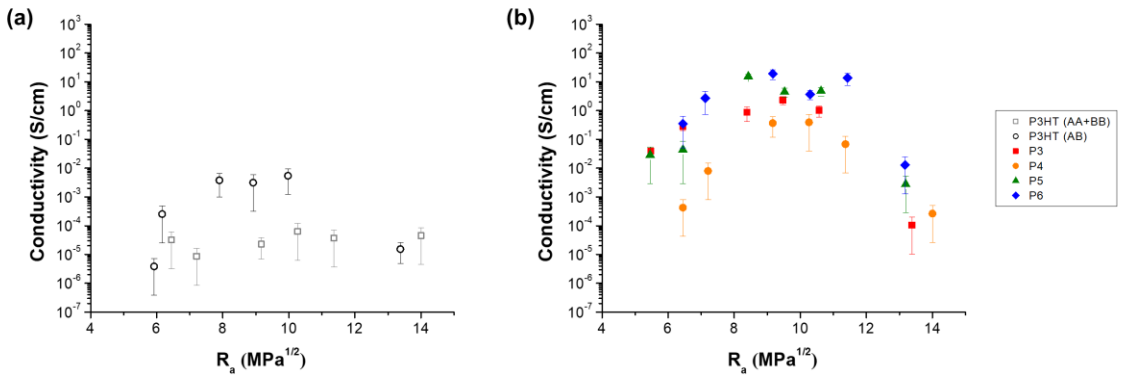

Figure 2.11. Conductivity of sequentially-doped thin films as a function of the solubility parameter distance between the polymer and solvent used for sequential doping. (a) **P3HT (AB)** and **P3HT (AA+BB)** and (b) the expanded thiophene-based copolymers. Doping was performed with six different solvents (THF, DCM, 50:50 acetone:DCM, 75:25 acetone:DCM, acetone, and DMF) at 1 mg/mL. Films were spin cast and doped on 1 in × 1 in glass slides and have film thicknesses ranging from 10-30 nm.

While the need for a marginal solvent to maximize conductivity has also been demonstrated for other systems,[80,81] HSPs provide a useful framework for selecting and creating a useful solvent system. In this work, solvent mixtures were used to tailor R_a values. Specifically, moderate R_a values were accessed by mixing DCM (low R_a) and acetone (near the high R_a border), resulting in high conductivities. This indicates that binary mixtures of poor or sub-optimal solvents can be used to tailor the R_a value, leading to an optimized conductivity. Additionally, for this series of thiophene-based copolymers, the trend of increasing conductivity with increasing spacing between alkyl side chains is also observed, but the effect is less prominent compared to the films made by solution doping. This indicates that altering the copolymer design by increasing the spacing length between alkyl side chains enhances conductivity by reducing steric demand along the chain backbone, which allows dopant molecules to access the backbone, perhaps without compromising the ability of the conjugated copolymers to organize through π-stacking interactions.

UV-Vis-NIR measurements of sequentially-doped thin films (Figure A.37-A.42) were used to gain insight into the efficiency of doping. However, unlike the solution-doped thin films, there is a lack of correlation between conductivity and $F4TCNQ^-$ absorbance (concentration), as shown in Figure 2.12. This indicates that in sequential doping, the amount of $F4TCNQ^-$ in the doped film is not the main factor that sets the conductivity. Rather, it is believed that micro-organization across multiple length scales plays a more important role,[40,82] which heightens the importance of using a marginal solvent to maintain

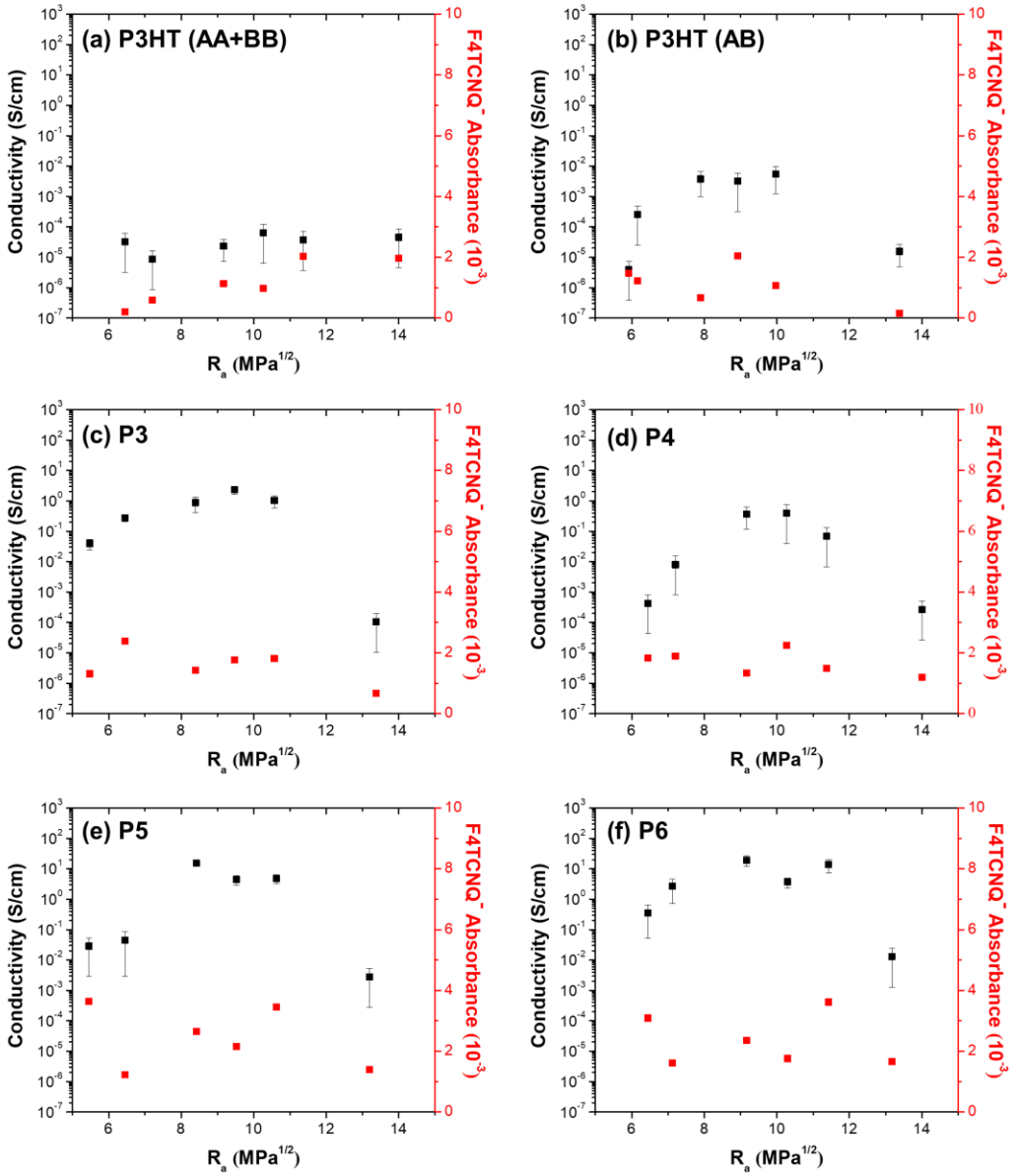

Figure 2.12. Comparison of measured conductivity and F4TCNQ⁻ absorbance in sequentially-doped thin films of (a) **P3HT (AA+BB)**, (b) **P3HT (AB)**, (c) **P3**, (d) **P4**, (e) **P5**, and (f) **P6** as a function of solubility parameter distance, R_a. The F4TCNQ⁻ absorbance is taken as the local maximum at 868 nm obtained from UV-Vis-NIR measurement and is normalized by film thickness. This normalized absorbance is proportional to F4TCNQ⁻ concentration.

the organization of the polymer film after doping, thereby enhancing conductivity.[26] The impact of solvent quality and dopant integration on thin film organization is something that should be addressed in a follow-on study.

2.4.5. Comparison of Solution and Sequential Doping

Solution doping is generally considered to be inferior to sequential doping when comparing electrical performance,[13,26] however this heuristic is not observed for all of the thiophene-based copolymers. The conductivities of the sequentially-doped thin films were very similar to that of the solution-doped films. Therefore, it is insightful to compare the amount of $F4TCNQ^-$ generated by each doping method to the film conductivity, as shown in Figure 2.13. To facilitate comparisons between the different copolymer designs, a set of common axis scales was used. Figure 2.13a shows that both solution and sequential doping were ineffective for **P3HT (AA+BB)**, as both methods resulted in films of low conductivity due to the regio-irregularity of the polymer. On the other hand, and despite also having overall low concentrations of $F4TCNQ^-$, a trend seems to emerge for **P3HT (AB)**: at low $F4TCNQ^-$ absorbance, a higher conductivity is seen with sequential doping. This indicates that reducing or eliminating aggregation that is prevalent in solution doping is a key element of promoting microstructural organization in the thin film that enhances electron transport. This contention is consistent with studies of doped P3HTs by Jacobs et al.[13] and Scholes et al.,[26] and a comprehensive analysis of a wide variety of conjugated polymers, including P3HTs, by Noriega et al.[27] The enhancement of conductivity with sequential doping becomes more apparent with the other copolymers: higher conductivities

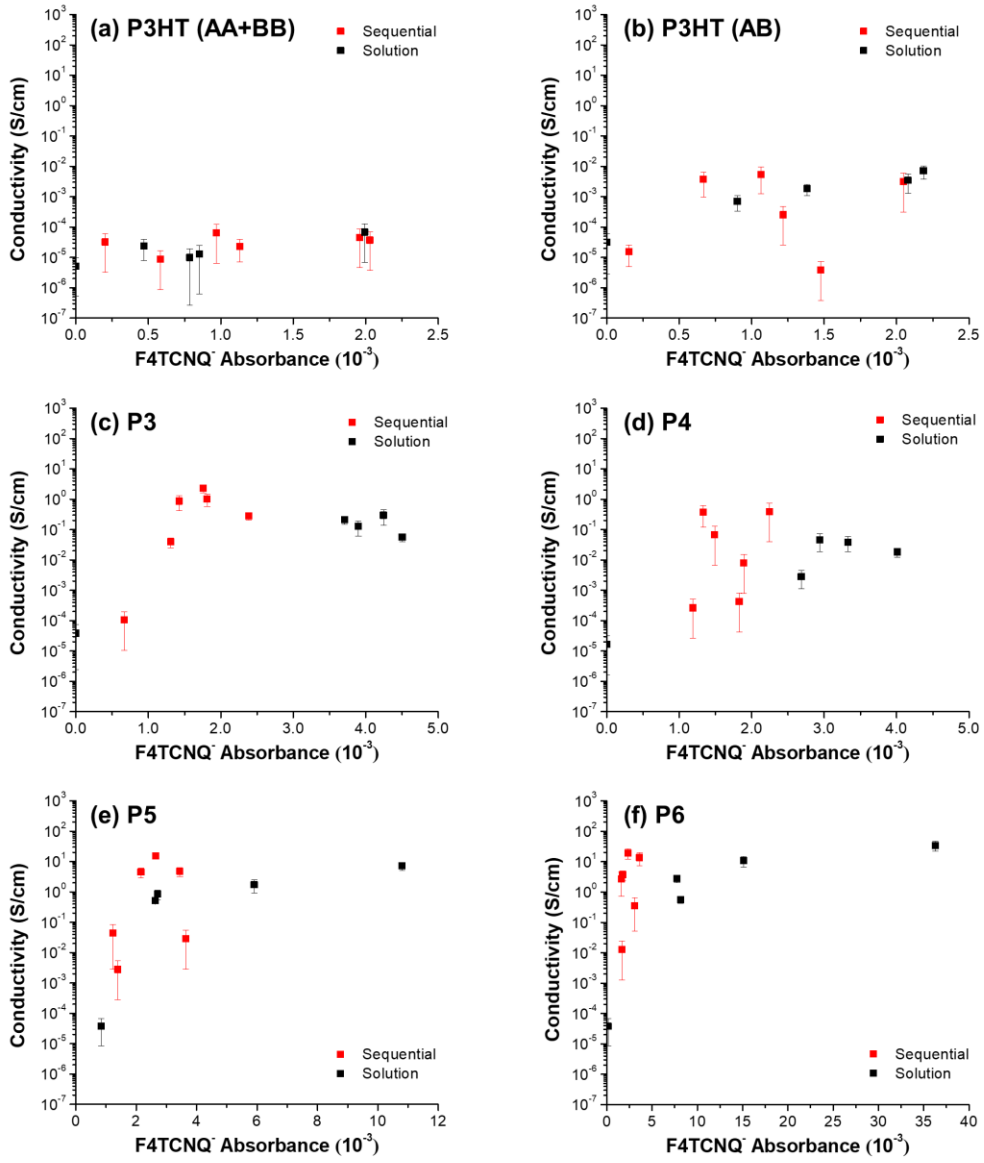

Figure 2.13. Comparison of F4TCNQ⁻ absorbance and conductivity for solution and sequentially-doped thin films of (a) **P3HT (AA+BB)**, (b) **P3HT (AB)**, (c) **P3**, (d) **P4**, (e) **P5**, and (f) **P6**. The F4TCNQ⁻ absorbance is taken as the local maximum at 868 nm obtained from UV-Vis-NIR measurement and is normalized by film thickness. This normalized absorbance is proportional to F4TCNQ⁻ concentration. For the expanded designs (**P3**, **P4**, **P5**, **P6**), it is clear that higher conductivities are reached at lower F4TCNQ⁻ concentrations.

are reached at lower concentrations of $F4TCNQ^-$ with sequential doping. Thereby, expanded designs also offer enhanced conductivity at lower concentrations of dopant while also increasing the conductivity by orders-of-magnitude compared to P3HT.

2.4.6. Core Expansion using Dithienothiophene

In an attempt to extend these studies of the effects that chain rigidity and coplanarity have on solubility, film morphology, and conductivity, another fused-ring copolymer utilizing dithieno[3,2-*b*:2',3'-d]thiophene as the spacing unit was proposed. The comonomer, **M7**, was synthesized via Suzuki coupling as shown in Scheme 2.3. This reaction was successful: **M7** was synthesized with an overall yield of 55% and confirmed with ^{1}H NMR as shown in Figure 2.14. Polymerization of this comonomer with 2,5-dibromo-3-hexyl-thiophene was attempted via DArP using the same conditions used for the other thiophene-based copolymers, as depicted in Scheme 2.4. As shown in Figure 2.15, the ^{1}H NMR of the resulting product did show signs of polymerization, specifically, the broadening of peaks. However, when the product was characterized via GPC, low molecular weight species were seen. This indicates that the product is mostly oligomeric (i.e., dimers, trimers, etc.) rather than polymeric. Therefore, in an attempt to increase the molecular weight of **P7**, the same polymerization reaction was performed but with reaction times extended to 48 h and 72 h. These longer reaction times were chosen since the mechanism of DArP results in a step-growth polymerization, and longer polymerization times generally lead to higher conversion (higher degree-of-polymerization). However, with both attempts, the same result was seen: only oligomeric species were formed.

Scheme 2.3. Synthesis of 2,6-bis(3-hexylthiophen-2-yl)di-thieno[3,2-*b*:2',3'-*d*]thiophene (**M7**) via Suzuki-Miyaura cross-coupling.

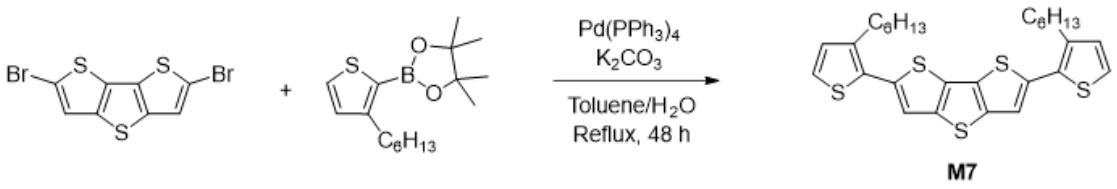

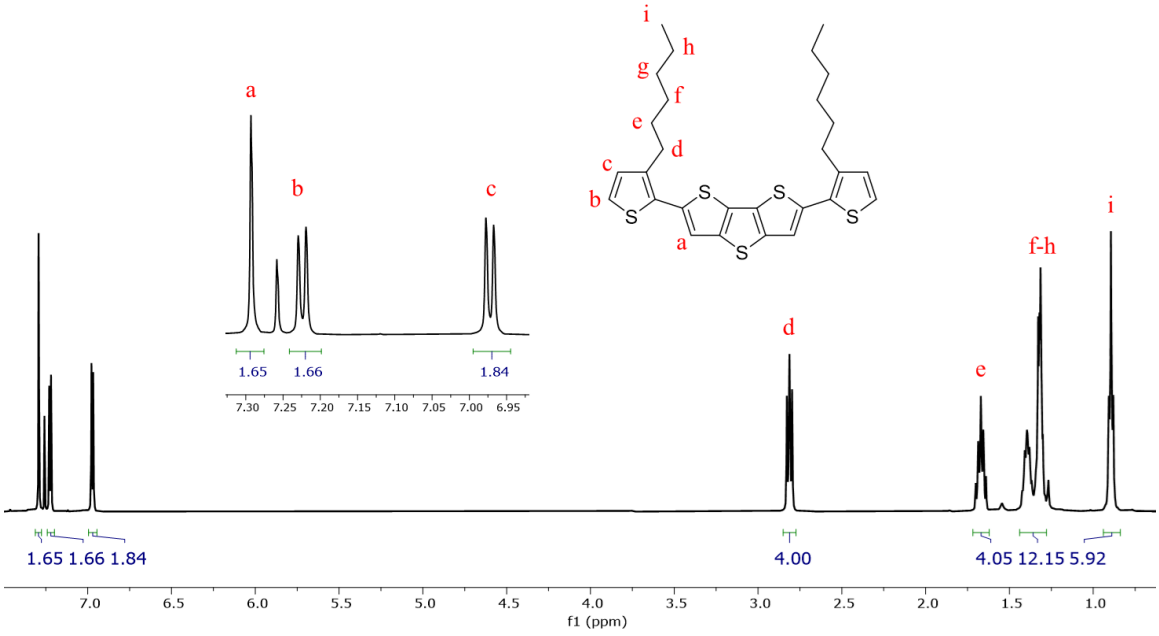

Figure 2.14. ^{1}H NMR spectrum of 2,6-bis(3-hexylthiophen-2-yl)di-thieno[3,2-*b*:2',3'-*d*]-thiophene (**M7**) in $CDCl_3$ with the inset highlighting the aromatic region.

Scheme 2.4. Synthesis of poly(2-(4,4'-dihexyl-[2,2'-bithiophen]-5-yl)-6-(3-hexyl-thiophen-2-yl)-dithieno[3,2-b:2',3'-d]thiophene) (**P7**) via DArP.

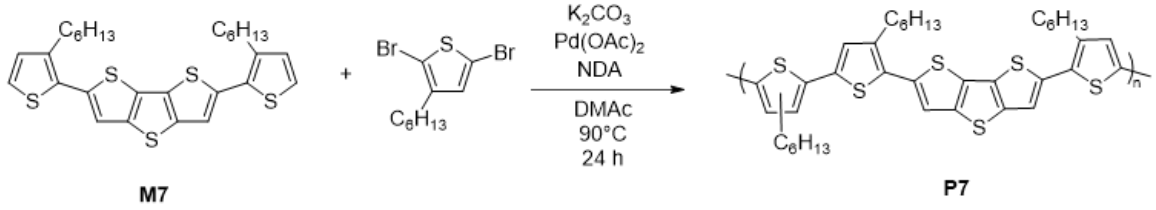

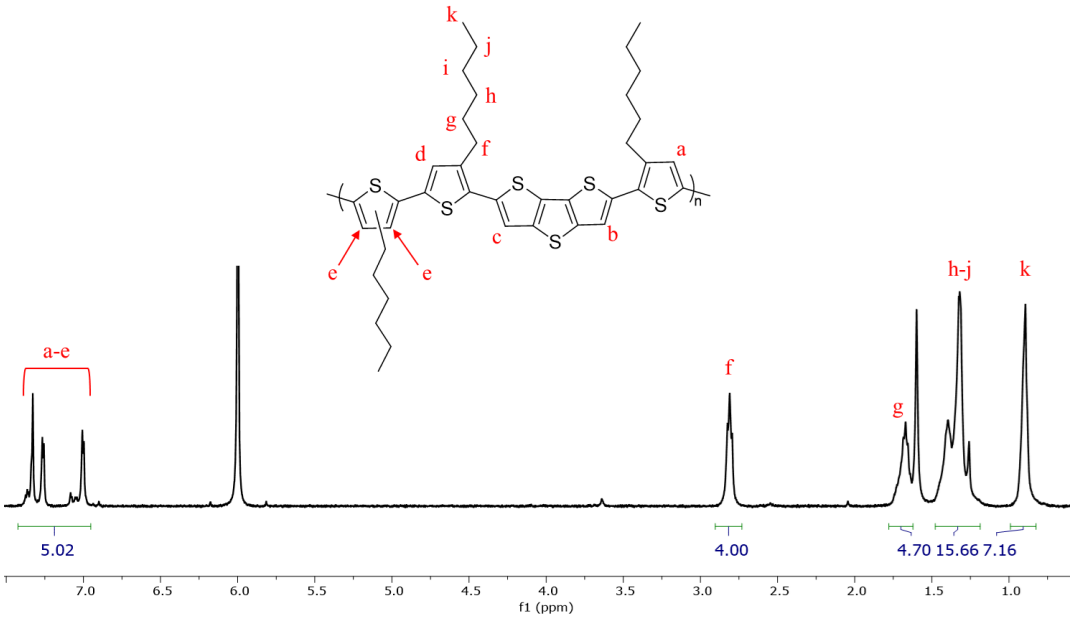

Figure 2.15. ^{1}H NMR spectrum of poly(2-(4,4'-dihexyl-[2,2'-bithiophen]-5-yl)-6-(3-hexyl-thiophen-2-yl)dithieno[3,2-b:2',3'-d]thiophene) (**P7**) in $C_2D_2Cl_4$.

It should be noted that reacting at a higher temperature was also considered in order to more effectively promote polymerization; however, with DArP, elevated temperatures may result in β-coupling and/or homocoupling.[42,44,45] This would further disrupt the regioregularity of the resultant polymer; therefore, increasing the temperature was not used as a strategy to increase molecular weight. The fact that no polymer was formed is attributed to sterics of the large, bulky comonomer, which seems to inhibit polymerization. Therefore, to circumvent this issue and increase the reactivity of the comonomers a new synthetic route to generate **P7** is proposed, as shown in Scheme 2.5. The proposed synthetic route starts with the synthesis of the comonomer, **M7-R2**. This was completed successfully at an overall yield of 32% and the structure confirmed with ^{1}H NMR, as shown in Figure 2.16. The proton assignments were consistent with reports by Ferrari et al. and Barbarella et al.[83,84] **M7-R2** was then polymerized with 2,6-dibromo- dithieno[3,2-*b*:2',3'-*d*]thiophene. The presence of the halogens on dithienothiophene provide a more reactive halogenated arene than the previous polymerization attempts due to the electron-richness of the fused-ring. Specifically, the electrophilicity of the carbon center which the halogens are attached to is increased, which in turn increases its susceptibility to undergo oxidative addition, facilitating DArP. However, despite this structural advantage, once again only oligomeric products were formed. In a final attempt to synthesize **P7**, this same reaction was run at an elevated temperatures (100 °C) and longer polymerization time (72 h). As stated earlier, increasing the temperature can cause β-coupling and/or homocoupling; however, a structural advantage of **M7-R2** is that the β- sites are protected by the hexyl side chains.

Scheme 2.5. Synthesis of (a) 3',4,4''-trihexyl-2,2':5',2''-terthiophene (**M7-R2**) via Stille cross-coupling and (b) copolymerization to form **P7** via DArP.

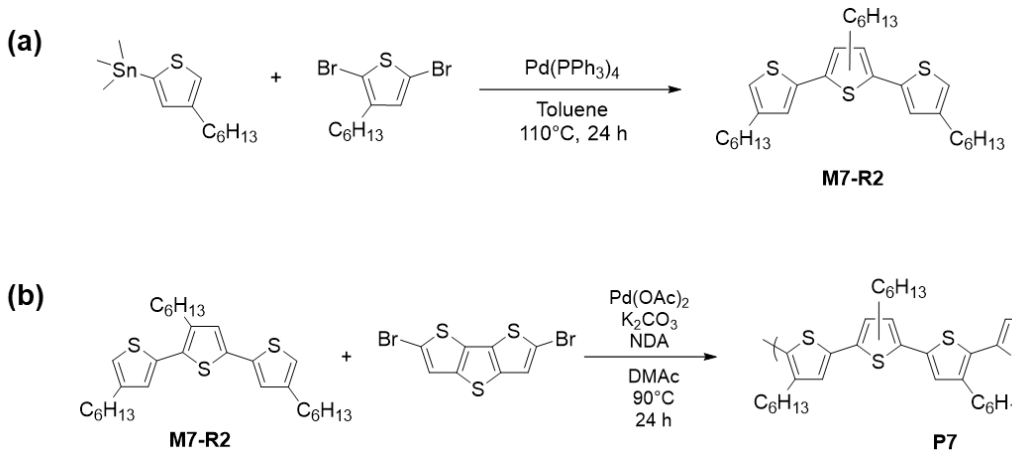

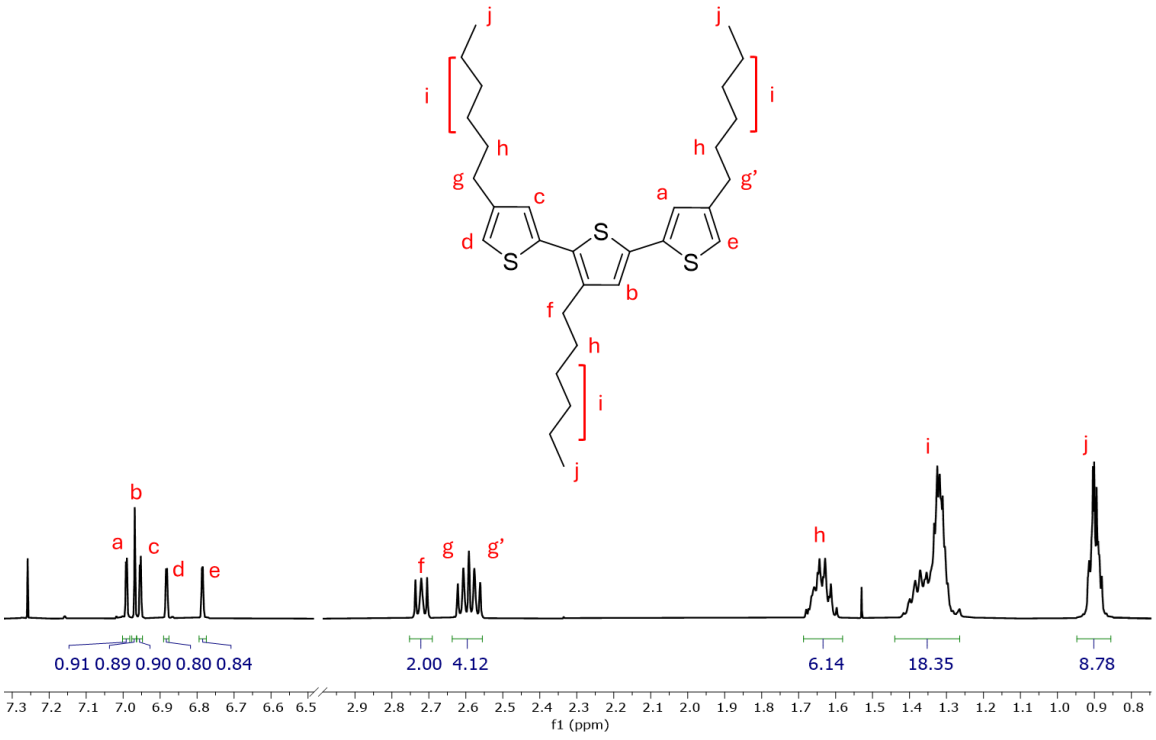

Figure 2.16. ^{1}H NMR of 3',4,4''-trihexyl-2,2':5',2''-terthiophene (**M7-R2**) in $CDCl_3$.

Therefore, β-coupling is expected to be minimized, even at elevated temperatures. Again, despite these changes in reaction conditions no polymer was formed. Therefore, expansion of the core with another fused ring structure could not be accomplished and studied in comparison to the other thiophene based copolymers (**P3**-**P6**). It may be possible to synthesize **P7** by more robust polymerization techniques, such as Stille or Suzuki-Miyaura cross-couplings, but these were not pursued in this dissertation research.

2.5. Conclusions

Thiophene-based copolymers were synthesized and characterized to evaluate the impact repeat unit structure has on solubility, film topography, and conductivity. Increasing the spacing length led to an increase in conductivity by multiple orders-of-magnitude (**P6** > **P5** > **P3** ≥ **P4**) for both solution and sequential doping relative to regioregular P3HT, which is attributed to the reduced steric demand along the backbone of the core expanded copolymers. The conductivity of sequentially-doped thin films showed a strong dependence on polymer-solvent interaction energy, as described by the differences in HSPs of the dopant solvent and polymer, R_a. This R_a-dependence appears universal for thiophene-based copolymers, with dopant solvents that give moderate R_a values (8-12 $MPa^{1/2}$), including solvent mixtures tailored to have moderate R_a values, resulting in the highest thin film conductivities. This universal dependence provides a basis for predicting an optimal solvent or solvent blend for sequential doping of thiophene-based polymers. The heuristic derived from studies of P3HT – that there is a significant increase in conductivity films are sequentially-doped, rather than solution-doped – was not observed in our studies of polythiophene copolymer thin films having decreased steric demand.

However, it is clear that sequential doping allows for higher conductivities to be achieved at lower concentrations of dopant for each copolymer. The higher conductivities associated with sequentially-doped thin films are believed to be related to their thin film organization; however, because relations between copolymer design, solvent quality, dopant integration, and thin film organization are known to be complex, those investigations are reserved for a follow-on study. Overall, this study provides detailed insights and expands the understanding of the phenomenon of chemical doping with respect to copolymer design and doping method, which may guide strategies to enhance electrical properties of more sophisticated conjugated polymer systems, rendering them suitable for applications in printed electronics, sensors, and other organic electronic devices.

Chapter 3. Enhancing Thin Film Morphology and Conductivity Through Serial Doping of Conjugated Thiophene-Based Copolymers

This chapter describes in part the work published in *ACS Applied Polymer Materials*, 2025, 7(17), 12083-12092. I synthesized and characterized all of the polymers described herein. I also performed all characterization including, absorbance, conductivity, and grazing-incidence wide-angle X-ray scattering (GIWAXS) measurements and analyzed the resulting data. Coauthors include Prof. Gila Stein, who advised on GIWAXS measurements and analysis, and Prof. S. Michael Kilbey II, who advised this research. This research was supported in part by the National Science Foundation (award #2204396).

3.1. Abstract

Chemical doping has been widely used to enhance the electrical performance of conjugated polymer thin films for organic electronic devices with specific attention given to dopant molecule selection, modifications of copolymer design to enhance dopant interactions, and the doping process itself. Here, a set of expanded core thiophene-based copolymers are doped via solution, sequential, or "serial" doping processes. Serial doping, which utilizes solution and sequential doping methods in succession, was utilized to investigate how the use of a two-step doping method impacts the doping efficiency, thin film conductivity, and morphology. Results show that serial doping with 2,3,5,6-tetrafluoro-7,7,8,8-tetracyanoquinodimethane (F4TCNQ) increases the conductivity of all of the thiophene-based copolymers relative to either one-step solution or sequential doping processes. This increase in conductivity of serial-doped films is not attributed to greater levels of incorporation of F4TCNQ; rather, the serial-doped thin films display more ordered crystalline microstructures, despite the pristine films having amorphous character. This indicates that serial doping enhances the conductivity by inducing crystallization. This

study also shows that as the spacing length between alkyl side chains of the expanded core copolymers is increased, the conductivity and the ordering of crystallites increases. Overall, this work provides insight into how copolymer design and the doping method impact conductivity through complex and intertwined relationships between dopant integration, effective electron transfer, and thin film microstructure.

3.2. Introduction

Conjugated polymers are widely studied for their use in thermoelectric devices, sensors, and printed electronics due to their flexible nature, low cost, processability, and use of naturally abundant elements.[1,3,62] The electrical performance of conjugated polymers can be optimized and/or tailored by using molecular dopants, where energetic offsets result in electron transfer that ultimately produces charge carriers. The polymer/dopant pair that has been studied most extensively is poly(3-hexylthiophene) (P3HT) and 2,3,5,6-tetrafluoro-7,7,8,8-tetracyanoquinodimethane (F4TCNQ), which feature well-aligned highest occupied molecular orbital (HOMO) and lowest unoccupied molecular orbital (LUMO) levels, respectively, which allows for effective p-type doping.[13,15,16,23,25,26,41] However, it is widely appreciated that the method used to incorporate the dopant significantly impacts processability, morphology, and conductivity.[13,25,26,30,32-34,85]

The most facile method of doping is solution doping, which relies on direct blending of separate solutions of the polymer and the dopant molecules. This method is proven to be effective in enhancing thin film conductivity; however, large amounts of dopant are required and charge transfer leads to a significant amount of aggregation of chains in solution, which can be detrimental to film morphology.[13,26] Therefore, a

sequential doping process is often used to prevent aggregation. This method requires that a pristine polymer film is created first, and then the dopant is added using a marginal solvent to swell the polymer chains, allowing the dopant to diffuse into the film.[13,26,30,86] The use of the pristine polymer film allows the morphology/chain alignment to be set prior to dopant integration and thus avoids the aggregation that arises from charge transfer during solution doping. Sequential doping is considered superior to solution doping because it preserves film morphology and requires less dopant while maintaining or enhancing the conductivity. Within this approach, it has also been shown recently that binary solvent mixtures can be used to strategically tailor polymer-solvent interaction energy in order to optimize film conductivity.[86]

A few doping strategies that modify the sequential doping process have been developed to further improve electrical performance. For instance, Fontana et al. demonstrated that evaporation-based sequential doping of P3HT with F4TCNQ yields electrical conductivities and degrees of doping that are similar to those realized by solution-based sequential doping.[25] They note that while the evaporation-based doping is more advantageous for large-area films, solution-based sequential doping is preferable for films with micrometer scale thicknesses.[25] In another use of evaporation-based sequential doping, Patel et al. also showed that vapor deposition of (tridecafluoro-1,1,2,2-tetrahydrooctyl)trichlorosilane (FTS) into thin films of poly(2,5-bis(3-tetradecylthiophen-2-yl)thieno[3,2-*b*]thiophene) (PBTTT-C_{14}) increased the thermoelectric performance (enhanced Seebeck coefficient and power factor) compared to the films that were sequential-doped via solution immersion.[87] Similarly, Vijayakumar showed that higher

thermoelectric power factors and high electrical conductivity could be achieved by a sequence of sequential doping steps using solutions of progressively higher dopant concentrations.[88] They showed that this so-called incremental concentration (ICD) doping preserved the microstructural ordering present in the initial films.[88]

Other studies have also investigated the impact of using a method that utilizes successive solution and sequential doping steps. For example, Chai et al. used a method called "Sequential-Twice-Doping" in which P3HT was solution-doped with F4TCNQ (at 7 mol%) and the resulting film was then sequentially-doped through immersion of the solution-doped film in an iron chloride ($FeCl_3$) solution.[33] The films created by this method exhibited an enhanced conductivity compared to films made by either solution- or sequential-doping only. Their assessments of morphology showed that the solution doping step doped the amorphous regions while the sequential doping step improved doping efficiency while maintaining the size of crystalline domains.[33] Similarly, Yoon et al. used what they termed "hybrid doping" in which thiophene-based polymers, including P3HT, were doped in solution with F4TCNQ at various levels (5-20 wt%), cast into a thin film, and then sequentially-doped by immersion in an F4TCNQ solution.[34] This hybrid doping method resulted in higher film conductivity compared to solution or sequential doping alone, which also maximized the thermoelectric power factor.[34] These doping methods that combine the use of solution and sequential doping show significant promise in terms of enhancing electrical performance, but thus far have been limited to studies that use dopant concentrations that establish modest or high levels of solution doping, where aggregation of polymer chains due to charge transfer is known to be prevalent.

More recently, it has been reported that doping efficiency may be improved by altering the repeat design of conjugated polymers in a way that increases the "space" between solubilizing side chains in order to enhance polymer-dopant interactions.[14,38,86,89] An example of this strategy of altering sterics along the backbone comes from Li et al. who showed that the incorporation of fused-ring thienothiophene spacer units into poly(quaterthiophene) enhanced doping efficiency by reducing the steric demand along the backbone, which ultimately led to higher conductivity in sequential-doped thin films.[14] Kim et al. showed that statistical copolymers of 3-hexylthiophene and thiophene exhibited conductivities 100 times higher than that of P3HT due to the formation of polymer-dopant-polymer co-crystals with short packing distances.[89] This co-crystallization is facilitated by the reduced side chain density as it enables the dopant to more closely interact with the polymer backbone.[89]

Herein, we report "serial" doping, a two-step doping process consisting of both solution and sequential doping, of a series of thiophene-based copolymers that are systematically altered to reduce side chain density. (We choose the term serial doping to clarify the process as having two doping steps that are performed in sequence, rather than hybrid doping, which can signify a blend or mixture.) A distinct aspect of this study is the use of low concentrations of F4TCNQ dopant in the solution doping step (1 mol%, which equates to < 0.4 wt%, depending on the copolymer used) to avoid aggregation. We investigate the impact that copolymer design and doping method have on thin film conductivity, dopant integration, and morphology. We find that serial doping is a superior doping method compared to either solution or sequential doping methods. Specifically, the

results show that for this series of thiophene-based copolymers, serial doping produces conductivities that are higher than either of the parent doping processes and promotes the formation of highly ordered crystallites.

3.3. Materials and Methods

3.3.1. Materials

2,5-bis(trimethylstannyl)thiophene (97%, Sigma), 2,5-bis(trimethylstannyl)-thieno[3,2-*b*]thiophene (97%, Sigma), 5,5'-dibromo-2,2'-bithiophene (98%, TCI), 5,5''-dibromo-2,2':5',2''-terthiophene (97%, Sigma), 2-bromo-3-hexylthiophene (97%, Sigma), 3-hexylthiophene-2-boronic acid pinacol ester (95%, Sigma), 3-hexylthiophene (99%, Sigma), tetrakis(triphenylphosphine)palladium(0) ($Pd(PPh_3)_4$, 99%, Sigma), palladium (II) acetate ($Pd(OAc)_2$, 98%, Sigma), potassium carbonate (99.7%, Fisher), neodecanoic acid (NDA, Sigma), magnesium sulfate ($MgSO_4$, 99.5%, Alfa Aesar), 2,3,5,6-tetrafluoro-7,7,8,8-tetracyanoquinodimethane (F4TCNQ, 99%, Ossila), toluene (99.85%, extra dry, Thermo Scientific), diethyl ether (anhydrous, Fisher), ethyl acetate (99%, Fisher), hexanes (98.5%, Fisher), dimethyl formamide (DMF, 99.8%, Thermo Scientific), N,N-dimethylacetamide (DMAc, 99.5%, extra dry, Thermo Scientific), methanol (99%, Fisher), acetone (99%, Fisher), chloroform (98%, Fisher), chlorobenzene (99.8%, anhydrous, Sigma), and graphite conductive adhesive (aqueous based, Alfa Aesar) were used as received. N-bromosuccinimide (NBS, 99%, Sigma) was recrystallized in water and vacuum dried prior to use.

3.3.2. Synthesis of Comonomers and Copolymers Procedures

2,5-dibromo-3-hexylthiophene and the series of expanded core comonomers were synthesized using the methods described in *Chapter 2*.[86] P3HT and the expanded core copolymers were synthesized via direct arylation polymerization (DArP), which was described in *Chapter 2*.[86]

3.3.3. Polymer Characterization

The ^{1}H NMR spectrum of each copolymer, acquired using a Varian VNMRS 500 MHz NMR, is presented in Figure B.1-B.5. Gel permeation chromatography (GPC) was used to determine number-average molecular weight (M_n) and dispersity (Đ) of each copolymer based on universal analysis. An Agilent 1260 Infinity II system was used for these measurements with a mobile phase of THF at 25 ℃ and a flow rate of 1 mL/min. Solutions for GPC measurements were made at a concentration of 4 mg/mL in THF and filtered with a 0.2 PTFE filter. The resultant molecular weights and dispersities are summarized in Table B.1 and the corresponding GPC traces are shown in Figure B.6.

3.3.4. DSC Measurements

Polymer samples were dried overnight in a vacuum oven. DSC samples with sample weights between ~3-7 mg were made in aluminum hermetic pans and an empty aluminum hermetic pan was used as a reference. A TA Instruments Q-2000 DSC was used to measure the thermograms from −50 to 300 °C at a rate of 10 °C/min. Both the heating and cooling cycles were measured twice. The first cycle was used to erase any thermal history of the polymers and analyses were performed on the second heating and cooling cycle.

3.3.5. Thin Film Preparations

Solution Doping. Solutions of 1 mol% F4TCNQ (relative to the total number of moles of thiophene repeat units in the chain, which equates to 0.30-0.40 wt% depending on the copolymer used) were made by mixing separately prepared solutions of the copolymer and F4TCNQ in chlorobenzene. For each solution, the final copolymer concentration after mixing was 30 mg/mL. The resultant polymer/dopant solution was then heated to 70 °C prior to deposition. Glass slides (1 in × 1 in) were cleaned with KimWipes^{TM}, washed with acetone and methanol, and dried with a stream of dry N_2 gas. The polymer/dopant solution (200 μL) was spin cast dynamically onto the clean glass slide at 1000 rpm for 40 s. The spin cast polymer film was allowed to dry for at least 10 minutes before adding contact points for conductivity measurements (see *Conductivity Measurements*). After adding contact points at the corners, the films were dried for an additional hour prior to any measurement.

Sequential Doping. The copolymer was dissolved in chlorobenzene (30 mg/mL) at 70 °C while F4TCNQ was dissolved in acetone at 1 mg/mL. Clean glass slides were prepared as described above. Then, the polymer was spin cast onto the clean glass slide by depositing 200 μL of polymer solution dynamically at 1000 rpm for 40 s. Immediately after spin casting, the thin film was submerged in the dopant solution for 30 s. The resulting sequentially-doped copolymer films were allowed to dry for at least 10 minutes.

Serial Doping. The same procedure described for solution doping was used and immediately after that, a second sequential doping step followed. The sequential doping procedure was performed by submerging the solution-doped thin film in the dopant

solution for 30 s. For each step, dopant concentrations were set to be equivalent to the single-step doping processes: In other words, solution doping used an F4TCNQ solution of 1 mol% F4TCNQ and the sequential doping step used an acetone solution at 1 mg/mL F4TCNQ. The resulting serial-doped copolymer films were allowed to dry for at least 10 minutes.

3.3.6. Conductivity Measurements

Conductive graphite adhesive was used to add contact points at each corner of the thin films. A Keithley 2450 Sourcemeter was used to perform current-voltage (I-V) sweeps from 0 to 1 V. Voltage was applied at the contact points across one edge and the current was measured across the contact points on the opposite edge in accordance with the Van der Pauw method, which requires measurement along each edge of the film.[57-59] A set of 3 replicate films were measured for each doping method. The sheet resistance (R_s) was calculated using the slope of the I-V curve and the Van der Pauw equation.[57] R_s and the film thicknesses, t, obtained from AFM scratch test measurements (described in *Appendix B* and summarized in Table B.2), were used to calculate the film resistivity, ρ. Conductivity, σ, was subsequently calculated as $\sigma = \rho^{-1}$.

3.3.7. Thin Film UV-Vis-NIR Measurements

UV-Vis-NIR spectra over the wavelength range $350 < \lambda\,(\text{nm}) < 2000$ were acquired from thin films using a Cary 5000 UV-Vis-NIR Spectrophotometer. This was done for as-cast and all doped thin films. A background spectrum acquired from a clean glass slide was used to baseline correct the spectra acquired for thin films and the corrected spectra were then normalized by film thickness. The absorbance ratio of $F4TCNQ^{-}$:polymer was

calculated using the absorbance at λ = 868 nm, which corresponds to the anionic form of F4TCNQ, $F4TCNQ^-$, and the absorbance at the λ_{max} for each of the respective polymers.

3.3.8. GIWAXS Measurements

Thin films were prepared as described above; however, an ozone treated silicon wafer substrate (critical angle = 0.22°) was used in place of glass. Measurements were performed using a Xenocs Xeuss 3.0 instrument. A Xenocs GeniX3D Cu source with a wavelength of 1.54 Å was used at an incident angle of 0.2°. The detector distance was set at 55 mm and each measurement was performed for 5 min. The resultant 2D images were used to produce 1D spectra based on a line cut in the out-of-plane.

3.4. Results and Discussion

3.4.1. Copolymer Synthesis and Characterization.

A series of thiophene-based copolymers with expanded cores were used to elucidate the impact that repeat unit design has on morphology and conductivity, with an emphasis on doping method. Inspired in part by the work of Li et al.[14], the expanded cores were designed with varying thiophene-based "spacing units" to increase the distance between hexyl side chains in the comonomers, which allows for more effective dopant integration within the copolymer due to reduced steric demand.[14,38,86] The expanded core copolymers feature spacing units of thiophene (**P3**), thieno[3:2,*b*]thiophene (**P4**), 2,2'-bithiophene (**P5**), and 2,2':5':2"-terthiophene (**P6**), as shown in Figure 3.1. **P3HT** with a regioregularity of 93% made via AB polymerization is used as a benchmark polymer. The copolymers **P3-P6** have a regioregularity of 50% due to the AA+BB polymerization of the symmetric

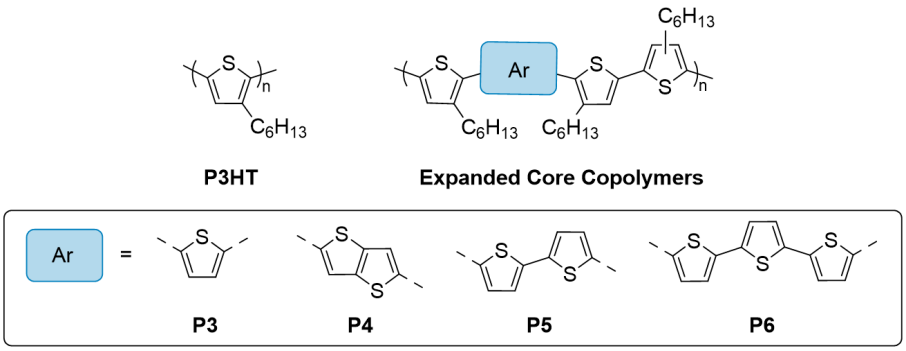

Figure 3.1. Structures of **P3HT** and the expanded core copolymers containing spacing units of thiophene (**P3**), thieno[3:2,*b*]thiophene (**P4**), 2,2'-bithiophene (**P5**), and 2,2':5',2''-terthiophene (**P6**).

expanded core comonomers with the asymmetric comonomer 2,5-dibromo-3-hexyl-thiophene. The molecular weights of the (co)polymers range from 6-16 kg/mol (Table B.1). As described in *Chapter 2*, based on these molecular weights, each polymer is well beyond its effective conjugation length;[86] therefore, any subsequent changes seen in optoelectronic or conductimetric measurements are believed to be attributed to repeat unit design and/or polymer self-assembly.

To first investigate the impact that spacing units have on thermal properties, DSC measurements were performed to identify the glass transition temperature (T_g), crystallization temperature (T_c), and melting temperature (T_m) of these polymers. The full DSC thermograms are shown in Figure B.7-B.11 and the values of T_g, T_c, and T_m are summarized in Table 3.1. First, **P3HT** does not exhibit a distinguishable T_g despite reports of P3HT having a weak T_g in the range of ~5-22 °C.[90,91] However, a clear T_c and T_m are observed, indicating that this highly regioregular polymer is semicrystalline, as expected. The value of T_m = 196 °C is consistent with reported values of T_m for P3HT, which range from ~190-230 °C depending on regioregularity and molecular weight.[92-95] The thermograms acquired for the expanded core copolymers show T_g transitions; however, these copolymers lack crystalline and melting transitions. This indicates that the copolymers **P3**-**P6** are amorphous in nature, which may be due to their inherent regio-irregularity. All have a higher T_g compared to the values reported for P3HT, with **P4** having the highest T_g due to the backbone rigidity resulting from its fused ring. The T_g values for the other expanded core copolymers follow the trend of **P3** < **P5** < **P6**, which is consistent

Table 3.1. T_g, T_c, and T_m for P3HT and the expanded core copolymers.

Polymer[a]	**T_g (°C)**	**T_c (°C)**	**T_m (°C)**
P3HT	n.m.	161	197
P3	29	-	-
P4	55	-	-
P5	35	-	-
P6	42	-	-

[a]*All values obtained from DSC thermograms acquired at 10 °C/min.*
n.m. - not measured

with the expected impact of increasing the spacing unit length (decreasing the side chain number density), which allows for more π-stacking interactions between the polymer chains.

3.4.2. Electrical Conductivity of Doped Copolymer Thin Films

Various doping methods have been developed to enhance the conductivity of conjugated polymer thin films, with the most prevalent methods being solution doping and sequential doping. These two doping methods are used here along with serial doping to assess impacts on conductivity and morphology. As shown in Figure 3.2, solution doping entails combining premixed solution of polymer and dopant and then spin casting this polymer/dopant solution onto the substrate to obtain solution-doped thin films. On the other hand, sequential doping involves taking a pristine polymer thin film and then, in a separate step, integrating the dopant by soaking the polymer film in a dopant solution. This method requires the use of a marginal solvent (with respect to the polymer) to ensure effective dopant integration without dissolution of the film. In this study, acetone is utilized because our prior work shows that it has a moderate polymer-solvent interaction energy with **P3HT** and the expanded core copolymers, which optimizes the conductivity realized by sequential doping.[86] While solution and sequential doping methods each add the dopant in a single step, serial doping subjects a solution-doped thin film to a second doping step that is analogous to sequential doping by soaking that film in a dopant solution (that is made using a marginal solvent). These processes are depicted in Figure 3.2.

Each of the copolymers, along with **P3HT**, were doped using these three methods

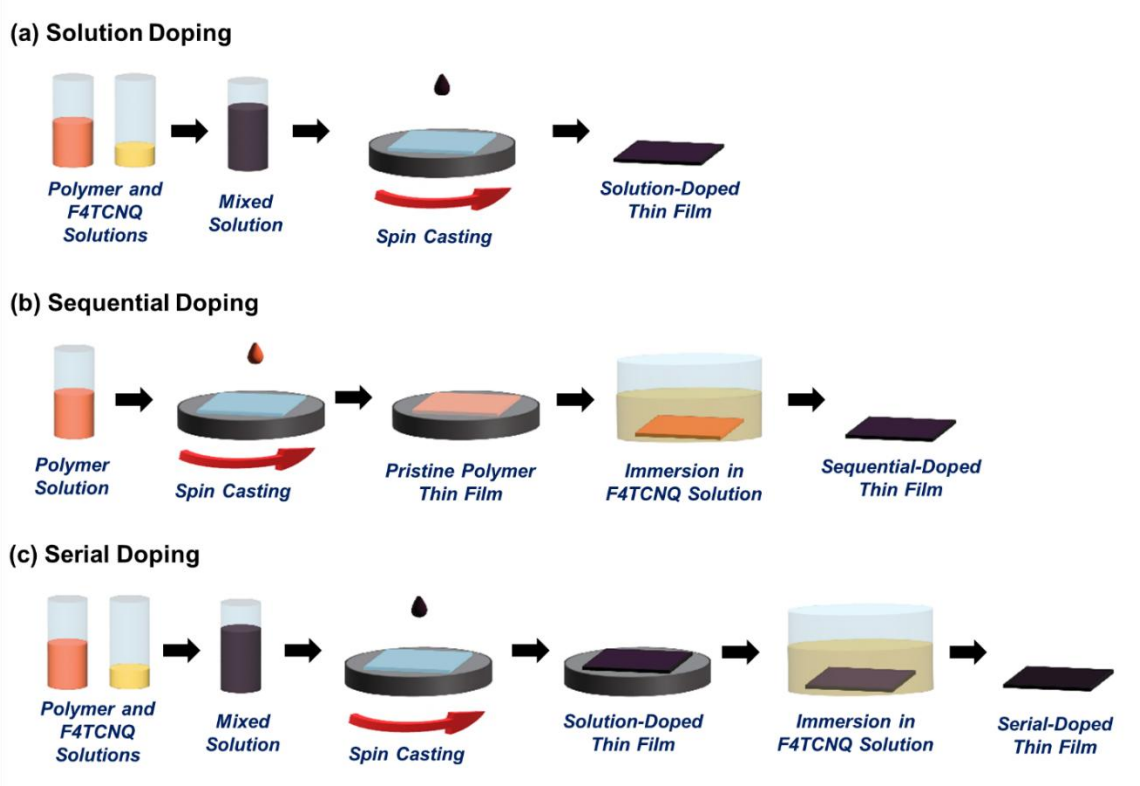

Figure 3.2. Schematic drawings illustrate (a) solution, (b) sequential, and (c) serial doping methods. Solution-doped thin films are cast from a solution made by mixing separate solutions of 30 mg/mL polymer and 1 mol% F4TCNQ in chlorobenzene at 70 °C. For sequential doping, a 30 mg/mL polymer solution in chlorobenzene at 70 °C is used to cast a pristine polymer film and then the film is submerged in a 1 mg/mL F4TCNQ solution in acetone for 30 s. Serial doping involves first creating the solution-doped thin film, followed by a second doping step in which the solution-doped thin film is submerged in a 1 mg/mL F4TCNQ solution in acetone for 30 s.

and thin film conductivities were subsequently measured. It should be appreciated that even though consistent solution concentrations and spin casting processes were used, the thin films have inherently different thicknesses, ranging from 62 to 300 nm (depending on the copolymer and doping method, Table B.2), because the polymers have different solubilities (manifests as different Hansen solubility parameters[86]). First and as shown in the inset of Figure 3.3, the solution-doped thin films have low conductivities that are in the range of ~10^{-4} – 10^{-1} S/cm. This is attributed to the small amount of dopant used (1 mol% with respect to the number of thiophenes units present in solution). There is a clear trend that as the size of spacing unit increases from thiophene to bithiophene to terthiophene, the conductivity also increases (**P3** ≤ **P5** < **P6**). This is attributed to the larger spacing units allowing for more effective dopant integration due to the decreased number density of side chains along the backbone. Notably, solution-doped **P4** films have a significantly higher conductivity compared to the other copolymers. This is ascribed to both the fused-ring structure promoting π-interactions and the reduced steric demand offered by the repeat unit design, which was also observed by Li et al. in their study of sequentially-doped thin films of poly(quaterthiophene) having thienothiophene spacing units (PQT-TT).[14] A more encompassing description of the thin film microstructure and its relation to conductivity will be presented in *Section 3.4.4.*

As seen in Figure 3.3, the conductivity measured for all polymer films prepared by sequential doping is three orders-of-magnitude higher than their solution-doped counterparts. This increase in conductivity is largely due to a significant increase in the

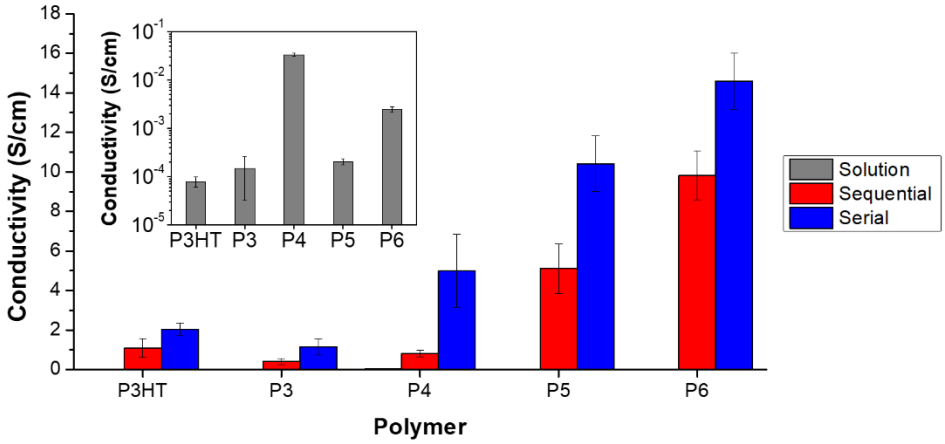

Figure 3.3. Conductivity of solution-, sequential-, and serial-doped thin films of **P3HT** and each expanded core copolymer (**P3**-**P6**). The inset shows the solution-doped thin film measurements on a log scale to visualize the data effectively. For solution doping, films were cast from a polymer solution having 1 mol% F4TCNQ. With sequential doping, the polymer thin films were submerged in an acetone solution containing 1 mg/mL F4TCNQ solution for 30 s. Serial doping used a two-step process in which a solution-doped film was made and then submerged in a 1 mg/mL F4TCNQ acetone solution in acetone for 30 s. Clearly, the increase in conductivity resulting from serial doping exceeds what would be expected from a purely additive result.

amount of dopant integrated into the thin film upon sequential doping compared to that resulting from solution doping. This is attributed to the low level of dopant used with solution doping (1 mol% F4TCNQ) and confirmed by measurements of the amount of dopant in the film, which are discussed in more detail in *Section 3.4.3*. The conductivities measured from sequentially-doped films again show that as the spacing unit is increased, there is an increase in conductivity: **P3** < **P5** < **P6**; however, unlike the solution-doped films, the sequentially-doped **P4** film no longer exhibits the highest conductivity. This arises due to changes in film microstructure as evidenced by GIWAXS measurements, which are presented in *Section 3.4.4*.

Figure 3.3 also clearly shows that serial doping results in a higher conductivity for each of the copolymer and **P3HT** films compared to sequential doping. The solution-doped thin films start with a very low conductivity, but the subsequent step of sequential doping results in the conductivity surpassing that of sequentially-doped films. This indicates that the two steps of the serial doping process are not additive, which suggests that this increase in conductivity is not directly caused by the amount of dopant introduced into the thin film. Rather, we contend that the increase in conductivity is largely impacted by the microstructure of the film, and this idea is discussed in more detail in *Section 3.4.4*.

3.4.3. UV-Vis-NIR Analysis of Doped Copolymer Thin Films

One indication of effective doping is the presence of anionic F4TCNQ ($F4TCNQ^{-}$) in doped systems, whether it be in solution or thin film. The formation of $F4TCNQ^{-}$ signifies an electron transfer from the conjugated polymer backbone to F4TCNQ; therefore, higher levels of $F4TCNQ^{-}$ indicate that more doping events have occurred. UV-

Vis-NIR measurements were used to evaluate the amount of dopant, specifically $F4TCNQ^-$, present in the thin films. Figure 3.4 shows spectra from as-cast, solution-, sequential-, and serial-doped thin films of **P3HT** and each core expanded copolymer (**P3**-**P6**). These spectra are normalized by film thickness, which makes the normalized absorbance directly proportional to concentration. The neutral polymer peaks of each polymer is labelled with black circles. The presence of $F4TCNQ^-$ is observed in the range of 728-955 nm, with the local maximum at 868 nm identified in each spectrum by an orange star.[16,23,86] Notably, the solution-doped thin films of each polymer have the lowest absorbance of $F4TCNQ^-$, indicating that less doping occurs and, as expected, these films have the lowest conductivities. Compared to solution-doped thin films, the absorbance of the neutral polymer peaks for sequential- and serial-doped films decreases as the $F4TCNQ^-$ peak increases, indicating these doping methods result in a greater occurrence of electron transfer. Although Figure 3.4a shows that sequentially-doped **P3HT** films have a higher $F4TCNQ^-$ absorbance than the corresponding serial-doped films, the conductivity of sequentially-doped **P3HT** films is lower than that of the serial-doped **P3HT** films. On the other hand, the serial-doped **P3** thin films (Figure 3.4b) have the highest concentration of $F4TCNQ^-$, which is consistent with those films having the higher conductivity. However, this small increase in $F4TCNQ^-$ for serial-doped **P3** films does not account for the ~3× increase in conductivity that was measured for serial-doped **P3** thin films compared to the sequential-doped films, which was seen in Figure 3.3. As shown in Figure 3.4c and 3.4d, sequential doping, while **P6** (Figure 3.4e) films show a higher absorbance of $F4TCNQ^-$

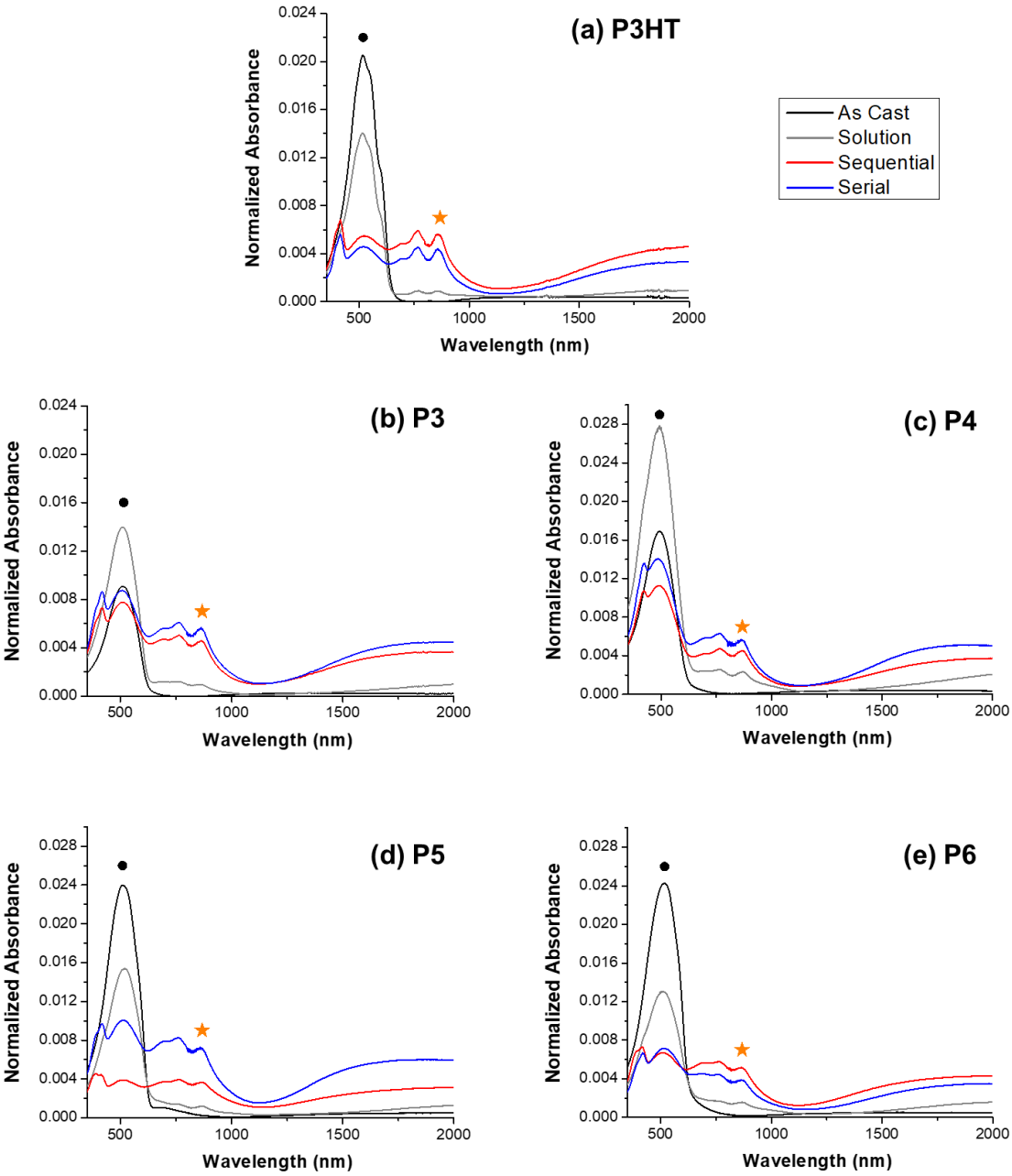

Figure 3.4. UV-Vis-NIR spectra of (a) **P3HT**, (b) **P3**, (c) **P4**, (d) **P5**, and (e) **P6** as-cast films and films doped via solution, sequential, and serial doping methods. The spectra are normalized by film thickness which makes the absorbance signal proportional to concentration. The black circles indicate the λ_{max} of each polymer, while the orange star indicates the peak attributed to $F4TCNQ^{-}$ (868 nm) that is used for analysis. The broad absorbance appearing at $\lambda > 1200$ nm signifies polaron formation.

with sequential doping. The inconsistency in the amount of $F4TCNQ^-$ present in serial-doped films further indicates that the amount of $F4TCNQ^-$ present in the thin film is not the sole contributor to conductivity, and it may also suggest that not every charge carrier pair that is formed contributes to conduction, as demonstrated by Pingel and Neher in their studies of P3HT and F4TCNQ.[19]

Additional insight into the doping effectiveness was generated from these spectra by calculating the ratio of absorbance of $F4TCNQ^-$ to neutral polymer. The absorbance of $F4TCNQ^-$ at 868 nm (identified by the orange stars in Figure 3.4) and the absorbance of each polymer at their respective λ_{max}, which was determined from their respective as-cast spectra, were used in this calculation. Figure 3.5 shows the correlation between conductivity and the ratio of $F4TCNQ^-$:neutral polymer for solution-, sequential-, and serial-doped thin films. For solution-doped thin films of **P3HT** and each core expanded copolymer, the $F4TCNQ^-$:polymer is very low, which is consistent with the low conductivities ($\sim 10^{-4}$ – 10^{-1} S/cm) that are observed from the plot inset in Figure 3.3. Compared to solution-doped films, films made using sequential doping or serial doping have higher $F4TCNQ^-$:polymer absorbance ratios and higher conductivities; however, there is no clear trend between absorbance ratio and conductivity for sequential- and serial-doped films. For **P3HT**, **P3**, and **P4**, the ratio of $F4TCNQ^-$:polymer remains relatively constant despite these films exhibiting an increase in conductivity from sequential doping to serial doping. With **P5** and **P6**, there is a decrease in the $F4TCNQ^-$:polymer ratio when comparing sequentially-doped to serial-doped films, even though an increase in

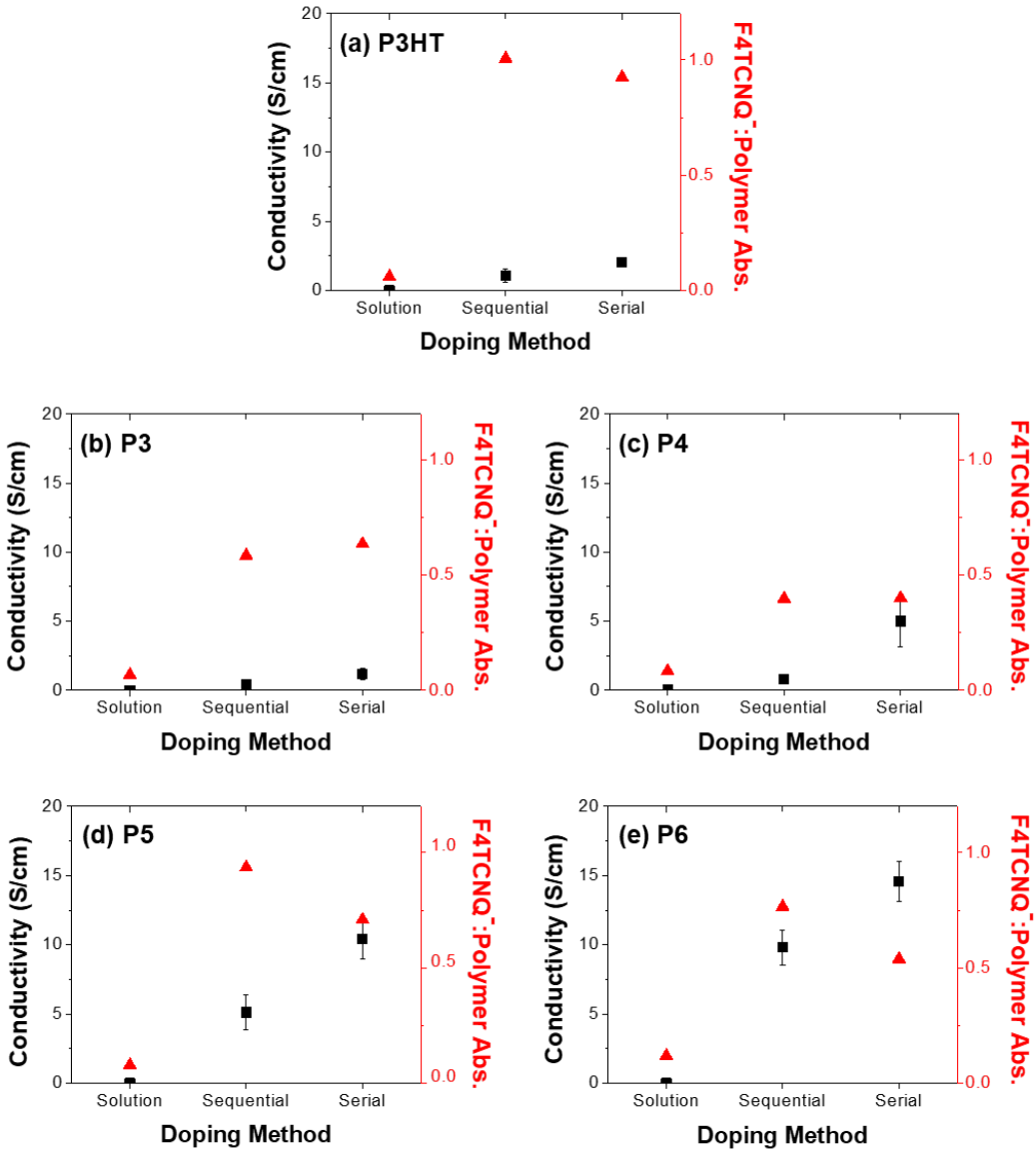

Figure 3.5. Comparison of conductivity and F4TCNQ^{-}:polymer absorbance ratio for thin films created by each doping method: (a) **P3HT**, (b) **P3**, (c) **P4**, (d) **P5**, and (e) **P6**. The ratio of F4TCNQ^{-}: polymer was calculated using the absorbance at 868 nm for F4TCNQ^{-} and the absorbance at the λ_{max} for each of the respective polymers. Common axis scales are used to enable comparisons. The lack of correlation between conductivity and relative level of effective charge transfer expressed by the absorbance ratio indicates that the changes in conductivity are not solely driven by the amount of F4TCNQ^{-} generated.

conductivity is observed. These findings again indicate that the difference in conductivity between sequential and serial doping is not solely driven by the amount of $F4TCNQ^-$ generated during doping and suggests that not all of the $F4TCNQ^-$ present in the thin film contributes to charge transport.

3.4.4. GIWAXS Measurements of Doped Copolymer Thin Films

The thin films were characterized using GIWAXS to gain insight into how the doping method and copolymer design impacts ordering. Figure 3.6 shows the 1D GIWAXS profiles in the out-of-plane direction for as-cast and solution-doped thin films of each polymer. We focus on the edge-on orientation because in-plane conductivity measurements were performed, and it has been shown that edge-on crystallites facilitate higher in-plane conductivity due to intermolecular charge transport occurring along the π-stacking direction.[54,55] The corresponding 2D images are presented in Figure 3.7 and Figure 3.8, respectively. For the as-cast films, **P3HT** has a well-defined (100) diffraction peak along with a weak (200) diffraction peak in the out-of-plane direction. The narrowness of the (100) peak along the azimuthal direction in the corresponding 2D image indicates that it adopts a predominantly edge-on orientation.[55,96] This finding is consistent with DSC measurements that indicate that **P3HT** is semi-crystalline. The as-cast thin films of the expanded core copolymers (Figure 3.6a) appear to be essentially amorphous, (consistent with DSC measurements exhibiting only a T_g), as there are no crystalline peaks with **P3** and only very weak (100) peaks with **P4**, **P5**, and **P6**. In addition, an amorphous halo is observed between 1-2 $Å^{-1}$ for each of the expanded core copolymers and **P3HT**. For

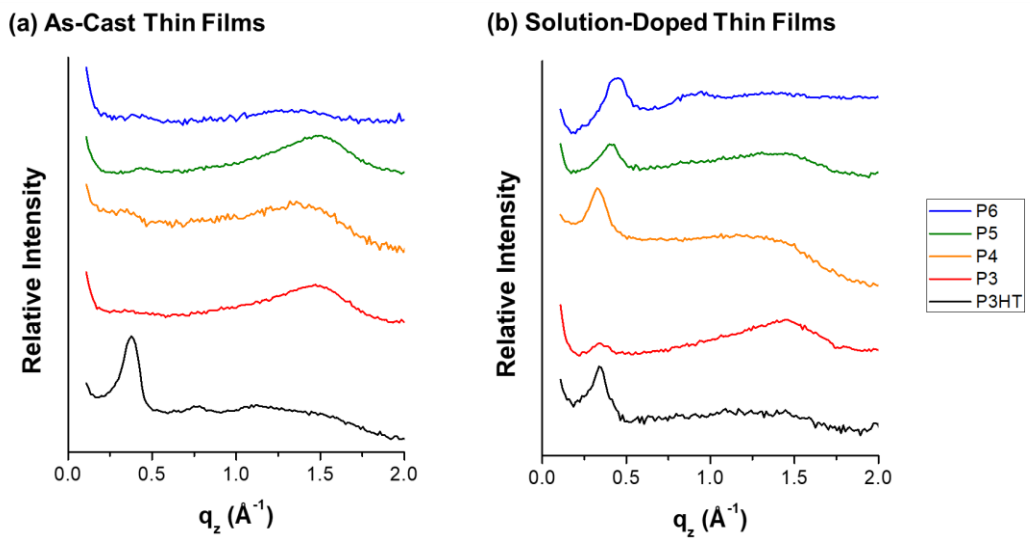

Figure 3.6. Out-of-plane 1D GIWAXS profiles of (a) as-cast and (b) solution-doped thin films. The y-axis is offset on a logarithmic scale to facilitate comparison. These out-of-plane profiles provide insight into the prevalence of edge-on crystallites in the films.

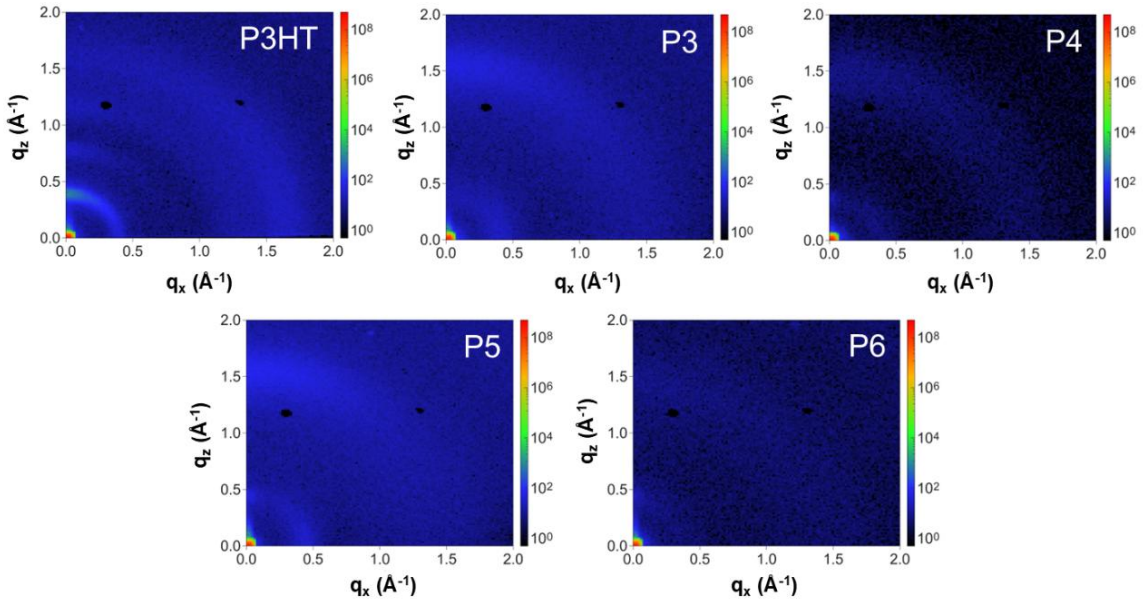

Figure 3.7. 2D GIWAXS images acquired from as-cast thin films of each polymer.

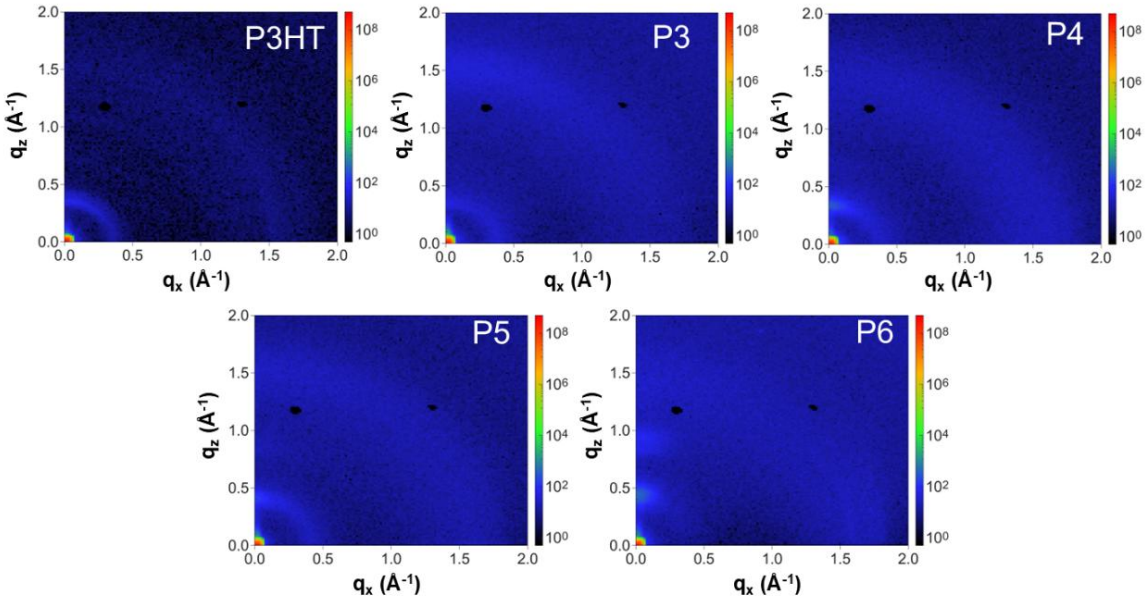

Figure 3.8. 2D GIWAXS images acquired from solution-doped (1 mol% F4TCNQ) thin films of each polymer.

solution-doped **P3HT** thin films, the crystalline peak is less defined, indicating the films are more disordered than the as-cast films, which is likely due to aggregation of chains that occurs upon electron transfer. Furthermore, and as summarized in Table 3.2, the out-of-plane *d*-spacing calculated from the (100) diffraction peak is larger for solution-doped **P3HT** thin films (18.6 Å) compared to as-cast **P3HT** films (16.7 Å). This indicates that the dopant is integrated within the lamellae, thus increasing the lamellar distance.[31,32] With the expanded core polymers, (100) crystalline peaks become more apparent in the solution-doped thin films, suggesting that the integration of the F4TCNQ dopant induces crystallization. Notably, solution-doped films of **P4** have a more well-defined crystalline peak than the other copolymers that feature expanded cores and exhibits the highest conductivity amongst the films made using this doping method. This indicates that presence of edge-on crystallites results in higher conductivity compared to the other solution-doped copolymer thin films.

Figure 3.9 shows the out-of-plane 1D GIWAXS profiles of sequential- and serial-doped thin films. The corresponding 2D images are shown in Figure 3.10 and Figure 3.11, respectively. Sequential doping is known to maintain the morphology of the pristine polymer thin films after doping[13,26,82] and this phenomenon is seen here with sequentially-doped **P3HT**. Specifically, sequentially-doped P3HT has a clear (100) peak with weak higher-order reflections, similar to the pristine films. With sequentially-doped **P3**, **P4**, and **P5,** the 1D profiles, which are presented in Figure 3.9a, are largely unchanged compared to their as-cast counterparts (Figure 3.6a) and the 2D images show Debye-Scherrer rings,

Table 3.2. Out-of-plane *d*-spacing of as-cast and doped thin films.

	Out-of-plane *d*-spacing (Å)[a]			
Polymer	**As-cast**	**Solution**	**Sequential**	**Serial**
P3HT	16.7	18.6	19.3	20.1
P3	-	18.6	20.1	19.3
P4	-	19.3	21.0	18.6
P5	-	15.6	17.9	18.6
P6	-	13.9	17.9	14.7

[a]*Calculated from the corresponding 1D GIWAXS profiles using the (100) diffraction peak.*

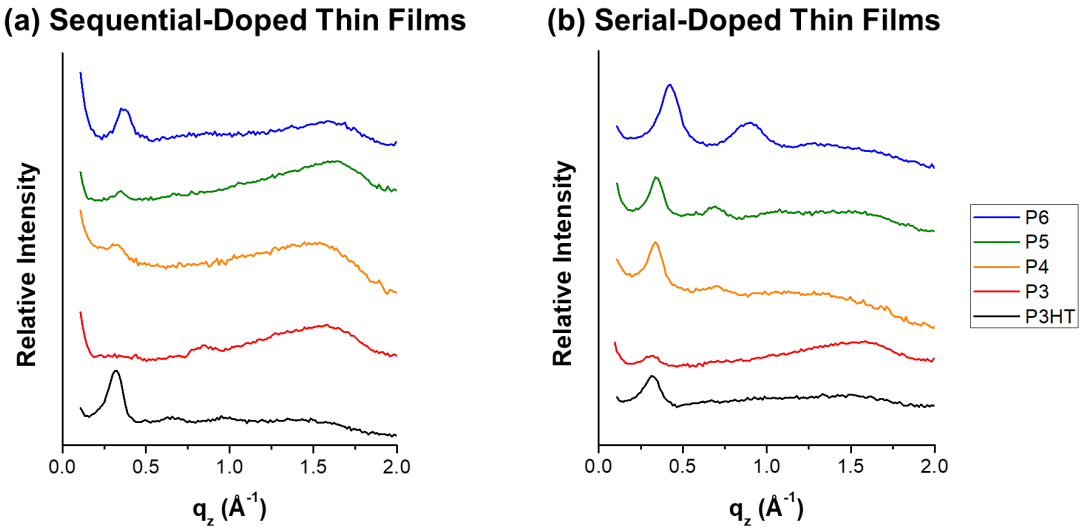

Figure 3.9. Out-of-plane 1D GIWAXS profiles of (a) sequential- and (b) serial-doped thin films. The y-axis is offset on a logarithmic scale to facilitate comparison.

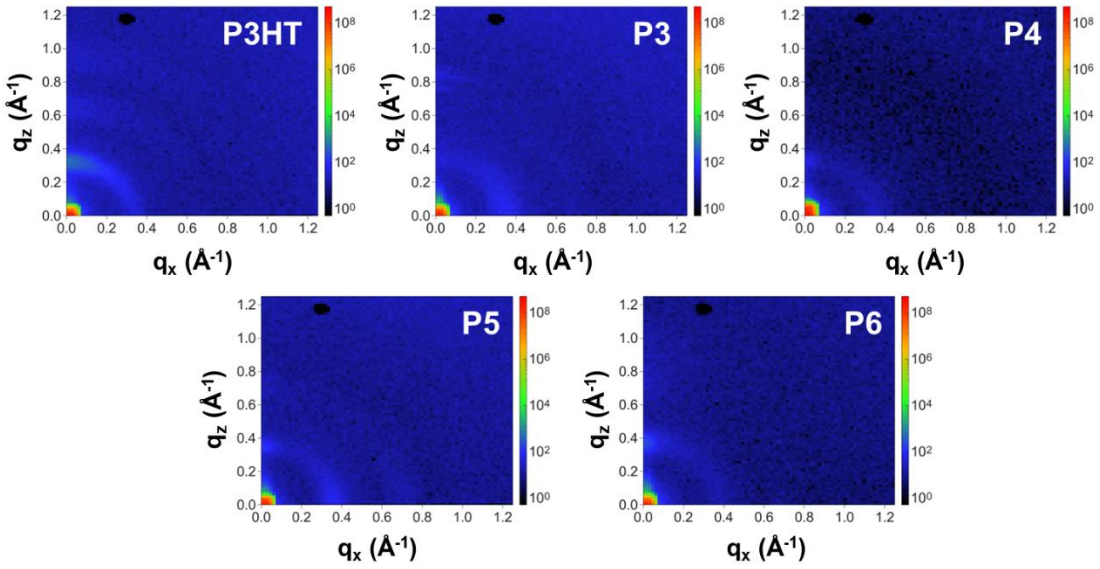

Figure 3.10. 2D GIWAXS images acquired from sequentially-doped thin films of each polymer.

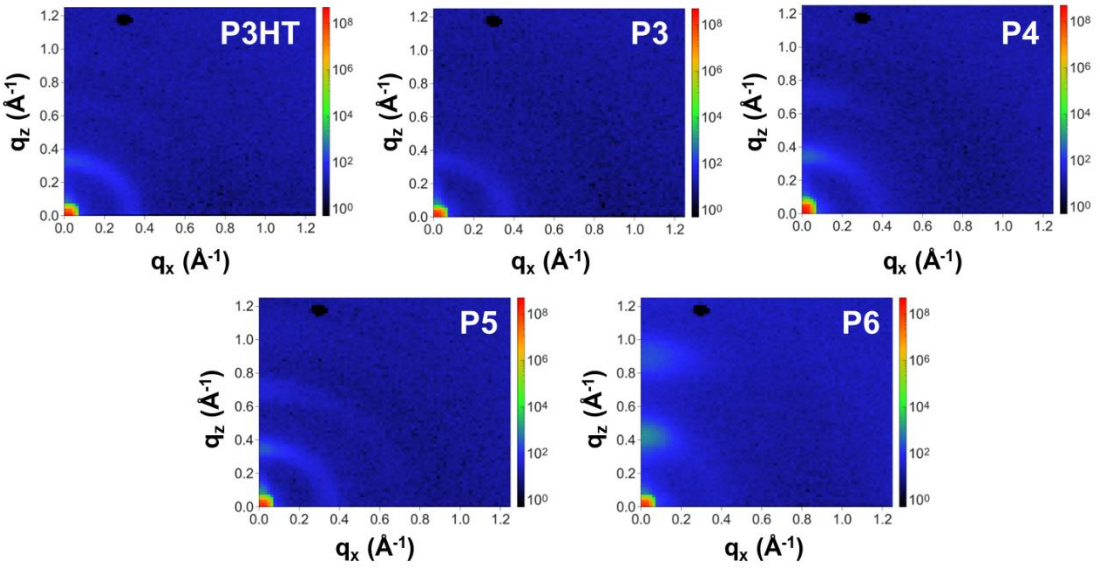

Figure 3.11. 2D GIWAXS images acquired from serial-doped thin films of each polymer.

demonstrating that crystallites adopt all possible orientations with respect to the plane of the film. A weak (100) diffraction peak emerges from the 1D profile of **P6** suggesting that the incorporation of the dopant promotes some ordering within the film. Also, each of the sequentially-doped thin films shows an increase in the out-of-plane *d*-spacing compared to solution-doped films (Table 3.2), suggesting that more dopant is integrated into the film. This contention is consistent with both the large increase in $F4TCNQ^{-}$:polymer absorbance ratio and the increase in conductivity observed for sequentially-doped thin films compared to films prepared by solution doping. Profiles and images from GIWAXS measurements of serial-doped films are shown in Figure 3.9b and Figure 3.11, respectively. The results suggest that **P3HT** exhibits a microstructure similar to its sequentially-doped films. **P3** now shows the presence of a weak (100) peak, which indicates a slight increase in order due to the second doping step; however, the diffuse (100) peak seen in the 2D image indicates there is no preferred orientation with respect to the substrate. On the other hand, **P4**, **P5**, and **P6** all show features that support a significant increase in order. Specifically, the out-of-plane 1D profiles obtained from each of these copolymer films (Figure 3.9b) display (100) diffraction peaks, similar to the sequentially-doped films; however, weaker (200) peaks are also observed. The appearance of a higher-order peak indicates a significant increase in structural ordering due to the second doping step. The 2D images (Figure 3.11) add additional support to the contention of a more ordered microstructure compared to their sequentially-doped counterparts, as multiple crystalline peaks are seen for **P4**, **P5**, and **P6**. This is most clearly seen with **P6**, which has very intense, narrow features in the out-of-plane direction, indicating a preferred crystalline orientation of edge-

on. This improved microstructural order is believed to be the predominant reason for the higher in-plane conductivity observed for serial-doped thin films compared to sequentially-doped films, as seen from Figure 3.3. Additionally, with serial doping the out-of-plane *d*-spacing decreases with spacing length according to **P3HT** > **P3** > **P4** = **P5** > **P6**. This indicates that the expanded core designs reduce steric demand and allow for more intimate interaction between F4TCNQ and repeat units along the backbone. This contention is supported by the work of Kim et al. in which random copolymers of 3-hexylthiophene and thiophene exhibited shorter packing distances than P3HT due to their reduced side chain density, which allows for co-crystallization of the polymer and dopant.[89]

3.5. Conclusions

A series of thiophene-based copolymers featuring expanded cores were used to assess the impact that spacing length between alkyl side chains has on thin film morphology and conductivity, with particular emphasis on the effect of the method of doping. Serial doping, a two-step process consisting of both solution doping and sequential doping steps, increased thin film conductivity in comparison to sequential doping even though the dopant concentrations used in the first step is low. This increase in conductivity with serial doping was not attributed to the amount of dopant or $F4TCNQ^-$ present in the film. Rather, this increase in conductivity is largely impacted by enhancements in crystalline content brought on by dopant integration. This is supported by the emergence of distinct (100) diffraction peaks in the serial-doped copolymer thin films, despite the pristine thin films being largely amorphous in character. Moreover, higher-order peaks were also present in the films subjected to serial doping that were made from copolymers

with larger spacing units (**P4**, **P5**, and **P6**). This finding suggests that the use of serial doping can overcome the predominantly amorphous character of a conjugated polymer thin film, leading to a more ordered microstructure, which in turn enhances conductivity. With serial-doped P3HT films, the enhancement of ordering and conductivity appears to be minimal, likely due to its intrinsic crystallinity.

In addition, this study again shows that as the spacing length between alkyl side chains in the expanded core copolymers is increased, the conductivity and the extent of microstructural ordering increases. Overall, this study provides key insights into how conductivity is affected by the complex interplay between dopant integration, efficient electron transfer, and thin film microstructure in thiophene-based polymer thin films. Ultimately, the serial doping process leads to more ordered microstructures despite the pristine polymer thin films exhibiting largely amorphous character, which indicates that polymers that are intrinsically semi-crystalline may not be needed to achieve higher conductivities.

Chapter 4. Impact of Analysis Method on Accuracy of Gel Permeation Chromatography Measurements of Thiophene-Based Conjugated Polymers

4.1. Abstract

Gel permeation chromatography (GPC) is a widely used method for characterizing the molecular weight of polymers. However, the rigidity and poor solubility of conjugated polymers, relative to calibration standards, can lead to inaccurate assessments of chain size. In this chapter, we compare the molecular weights of a series of thiophene-based copolymers determined using conventional calibration and universal calibration to assess which method yields the most accurate results in comparison to triple detection measurements. Triple detection, which does not rely on calibration standards, is considered an absolute method for determining weight-average molecular weight (M_w). Results show that the M_w obtained from conventional calibration largely deviates from the M_w determined via triple detection and the deviation in M_w correlates with the Mark-Houwink parameters of the polymers, which highlights the significance polymer shape in solution. We also demonstrate that the accuracy of universal calibration depends on whether 100% mass recovery is assumed or the known refractive index increment (d*n*/d*c*) is used. Assuming 100% mass recovery leads to deviations in M_w values due to possible polymer adsorption on the column, which reduces the actual mass recovery and results in an underestimation of d*n*/d*c*. In contrast, using the known d*n*/d*c* of the conjugated polymer provides M_w values that closely match those obtained via triple detection. Overall, this study demonstrates that universal calibration is the most accurate GPC calibration method for thiophene-based conjugated polymers provided that the d*n*/d*c* of the polymer is known.

4.2. Introduction

Accurate characterization of polymer molecules is of the utmost importance because molecular weight impacts thermal transitions temperatures, viscosity, and optoelectronic properties.[97-100] Therefore, reliable and accurate molecular weight measurements are necessary. Common methods to determine the molecular weight of polymers include gel permeation chromatography (GPC), which is usually a relative method, and static light scattering (SLS) or nuclear magnetic resonance (NMR) spectroscopy, both of which are absolute methods.[101-105]

With GPC measurements, there are three possible methods of molecular weight determination: 1) conventional calibration, 2) universal calibration, and 3) triple detection. Conventional calibration relies on measuring the refractive index difference (from the solvent) as a function of time.[53] Because the flow rate is precisely controlled and held constant, time is directly correlated to elution volume. The elution volume of the polymer sample is used to determine the molecular weight based on the molecular weight of a set of standards of known molecular weight.[53,101] This method relies entirely on elution volume, which is dependent on the movement of the polymer coils through the stationary phase and their size relative to the pore size of the stationary phase.[53,101] Therefore, it assumes that each polymer has similar coil size and/or swelling characteristics in the mobile phase as the polymer standards. This is not true in many cases, especially with conjugated polymers because they are significantly stiffer than typical well-defined flexible polymers, such as polystyrenes, which are commonly-used standards.[72,106-108] Therefore, universal calibration is often used to characterize polymers that are structurally

different from polymer standards.[109,110] Universal calibration relies on measurement of the viscosity of the polymer as well as its elution volume. The specific viscosity (η_{sp}) is measured using a viscometer and then the concentration (determined from the differential refractive index) is used to calculate intrinsic viscosity using the following equation: $[\eta] = \eta_{sp}/c$.[111,112] The product of [η] and molecular weight is proportional to hydrodynamic volume, which is correlated to the elution volume (retention time).[109,110,113] As a result, the molecular weight of the sample can be determined more accurately when the viscosity of the polymer and/or the polymer-solvent interactions are different from that of the polymer standards. However, universal calibration still has its limitations. Specifically, it typically assumes 100% mass recovery to estimate the refractive index increment (dn/dc) of the sample polymer to, in turn, determine the concentration that is used to calculate [η]. This assumption is often not valid because some polymers adsorb onto the GPC column, thereby lowering the mass recovery.[104] As a result, GPC with triple detection, which combines the use of refractive index, viscosity, and light scattering detectors to determine molecular weight, is used to combat the issues encountered with both conventional and universal calibrations. The caveat with triple detection is the dn/dc of the polymer must be precisely known, otherwise accurate measurements cannot be made.[111] However, triple detection offers the benefit of allowing the absolute molecular weight to be determined because this method does not rely on the use of polymer standards; rather a partial Zimm plot is utilized to determine M_w.[111]

Molecular weight characterization is often difficult with conjugated polymers due to their stiffness and low solubility in many solvents, including those used as the mobile

phase in GPC. Therefore, some work has been done to evaluate the accuracy of the GPC measurements of conjugated polymers. Fair et al. showed that GPC measurements of poly(3-hexylthiophene) (P3HT) and polydioctylflourene (PFO) made using universal calibration are reliable and accurate when compared with molecular weights measured by SLS, specifically when the d*n*/d*c* of the polymer is known.[104] Holdcroft found that using Mark-Houwink constants to calibrate GPC columns, specifically for P3HT, allowed for accurate determination of molecular weights in comparison to those obtained by embulliometry, which is an absolute method.[114] However, to the best of our knowledge, there are no studies that examine how structural changes in conjugated polymers impact molecular weight characterization, specifically with GPC analysis.

Herein, we examine the molecular weight characterization of a series of thiophene-based copolymers using conventional calibration, universal calibration, and triple detection. Molecular weights determined by triple detection are considered absolute because this method does not rely on calibrations produced with polymer standards. Various quantities that depend on polymer-solvent interactions, such as Mark-Houwink parameters and intrinsic viscosity, are investigated to determine what properties lead to inaccuracy in the GPC measurements. We find that universal calibration analysis is the most accurate measurement of M_w, as long as the d*n*/d*c* is known. This is true for all the thiophene based-copolymers studied.

4.3. Materials and Methods

4.3.1. Materials

2,5-bis(trimethylstannyl)thiophene (97%, Sigma), 2,5-bis(trimethylstannyl)-thieno[3,2-*b*]thiophene (97%, Sigma), 5,5'-dibromo-2,2'-bithiophene (98%, TCI), 5,5''-dibromo-2,2':5',2''-terthiophene (97%, Sigma), 2-bromo-3-hexylthiophene (97%, Sigma), 3-hexylthiophene-2-boronic acid pinacol ester (95%, Sigma), 3-hexylthiophene (99%, Sigma), tetrakis(triphenylphosphine)palladium(0) ($Pd(PPh_3)_4$, 99%, Sigma), palladium (II) acetate ($Pd(OAc)_2$, 98%, Sigma), potassium carbonate (99.7%, Fisher), neodecanoic acid (NDA, Sigma), magnesium sulfate ($MgSO_4$, 99.5%, Alfa Aesar), toluene (99.85%, extra dry, Thermo Scientific), diethyl ether (anhydrous, Fisher), ethyl acetate (99%, Fisher), hexanes (98.5%, Fisher), dimethyl formamide (DMF, 99.8%, Thermo Scientific), N,N-dimethylacetamide (DMAc, 99.5%, extra dry, Thermo Scientific), methanol (99%, Fisher), acetone (99%, Fisher), chloroform (98%, Fisher) and tetrahydrofuran (THF, HPLC Grade, Fisher) were used as received. N-bromosuccinimide (NBS, 99%, Sigma), was recrystallized in water and vacuum dried prior to use.

4.3.2. Synthesis of Expanded Core Copolymers

Comonomers (**M3**, **M4**, **M5**, and **M6**) were synthesized via Suzuki-Miyaura and Stille cross-couplings and the polymers (**P3HT**, **P3**, **P4**, **P5**, and **P6**) were synthesized via DArP as described in *Chapter 2*. A standard polystyrene sample (Sigma-Aldrich, M_w = 23 kg/mol and Đ = 1.06) was used for comparison.

4.3.3. Measurement of d*n*/d*c*

The refractive index increment (d*n*/d*c*) of each (co)polymer was measured using Wyatt Optilab T-rEX. Five samples of various concentration (0.5, 1.0, 1.5, 2.0, and 2.5 mg/mL) were made in HPLC grade THF and filtered with a 0.2 PTFE filter. Prior to the first sample injection, pure HPLC grade THF was injected into the refractometer at 0.2 mL/min. The detector was purged for 5 min and then allowed to stabilize for 5 min. After that step, data collection was started and a 5 min baseline was established with the pure solvent. Then, the first polymer sample was injected at 0.2 mL/min for 5 min while data (refractive index) continued to be collected. Pure solvent was then injected at 0.2 mL/min for 5 min to reestablish the baseline. This process was repeated until all solutions were measured, from lowest concentration to highest concentration.

4.3.4. GPC Measurements

GPC measurements were used to determine the number-average molecular weight (M_n), weight-average molecular weight (M_w), and dispersity (Đ) based on conventional analysis, universal analysis, and triple detection. An Agilent 1260 Infinity II system was used for these measurements, and the system used THF as the mobile phase at 25 °C at a flow rate of 1 mL/min. Solutions for GPC measurements were made at a concentration of 4 mg/mL in THF and filtered with a 0.2 PTFE filter. Mark-Houwink parameters were determined from the viscometry data obtained during the corresponding GPC measurement.

4.4. Results and Discussion

4.4.1. GPC Characterization of Expanded Core Copolymers

GPC measurements are commonly used to determine the molecular weight of polymers; however, inaccurate results can be obtained when using relative methods in which the molecular weight of a sample is estimated based on calibrations made with standards, typically polystyrene, of known molecular weight. This is especially true in the case of conjugated polymers because their flexibility and polymer-solvent interaction energies are vastly different from those of polymer standards. Therefore, in this work, analyses of polymer molecular weight based on conventional and universal calibrations are compared to that obtained by triple detection for a series of polythiophene samples. The thiophene-based copolymers were synthesized as described in *Chapter 2* and the structures are depicted in Figure 4.1. Polystyrene (PS) is used as a reference since it is the polymer that is used most commonly for calibration of GPC instruments that use an organic solvent (THF) as the mobile phase and run at room temperature, while poly(3-hexylthiophene) (**P3HT**) is used as a benchmark thiophene-based polymer. Each expanded core copolymer structure varies through the addition of a spacer unit between the alkyl chains. Specifically, the spacer units are thiophene (**P3**), thienothiophene (**P4**), bithiophene (**P5**), and terthiophene (**P6**). This alteration of the backbone has been shown to impact polymer-solvent interaction energy, which was specifically described using Hansen solubility parameters (*Chapter 2*), and thus we expect this sequence of thiophene-based copolymers to show differences in GPC analysis.

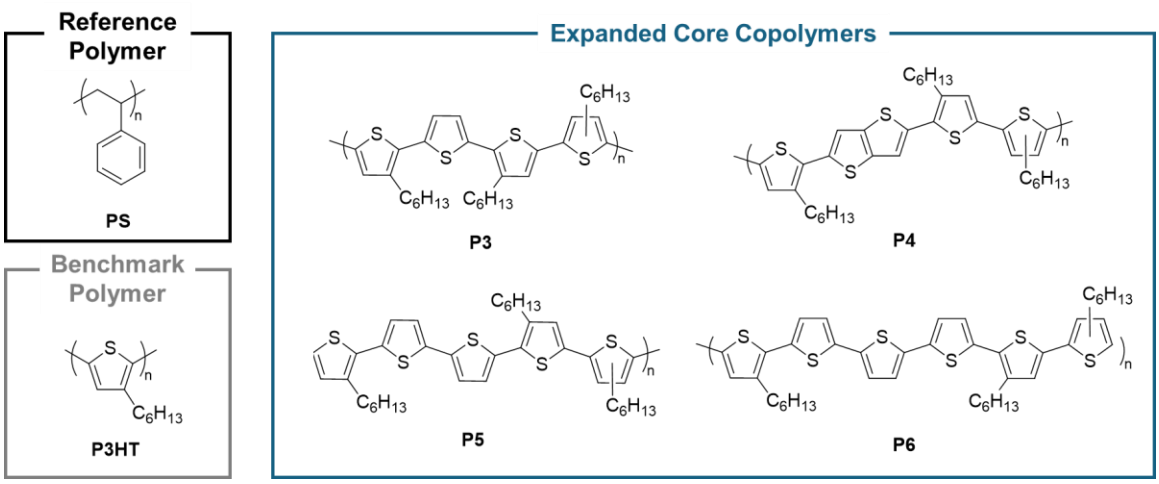

Figure 4.1. Structures of the reference polymer (polystyrene, PS), the benchmark thiophene-based conjugated polymer (poly-3-hexythiophene, **P3HT**), and the expanded core copolymers (**P3**, **P4**, **P5**, and **P6**).

For accurate molecular weight determination via triple detection, it is necessary to know the d*n*/d*c* of the polymer because this method relies on the generation of a partial Zimm plot. The change in refractive index (dRI) as a function of concentration was measured for each copolymer in THF at 25 °C and the results are shown in Figure 4.2. The d*n*/d*c* value of each polymer was determined from the slope of the line and is summarized in Table 4.1. It should be noted that measurements of polystyrene were also performed to ensure accuracy of the measurement, and the resulting d*n*/d*c* value agrees with the reported value of 0.185 mL/g.[47] **P3HT** has a large increase in d*n*/d*c* compared to polystyrene. This is expected since **P3HT** is a semi-flexible polymer and adopts a more rod-like conformation. This contention is in agreement with reported persistence lengths of P3HT (20-30 Å[72,108]) and polystyrene (~13 Å[106,107]). Additionally, increases in polarizability are known to increase the refractive index and d*n*/d*c* of a material, as captured by the Lorentz-Lorenz equation.[53,115,116] Therefore, the presence of polarizable thiophene units also contributes to the increase in d*n*/d*c*. Furthermore, with the expanded core copolymers, d*n*/d*c* increases compared to **P3HT**, with **P3HT** < **P3** < **P4** < **P5** < **P6**. This is attributed to the spacer unit decreasing the steric demand along the polymer backbone which in turn allows for increased interchain interactions, thereby resulting in increased d*n*/d*c* values.

With the measured d*n*/d*c* values, the molecular weight of each (co)polymer was determined using triple detection. Again, this method does not require comparison to polymer standards, since it uses a partial Zimm method, which is analogous to SLS measurements at a single concentration. Thus, the molecular weight determined

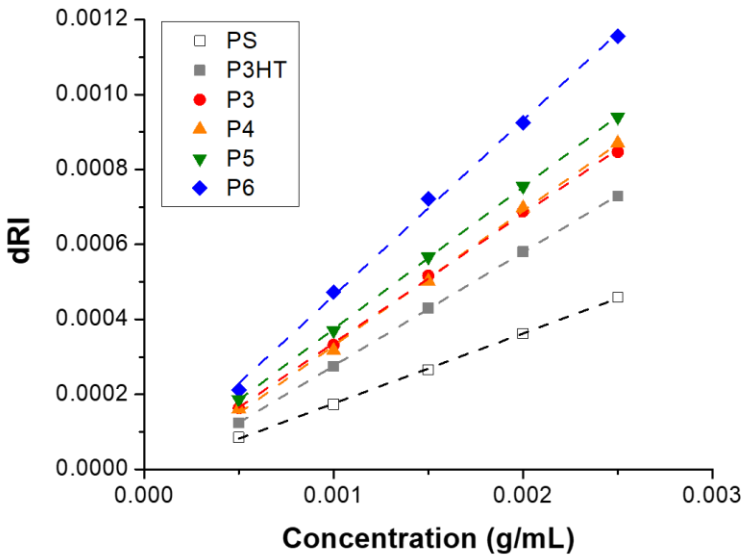

Figure 4.2. Change in refractive index (dRI) as a function of concentration for PS, **P3HT**, and each of the expanded core polymers (**P3**-**P6**). The slope of each line is the d*n*/d*c* of that polymer.

Table 4.1. Experimentally determined d*n*/d*c* values for PS, **P3HT**, and each of the expanded core copolymer (**P3**-**P6**).

Polymer	**d*n*/d*c* (mL/g)**
PS	0.1872 ± 0.0023
P3HT	0.3032 ± 0.0014
P3	0.3443 ± 0.0049
P4	0.3594 ± 0.0073
P5	0.3788 ± 0.0020
P6	0.4677 ± 0.0125

using triple detection will be considered the absolute molecular weight in this work. The weight-average molecular weight (M_w) and dispersity (Đ) for each of the thiophene-based polymers studied are shown in Table 4.2. The M_w of each polymer falls within the range of 19.8 kg/mol to 27.9 kg/mol. This fairly narrow range of molecular weights allows for conclusions to be made without the consideration of molecular weight dependence.

M_w values obtained from conventional calibration analysis are compared to those determined via triple detection in Figure 4.3. It should be noted that the x = y line is included in the figure to easily guide the reader to what is expected if the molecular weight matches that determined by triple detection, which is considered the "true" M_w in this work. For each of the thiophene-based polymers the M_w values obtained from conventional calibration analysis were higher than the M_w obtained from triple detection. Conventional calibration depends entirely on elution volume, so the hydrodynamic volume of the conjugated polymers must be larger than that of the polymer standard of the same molecular weight, which leads to a larger molecular weight being determined by conventional analysis. To explore how polymer shape can impact GPC results, the Mark-Houwink parameters, which are defined as *K* and *a* in the Mark-Houwink equation ($[\eta] = KM^a$), are quantified. The *K* value determines the proportionality between intrinsic viscosity and molecular weight, with larger values indicating that even at low molecular weight there can be a significant increase the solution viscosity.[117] The *a* value indicates the shape of the polymer in solution. If $a < 0.5$ the polymer is a compact coil/sphere, if *a* is 0.5-0.8 the polymer is a random coil, and if $a > 0.8$ the polymer is rod-like.[47,53,117]

Table 4.2. Weight-average molecular weight (M_w) and dispersity (Đ) of PS, **P3HT**, and each of the expanded core copolymers (**P3-P6**) determined via triple detection.

Polymer	M_w (kg/mol)	Đ
PS	22.8	1.1
P3HT	29.7	2.6
P3	27.9	2.1
P4	19.8	1.8
P5	29.7	2.1
P6	21.2	2.2

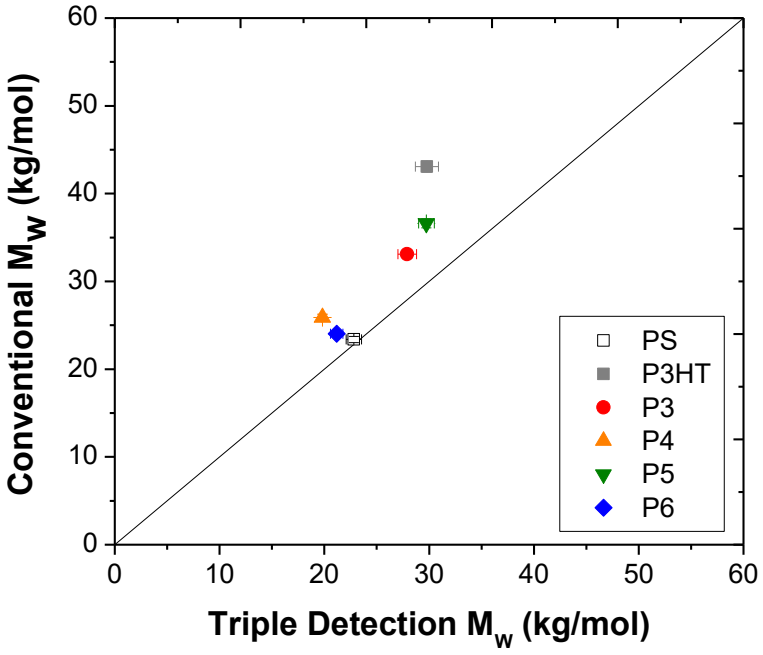

Figure 4.3. Comparison of M_w determined via conventional calibration analysis (y-axis) and triple detection (x-axis). The x=y line is a visual guide for what is expected if the M_w value of conventional analysis matches that of the M_w determined from triple detection.

Viscometry measurements were used to make Mark-Houwink plots (Figure C.7-C.12) and determine the resultant Mark-Houwink parameters, which are summarized in Table 4.3. As expected, the values of *K* and *a* determined for PS indicate that PS is a well-solvated, flexible polymer in THF. **P3HT** shows an increase in *K* and decrease in *a* compared to PS. The value of $a = 0.52$ for **P3HT** suggests that **P3HT** takes on the shape of a random coil, while the much higher *K* value (compared to PS) indicates that the solution viscosity increases dramatically with increases in molecular weight, thus suggesting a more rigid polymer backbone. The copolymers that have expanded cores (**P3-P6**) also have large *K* values (> 0.16 mL/g), which suggests the copolymers are more rigid than PS, as expected, but they all feature $a < 0.5$, which is indicative of a compact coil. Although, values of *K* and *a* appear contradictory for the expanded core copolymers, the unexpected *a* values are attributed to decreased solubility/solvation of the copolymers in THF. The reduced solubility in THF leads to compact coils instead of the expected rod-like conformations; however, the higher *K* values still indicate that the viscosity is heavily impacted by an increase in molecular weight, which is indicative of a more rigid backbone. Thus, it is believed that the Mark-Houwink parameters would be in greater agreement with each other if a good solvent, such as chloroform or chlorobenzene, was used.

To evaluate how the shape of the polymer relates to the GPC measurements, the percent deviation of the M_w obtained from conventional calibration compared to the absolute M_w determined via triple detection was plotted against the Mark-Houwink parameter, *a*. As seen in Figure 4.4, as the value of *a* increases the deviation in the

Table 4.3. Mark-Houwink parameters, *K* and *a*, for PS, **P3HT**, and each of the expanded core copolymer (**P3**-**P6**).

Polymer	*K* (mL/g)	*a*
PS	0.013	0.71
P3HT	0.193	0.52
P3	0.666	0.37
P4	0.310	0.44
P5	0.163	0.42
P6	0.989	0.35

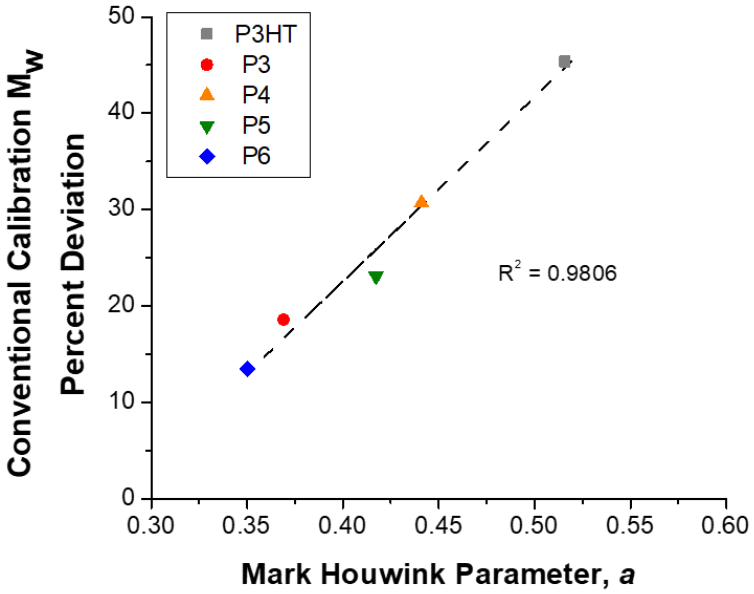

Figure 4.4. Relationship between the Mark-Houwink parameter, *a*, and the percent deviation in the M_w obtained from conventional calibration from the M_w obtained from triple detection.

M_w measurement also increases. This is attributed to the shape that the conjugated polymer takes on. First, **P3HT** has the highest *a* value of 0.52 which is indicative of a random coil. The semiflexible nature of **P3HT**, compared to the polymer standard PS, suggests that if the polymer takes on a random coil the hydrodynamic value will be larger than expected, thus leading to an increase in the measured M_w determined via conventional analysis. The expanded core copolymers have values of *a* that are less than 0.5, which signifies they behave as compact coils due to decreased solubility in THF. When the polymers take on the shape of a compact coil, the hydrodynamic volume is decreased compared to a random coil of the same molecular weight.[118] Thus, a compact coil will elute at longer times compared to a random coil of the same molecular weight. It is believed that if the measurements were repeated in a good solvent, such as chloroform or chlorobenzene, the deviation would be larger than seen here because the expanded core copolymers would adopt a random coil shape ($a > 0.5$). Overall, these measurements validate that the stark differences in backbone structure and polymer-solvent interactions make conventional calibration analysis a less accurate descriptor of molecular weight for conjugated polymers

Universal calibration was developed to account for the shape and intrinsic viscosity of polymers, enhancing the accuracy of GPC measurements for polymers that differ from the reference standard.[109,110,113] This method typically assumes 100% mass recovery, which allows d*n*/d*c* to be calculated (estimated). That value is then used to calculate the concentration of the sample throughout the measurement. This concentration is subsequently used to determine the specific viscosity and, ultimately, the molecular weight. In this study, the molecular weight of each polymer was determined using universal

calibration in two ways: (1) by assuming 100% mass recovery and (2) by using the experimentally measured d*n*/d*c* values (Table 4.1). Figure 4.5 shows the comparison of the universal calibration methods to triple detection. As seen in Figure 4.5a, by assuming 100% mass recovery, the molecular weights again deviate from the M_w obtained from triple detection, even in the case of PS. On the other hand, when the measured d*n*/d*c* is used, as seen in Figure 4.5b, the molecular weights match those measured via triple detection, although **P5** and **P6** have slightly high deviations from triple detection (13% and 11%, respectively), which is likely due to their decreased solubility in THF compared to **P3HT**.

The disparity in molecular weight measurements between the two universal calibration methods is attributed to the mass recovery of the polymer and subsequently the estimated d*n*/d*c* values. Figure 4.6a shows the percent deviation of the d*n*/d*c* estimated when assuming 100% mass recovery compared to the known mass recovery. As the mass recovery increases, the deviation d*n*/d*c* decreases, as expected. When assuming 100% mass recovery, the software estimates the d*n*/d*c* using the concentration of the sample that was injected; however, in each case (except for **P5**) the mass recovery is less than 100%, meaning that some of the polymer adsorbs on the column, is caught in the guard column, or sticks to the injection needle. As a result, the concentration of the eluted sample is lower than perceived based on the sample concentration and injection volume, which are inputs for the measurement. Thus, the estimated d*n*/d*c* values are only accurate when the mass recovery is close to 100%. In Figure 4.6b, the deviations the d*n*/d*c* values are then compared to the percent deviation of the universal M_w obtained using 100% mass recovery

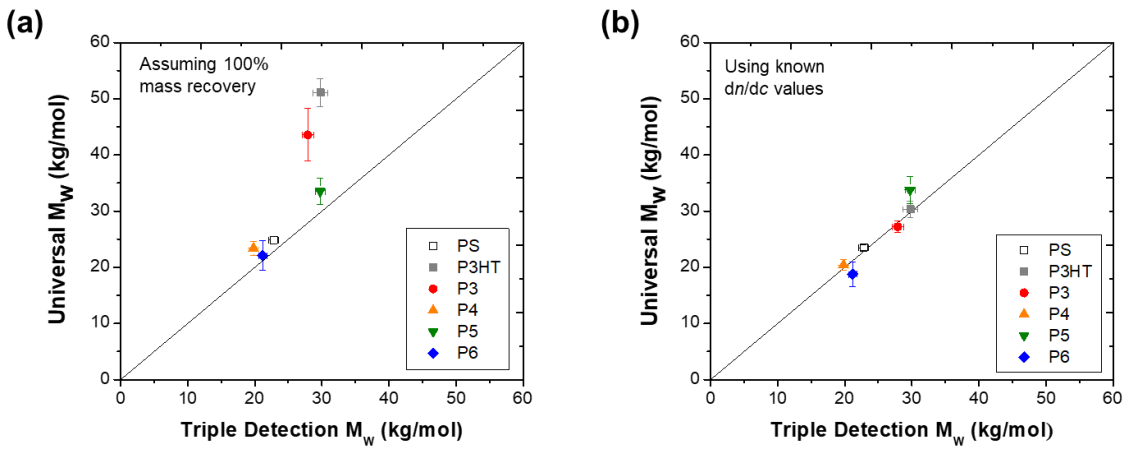

Figure 4.5. Comparison of M_w measured via triple detection to M_w measured via universal calibration (a) assuming 100% mass recovery and (b) using the measured d*n*/d*c* values. This shows that assuming 100% mass recovery leads to large deviations in M_w from triple detection in some cases; however, when using the measured d*n*/d*c* the M_w values obtained from universal calibration match closely with M_w determined from triple detection.

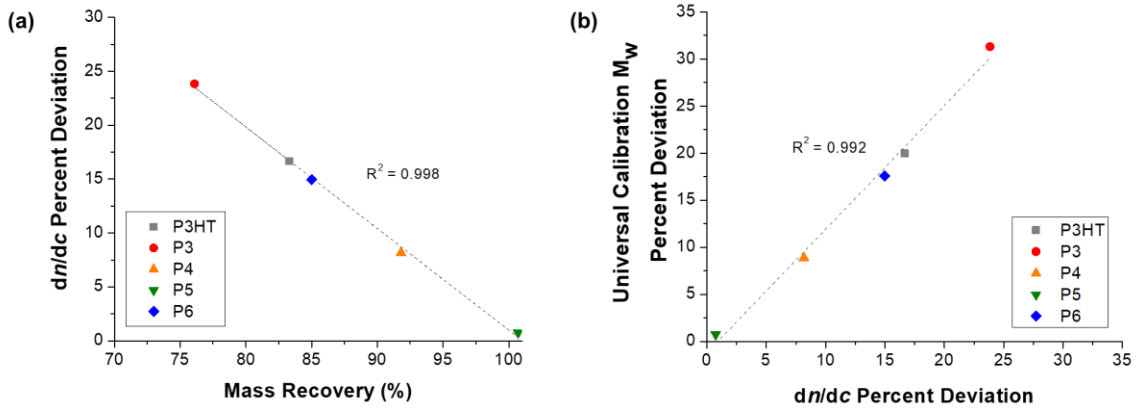

Figure 4.6. (a) Relationship of mass recovery and percent deviation in the estimated d*n*/d*c* when 100% mass recovery is assumed from the measured d*n*/d*c*. (b) Relationship of the percent deviation of d*n*/d*c* and the percent deviation of molecular weights obtained from universal calibration when 100% mass recovery is assumed and universal calibration when the measured d*n*/d*c* is used. This shows that lower mass recoveries result in higher deviations in the estimated d*n*/d*c* and measured M_w, therefore, the assumption of 100% mass recovery can lead to inaccuracies in molecular weight measurements.

(which uses the estimated d*n*/d*c*) relative to the universal M_w obtained by using the measured d*n*/d*c*. As the deviation in the estimated d*n*/d*c* increases, the deviation in the measured M_w also increases. This indicates that lower mass recovery, and thus underestimation of d*n*/d*c*, largely contributes to the deviation in the measured M_w. This is due to the use of the d*n*/d*c* to calculate concentration and ultimately [η], which is used in calibration. The mass recovery cannot be controlled, therefore universal calibration is more accurate when the known d*n*/d*c* of a sample is used, thereby eliminating any error that is based on assuming complete mass recovery.

4.4.2. Absolute M_n and M_w Characterization of P3HT

Thus far, the discussion of molecular weight characterization has been solely focused on M_w; however, with conjugated polymers it is critical to accurately know M_n as well. M_n describes the number of repeat units in a polymer chain, which is used to determine if a conjugated polymer is beyond its effective conjugation length. In the previous section, we determined that universal calibration, when the d*n*/d*c* is known, is the most accurate for the determination of M_w when compared to the absolute M_w determined via triple detection. However, when comparing the M_n and the dispersity of universal calibration and triple detection, the values vary dramatically, as shown in Table 4.4.

Therefore, a study was initiated to measure the absolute M_n and M_w of a conjugated polymer, using those to obtain the dispersity and, therefore, generating a more complete assessment of the accuracy of the various GPC measurements. ^{1}H NMR was selected as the method to measure the absolute M_n while SLS was chosen as the method to measure

Table 4.4. Number-average molecular weight and dispersity of **P3HT** and each core expanded copolymer (**P3**-**P6**) measured via universal calibration and triple detection.

	Universal Calibration		Triple Detection	
Polymer	**M_n (kg/mol)**	**Đ**	**M_n (kg/mol)**	**Đ**
P3HT	8.8	3.4	11.6	2.6
P3	9.5	2.9	13.2	2.1
P4	8.3	2.5	11.3	1.8
P5	9.2	3.7	14.1	2.1
P6	5.6	3.4	9.8	2.2

the absolute M_w. When using ^{1}H NMR to determine the molecular weight of a polymer, it is imperative to have end groups with characteristic peaks that are distinct from protons of the repeat unit(s). Unfortunately, due to the AA+BB nature of the polymerization of the expanded core copolymers, the end groups are not unique (or distinctive) because the terminal repeat unit(s) could be from either comonomer. In this situation, the end groups could be an arene or haloarene (possessing either an aryl proton (−H) or arylhalide (−Br), which would complicate the installation of an end group with unique resonance signatures). Therefore, for this study, P3HT polymerized via an AB polymerization was deemed to be the ideal candidate because it would have terminal haloarene containing a −Br. Although −Br does not have a signature in ^{1}H NMR, the first methylene protons of the adjacent hexyl chain of the terminal haloarene do; however, this peak overlaps with the signature of the first methylene protons of the hexyl side chain of the polymer chain. Thus, a post-polymerization Suzuki coupling of a P3HT, synthesized by DArP of 2-bromo-3-hexylthiophene, was used to modify the end group by installing a 4-methoxyphenyl group to form **P3HT-PhOMe**. This strategy resulted in a thiophene-based conjugated polymer with a distinct end group, as shown in Scheme 4.1. The distinct peaks from the methoxy protons of the 4-methoxyphenyl unit can be used as the reference peak for molecular weight determination by end group analysis. The resultant ^{1}H NMR of **P3HT-PhOMe** is shown in Figure 4.7, where the peak at 3.86 ppm corresponds to the methoxy protons of the end group. This peak is normalized to 3 protons and the β-proton of the P3HT repeat unit at 6.98 ppm is found to integrate to ~198 (X_n = 198). This indicates that **P3HT-PhOMe**

Scheme 4.1. Post-polymerization end group modification of **P3HT**.

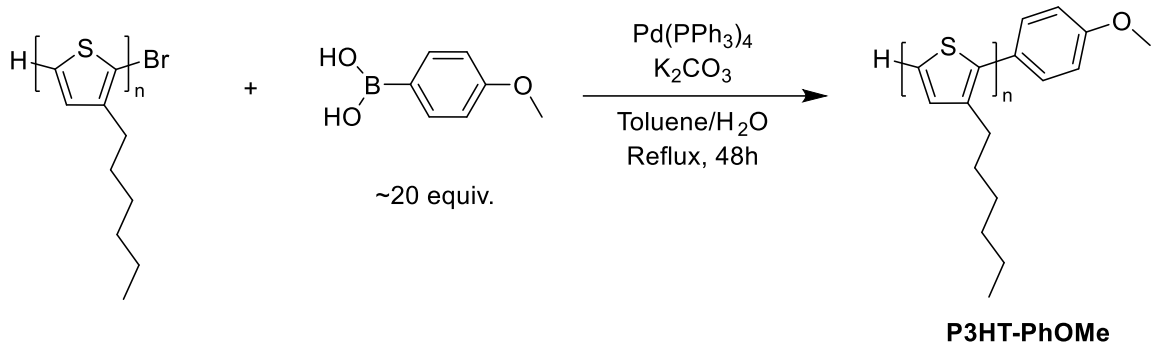

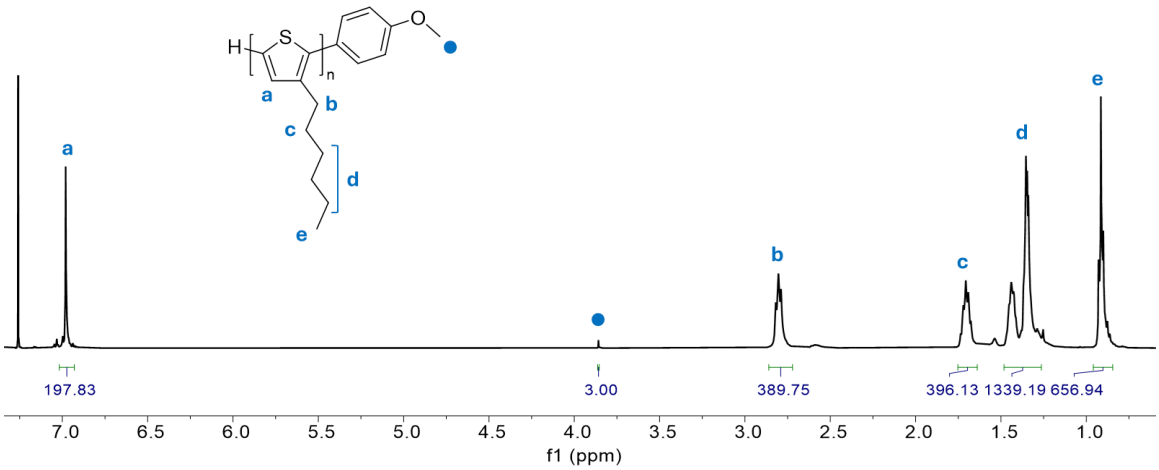

Figure 4.7. ^{1}H NMR of **P3HT-PhOMe**. The peak at 3.86 ppm associated with the methoxy end group is normalized to 3 protons, which results in a X_n of 198 based on the integration of the β-proton of the thiophene (a). This X_n is also consistent with the integrations of b and c aliphatic protons.

has an M_n = 33.0 kg/mol. In comparison to M_n values determined from GPC measurements, shown in Table 4.5, the most accurate measurement appears to be triple detection; however, the difference in M_n values is ~10 kg/mol. Therefore, for a more comprehensive understanding, SLS measurements were attempted. However, due to poor light scattering signals at low concentrations and absorbance of the laser light (633 nm) at high concentrations, a useful Zimm plot could not be obtained by SLS.

4.4.3. Proposed Alternative for Absolute M_n and M_w Characterization

To avoid the issue of absorption of the laser light in SLS measurements, a copolymer containing thiophene and fluorene has been proposed, as these copolymers are known to have absorbance profiles in solution that end at ~500 nm.[119] This absorbance at lower energy (compared to the thiophene-based copolymers and **P3HT**) would allow for molecular weight determination by SLS without absorption of the laser light. The proposed synthetic scheme is shown in Scheme 4.2, where Suzuki cross-coupling of 9,9-dioctyl-2,7-dibromofluorene with 3-hexylthiophene-2-pinacol ester boronic acid is used to create form an AB monomer, identified here as a **Fl-Th** monomer. This AB monomer can be polymerized via DArP to obtain the **P(Fl-Th)**, which will have a −Br end group that can be accessed by Suzuki-Miyaura coupling to install a 4-methoxyphenyl end group. This approach will also allow the absolute M_n to also be obtained for this polymer via ^{1}H NMR. By determining the absolute M_n and absolute M_w of **P(Fl-Th)-PhOMe**, the dispersity can be calculated. These descriptions of polymer size will provide a more comprehensive insight into the accuracy of GPC measurements of conjugated polymers.

Table 4.5. M_n and Đ of **P3HT-PhOMe** determined via GPC and NMR measurements.

Technique	Method	M_n (kg/mol)	Đ
GPC	Conventional	19.9	2.9
GPC	Universal[a]	7.3	5.7
GPC	Triple Detection	24.6	1.9
NMR	End Group Analysis	33.0	–

[a]*Universal calibration was performed using the measured dn/dc value of P3HT.*

Scheme 4.2. Proposed synthetic route for a fluorene-thiophene containing copolymer for molecular weight analysis.

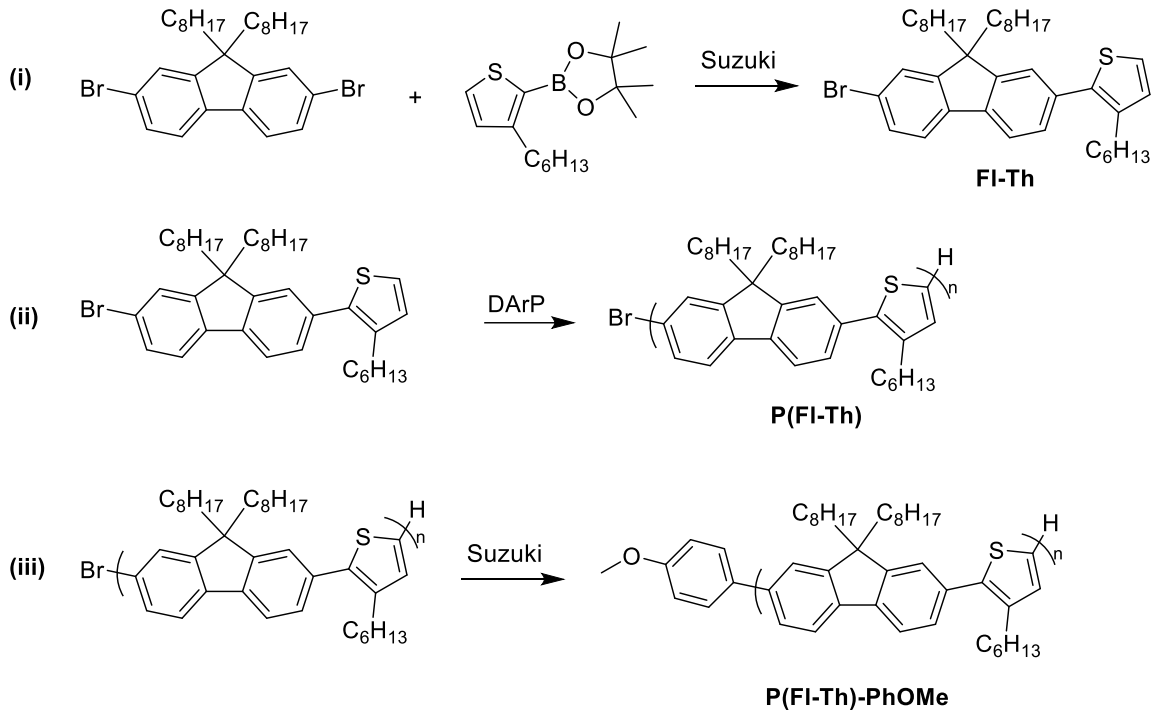

4.5. Conclusions

The accuracy of conventional and universal GPC measurements, with respect to triple detection, were assessed using a **P3HT** and a series of thiophene-based copolymers featuring expanded cores. The M_w values obtained from conventional calibration of **P3HT** and each of the expanded core copolymer (**P3**-**P6**) showed a large deviation from those measured via triple detection. This deviation in M_w was attributed to Mark-Houwink parameters, which describe the shape of the polymer in solution, where larger *a* values lead to larger deviations in M_w. Furthermore, the accuracy of the M_w determined with universal calibration analysis varies dramatically depending on whether 100% mass recovery is assumed (and used to calculate d*n*/d*c*) or if the d*n*/d*c* value is measured and used. When 100% mass recovery is used, the error in the measurements is higher due to underestimation of the d*n*/d*c* value. The error in d*n*/d*c* estimation is likely due to polymer adsorbing to the column, which lowers the actual mass recovery and alters the concentration of the eluted sample. Thus, when the known d*n*/d*c* value is used with universal calibration analysis, M_w values that closely match those obtained from triple detection are observed.

Additional work focused on analysis of M_n is now needed to give a clearer and more comprehensive picture of the accuracy of GPC measurements for conjugated polymers. The absolute M_n of an end group-modified P3HT (**P3HT-PhOMe**) was obtained using ^{1}H NMR. It appears that triple detection gives the closest approximation of this value; however, the difference in the M_n values was ~10 kg/mol. Therefore, SLS were attempted to determine how accurate the M_w values were. Unfortunately, with **P3HT-PhOMe**, at low concentrations the scattering signal was too low and at higher concentrations the polymer

absorbed the laser light, which prevented definitive results from being obtained. Thus, future work using a fluorene-thiophene copolymer is proposed to acquire accurate absolute M_n and M_w for a complete comparison to GPC measurements.

Chapter 5. Solvent-Dependent Conductivity of Sequentially-Doped Conjugated Polymers: Universal Relationship Between Solvent-Polymer Interaction Energy and Conductivity

This chapter describes research being prepared for submission to *ACS MacroLetters*. I synthesized and characterized P3HT and performed the experiments and analyses associated with determining solubility parameters, UV-Vis absorbance measurements, conductivity measurements, and grazing-incidence wide angle X-ray scattering (GIWAXS) measurements for all of the polymers used in these studies. Coauthors include Vanessa Phan and Prof. Graham S. Collier of the University of Southern Mississippi, who provided the P(EDOT-*co*-ProDOT) and P(DHPP-*co*-DPP) copolymers used and performed ^{1}H NMR and GPC characterization of these polymers, and Prof. S. Michael Kilbey II, who advised this work.

5.1. Abstract

Sequential doping enhances the conductivity of conjugated polymer thin films but requires the use of a marginal solvent that allows dopant diffusion without dissolving the film. Identifying such solvents for new, complex conjugated polymers is challenging due to limited solubility data. In this study, a series of conjugated polymers are sequentially doped with 2,3,5,6-tetrafluoro-7,7,8,8-tetracyanoquinodimethane (F4TCNQ) using various solvents and solvent blends to investigate how polymer-solvent interaction energies influence thin film conductivity and morphology. Results show that thin film conductivity correlates with the polymer-solvent solubility distance (R_a), with peak conductivities observed for each copolymer at moderate R_a values. Notably, the optimal R_a shifts depending on the polarity of the polymer. This finding correlates with the formation of $F4TCNQ^{-}$ and the crystallinity of the doped films. Overall, this work provides support for and reinforces the concept of universal solvent-dependent behavior in sequentially-

doped thin films, which offers a predictive framework for selecting marginal solvents or solvent blends for any conjugated polymer.

5.2. Introduction

Conjugated polymers are considered highly promising materials for applications in organic electronic devices, owing to their optoelectronic and physical properties.[3,60,120-122] However, to achieve metal-like electrical performance, chemical dopants are used to facilitate the formation of charge carriers that contribute to conduction. One of the most extensively studied p-type systems is that of poly(3-hexylthiophene) (P3HT) and 2,3,5,6-tetrafluoro-7,7,8,8-tetracyanoquinodimethane (F4TCNQ) due to their energy level alignment, which allows for efficient electron transfer from the polymer to the dopant[13,15,16,19]

Significant work has focused on optimizing the method in which the dopant is integrated into thin films to further enhance conductivity.[13,25,26,30,32-34,80] Traditional solution doping is a simple method in which separately prepared polymer and dopant solutions are mixed, and then the combined solution is used to cast a film; however, this process typically requires high levels of dopant and results in aggregation due to the formation of polar charged complexes in organic solvents used to dissolve the polymer and dopant.[13,16] Thus, sequential doping is used to prevent aggregate formation by using marginal solvents to dope pristine polymer films, thereby preserving the crystalline microstructure of the parent film. [13,26,30,86] Most sequential doping studies have focused on P3HT or involved only a single solvent or solvent blend, prompting increased interest in systematically studying solvent effects on conductivity. For instance, Yoon et al.

demonstrated that dopant solvents with moderate solubility for the polymer and good wettability with the thin film led to enhanced charge carrier generation and, consequently, higher conductivities.[30] Jang et al. also showed that solvents that are located at the periphery of the polymer solubility sphere and have high affinity for the dopant lead to enhanced doping efficiency.[123] In our previous work, we found that P3HT and a series of thiophene-based copolymers with expanded cores exhibited universal behavior in terms of how the conductivity of sequentially-doped thin films depended on polymer-solvent interaction energy. Specifically, our work showed that solvents with moderate solubility parameter distance (R_a values) yielded the highest conductivities.[86]

Here, we extend this concept of universality by comparing the conductivity of sequential-doped conjugated polymers having varied monomeric constituents and polarity. Specifically, we examine behaviors of **P3HT**, a thiophene-based conjugated polymer, poly(3,4-ethylenedioxythiophene-*co*-3,4-propylenedioxythiophene) (**P(EDOT-*co*-ProDOT**)), which is composed of electron-rich dioxythiophenes, and poly(1,4-dihydropyrrolo[3,2-b]pyrrole-*co*-3,6-bis(2-thienyl)-2,5-dihydropyrrolo[3,4-c]pyrrole-1,4-dione) (**P(DHPP-*co*-DPP**)), which is an alternating copolymer consisting of donor and acceptor motifs. Both copolymers exhibit similar solvent-dependent behavior, where solvents with moderate solubility parameter distances (R_a values) yield the highest conductivity, with small changes in the optimal R_a range based on the solubililty and polarity of the polymer.

5.3. Materials and Methods

5.3.1. Materials

2-bromo-3-hexylthiophene (97%, Sigma), palladium (II) acetate ($Pd(OAc)_2$, 98%, Sigma), potassium carbonate (99.7%, Fisher), cesium carbonate (Cs_2CO_3, 99%, Sigma), neodecanoic acid (NDA, Sigma), tricyclohexylphosphine tetrafluoroborate (97%, Sigma), 2,3,5,6-tetrafluoro-7,7,8,8-tetracyanoquinodimethane (F4TCNQ, 99%, Ossila), N,N-dimethylacetamide (DMAc, 99.5%, extra dry, Thermo Scientific), methanol (99%, Fisher), acetone (99%, Fisher), chloroform (98%, Fisher), dichloromethane (DCM, 99%, Fisher), dimethylformamide (DMF, 99%, Fisher), dimethyl sulfoxide (DMSO, 99%, Fisher), tetrahydrofuran (THF, 99%, Fisher) chlorobenzene (99.8%, anhydrous, Sigma), cylcopentyl methylether (CPME, ≥99.9%, Sigma), and graphite conductive adhesive (aqueous based, Electron Microscopy Supplies) were used as received.

5.3.2. Synthesis of P3HT and the Copolymers

*Synthesis of poly(3-hexylthiophene) (**P3HT**).* 2-bromo-3-hexylthiophene (1 equiv.) was added to a dry 100 mL round bottom flask while under positive argon pressure. Neodecanoic acid (NDA, 0.3 equiv.), K_2CO_3 (2.4 equiv.), and palladium(II) acetate (($Pd(OAc)_2$, 0.02 equiv.) were added to the reaction flask while maintaining positive argon pressure. The flask was sealed with a rubber septum. Then, dry and degassed dimethylacetamide (DMAc, 0.1 M) was transferred to the flask via syringe. The reaction mixture was stirred at 90 °C for 24 h. After this time, the reaction mixture was precipitated into cold methanol and recovered in a cellulose Soxhlet thimble. A series of Soxhlet extractions using methanol, acetone, and hexanes (each for 24 h) were used to wash and

purify the polymer. After these Soxhlet extractions, a final extraction with chloroform was done to collect the polymer in solution. The resultant polymer solution was concentrated via rotary evaporation to obtain the final product.

*Synthesis of poly(3,4-ethylenedioxythiophene-co-3,4-propylenedioxythiophene) (**P(EDOT-co-ProDOT)**).* $Pd(OAc)_2$ (2 mol %, 8.5 mg), PivOH (0.3 mol equiv, 61.3 mg), K_2CO_3 (2.5 mol equiv, 691 mg), and 2,5-dibromo-3,4-ethylenedioxythiophene (2.0 mmol, 599.9 mg) were added to a Schlenk flask equipped with a Teflon stir bar and sealed with a rubber septum. The atmosphere was subsequently rendered inert via three vacuum/refill cycles with Ar. ProDOT (2.0 mmol, 881.4 mg) was weighed in a vial and transferred to the reaction flask via a syringe using degassed DMAc. The reaction flask was lowered into an oil bath set to 140 °C and was stirred for 24 h. After the allotted reaction time, the reaction flask was removed from the oil bath and cooled to room temperature. The reaction mixture was then precipitated into a copious amount of methanol (MeOH) and stirred for 1 h. After 1 h, the precipitate was collected in a Soxhlet thimble and the polymer was purified with subsequent washes with MeOH and acetone followed by extraction with chloroform. The solution was concentrated via rotary evaporation and then reprecipitated in MeOH. The precipitate was then collected via vacuum filtration, washed with MeOH (300 mL), and dried under vacuum to attain a dark-purple solid.

*Synthesis of poly(1,4-dihydropyrrolo[3,2-b]pyrrole-co-3,6-bis(2-thienyl)-2,5-di-hydro-pyrrolo-[3,4-c]pyrrole-1,4-dione) (**P(DHPP-co-DPP)**).* All solid materials including the Br_2DHPP monomer (0.193 mmol, 200 mg), H_2DPP monomer (0.193 mmol, 166.4 mg), $Pd(OAc)_2$ (2 mol%, 0.9 mg), tricylcohexylphosphine tetrafluoroborate

($PCy_3 \cdot HBF_4$) (2 mol%, 1.4 mg), PivOH (30 mol%, 5.9 mg), and Cs_2CO_3 (2 eq., 125.9 mg) were added to a 10 mL pressure vessel followed by flowing Ar into the vessel for ~10 min to displace the air atmosphere. While under Ar, 5 mL of cyclopentyl methylether (CPME) was added to the vessel via syringe for a reaction concentration of 0.1 M with respect to the DHPP and DPP comonomers. Immediately after solvent addition, the pressure vessel cap was securely fastened by hand while flowing Ar around joint. The reaction was lowered into an oil bath set to 130 °C and the reaction was allowed to proceed overnight (~ 20 h). After the allotted time, the reaction flask was removed from the oil bath and cooled to room temperature. The reaction mixture was precipitated into an excessive amount of MeOH (~175 – 200 mL) and stirred for 1 h. The precipitate was then collected in a Soxhlet thimble, and the polymer was purified via subsequent washes with MeOH and acetone before extraction with toluene. The extracted solution was concentrated via rotary evaporation and then reprecipitated into MeOH. The precipitate was then filtered via vacuum filtration, washed with MeOH, and dried under vacuum overnight to yield a dark purple solid.

5.3.3. Polymer Characterization

The ^{1}H NMR spectrum of each copolymer is presented in Figure D.1-D.3. The number-average molecular weight (M_n) and dispersity (Đ) of **P3HT** were assessed using an Agilent 1260 Infinity II system with a mobile phase of THF at 25 °C and a flow rate of 1 mL/min. The sample was made at 4 mg/mL in THF and filtered through a 0.2 μm PTFE filter prior to injection. The molecular weights of **P(EDOT-*co*-ProDOT)** and **P(DHPP-*co*-DPP)** were determined using a Tosoh EcoSEC Elite GPC system operating with chloroform as the mobile phase at 35 °C with a flow rate of 0.35 mL/min or a Tosoh High

Temperature GPC system using trichlorobenzene at 135 °C with a flow rate of 1 mL/min, respectively. Both samples were filtered through a 0.45 μm PTFE filter prior to injection. Analysis was done using conventional calibration analysis. The results of GPC measurements are summarized in Table D.1.

5.3.4. Hansen Solubility Parameter Determination

For each polymer, 1 mg of the polymer was added to 1 mL of a solvent (or solvent blend). The homogeneity of the solution was evaluated based on visual observations and each solution was given a score of 1 (soluble) or 0 (not soluble). For those solutions deemed to be partially soluble at room temperature, the sample was heated gently. If the (co)polymer subsequently dissolved and the solution remained homogenous for more than 1 h, it was deemed soluble and given a score of 1. These solubility scores were entered in the Excel spreadsheet accessible from Díaz del los Ríos and Ramos' work.[49] Using the embedded formulae and data solver in Excel, the HSPs of each copolymer were calculated based on these observations.

5.3.5. Thin Film Preparation

The polymers were dissolved in chlorobenzene (10 mg/mL) at 70 °C while F4TCNQ was dissolved in the indicated dopant solvent (1 mg/mL) at room temperature. Thin films were created on glass substrates (cleaned with acetone and methanol) by spin casting 200 μL of the polymer solution dynamically at 1000 rpm for 40s. For doped thin films, immediately after film deposition, the dopant was spin cast onto the polymer thin film statically at 1000 rpm for 40s. The resulting doped polymer films were allowed to dry

for at least 10 minutes prior to addition of contact points (see *5.3.7. Conductivity Measurements*).

5.3.6. AFM Film Thickness Measurements

To measure the thickness of each film, a scratch test was performed. Specifically, a razor blade was used to scratch the film, thereby displacing the polymer film and exposing the glass substrate. An Asylum Atomic Force Microscope was used in tapping mode fitted with an AC200TS tip (spring constant of 9 N/m and resonance frequency of 150 kHz) to acquire images of 20 μm × 20 μm at the scratch interface. The film thickness was taken as the height difference between the polymer film and glass substrate and the measured values are summarized in Table D.2.

5.3.7. Conductivity Measurements

Conductive graphite adhesive was added at each corner of the doped thin films as contact points. Voltage was applied from 0 to 1 V at the contact points across one edge and the current was measured along the contact points on the opposite edge using a Keithley 2450 Sourcemeter. This was repeated along each edge of the film in accordance with the Van der Pauw method, resulting in four replicate measurements per sample.[57,58] The sheet resistance, R_s, was calculated using the slope of the I-V curve. R_s, along with the film thicknesses, t, obtained from AFM measurements, were used to calculate the film resistivity, ρ. Subsequently, conductivity, σ, was calculated using: $\sigma = \rho^{-1}$.

5.3.8. Thin Film UV-Vis Measurements

UV-Vis spectra were acquired for as-cast and doped thin films using a Thermo Scientific Evolution 300 UV-Vis Spectrophotometer in the wavelength range of 350 to

1100 nm. A clean glass slide was used as the background spectrum to baseline correct the spectra acquired for thin films. Each spectrum was then normalized by film thickness, allowing for absorbance values to be proportional to concentration. The absorbance values at the wavelengths corresponding to the F4TCNQ anion, $F4TCNQ^-$, (868 nm) and the neutral polymer (λ_{max} of each respective polymer determined from the as-cast spectra) were used to calculate the $F4TCNQ^-$:Polymer ratio.

5.3.9. GIWAXS Measurements

Thin films were prepared on ozone treated silicon wafer substrates (critical angle = 0.22°) using the same procedure described above. Measurements were performed using a Xenocs Xeuss 3.0 instrument and a Xenocs GeniX3D Cu source with a wavelength of 1.54 Å at an incident angle of 0.2°. The detector distance was set at 55 mm and each measurement was performed for 5 min. The resultant 2D images were used to produce 1D spectra based on a line cut in the out-of-plane direction.

5.4. Results and Discussion

The work in *Chapter 2* describes a universal solvent-dependent conductivity for a series of thiophene-based copolymers. The research described in this chapter intends to test and extend this concept of universality by examining more complex copolymers. Specifically, a **P(EDOT-*co*-ProDOT)** and a **P(DHPP-*co*-DPP)** that have been previously reported are utilized.[124,125] P3HT is used for comparison since it is a benchmark polymer for thiophene-containing polymers and showed clear solvent-dependent behavior in our prior work.[86] The structures of these polymers are depicted in Figure 5.1.

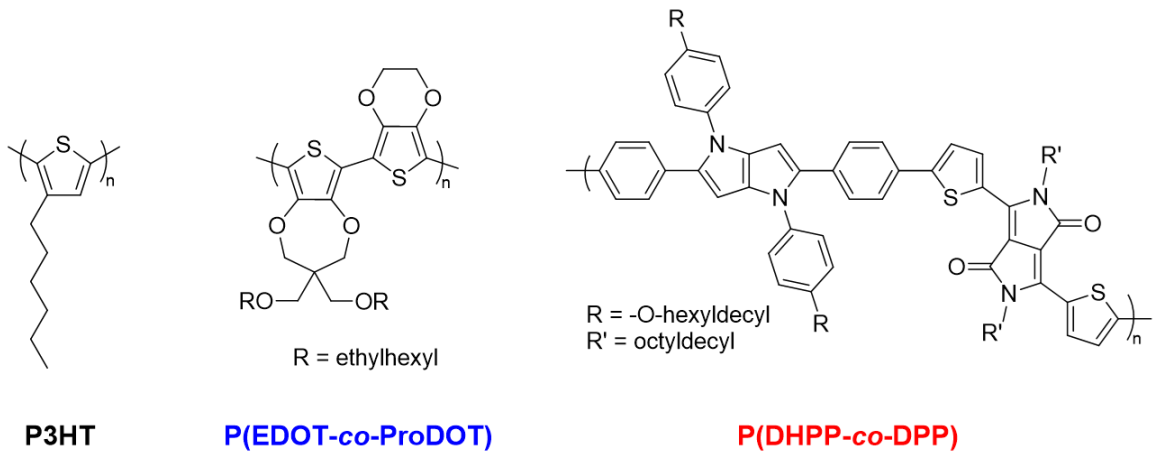

P3HT **P(EDOT-*co*-ProDOT)** **P(DHPP-*co*-DPP)**

Figure 5.1. Structures of **P3HT**, **P(EDOT-*co*-ProDOT),** and **P(DHPP-*co*-DPP)**.

To evaluate the solubility of each of these polymers, the Hansen solubility parameters (HSPs) were measured by observing the solubility of the respective polymer in various solvents and solvent blends as described by Díaz de los Ríos and Ramos.[49] The dispersive, polar, and hydrogen-bonding components, δ_D, δ_P, δ_H, respectively, of the HSPs are summarized in Table 5.1. First, each copolymer has a relatively high δ_D value, which is attributed to the π-stacking interactions between their conjugated backbones. The δ_P and δ_H values of **P(EDOT-*co*-ProDOT)** are much higher than **P3HT** and **P(DHPP-*co*-DPP)**, as expected, due to the presence of cyclic ether moieties along the thiophene backbone. These ether linkages allow for S-O interactions which increase the planarity of the backbone. On the other hand, **P(DHPP-*co*-DPP)** has the lowest values of δ_P and δ_H, which is attributed to the presence of the highly non-polar DHPP comonomer. It must also be appreciated that both **P(EDOT-*co*-ProDOT)** and **P(DHPP-*co*-DPP)** are soluble in fewer solvents than **P3HT**, and due to their limited solubility, to obtain reasonable fits of the HSPs, the solubility sphere radius (R_o) was lowered, as shown in Table 5.1. The smaller R_o values are likely due to the more complex structures of the copolymers as well as the relatively high molecular weight (Table D.1) of each of these copolymers.

A series of solvents and solvent blends—DCM, THF, acetone, DMF, DMSO, and 50:50 acetone:THF—were used to evaluate the solvent-quality dependent behavior in the sequential doping process, which was shown to lead to an optimum conductivity for thiophene-based copolymers.[86] The solubility parameter distance (R_a) for each solvent-copolymer pair was calculated using Equation 5.1, where the lowercase subscripts *p* and *s*

Table 5.1. Hansen solubility parameters (HSPs), radius of solubility sphere (R_o), and quality of data fit for **P3HT**, **P(EDOT-co-ProDOT)**, and **P(DHPP-co-DPP)**.

Polymer	δ_D (MPa$^{1/2}$)	δ_P (MPa$^{1/2}$)	δ_H (MPa$^{1/2}$)	R_o	Fit
P3HT	18.3	2.8	3.8	6.45	1.0
P(EDOT-*co*-ProDOT)	19.5	5.1	7.3	5.50	0.90
P(DHPP-*co*-DPP)	19.0	2.5	3.5	3.00	0.99

on the three HSP components correspond to the polymer and solvent, respectively.[49] The resultant R_a values of each polymer-solvent pair are summarized in Table 5.2, where lower values indicate greater solubility of the polymer and higher values indicate poorer solubility.

$$R_a = (4(\delta_{D_p} - \delta_{D_s})^2 + (\delta_{P_p} - \delta_{P_s})^2 + (\delta_{H_p} - \delta_{H_s})^2)^{1/2} \quad \text{(Eq. 5.1)}$$

Additionally, the distance between the solvent HSPs and the vector between the polymer and dopant HSPs (d) was calculated using Equation 5.2, where $\overrightarrow{PS}$ is the vector between the polymer and solvent HSPs and $\overrightarrow{PD}$ is the vector between the polymer and dopant HSPs. The d-values of each polymer solvent-pair are summarized in Table 5.3. Lower d values indicate that the solvent, as located in the Hansen space, is positioned closer to the vector path from the polymer to dopant, which indicates a higher affinity for both the polymer and dopant. The solubility sphere of each polymer and the dopant along with the solvents used for doping are depicted in Figure D.4-D.6.

$$d = \frac{\left\|\overrightarrow{PS} \times \overrightarrow{PD}\right\|}{\left\|\overrightarrow{PD}\right\|} \quad \text{(Eq. 5.2)}$$

For each sequentially doped thin film, pristine polymer films were first made by spin casting 10 mg/mL polymer solutions in chlorobenzene. The dopant solution was then spin cast directly onto the polymer film, and for the various solvents used, the F4TCNQ concentration in the dopant solution was fixed at 1 mg/mL in each solvent. The conductivity of the doped films was measured using the Van der Pauw method and the resultant conductivities are shown in Figure 5.2. First, as previously reported[86] and seen

Table 5.2. Summary of R_a values for each polymer-solvent pair based on their respective HSPs.

	R_a (MPa$^{1/2}$)					
Polymer	**THF**	**DCM**	**50:50 Acetone:THF**	**Acetone**	**DMF**	**DMSO**
P3HT	5.90	6.20	7.82	10.00	13.40	–
P(EDOT-*co*-ProDOT)	5.52	5.50	7.47	9.63	10.37	11.86
P(DHPP-*co*-DPP)	7.13	7.27	9.07	11.19	14.05	–

Table 5.3. Summary of *d*-values for each polymer-solvent pair based on the respective HSPs of the polymer, solvent, and dopant.

	d-value (MPa$^{1/2}$)					
Polymer	**THF**	**DCM**	**50:50 Acetone:THF**	**Acetone**	**DMF**	**DMSO**
P3HT	1.82	1.35	0.46	1.88	6.65	–
P(EDOT-*co*-ProDOT)	2.61	1.91	2.20	2.85	5.05	8.16
P(DHPP-*co*-DPP)	1.77	0.80	0.04	1.79	6.38	–

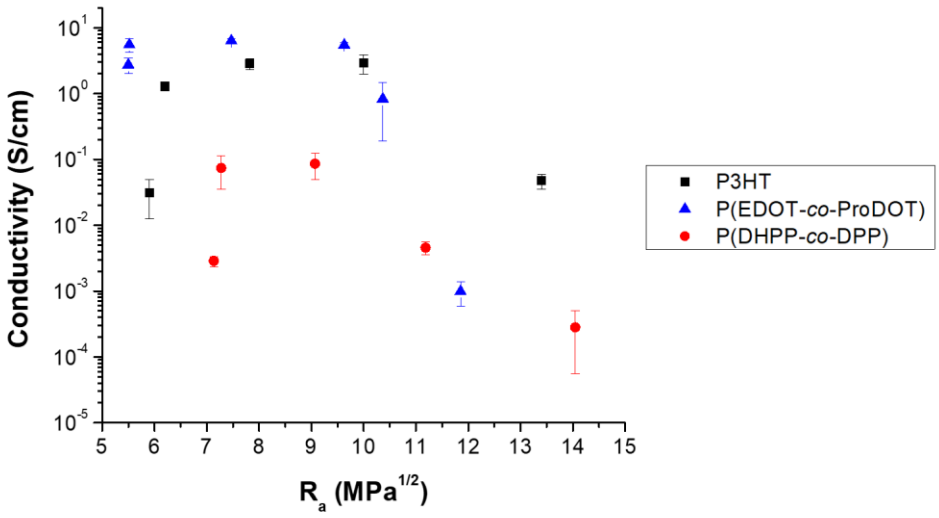

Figure 5.2. Conductivity measurements of **P3HT**, **P(EDOT-*co*-ProDOT)**, and **P(DHPP-*co*-DPP)** thin films doped via sequential doping as a function of R_a values. R_a was calculated for each polymer-solvent pair and the solvents used are DCM, THF, acetone, DMF, DMSO, and 50:50 acetone:THF. Each polymer shows a clear R_a-dependent conductivity in which moderate R_a values yield the highest conductivity.

here, **P3HT** shows clear solvent-dependent conductivity with a characteristic a rise, plateau, then fall-off in conductivity. The plateau in conductivity at moderate R_a values and fall-off in conductivity at high R_a values (>10 $MPa^{1/2}$) is also observed with each of the copolymers; however, there are distinct differences for the solvents with the lowest R_a for each polymer.

First, with **P3HT** the low-R_a solvent THF (R_a = 5.90 $MPa^{1/2}$) lies well within the solubility sphere of P3HT (R_o = 6.45 $MPa^{1/2}$), leading to dissolution of the film (evidenced by a decrease in film thickness, Table D.2) and, ultimately, reduced conductivity. This indicates that solvents that are useful for doping must be closer to the edge (or outside) of the polymer solubility sphere to achieve higher conductivity. With **P(EDOT-*co*-ProDOT)** the lowest R_a solvent DCM (R_a = 5.50 $MPa^{1/2}$) is located on the edge of the polymer solubility sphere, therefore, there is little change in conductivity between the solvents with lower R_a values. On the other hand, due to the limited solubility of **P(DHPP-*co*-DPP)**, none of the solvents used in this study were within the polymer solubility sphere. However, there is a steep rise in conductivity between the films doped using THF (R_a = 7.13 $MPa^{1/2}$) and DCM (R_a = 7.27 $MPa^{1/2}$) despite a relatively small change in R_a value. Therefore, it is believed that this difference in conductivity is also attributed to the distance between the HSPs of the solvent and the vector between the polymer and dopant (d). For THF d = 1.77 $MPa^{1/2}$ and for DCM d = 0.80 $MPa^{1/2}$, which indicates that DCM has a higher affinity for the polymer and dopant, resulting in enhanced doping efficiency and increased conductivity. This finding indicates that the R_a value is not the only consideration for

solvent selection: Rather a doping solvent with a small *d*-value such that it lies close to the polymer-dopant axis appears to be ideal, especially for polymers of limited solubility.

Additionally, the conductivity of the sequentially doped polymers follows the trend of **P(EDOT-*co*-ProDOT)** > **P3HT** > **P(DHPP-*co*-DPP)**. This is attributed to a greater level of incorporation of the dopant in the film and, ultimately, more doping events. The interaction between the polymer and dopant solvent was evaluated by observing the amount of doping, which is achieved by electron transfer from the polymer to the dopant, that occurs in doped thin films. Specifically, UV-Vis absorbance spectra (Figure D.7-D.9) were obtained to observe the formation of $F4TCNQ^-$ (868 nm) and disappearance of the neutral polymer peak (λ_{max} of the respective polymer). The absorbance ratio of $F4TCNQ^-$:Polymer was calculated and correlated to R_a, as shown in Figure 5.3. First, a comparison of the $F4TCNQ^-$:Polymer absorbance ratio of each of the polymers shows the same trend seen with conductivity: **P(EDOT-*co*- ProDOT)** > **P3HT** > **P(DHPP-*co*-DPP)**. This trend indicates that higher levels of effective doping, as evidenced by the formation of $F4TCNQ^-$, contributes to higher levels of conductivity.

Second, $F4TCNQ^-$:Polymer absorbance ratios for each of the copolymers show solvent-dependence. Specifically, with **P3HT** and **P(EDOT-*co*-ProDOT)**, partial dissolution of the film by solvents that result in low R_a values to cause inconsistent and low levels of dopant incorporation. With **P(DHPP-*co*-DPP)**, the low $F4TCNQ^-$:Polymer absorbance ratio at low R_a is believed to be exacerbated by also having a higher *d*-value (lower affinity to the polymer and dopant). At high R_a values for each polymer, the solvent

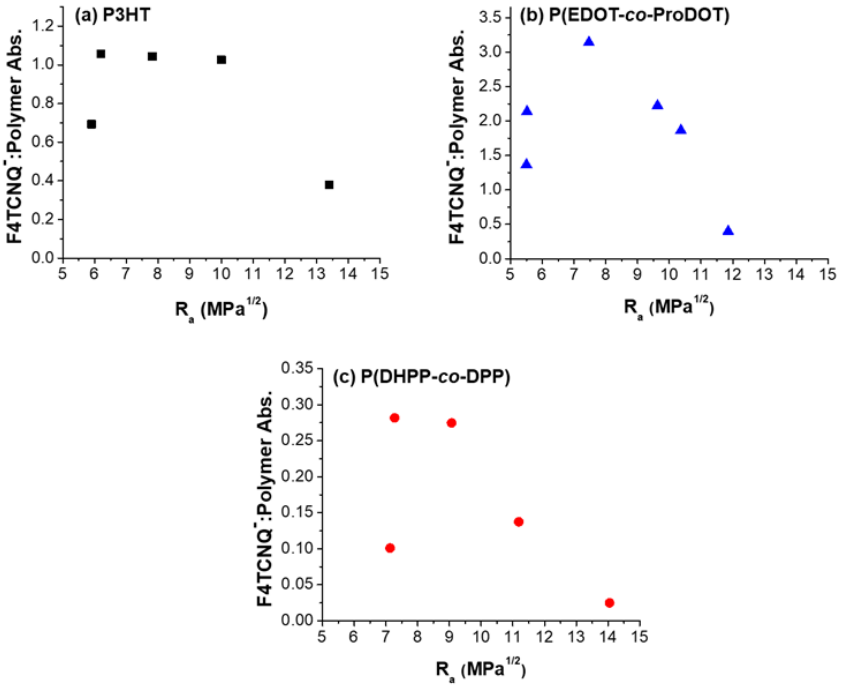

Figure 5.3. Absorbance ratio of F4TCNQ^{-}:Polymer as a function of R_a value for sequentially doped thin films made from (a) **P3HT**, (b) **P(EDOT-*co*-ProDOT)**, and (c) **P(DHPP-*co*-DPP)**. The absorbance ratio shows the same R_a-dependence as conductivity, indicating that the solvent-polymer interaction energy influences dopant integration and formation of F4TCNQ^{-}, which largely regulates thin film conductivity.

is unable to swell the polymer, which limits dopant penetration beyond the polymer–solvent interface and results in significantly lower F4TCNQ^{-}:Polymer absorbance ratios and conductivities. In contrast, moderate R_a values indicate that the solvent is able to swell the copolymer chains, promoting effective dopant integration and resulting in high F4TCNQ^{-}:Polymer absorbance ratios and enhanced levels of conductivity. This finding lends additional support to the contention that the level of effective dopant integration that results in the formation of F4TCNQ^{-} directly correlates with thin film conductivity.

While quantification of doping levels offers necessary insight into the film conductivity, the morphology of these films also needs to be considered. Because sequential doping is known to preserve the morphology of parent polymer thin films,[13,26] grazing-incidence wide-angle x-ray scattering (GIWAXS) is used to investigate how the solvent used for doping impacts this well-known heuristic. The out-of-plane 1D GIWAXS profiles are shown in Figure 5.4 and the corresponding 2D images are shown in Figure 5.5-5.7. There is some level of crystallinity in each of the as-cast films, as evidenced by the presence of (100) diffraction peaks. Upon doping, (100) peaks are observed for all doped thin films, indicating that sequential doping largely maintains the crystalline microstructure of the parent films; however, there are some key points to be made concerning the differences between dopant solvents. First, with **P3HT**, films doped using solvents with moderate R_a values, acetone and 50:50 acetone:THF, show higher order (200) diffraction peaks, indicating that the incorporation of the dopant slightly enhances the crystalline ordering of the thin film. This phenomenon has been reported for sequential doping of

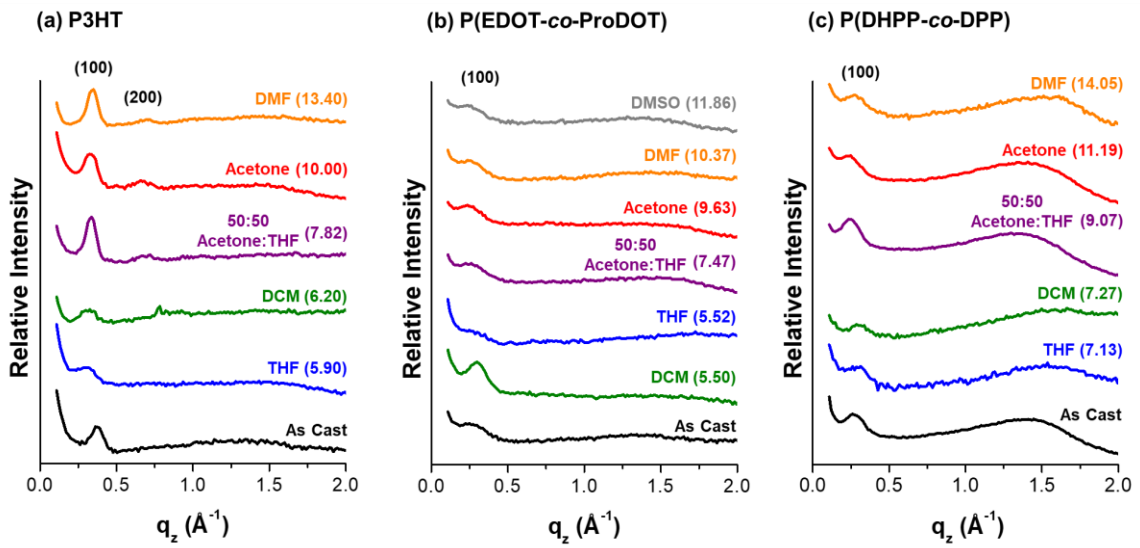

Figure 5.4. Out-of-plane 1D GIWAXS profiles of sequentially doped (a) **P3HT**, (b) **P(EDOT-*co*-ProDOT)**, and (c) **P(DHPP-*co*-DPP)** thin films with various solvents. The color of each profile corresponds to the dopant solvent used (e.g., blue is THF) and the respective R_a values for the solvent-polymer pair are given (in parentheses). For each polymer, the traces are ordered, from the bottom to the top, from good solvent (low R_a) to poor solvent (high R_a).

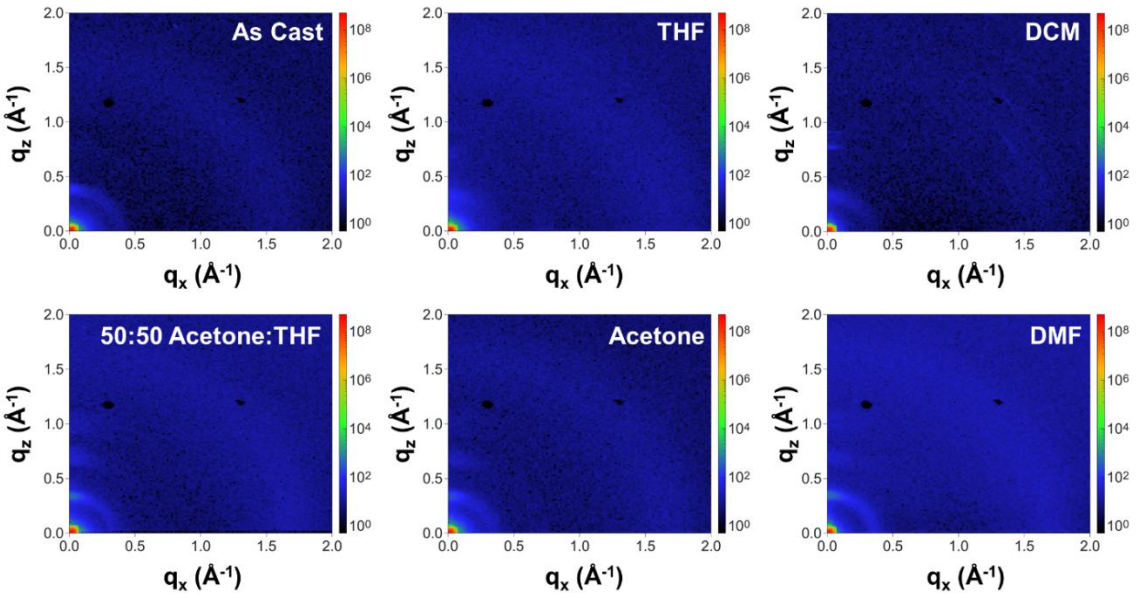

Figure 5.5. 2D GIWAXS images of as-cast and doped thin films made from **P3HT**. Images are arranged (left to right, row by row) in order of decreasing solvent quality (R_a value).

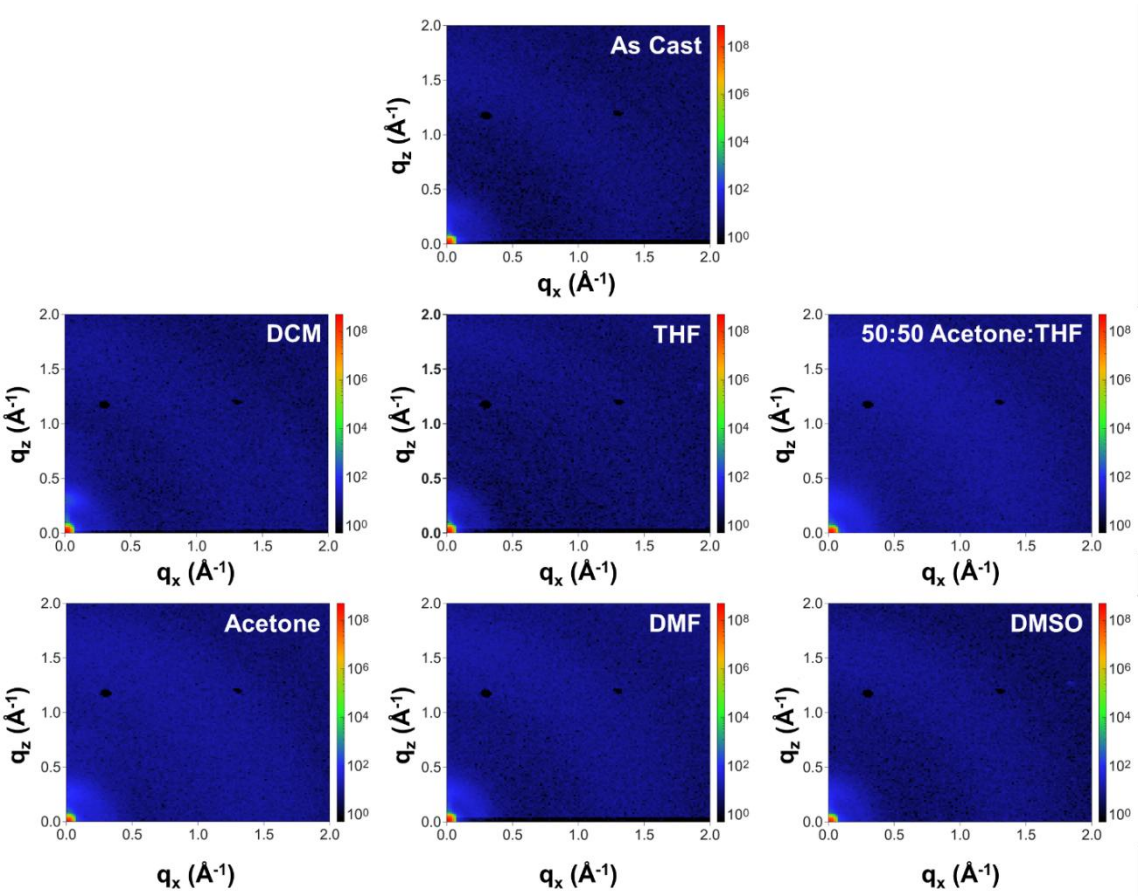

Figure 5.6. 2D GIWAXS images of as-cast and doped thin films made from **P(EDOT-*co*-ProDOT)**. Images are arranged (left to right, row by row) in order of decreasing solvent quality (R_a value).

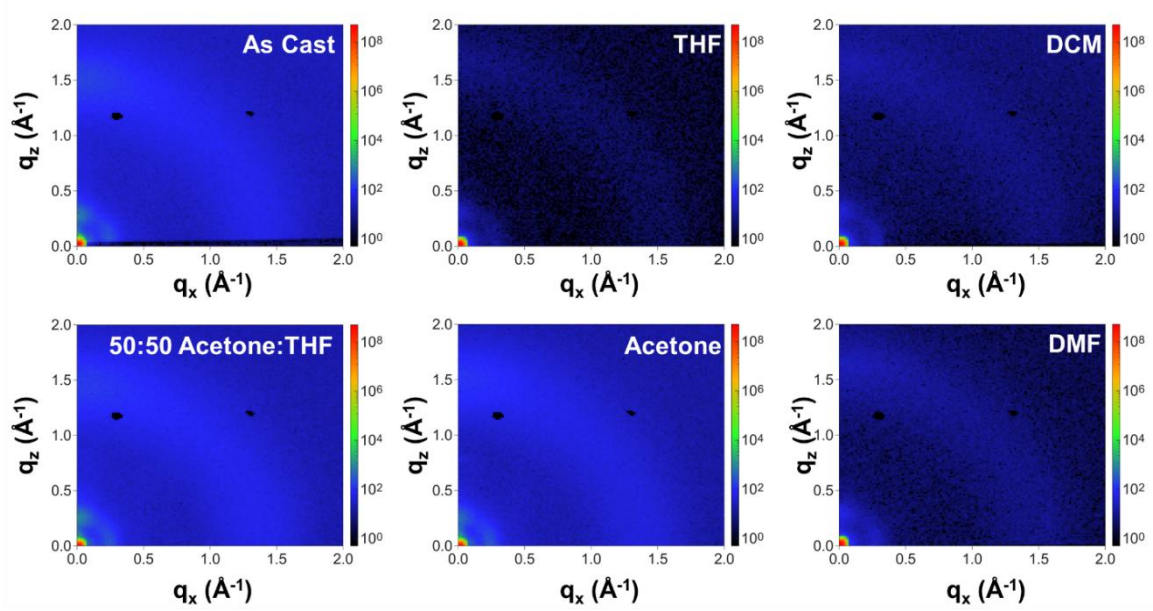

Figure 5.7. 2D GIWAXS images of as-cast and doped thin films made from **P(DHPP-*co*-DPP)**. Images are arranged (left to right, row by row) in order of decreasing solvent quality (R_a value).

P3HT with low concentrations of dopant.[32,126] Also, as summarized in Table 5.4, the *d*-spacing for each of the doped **P3HT** films increases compared to the as-cast films, indicating that the dopant has integrated into the lamellae.[26,31,32] It should also be appreciated that there is a weak (200) peak in the profile of **P3HT** after sequential doping using DMF, which, as indicated by the R_a value of 13.40 $MPa^{1/2}$, is a non-solvent for the film. The appearance of the weak (200) feature may be due to some dopant integration at the polymer-solvent interface, which is evidenced and supported by the low $F4TCNQ^-$:Polymer absorbance ratio observed in Figure 5.3. Also, the increase in *d*-spacing when **P3HT** films are doped using the poor solvent DMF is smaller in comparison to films that are sequentially-doped using other solvents. This supports the idea that there is a low level of dopant integration, which is in agreement with the $F4TCNQ^-$:Polymer absorbance ratio, despite the appearance of a weak (200) peak. Additionally, **P3HT** films doped using 50:50 acetone:THF, which is the solvent with the lowest *d*-value (0.46 $MPa^{1/2}$), exhibit the highest crystalline order of the doped **P3HT** films, indicating that the use of a solvent with affinity for both the polymer and dopant in the doping process aids in enhancing crystalline behavior.

Turning to the 1D profiles of **P(EDOT-*co*-ProDOT)**, there is little change in the intensity and breadth of the (100) diffraction peak upon doping, except for films doped using DCM as the solvent (R_a =5.5 $MPa^{1/2}$). Again, this enhancement in crystallinity is attributed to DCM having the lowest *d*-value (1.91 $MPa^{1/2}$) for this polymer. Additionally, the *d*-spacing measured for the film doped by using DCM as the solvent decreases

Table 5.4. Summary of *d*-spacing values obtained from the (100) diffraction peaks of the out-of-plane 1D GIWAXS profiles.

	***d*-spacing (Å)**		
Dopant Solvent	**P3HT**	**P(EDOT-*co*-ProDOT)**	**P(DHPP-*co*-DPP)**
As-cast	17.0	25.8	24.3
THF	21.0	–*	24.7
DCM	20.0	21.7	20.9
50:50 Acetone:THF	19.0	26.3	26.1
Acetone	19.3	27.4	27.7
DMF	18.4	25.6	24.3
DMSO	–	27.9	–

**could not be calculated from the 1D profile*

compared to the as-cast film, which suggests that the dopant is not present in the lamellae despite the apparent increased ordering of crystallites. The contention that dopant is not integrating into the lamellae is suppored by the lower $F4TCNQ^-$:Polymer absorbance ratio seen in Figure 5.3. Lastly, when **P(EDOT-*co*-ProDOT)** thin films are doped with the solvents of moderate R_a, acetone and 50:50 acetone:THF, the *d*-spacing increases compared to the as-cast film, which is consistent with UV-Vis measurements that indicate effective dopant integration.

As seen in Figure 5.4c, **P(DHPP-*co*-DPP)** thin films exhibit a (100) diffraction peak as well as a distinct and broad amorphous peak (1.0 – 2.0 Å). This amorphous character is consistent with previous DSC measurements that revealed that this copolymer had no thermal transitions.[124] When **P(DHPP-*co*-DPP)** is sequentially-doped, the microstructure of the as-cast film is preserved with each of the solvents used for sequential doping. In Table 5.4, it is seen that **P(DHPP-*co*-DPP)** thin films doped using THF and DMF—the solvents on the low and high ends of R_a values—produce minimal changes in *d*-spacing, indicating low incorporation of the dopant (which is also evidenced by the low $F4TCNQ^-$:Polymer ratios seen from UV-Vis-NIR measurements). **P(DHPP-*co*-DPP)** thin films doped using DCM as the solvent exhibited a small decrease in *d*-spacing compared to the as-cast films despite showing a relatively high concentration of $F4TCNQ^-$ in the UV-Vis spectrum. However, **P(DHPP-*co*-DPP)** films doped using acetone and 50:50 acetone:THF as solvents show an increase in *d*-spacing. This is attributed to the integration of F4TCNQ in the lamellae, which ultimately leads to an increase in $F4TCNQ^-$ concentration and higher conductivity (compared to films that use THF and DCM as

solvents for sequential doping). Lastly, as seen with the other polymers, **P(DHPP-*co*-DPP)** films that were doped using the solvent with the lowest *d*-value (50:50 acetone:THF, 0.80 $MPa^{1/2}$) exhibited the most well-defined diffraction peaks, indicating an enhancement in crystallinity.

5.5. Conclusions

Overall, these insights provide additional support for the idea of universal solvent-dependent conductivity in conjugated polymer thin films that are sequentially-doped with F4TCNQ. While this solvent-dependence has been known empirically, it is formalized through R_a, which is based in thermodynamics. More significantly, the use of R_a provides predictive capabilities – if the HSPs of a polymer are known, optimum conductivities can be targeted by choosing a solvent that gives a moderate R_a and a *d*-value that is close to the polymer-solvent axis. For each polymer discussed here, there is solvent quality-dependent conductivity in which a rise, plateau, and fall-off in conductivity is observed as R_a is increased. However, R_a values that optimize conductivity for other conjugated polymers occur at slightly shifted values compared to **P3HT**, due to differences in the solubility of the polymer, specifically the size of the solubility sphere and the positioning of the vector connecting the HSPs of the polymer and dopant. This solvent-quality dependence was also seen in measurements of the amount of $F4TCNQ^-$ present in the thin films, indicating that the level of doping significantly impacts the resultant conductivity. However, thin film morphology also plays a critical role in conductivity. It was observed that thin films doped using marginal solvents were observed to maintain (and in some cases, showed enhancements in) the crystalline ordering compared to their as-cast counterparts, with the

highest level of ordering being observed when solvents of low *d*-value are used. With the addition of conjugated polymers consisting of dioxythiophene and donor-acceptor motifs, this study provides additional insight into the concept of universality of solvent quality-dependent conductivity, which was observed in our previous work. Overall, it is anticipated that this research will guide future strategies for sequential doping of complex conjugated copolymers.

Chapter 6. Conclusions and Future Work

6.1. Conclusions

Chemical doping is commonly used to enhance the conductivity of conjugated polymers; however, most approaches, are built on long-standing methods and lack essential physical information that guides their implementation to new materials. In addition, there are no standardized methods for describing doping to achieve optimal conductivity across a variety of conjugated polymers. The work described in this dissertation aims to provide necessary, fundamental insight and a framework for determining optimal doping conditions for conjugated polymer thin films. This was achieved through studies of thiophene-based copolymers having systematic modifications to their polymeric backbone through the regular integration of spacing units and the impact of solvent type and doping conditions on electrical conductivity of their doped thin films. This approach offers insights into the design-structure–property relationships, capturing links between monomer design, polymer solubility, film morphology, and conductivity.

In *Chapter 2*, solution and sequential doping methods were compared for a series of expanded core copolymers. It was found that increasing the length of the spacing unit led to significantly higher conductivities (relative to the benchmark poly(3-hexylthiophene)) with both doping methods. The increases in conductivity are attributed to enhanced interactions between the dopant and polymer backbone due to reduced steric demand, which facilitates more effective doping. Additionally, sequential doping resulted in higher conductivity at lower doping levels compared to solution doping, indicating that it is a more efficient doping method. Sequential doping was further assessed by measuring the

conductivity of thin films doped with F4TCNQ using various solvents. The solvents with moderate R_a values yielded doped films with the highest conductivities, due to the ability of the solvent to swell the polymer chains and enable effective dopant integration. This solvent-dependent behavior was consistently observed across all of the thiophene-based copolymers studied, providing the basis for identifying optimal solvents or solvent blends for doping.

In *Chapter 5*, this concept of universality in sequential doping was further validated by studying two more complex copolymers: **P(EDOT-*co*-ProDOT)**, a dioxythiophene-based copolymer, and **P(DHPP-*co*-DPP)**, a donor–acceptor copolymer. Both systems exhibited similar solvent-dependent trends in electrical conductivity, with moderate R_a values yielding the highest conductivities. However, slight shifts in the optimal R_a values were observed, depending on the polarity and solubility of the polymer, as estimated from HSPs. Overall, the solvent-dependent conductivity of sequentially doped conjugated polymers appears to be universal, offering a predictive framework for selecting optimal solvents or solvent blends to achieve high conductivity for conjugated polymers thin films.

The method of doping was studied in detail in *Chapter 3* using the same set of expanded core thiophene-based copolymers. In this chapter, solution and sequential doping were compared to serial doping, which consists of successive steps of solution doping and sequential doping. It was found that thin films doped via serial doping exhibited higher conductivities than those doped solely through solution or sequential methods. The observed enhancements in conductivity were not due to a simple additive effect of increased dopant integration; rather, it was attributed to increased crystallinity in the thin

films, as evidenced by GIWAXS measurements. Notably, thin films prepared via serial doping displayed enhanced crystalline order despite the pristine polymers exhibiting largely amorphous characteristics. This suggests that the serial doping process induces crystallite formation. These findings demonstrate that serial doping offers a doping strategy to significantly enhance conductivity, particularly for amorphous conjugated polymers.

Lastly, *Chapter 4* explores the molecular weight characterization of conjugated polymers. Conjugated polymers are known to behave differently in solution because their chemical design involves cyclic (hetero)aromatic backbone units; however, GPC measurements typically rely on calibration standards of flexible polymers, such as polystyrene. In this chapter, the various common analyses used in GPC were compared for their accuracy in measuring molecular weight in comparison to triple detection. These studies demonstrated that conventional calibration overestimates the M_w of conjugated polymers and the deviation from values determined by triple detection correlates with the Mark-Houwink parameters of the polymer. Specifically, polymers with higher *a*-values exhibited greater deviation due to their more swollen conformation in solution compared to the reference polymer, polystyrene. As the *a*-value increases, the polymer's hydrodynamic volume also increases, leading to an overestimation of M_w relative to its absolute molecular weight. Universal calibration was also evaluated. When 100% mass recovery was assumed, the M_w was overestimated because 100% of the mass was not recovered, which in turn led to the d*n*/d*c* values being underestimated. However, when the measured d*n*/d*c* value of the polymer was used in universal calibration, the M_w was found to closely match the value obtained by triple detection. Overall, this work shows that

analysis using universal calibration with the experimentally-measured values of d*n*/d*c* provides the most accurate M_w estimation for thiophene-based conjugated polymers.

In total, this dissertation research contributes to a deeper understanding of design-structure–property relationships of conjugated polymers by linking solubility, morphology, and conductivity, with a strong emphasis on chemical doping. It presents a systematic investigation of how spacing units can be used to improve conductivity despite the impact on solubility of fewer solubilizing side chains (lower number density). Additionally, my research findings validate the concept of universal solvent-dependence for sequential doping, which thereby offers a predictive framework for selecting optimal solvents for sequential doping that would be applicable to any conjugated polymers. Finally, serial doping is proposed as a strategy to enhance both conductivity and crystallinity in amorphous conjugated polymers. Collectively, this work lays the foundation for developing doping procedures that can be broadly applied across conjugated polymer systems for use in organic electronic devices.

6.2. Future Work

6.2.1. Impact of Regioregularity on Conductivity and Morphology

It is well known that regioregularity dramatically impacts the properties of P3HT in solution and in thin films. This was demonstrated in part in *Chapter 2*, where **P3HT (AA+BB)**, which is regio-irregular, exhibited a higher E_{gap}, solubility in more solvents, and lower conductivity than its regioregular counterpart. The expanded core copolymers discussed throughout this dissertation are known to be regio-irregular due to the AA+BB polymerization used. However, despite the inherent regio-irregularity of these polymers

they exhibited high performance in terms of film conductivity. These observations catalyze a series of follow-on studies that examine how regioregularity of conjugated polymers with expanded cores impact their solubility, film morphology, and conductivity.

Specifically, the synthesis and study of regioregular and regio-irregular versions of polymers containing thiophene, bithiophene, and terthiophene spacing units is proposed (Figure 6.1). This systematically-tailored set of polymers will provide insight into the spacing distance required before regioregularity is no longer necessary for achieving high conductivity. Additionally, the expanded core copolymers used in this dissertation research were amorphous, as evidenced by DSC measurements. Thus, this proposed study would provide insight into whether the amorphous character is due to the presence of the spacing unit or the regio-irregularity.

6.2.2. Additives to Induce Crystallinity

There are many studies utilizing small molecules to induce order within conjugated polymer thin films.[127,128] One such example is the use of iodoalkanes, which have been used in solution processing of films due to their high boiling points. The use of these additives slows the evaporation rate of the solvents, thereby giving polymer chains more time to self-assemble. In *Chapter 3*, the enhancement of crystalline order in the thin films through serial doping is seen to greatly improve the conductivity; therefore, it is proposed to extend these studies by examining the use of iodoalkanes to induce or promote crystallinity in thin films.

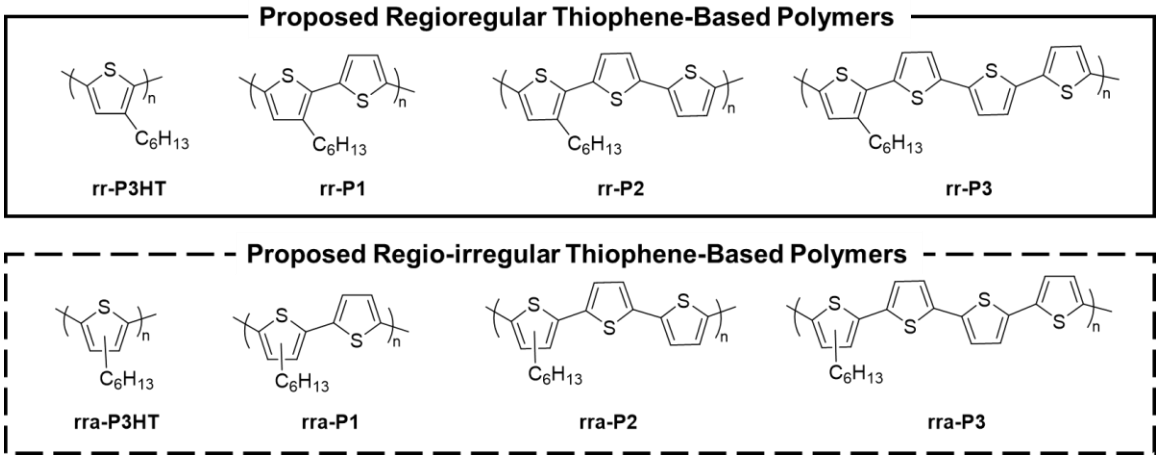

Figure 6.1. Proposed structures of regioregular (top) and regio-irregular (bottom) expanded core polymers, which can be used to examine the impact of regioregularity on film structure and properties.

It is believed that the incorporation of iodoalkanes, such as dioidooctane or dioiodohexane, in polymer solutions will improve the crystallinity of pristine polymer films, and this will enable higher levels of conductivity to be achieved upon sequential doping of their thin films. Additionally, the most prevalent problem with solution doping is the formation of aggregates within solution and the resultant thin film. This proposed study would indicate if the small molecule additive could be used to circumvent these issues to improve film morphology and conductivity. Overall, this study would increase the understanding of the effects that small molecule additives have on thin film morphology and ultimately conductivity, offering insight into methods to improve chemical doping.

6.2.3. Extensions into Donor-Acceptor Copolymers

This dissertation research focused on a set of thiophene-based copolymers to establish a foundation for understanding design-structure-property relationships involving electrical conductivity through chemical doping. However, extensive research has been devoted to synthesizing and characterizing more structurally- and chemically-complex copolymers with the idea that those "state-of-art" materials lead to higher levels of conductivity. One notable class of copolymers is donor–acceptor copolymers, in which internal charge transfer occurs due to electron-rich donor moieties "pushing" electrons toward the more electron-deficient acceptor units. The acceptor groups, in turn, "pull" electrons due to their inherent electron deficiency. This "push–pull" design facilitates intramolecular charge transfer along the polymer backbone, which improves charge mobility and lowers bandgap.[18,60,129]

A series of studies analogous to those described in *Chapter 2* but using donor–acceptor copolymers containing diketopyrrolopyrrole (DPP) and thiophene units would provide valuable insight into how spacing units and doping methods influence conductivity in more sophisticated conjugated copolymers. Due to the presence of the fused ring structures and polar functionalities in DPP, the solubility profiles of these copolymers would differ significantly from those of the thiophene-based systems. This was described in *Chapter 5* with **P(DHPP-co-DPP)**; however, that study was limited to a single DPP-containing copolymer and a single doping method.

A more systematic investigation of donor–acceptor copolymers containing DPP would enhance our understanding of the applicability and universality of the various doping approaches utilized in my research. Additionally, these studies could determine whether serial doping is effective across different classes of conjugated polymers. Ultimately, this proposed work would lay the groundwork for developing a universal doping methodology, informed by the principles and outcomes established here for thiophene-based copolymers.

References

(1) Guo, X.; Baumgarten, M.; Müllen, K. Designing π-Conjugated Polymers for Organic Electronics. *Prog. Polym. Sci.* **2013**, *38* (12), 1832-1908.

(2) Scharber, M. C.; Sariciftci, N. S. Low Band Gap Conjugated Semiconducting Polymers. *Adv. Mater. Technol.* **2021**, *6* (4), 2000857.

(3) Rasmussen, S. C. Conjugated and Conducting Organic Polymers: The First 150 Years. *ChemPlusChem* **2020**, *85* (7), 1412-1429.

(4) Shirakawa, H.; Louis, E. J.; MacDiarmid, A. G.; Chiang, C. K.; Heeger, A. J. Synthesis of Electrically Conducting Organic Polymers: Halogen Derivatives of Polyacetylene, (CH)x. *J. Chem. Soc. Chem. Comm.* **1977**, (16), 578-580.

(5) Shirakawa, H.; Ito, T.; Ikeda, S. Electrical Properties of Polyacetylene with Various Cis-Trans Compositions. *Die Makromolekulare Chemie* **1978**, *179* (6), 1565-1573.

(6) Pron, A.; Rannou, P. Processible Conjugated Polymers: From Organic Semiconductors to Organic Metals and Superconductors. *Prog. Polym. Sci.* **2002**, *27* (1), 135-190.

(7) Moliton, A.; Hiorns, R. C. Review of Electronic and Optical Properties of Semiconducting π-Conjugated Polymers: Applications in Optoelectronics. *Polym. Int.* **2004**, *53* (10), 1397-1412.

(8) Liu, Y.; Gao, S.; Zhang, X.; Xin, J. H.; Zhang, C. Probing the Nature of Charge Carriers in One-Dimensional Conjugated Polymers: A Review of the Theoretical Models, Experimental Trends, and Thermoelectric Applications. *J. Mater. Chem. C* **2023**, *11* (1), 12-47.

(9) Anslyn, E. V.; Dougherty, D. A. *Modern Physical Organic Chemistry*; University Science Books, 2006.

(10) Wu, W.-N.; Zheng, Q.-B.; Liu, C.-L. Recent Progress in p-Type Doped Conjugated Polymer-Based Thermoelectric Thin Films. *Synthetic Met.* **2024**, *307*, 117682.

(11) Lu, Y.; Wang, J. Y.; Pei, J. Achieving Efficient n-Doping of Conjugated Polymers by Molecular Dopants. *Acc. Chem. Res.* **2021**, *54* (13), 2871-2883.

(12) Scaccabarozzi, A. D.; Basu, A.; Aniés, F.; Liu, J.; Zapata-Arteaga, O.; Warren, R.; Firdaus, Y.; Nugraha, M. I.; Lin, Y.; Campoy-Quiles, M.; Koch, N.; Müller, C.; Tsetseris, L.; Heeney, M.; Anthopoulos, T. D. Doping Approaches for Organic Semiconductors. *Chem. Rev.* **2022**, *122* (4), 4420-4492.

(13) Jacobs, I. E.; Aasen, E. W.; Oliveira, J. L.; Fonseca, T. N.; Roehling, J. D.; Li, J.; Zhang, G.; Augustine, M. P.; Mascal, M.; Moulé, A. J. Comparison of Solution-Mixed and Sequentially Processed P3HT:F4TCNQ Films: Effect of Doping-Induced Aggregation on Film Morphology. *J. Mater. Chem. C* **2016**, *4* (16), 3454-3466.

(14) Li, H.; DeCoster, M. E.; Ming, C.; Wang, M.; Chen, Y.; Hopkins, P. E.; Chen, L.; Katz, H. E. Enhanced Molecular Doping for High Conductivity in Polymers with Volume Freed for Dopants. *Macromolecules* **2019**, *52* (24), 9804-9812.

(15) Zhang, Y.; Elawad, M.; Yu, Z.; Jiang, X.; Lai, J.; Sun, L. Enhanced Performance of Perovskite Solar Cells with P3HT Hole-transporting Materials via Molecular p-Type Doping. *RSC Adv.* **2016**, *6* (110), 108888-108895.

(16) Duong, D. T.; Wang, C.; Antono, E.; Toney, M. F.; Salleo, A. The Chemical and Structural Origin of Efficient p-type Doping in P3HT. *Org. Electron.* **2013**, *14* (5), 1330-1336.

(17) Du, T.; Liu, Y.; Wang, C.; Deng, Y.; Geng, Y. n-Type Conjugated Polymers Based on an Indandione-Terminated Quinoidal Building Block. *Macromolecules* **2022**, *55* (14), 5975-5984.

(18) Yan, X.; Xiong, M.; Li, J. T.; Zhang, S.; Ahmad, Z.; Lu, Y.; Wang, Z. Y.; Yao, Z. F.; Wang, J. Y.; Gu, X.; Lei, T. Pyrazine-Flanked Diketopyrrolopyrrole (DPP): A New Polymer Building Block for High-Performance n-Type Organic Thermoelectrics. *J. Am. Chem. Soc.* **2019**, *141* (51), 20215-20221.

(19) Pingel, P.; Neher, D. Comprehensive Picture of p-Type Doping of P3HT with the Molecular Acceptor F4TCNQ. *Phys. Rev. B* **2013**, *87* (11), 115209.

(20) Wu, E. C.; Salamat, C. Z.; Ruiz, O. L.; Qu, T.; Kim, A.; Tolbert, S. H.; Schwartz, B. J. Counterion Control and the Spectral Signatures of Polarons, Coupled Polarons, and Bipolarons in Doped P3HT Films. *Adv. Funct. Mater.* **2023**, *33* (19), 2213652.

(21) Enengl, C.; Enengl, S.; Pluczyk, S.; Havlicek, M.; Lapkowski, M.; Neugebauer, H.; Ehrenfreund, E. Doping-Induced Absorption Bands in P3HT: Polarons and Bipolarons. *ChemPhysChem* **2016**, *17* (23), 3836-3844.

(22) Dexter Tam, T. L.; Moudgil, A.; Teh, W. J.; Wong, Z. M.; Handoko, A. D.; Chien, S. W.; Yang, S.-W.; Yeo, B. S.; Leong, W. L.; Xu, J. Polaron Delocalization Dependence of the Conductivity and the Seebeck Coefficient in Doped Conjugated Polymers. *J. Phys. Chem. B* **2022**, *126* (9), 2073-2085.

(23) Untilova, V.; Zeng, H.; Durand, P.; Herrmann, L.; Leclerc, N.; Brinkmann, M. Intercalation and Ordering of F6TCNNQ and F4TCNQ Dopants in Regioregular Poly(3-hexylthiophene) Crystals: Impact on Anisotropic Thermoelectric Properties of Oriented Thin Films. *Macromolecules* **2021**, *54* (13), 6073-6084.

(24) Fernandez, H.; El Haitami, A.; Spagnoli, S.; Fontaine, P.; Cantin, S. Coprocessing of F4TCNQ Dopant and Poly(3-alkylthiophene) in a Two-Dimensional Bilayer. *Macromolecules* **2024**, *57* (15), 7184-7196.

(25) Fontana, M. T.; Stanfield, D. A.; Scholes, D. T.; Winchell, K. J.; Tolbert, S. H.; Schwartz, B. J. Evaporation vs Solution Sequential Doping of Conjugated Polymers: F4TCNQ Doping of Micrometer-Thick P3HT Films for Thermoelectrics. *J. Phys. Chem. C* **2019**, *123* (37), 22711-22724.

(26) Scholes, D. T.; Hawks, S. A.; Yee, P. Y.; Wu, H.; Lindemuth, J. R.; Tolbert, S. H.; Schwartz, B. J. Overcoming Film Quality Issues for Conjugated Polymers Doped with F4TCNQ by Solution Sequential Processing: Hall Effect, Structural, and Optical Measurements. *J. Phys. Chem. Lett.* **2015**, *6* (23), 4786-4793.

(27) Noriega, R.; Rivnay, J.; Vandewal, K.; Koch, F. P.; Stingelin, N.; Smith, P.; Toney, M. F.; Salleo, A. A General Relationship Between Disorder, Aggregation and Charge Transport in Conjugated Polymers. *Nat. Mater.* **2013**, *12* (11), 1038-1044.

(28) Pingel, P.; Zen, A.; Abellón, R. D.; Grozema, F. C.; Siebbeles, L. D. A.; Neher, D. Temperature-Resolved Local and Macroscopic Charge Carrier Transport in Thin P3HT Layers. *Adv. Funct. Mater.* **2010**, *20* (14), 2286-2295.

(29) Guchait, S.; Herrmann, L.; Kadri, K.; Leclerc, N.; Tran Van, F.; Brinkmann, M. Impact of Regioregularity on Alignment and Thermoelectric Properties of Sequentially Doped and Oriented Films of Poly(3-hexylthiophene). *ACS Appl. Polym. Mater.* **2023**, *5* (7), 5676-5686.

(30) Yoon, S. E.; Han, J. M.; Seo, B. E.; Kim, S.-W.; Kwon, O. P.; Kim, B.-G.; Kim, J. H. Optimized Selection of Dopant Solvents for Improving the Sequential Doping Efficiency of Conjugated Polymers. *Org. Electron.* **2021**, *90*, 106061.

(31) Stanfield, D. A.; Wu, Y.; Tolbert, S. H.; Schwartz, B. J. Controlling the Formation of Charge Transfer Complexes in Chemically Doped Semiconducting Polymers. *Chem. Mater.* **2021**, *33* (7), 2343-2356.

(32) He, J.; Shan, H.; Zhu, B.; Cao, X.; Zhou, J.; Huo, H. Correlation of Dopant Solution on Doping Mechanism and Performance of F4TCNQ-Doped P3HT. *J. Polym. Sci.* **2024**, *62* (22), 4993-5003.

(33) Chai, H.; Xu, Z.; Li, H.; Zhong, F.; Bai, S.; Chen, L. Sequential-Twice-Doping Approach Toward Synergistic Optimization of Carrier Concentration and Mobility in Thiophene-Based Polymers. *ACS Appl. Electron. Mater.* **2022**, *4* (10), 4947-4954.

(34) Yoon, S. E.; Kang, Y.; Jeon, G. G.; Jeon, D.; Lee, S. Y.; Ko, S.-J.; Kim, T.; Seo, H.; Kim, B.-G.; Kim, J. H. Exploring Wholly Doped Conjugated Polymer Films Based on Hybrid Doping: Strategic Approach for Optimizing Electrical Conductivity and Related Thermoelectric Properties. *Adv. Funct. Mater.* **2020**, *30* (42), 2004598.

(35) Mei, J.; Bao, Z. Side Chain Engineering in Solution-Processable Conjugated Polymers. *Chem. Mater.* **2014**, *26* (1), 604-615.

(36) Shih, Y.-H.; Chen, G.-L.; Liu, P.-H.; Tseng, K.-W.; Lee, W.-Y.; Chen, W.-C.; Wang, L.; Chueh, C.-C. Revealing the Effect of Branched Side Chain Length on Polymer Aggregation and Paracrystallinity for Improved Mobility–Stretchability Properties. *ACS Appl. Electron. Mater.* **2024**, *6* (3), 1797-1808.

(37) Yao, Z.-F.; Wang, J.-Y.; Pei, J. Side Chain Engineering Toward Chemical Doping of Conjugated Polymers. *Acc. Chem. Res.* **2025**, *58* (9), 1496-1508.

(38) Nam, G.-H.; Sun, C.; Chung, D. S.; Kim, Y.-H. Enhancing Doping Efficiency of Diketopyrrolopyrrole-Copolymers by Introducing Sparse Intramolecular Alkyl Chain Spacing. *Macromolecules* **2021**, *54* (17), 7870-7879.

(39) Stewart, K.; Pagano, K.; Tan, E.; Daboczi, M.; Rimmele, M.; Luke, J.; Eslava, S.; Kim, J.-S. Understanding Effects of Alkyl Side-Chain Density on Polaron Formation Via Electrochemical Doping in Thiophene Polymers. *Adv. Mater.* **2024**, *36* (20), 2211184.

(40) Hynynen, J.; Kiefer, D.; Yu, L.; Kroon, R.; Munir, R.; Amassian, A.; Kemerink, M.; Müller, C. Enhanced Electrical Conductivity of Molecularly p-Doped Poly(3-hexylthiophene) Through Understanding the Correlation with Solid-State Order. *Macromolecules* **2017**, *50* (20), 8140-8148.

(41) Nagamatsu, S.; Pandey, S. S. Ordered Arrangement of F4TCNQ Anions in Three-Dimensionally Oriented P3HT Thin Films. *Sci. Rep.* **2020**, *10* (1), 20020.

(42) Gobalasingham, N. S.; Thompson, B. C. Direct Arylation Polymerization: A Guide to Optimal Conditions for Effective Conjugated Polymers. *Prog. Polym. Sci.* **2018**, *83*, 135-201.

(43) Leclerc, M.; Brassard, S.; Beaupré, S. Direct (Hetero)arylation Polymerization: Toward Defect-Free Conjugated Polymers. *Polym. J.* **2020**, *52* (1), 13-20.

(44) Rudenko, A. E.; Thompson, B. C. Optimization of Direct Arylation Polymerization (DArP) Through the Identification and Control of Defects in Polymer Structure. *J. Polym. Sci. Pol. Chem.* **2015**, *53* (2), 135-147.

(45) Rudenko, A. E.; Wiley, C. A.; Tannaci, J. F.; Thompson, B. C. Optimization of Direct Arylation Polymerization Conditions for the Synthesis of Poly(3-hexylthiophene). *J. Polym. Sci. Pol. Chem.* **2013**, *51* (12), 2660-2668.

(46) Nakabayashi, K. Direct Arylation Polycondensation as Conjugated Polymer Synthesis Methodology. *Polym. J.* **2018**, *50* (7), 475-483.

(47) Stevens, M. P. *Polymer Chemistry: An Introduction*; Oxford University Press, 1999.

(48) Venkatram, S.; Kim, C.; Chandrasekaran, A.; Ramprasad, R. Critical Assessment of the Hildebrand and Hansen Solubility Parameters for Polymers. *J. Chem. Inf. Model.* **2019**, *59* (10), 4188-4194.

(49) Díaz de los Ríos, M.; Hernández Ramos, E. Determination of the Hansen Solubility Parameters and the Hansen Sphere Radius with the Aid of the Solver Add-in of Microsoft Excel. *SN Appl. Sci.* **2020**, *2* (4), 676.

(50) Mahmood, A.; Wang, J. L. A Review of Grazing Incidence Small- and Wide-Angle X-Ray Scattering Techniques for Exploring the Film Morphology of Organic Solar Cells. *Sol. RRL* **2020**, *4* (10), 2000337.

(51) Di Pietro, R.; Erdmann, T.; Carpenter, J. H.; Wang, N.; Shivhare, R. R.; Formanek, P.; Heintze, C.; Voit, B.; Neher, D.; Ade, H.; Kiriy, A. Synthesis of High-Crystallinity DPP

Polymers with Balanced Electron and Hole Mobility. *Chem. Mater.* **2017**, *29* (23), 10220-10232.

(52) Xiao, Y.; Lu, X. Morphology of Organic Photovoltaic Non-Fullerene Acceptors Investigated by Grazing Incidence X-ray Scattering Techniques. *Mater. Today Nano* **2019**, *5*, 100030.

(53) Hiemenz, P. C.; Lodge, T. P. *Polymer Chemistry: Second Edition*; CRC Press, 2007.

(54) Salleo, A. Charge Transport in Polymeric Transistors. *Mater. Today* **2007**, *10* (3), 38-45.

(55) Son, S. Y.; Park, T.; You, W. Understanding of Face-On Crystallites Transitioning to Edge-On Crystallites in Thiophene-Based Conjugated Polymers. *Chem. Mater.* **2021**, *33* (12), 4541-4550.

(56) Van der Pauw, L. J. A Method of Measuring the Resistivity and Hall Coefficient on Lamellae of Arbitrary Shape. *Philips Tech. Rev.* **1958**, *13* (1), 1-9.

(57) Chwang, R.; Smith, B. J.; Crowell, C. R. Contact Size Effects on Van der Pauw Method for Resistivity and Hall-Coefficient Measurement. *Solid State Electron.* **1974**, *17* (12), 1217-1227.

(58) Ramadan, A. A.; Gould, R. D.; Ashour, A. On the Van der Pauw Method of Resistivity Measurements. *Thin Solid Films* **1994**, *239* (2), 272-275.

(59) Rouget, G.; Chaouki, H.; Picard, D.; Ziegler, D.; Alamdari, H. Electrical Resistivity Measurement of Carbon Anodes using the Van der Pauw Method. *Metals* **2017**, *7* (9), 369-386.

(60) Su, Y.-W.; Lan, S.-C.; Wei, K.-H. Organic Photovoltaics. *Mater. Today* **2012**, *15* (12), 554-562.

(61) Chen, L. X. Organic Solar Cells: Recent Progress and Challenges. *ACS Energy Lett.* **2019**, *4* (10), 2537-2539.

(62) Meng, D.; Zheng, R.; Zhao, Y.; Zhang, E.; Dou, L.; Yang, Y. Near-Infrared Materials: The Turning Point of Organic Photovoltaics. *Adv. Mater.* **2022**, *34* (10), 2107330.

(63) Xiong, M.; Yan, X.; Li, J. T.; Zhang, S.; Cao, Z.; Prine, N.; Lu, Y.; Wang, J. Y.; Gu, X.; Lei, T. Efficient n-Doping of Polymeric Semiconductors through Controlling the Dynamics of Solution-State Polymer Aggregates. *Angew. Chem. Int. Ed.* **2021**, *60* (15), 8189-8197.

(64) Kiefer, D.; Kroon, R.; Hofmann, A. I.; Sun, H.; Liu, X.; Giovannitti, A.; Stegerer, D.; Cano, A.; Hynynen, J.; Yu, L.; Zhang, Y.; Nai, D.; Harrelson, T. F.; Sommer, M.; Moule, A. J.; Kemerink, M.; Marder, S. R.; McCulloch, I.; Fahlman, M.; Fabiano, S.; Muller, C. Double Doping of Conjugated Polymers with Monomer Molecular Dopants. *Nat. Mater.* **2019**, *18* (2), 149-155.

(65) Watts, K. E.; Clary, K. E.; Lichtenberger, D. L.; Pemberton, J. E. FTIR Spectroelectrochemistry of F4TCNQ Reduction Products and Their Protonated Forms. *Anal. Chem.* **2020**, *92* (10), 7154-7161.

(66) Makula, P.; Pacia, M.; Macyk, W. How To Correctly Determine the Band Gap Energy of Modified Semiconductor Photocatalysts Based on UV-Vis Spectra. *J. Phys. Chem. Lett.* **2018**, *9* (23), 6814-6817.

(67) Yang, Y.; Liu, Z.; Zhang, G.; Zhang, X.; Zhang, D. The Effects of Side Chains on the Charge Mobilities and Functionalities of Semiconducting Conjugated Polymers Beyond Solubilities. *Adv. Mater.* **2019**, *31* (46), 1903104.

(68) Pouliot, J. R.; Wakioka, M.; Ozawa, F.; Li, Y.; Leclerc, M. Structural Analysis of Poly(3-hexylthiophene) Prepared via Direct Heteroarylation Polymerization. *Macromol. Chem. Phys.* **2016**, *217* (13), 1493-1500.

(69) Rissler, J. Effective Conjugation Length of π-Conjugated Systems. *Chem. Phys. Lett.* **2004**, *395* (1-3), 92-96.

(70) de Oliveira, E. F.; Lavarda, F. C. Structure of P3HT in the Solid State. *J. Polym. Sci. Pol. Phys.* **2013**, *51* (18), 1350-1354.

(71) Nakanishi, H.; Sumi, N.; Aso, Y.; Otsubo, T. Synthesis and Properties of the Longest Oligothiophenes: The Icosamer and Heptacosamer. *J. Org. Chem.* **1998**, *63* (24), 8632-8633.

(72) McCulloch, B.; Ho, V.; Hoarfrost, M.; Stanley, C.; Do, C.; Heller, W. T.; Segalman, R. A. Polymer Chain Shape of Poly(3-alkylthiophenes) in Solution Using Small-Angle Neutron Scattering. *Macromolecules* **2013**, *46* (5), 1899-1907.

(73) Danielsen, S. P. O.; Bridges, C. R.; Segalman, R. A. Chain Stiffness of Donor–Acceptor Conjugated Polymers in Solution. *Macromolecules* **2022**, *55* (2), 437-449.

(74) Machui, F.; Langner, S.; Zhu, X.; Abbott, S.; Brabec, C. J. Determination of the P3HT:PCBM Solubility Parameters via a Binary Solvent Gradient Method: Impact of Solubility on the Photovoltaic Performance. *Sol. Energ. Mat. Sol. C* **2012**, *100*, 138-146.

(75) King, M.; Gottlieb, D.; Boucher, D. Impact of Regioregularity on the Solubility Parameters of Poly(3-hexylthiophene). *J. Polym. Sci.* **2022**, *60* (19), 2769-2783.

(76) Obata, S.; Shimoi, Y. Molecular Arrangements of Regioregular and Regiorandom Poly(3-hexylthiophene): Molecular Dynamics Simulations. *Trans. Mat. Res. Soc. Japan* **2012**, *37* (2), 311-314.

(77) Park, H.; Ma, B. S.; Kim, J.-S.; Kim, Y.; Kim, H. J.; Kim, D.; Yun, H.; Han, J.; Kim, F. S.; Kim, T.-S.; Kim, B. J. Regioregular-block-Regiorandom Poly(3-hexylthiophene) Copolymers for Mechanically Robust and High-Performance Thin-Film Transistors. *Macromolecules* **2019**, *52* (20), 7721-7730.

(78) Jia, H. P.; Gowrisanker, S.; Pant, G. K.; Wallace, R. M.; Gnade, B. E. Effect of Poly(3-hexylthiophene) Film Thickness on Organic Thin Film Transistor Properties. *J. Vac. Sci. Technol. A* **2006**, *24* (4), 1228-1232.

(79) Hong, C. T.; Yoo, Y.; Kang, Y. H.; Ryu, J.; Cho, S. Y.; Jang, K.-S. Effect of Film Thickness and Crystallinity on the Thermoelectric Properties of Doped P3HT Films. *RSC Adv.* **2015**, *5* (15), 11385-11391.

(80) Aguirre, J. C.; Hawks, S. A.; Ferreira, A. S.; Yee, P.; Subramaniyan, S.; Jenekhe, S. A.; Tolbert, S. H.; Schwartz, B. J. Sequential Processing for Organic Photovoltaics: Design Rules for Morphology Control by Tailored Semi-Orthogonal Solvent Blends. *Adv. Energy Mater.* **2015**, *5* (11), 1402020.

(81) Fujimoto, R.; Yamashita, Y.; Kumagai, S.; Tsurumi, J.; Hinderhofer, A.; Broch, K.; Schreiber, F.; Watanabe, S.; Takeya, J. Molecular Doping in Organic Semiconductors:

Fully Solution-Processed, Vacuum-free Doping with Metal–Organic Complexes in an Orthogonal Solvent. *J. Mater. Chem. C* **2017**, *5* (46), 12023-12030.

(82) Untilova, V.; Biskup, T.; Biniek, L.; Vijayakumar, V.; Brinkmann, M. Control of Chain Alignment and Crystallization Helps Enhance Charge Conductivities and Thermoelectric Power Factors in Sequentially Doped P3HT:F4TCNQ Films. *Macromolecules* **2020**, *53* (7), 2441-2453.

(83) Ferrari, M.; Mucci, A.; Schenetti, L.; Malmusi, L. Complete Assignment of the Aliphatic Chains in Dimers, Trimers and Polymer of 3-hexylthiophene Through 2D-NMR Spectroscopy. *Magn. Reson. Chem.* **2005**, *33* (8), 657-663.

(84) Barbarella, G.; Bongini, A.; Zambianchi, M. Regiochemistry and Conformation of Poly(3-hexylthiophene) via the Synthesis and the Spectroscopic Characterization of the Model Configurational Triads. *Macromolecules* **1994**, *27* (11), 3039-3045.

(85) Zhang, Y.; de Boer, B.; Blom, P. W. M. Controllable Molecular Doping and Charge Transport in Solution-Processed Polymer Semiconducting Layers. *Adv. Funct. Mater.* **2009**, *19* (12), 1901-1905.

(86) Linhart, A. N.; Sabury, S.; O'Connell, C. E.; Kilbey, S. M., II. Universality in Solvent-Dependent Conductivity of Conjugated Thiophene-Based Copolymers with Expanded Core Monomer Designs. *Chem. Mater.* **2025**, *37* (4), 1667-1680.

(87) Patel, S. N.; Glaudell, A. M.; Kiefer, D.; Chabinyc, M. L. Increasing the Thermoelectric Power Factor of a Semiconducting Polymer by Doping from the Vapor Phase. *ACS Macro Lett.* **2016**, *5* (3), 268-272.

(88) Vijayakumar, V.; Durand, P.; Zeng, H.; Untilova, V.; Herrmann, L.; Algayer, P.; Leclerc, N.; Brinkmann, M. Influence of Dopant Size and Doping Method on the Structure and Thermoelectric Properties of PBTTT Films Doped with F6TCNNQ and F4TCNQ. *J. Mater. Chem. C* **2020**, *8* (46), 16470-16482, 10.1039/D0TC02828B.

(89) Kim, J.; Guo, J.; Sini, G.; Sørensen, M. K.; Andreasen, J. W.; Woon, K. L.; Coropceanu, V.; Paleti, S. H. K.; Wei, H.; Peralta, S.; Mallouki, M.; Müller, C.; Hu, Y.; Bui, T.-T.; Wang, S. Remarkable Conductivity Enhancement in P-doped Polythiophenes via Rational Engineering of Polymer-Dopant Interactions. *Mater. Today Adv.* **2023**, *18*, 100360.

(90) Xie, R.; Lee, Y.; Aplan, M. P.; Caggiano, N. J.; Müller, C.; Colby, R. H.; Gomez, E. D. Glass Transition Temperature of Conjugated Polymers by Oscillatory Shear Rheometry. *Macromolecules* **2017**, *50* (13), 5146-5154.

(91) Ngo, T. T.; Nguyen, D. N.; Nguyen, V. T. Glass Transition of PCBM, P3HT and Their Blends in Quenched State. *Adv. Nat. Sci.-Nanosci.* **2012**, *3* (4), 045001.

(92) Fei, Z.; Boufflet, P.; Wood, S.; Wade, J.; Moriarty, J.; Gann, E.; Ratcliff, E. L.; McNeill, C. R.; Sirringhaus, H.; Kim, J.-S.; Heeney, M. Influence of Backbone Fluorination in Regioregular Poly(3-alkyl-4-fluoro)thiophenes. *J. Am. Chem. Soc.* **2015**, *137* (21), 6866-6879.

(93) Sakai-Otsuka, Y.; Nishiyama, Y.; Putaux, J.-L.; Brinkmann, M.; Satoh, T.; Chen, W.-C.; Borsali, R. Competing Molecular Packing of Blocks in a Lamella-Forming Carbohydrate-block-poly(3-hexylthiophene) Copolymer. *Macromolecules* **2020**, *53* (20), 9054-9064.

(94) Spoltore, D.; Vangerven, T.; Verstappen, P.; Piersimoni, F.; Bertho, S.; Vandewal, K.; Van den Brande, N.; Defour, M.; Van Mele, B.; De Sio, A.; Parisi, J.; Lutsen, L.; Vanderzande, D.; Maes, W.; Manca, J. V. Effect of Molecular Weight on Morphology and Photovoltaic Properties in P3HT:PCBM Solar Cells. *Org. Electron.* **2015**, *21*, 160-170.

(95) Zhu, S.; Peng, J. Enhanced Solvent and Thermal Stability in Cross-Linkable Conjugated Statistical Copolymers for Organic Field-Effect Transistors. *Chemistry – A European Journal* **2023**, *29* (15), e202203571.

(96) Osaka, I.; Takimiya, K. Backbone Orientation in Semiconducting Polymers. *Polymer* **2015**, *59*, A1-A15.

(97) Spann, R.; Boucher, D. Impact of Molecular Weight on the Solubility Parameters of Poly(3-hexylthiophene). *J. Polym. Sci.* **2023**, *61* (6), 503-514.

(98) Biswas, C. S.; Patel, V. K.; Vishwakarma, N. K.; Tiwari, V. K.; Maiti, B.; Maiti, P.; Kamigaito, M.; Okamoto, Y.; Ray, B. Effects of Tacticity and Molecular Weight of Poly(N-isopropylacrylamide) on Its Glass Transition Temperature. *Macromolecules* **2011**, *44* (14), 5822-5824.

(99) Sutton, C.; Yang, Y.; Zhang, D.; Yang, W. Single, Double Electronic Excitations and Exciton Effective Conjugation Lengths in π-Conjugated Systems. *J. Phys. Chem. Lett.* **2018**, *9* (14), 4029-4036.

(100) Pearson, D. S.; Pincus, P. A.; Heffner, G. W.; Dahman, S. J. Effect of Molecular Weight and Orientation on the Conductivity of Conjugated Polymers. *Macromolecules* **1993**, *26* (7), 1570-1575.

(101) Williams, T. Gel Permeation Chromatography: A Review. *J. Mater. Sci.* **1970**, *5* (9), 811-820.

(102) Päch, M.; Zehm, D.; Lange, M.; Dambowsky, I.; Weiss, J.; Laschewsky, A. Universal Polymer Analysis by 1H NMR Using Complementary Trimethylsilyl End Groups. *J. Am. Chem. Soc.* **2010**, *132* (25), 8757-8765.

(103) Hatada, K.; Kitayama, T.; Ute, K.; Terawaki, Y.; Yanagida, T. End-Group Analysis of Poly(methyl methacrylate) Prepared with Benzoyl Peroxide by 750 MHz High-Resolution 1H NMR Spectroscopy. *Macromolecules* **1997**, *30* (22), 6754-6759.

(104) Fair, R. A.; Xie, R.; Lee, Y.; Colby, R. H.; Gomez, E. D. Molecular Weight Characterization of Conjugated Polymers Through Gel Permeation Chromatography and Static Light Scattering. *ACS Appl. Polym. Mater.* **2021**, *3* (9), 4572-4578.

(105) Suzuki, H. Light Scattering Characterisation of Polymers I. An Extension of the Zimm Plot. *British Polymer Journal* **1979**, *11* (1), 35-40.

(106) Matsuba, G.; Kaji, K.; Nishida, K.; Kanaya, T.; Imai, M. Conformational Change and Orientation Fluctuations of Isotactic Polystyrene Prior to Crystallization. *Polym. J.* **1999**, *31* (9), 722-727.

(107) Yoon, D. Y.; Flory, P. J. Persistence Vectors for Polypropylene, Polystyrene, and Poly(methyl methacrylate) Chains. *J. Polym. Sci. Polym. Phys. Ed.* **1976**, *14* (8), 1425-1431.

(108) Tsourtou, F. D.; Peristeras, L. D.; Apostolov, R.; Mavrantzas, V. G. Molecular Dynamics Simulation of Amorphous Poly(3-hexylthiophene). *Macromolecules* **2020**, *53* (18), 7810-7824.

(109) Ambler, M. R. Universal Calibration in GPC: A New Approach for the Calculation of Molecular Weights. *J. Polym. Sci. Polym. Chem. Ed.* **1973**, *11* (1), 191-201.

(110) Coll, H.; Gilding, D. K. Universal Calibration in GPC: A Study of Polystyrene, Poly-α-methylstyrene, and Polypropylene. *J. Polym. Sci. A2* **1970**, *8* (1), 89-103.

(111) A Guide to Multi-Detector Gel Permeation Chromatography. Agilent Technologies: 2012.

(112) Striegel, A. M. Viscometric Detection in Size-Exclusion Chromatography: Principles and Select Applications. *Chromatographia* **2016**, *79* (15), 945-960.

(113) Grubisic, Z.; Rempp, P.; Benoit, H. A Universal Calibration for Gel Permeation Chromatography. *J. Polym. Sci. Pol. Phys.* **1996**, *34* (10), 1707-1713.

(114) Holdcroft, S. Determination of Molecular Weights and Mark–Houwink constants for Soluble Electronically Conducting Polymers. *J. Polym. Sci. Pol. Phys.* **1991**, *29* (13), 1585-1588.

(115) Zhao, H.; Brown, P. H.; Schuck, P. On the Distribution of Protein Refractive Index Increments. *Biophys J* **2011**, *100* (9), 2309-2317.

(116) Ji, L.; Liu, L.-Y.; Cho, M.; Karaaslan, M. A.; Renneckar, S. Revisiting the Molar Mass and Conformation of Derivatized Fractionated Softwood Kraft Lignin. *Biomacromolecules* **2022**, *23* (3), 708-719.

(117) What is the Mark-Houwink Equation - and How Do You Use it for Polymer Characterization? Malvern Panalytical: 2025.

(118) Wang, X.; Qiu, X.; Wu, C. Comparison of the Coil-to-Globule and the Globule-to-Coil Transitions of a Single Poly(N-isopropylacrylamide) Homopolymer Chain in Water. *Macromolecules* **1998**, *31* (9), 2972-2976.

(119) Taniguchi, K.; Kurioka, T.; Sato, K.; Tomita, I.; Inagi, S. Electrochemical Postfunctionalization of Thiophene–Fluorene Alternating Copolymers via Anodic C–H Phosphonylation. *Macromolecules* **2024**, *57* (10), 5028-5037.

(120) Jordan, R. S.; Wang, Y. 3D Printing of Conjugated Polymers. *J. Polym. Sci. Pol. Phys.* **2019**, *57* (23), 1592-1605.

(121) Kee, S.; Zhang, P.; Travas-Sejdic, J. Direct Writing of 3D Conjugated Polymer Micro/Nanostructures for Organic Electronics and Bioelectronics. *Polym. Chem.* **2020**, *11* (28), 4530-4541.

(122) Wang, M.; Baek, P.; Akbarinejad, A.; Barker, D.; Travas-Sejdic, J. Conjugated Polymers and Composites for Stretchable Organic Electronics. *J. Mater. Chem. C* **2019**, *7* (19), 5534-5552.

(123) Jang, S.; Zapata-Arteaga, O.; Villalva, D. R.; Ma, G.; Bates, A.; Sharma, A.; Emwas, A.-H.; Zhang, Y.; Han, J.; Gu, X.; Baran, D. Leveraging Solvent Affinity for Phase-Selective Doping to Enhance Doping Efficiency in a DPP-Based n-type Conjugated Polymer. *Materials Horizons* **2025**, *12* (16), 6322-6333, 10.1039/D4MH01805B.

(124) Bell, K.-J. J.; Sabury, S.; Phan, V.; Wagner, E. M.; Hawks, A. M.; Bartlett, K. A.; Collier, G. S. Synthesis of 1,4-Dihydropyrrolo[3,2-b]pyrrole-Containing Donor–Acceptor Copolymers and Their Optoelectronic Properties. *J. Polym. Sci.* **2024**, *62* (13), 2975-2987.

(125) Umar, A. R.; Dorris, A. L.; Kotadiya, N. B.; Giebink, N. C.; Collier, G. S.; Grieco, C. Probing Polaron Environment in a Doped Polymer via the Photoinduced Stark Effect. *J. Phys. Chem. C* **2023**, *127* (20), 9498-9508.

(126) Tang, K.; Shaw, A.; Upreti, S.; Zhao, H.; Wang, Y.; Mason, G. T.; Aguinaga, J.; Guo, K.; Patton, D.; Baran, D.; Rondeau-Gagné, S.; Gu, X. Impact of Sequential Chemical Doping on the Thin Film Mechanical Properties of Conjugated Polymers. *Chem. Mater.* **2025**, *37* (2), 756-765.

(127) Hailegnaw, B.; Adam, G.; Yohannes, T. Effect of Short Chain Iodoalkane Solvent Additives on Photovoltaic Performance of Poly(3-hexylthiophene) and Phenyl-C61-butyric Acid Methyl Ester Based Bulk Heterojunction Solar Cells. *Thin Solid Films* **2015**, *589*, 272-277.

(128) Wang, W.; Song, L.; Magerl, D.; Moseguí González, D.; Körstgens, V.; Philipp, M.; Moulin, J.-F.; Müller-Buschbaum, P. Influence of Solvent Additive 1,8-Octanedithiol on P3HT:PCBM Solar Cells. *Adv. Funct. Mater.* **2018**, *28* (20), 1800209.

(129) Dhar, J.; Venkatramaiah, N.; A, A.; Patil, S. Photophysical, Electrochemical and Solid State Properties of Diketopyrrolopyrrole Based Molecular Materials: Importance of the Donor Group. *J. Mater. Chem. C* **2014**, *2* (17), 3457-3466.

(130) Qu, S.; Ming, C.; Yao, Q.; Lu, W.; Zeng, K.; Shi, W.; Shi, X.; Uher, C.; Chen, L. Understanding the Intrinsic Carrier Transport in Highly Oriented Poly(3-hexylthiophene): Effect of Side Chain Regioregularity. *Polymers - Basel* **2018**, *10* (8), 815.

Appendices

Appendix A. Supplementary Information for Chapter 2

A.1. ^{1}H and ^{13}C NMR of Comonomers

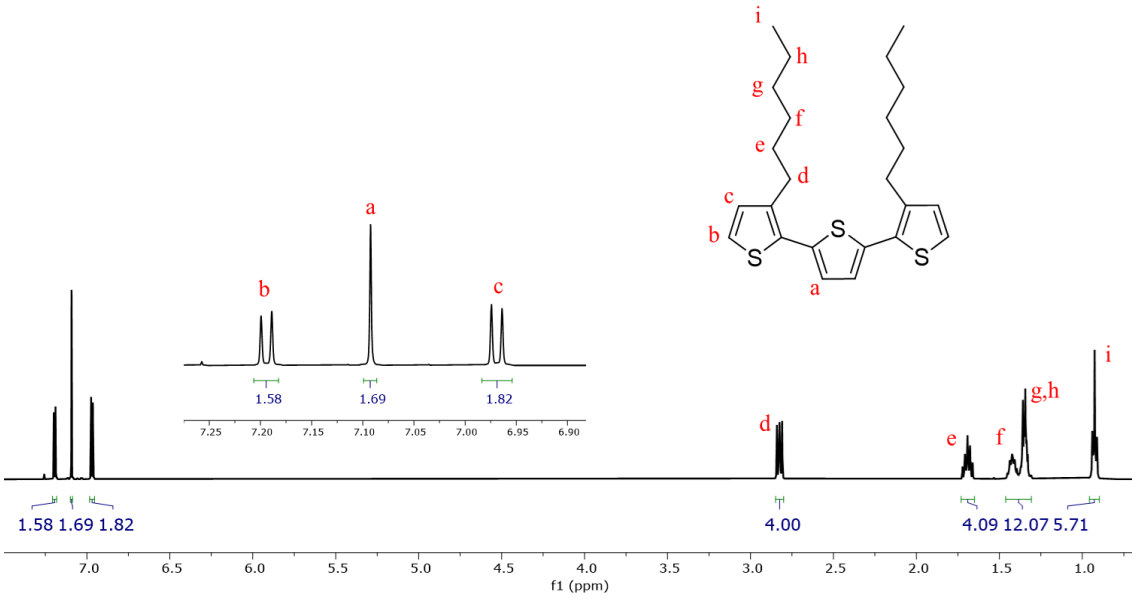

Figure A.1. ^{1}H NMR spectrum of 3,3”-dihexyl-2,2’:5’,2”-terthiophene (M3) in $CDCl_3$ with the inset highlighting. the aromatic region.

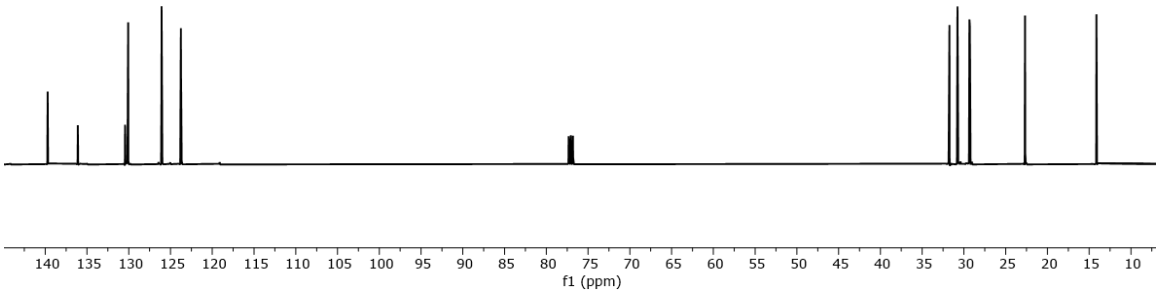

Figure A.2. ^{13}C NMR spectrum of 3,3"-dihexyl-2,2':5',2"-terthiophene (M3) in $CDCl_3$.

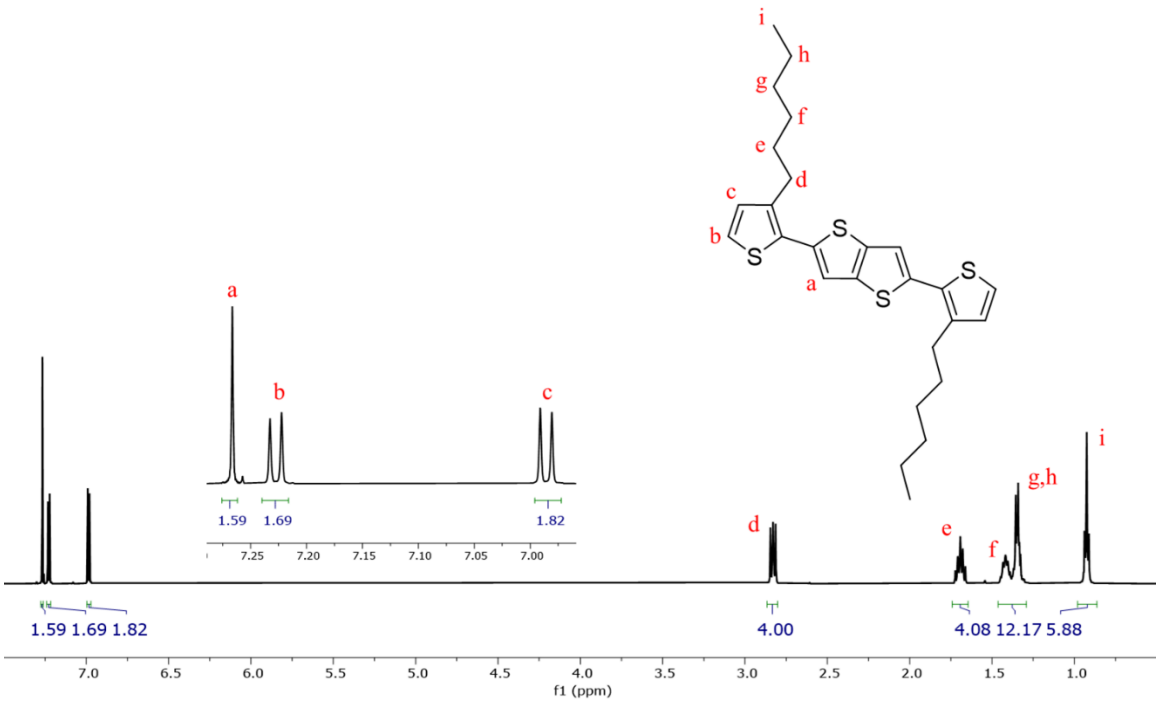

Figure A.3. ^{1}H NMR spectrum of 2,5-bis(3-hexylthiophen-2-yl)thieno[3,2-*b*]thiophene (**M4**) in $CDCl_3$ with the inset highlighting the aromatic region.

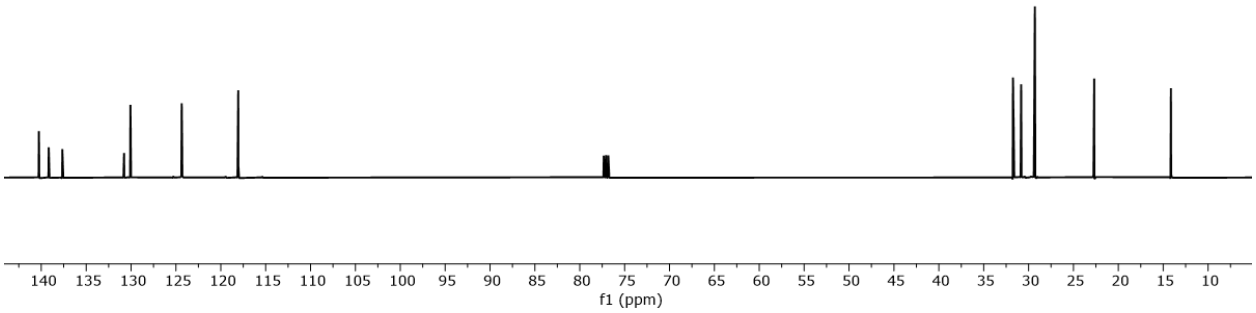

Figure A.4. ^{13}C NMR spectrum of 2,5-bis(3-hexylthiophen-2-yl)thieno[3,2-b]thiophene (**M4**) in $CDCl_3$.

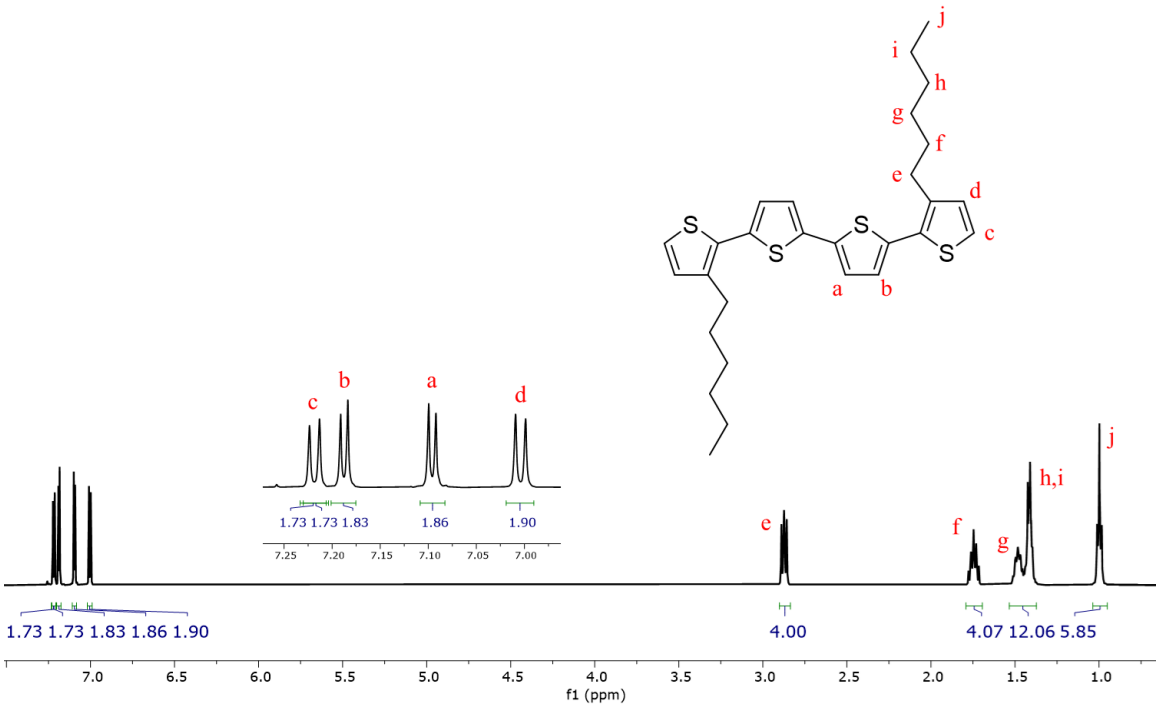

Figure A.5. ^{1}H NMR spectra of 3,3'''-dihexyl-2,2':5',2'':5'',2'''-quaterthiophene (**M5**) in $CDCl_3$ with the inset highlighting the aromatic region.

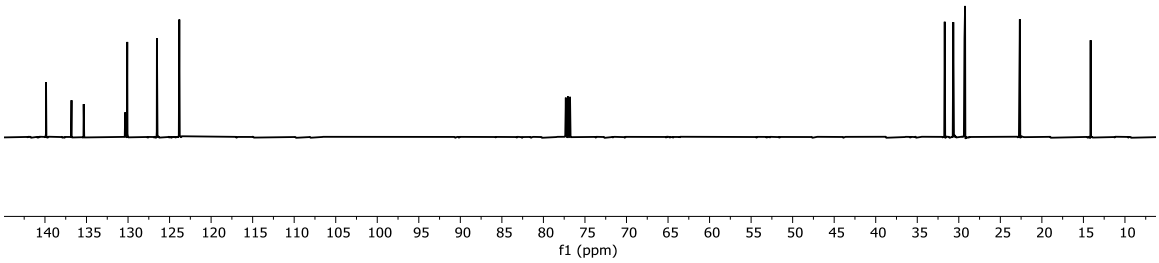

Figure A.6. ^{13}C NMR spectrum of 3,3'''-dihexyl-2,2':5',2'':5'',2'''-quaterthiophene (**M5**) in $CDCl_3$.

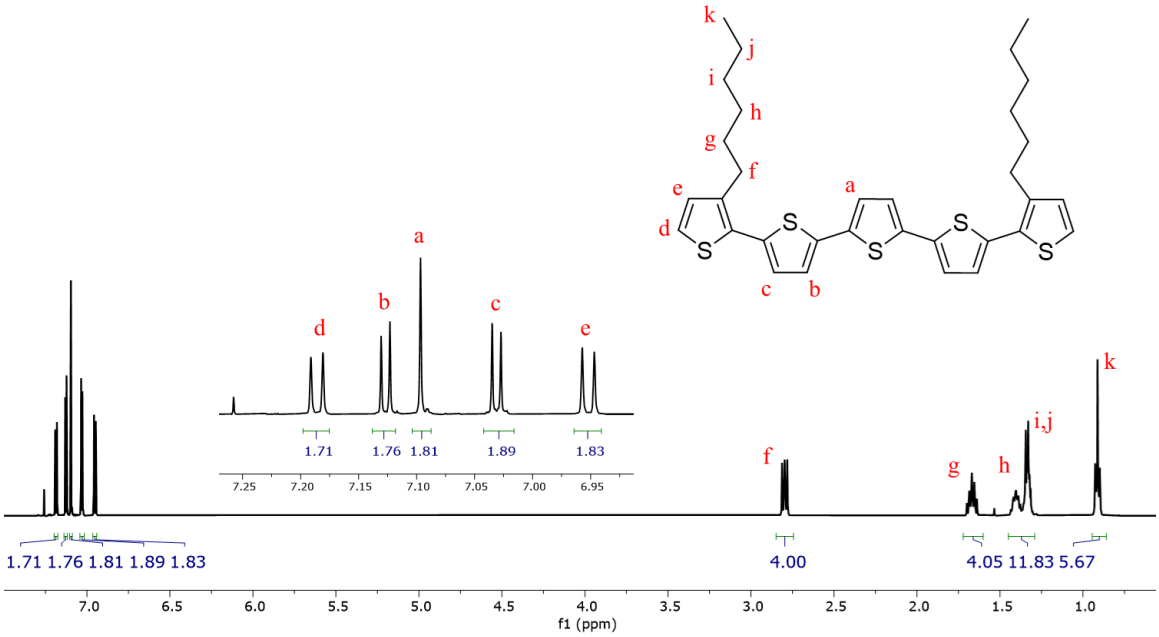

Figure A.7. ^{1}H NMR spectrum of 3,3""-dihexyl-2,2':5',2":5",2"':5"',2""-quinquethiophene (**M6**) in $CDCl_3$ with the inset highlighting the aromatic region.

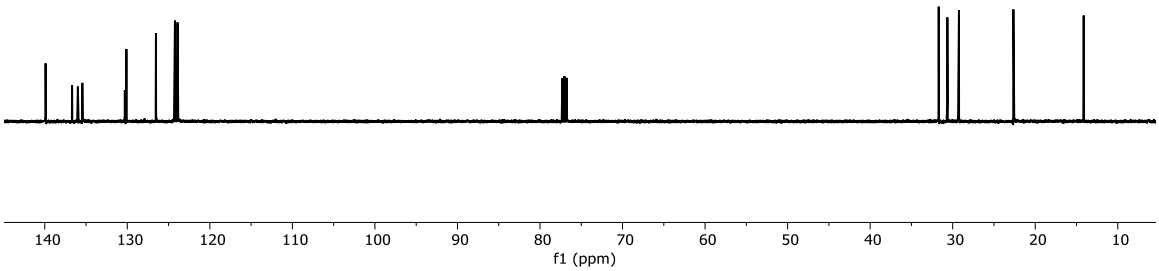

Figure A.8. ^{13}C NMR spectrum of 3,3""-dihexyl-2,2':5',2":5",2"':5"',2""-quinquethiophene (**M6**) in $CDCl_3$.

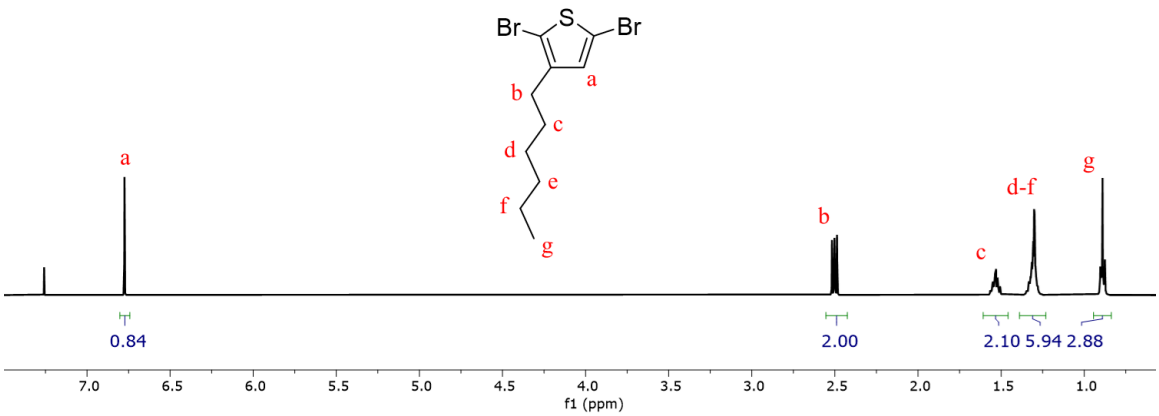

Figure A.9. ^{1}H NMR spectrum of 2,5-dibromo-3-hexylthiophene in $CDCl_3$.

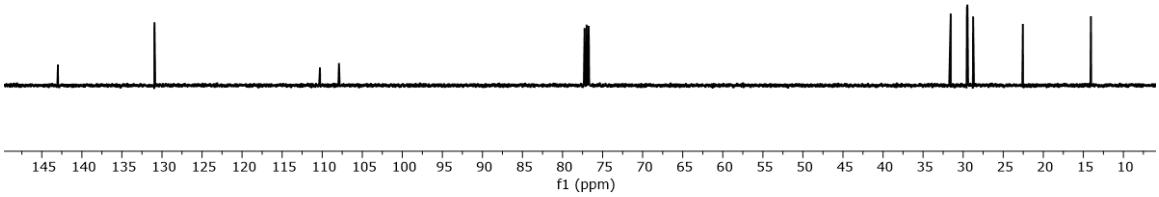

Figure A.10. ^{13}C NMR spectrum of 2,5-dibromo-3-hexylthiophene in $CDCl_3$.

A.2. ^{1}H NMR Spectra of Synthesized Polymers and Copolymers

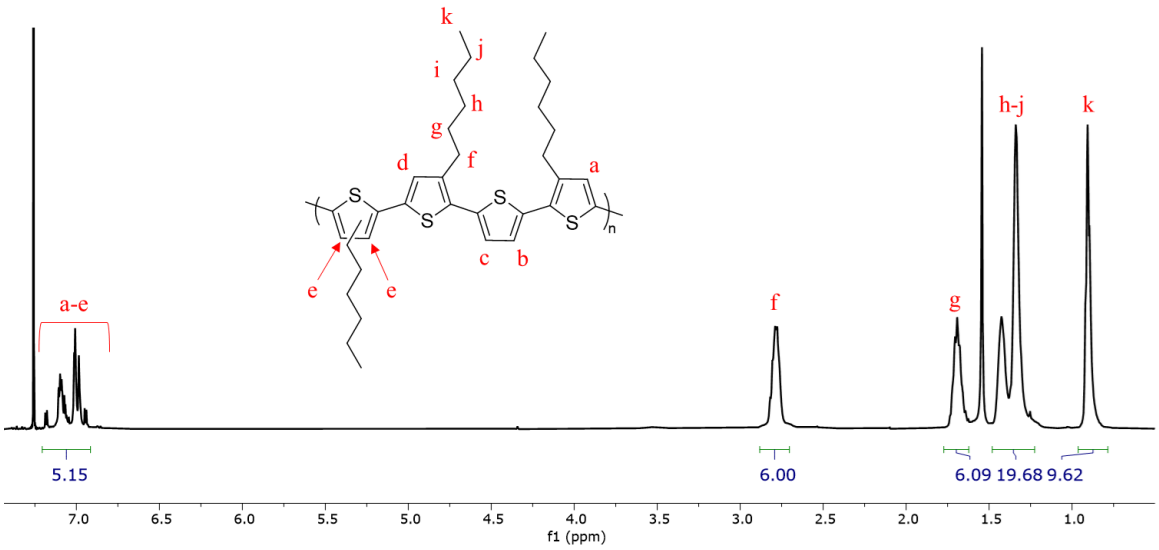

Figure A.11. ^{1}H NMR spectrum of poly(3,3"',4"'-trihexyl-2,2':5',2":5",2"'-quaterthiophene) (**P3**) in $CDCl_3$.

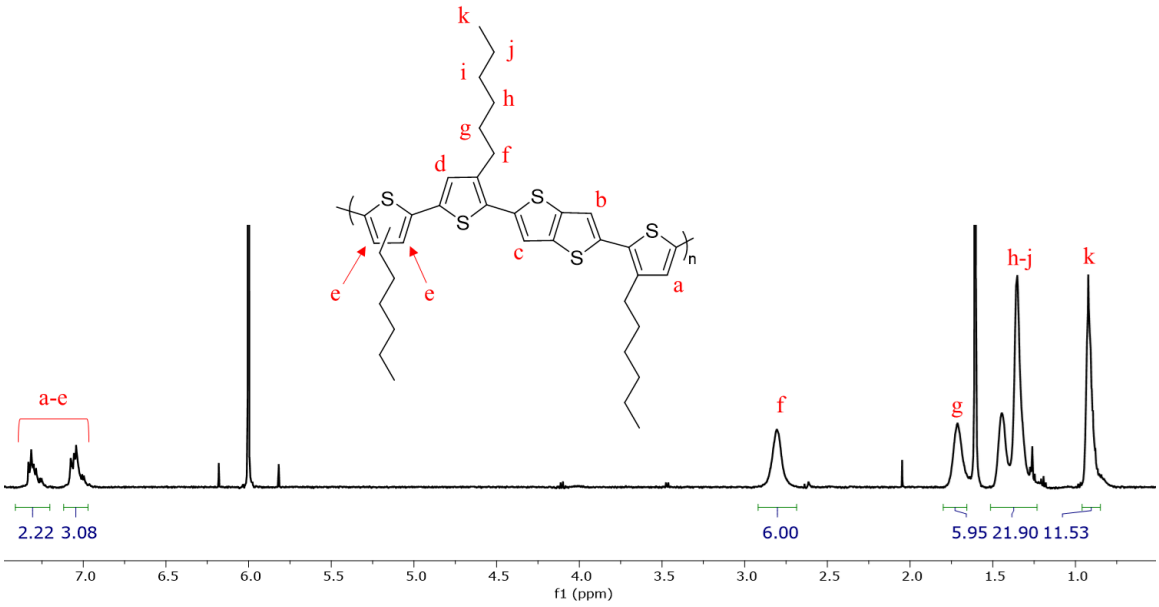

Figure A.12. ^{1}H NMR spectrum of poly(2-(4,4'-dihexyl-[2,2'-bithiophen]-5-yl)-5-(3-hexyl-thiophen-2-yl)thieno[3,2-*b*]thiophene) (**P4**) in $C_2D_2Cl_4$.

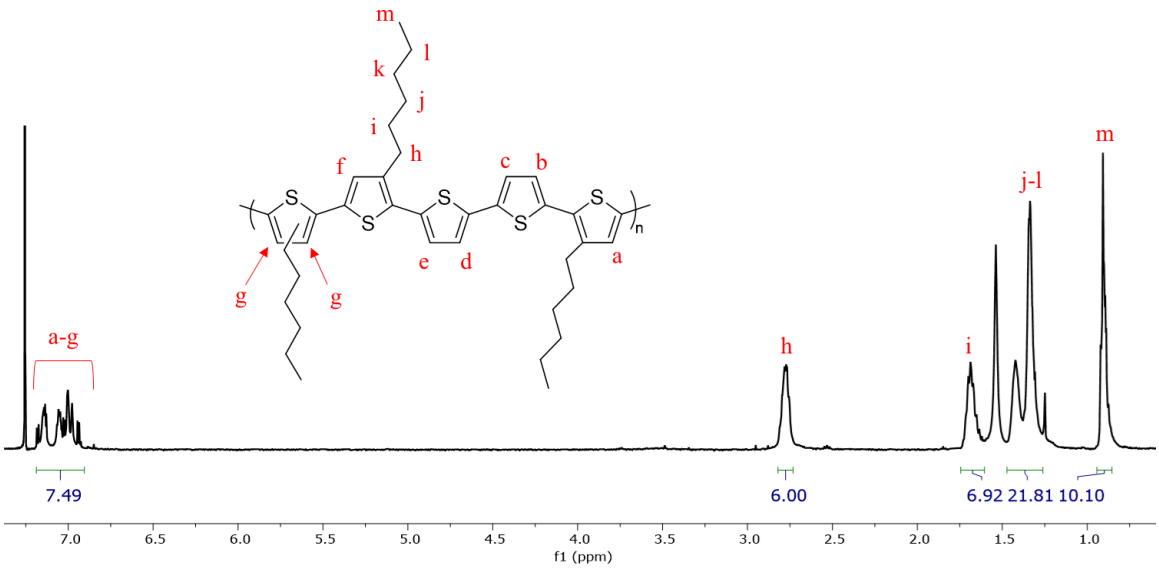

Figure A.13. ^{1}H NMR spectrum of poly(3,3'''',4''''-trihexyl-2,2':5',2'':5'',2''':5''',2'''' quinque-thiophene) (**P5**) in $CDCl_3$.

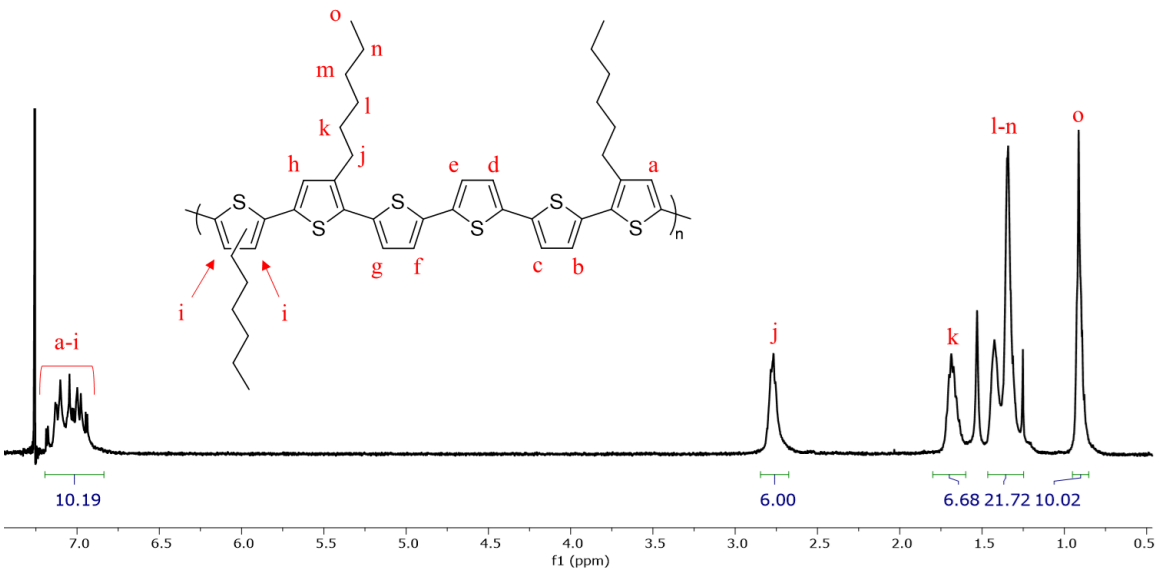

Figure A.14. [1]H NMR spectrum of poly(3,3"",4""-trihexyl-2,2':5',2":5",2"':5"',2"":5"",2""'-sexi-thiophene) (**P6**) in $CDCl_3$. Note the high integration for the aromatic peak is attributed to the regio-irregularity of the polymer as described by Qu et al.[130]

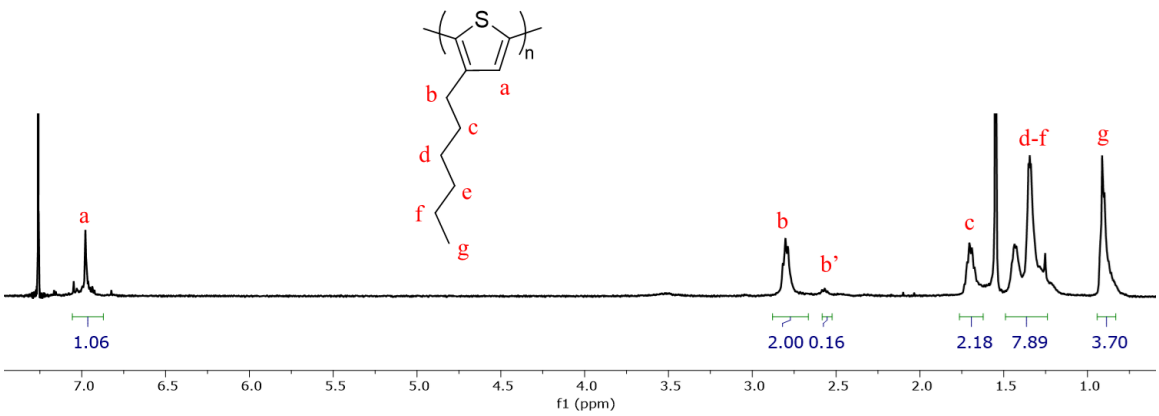

Figure A.15. [1]H NMR spectrum of poly(3-hexylthiophene) (AB) (**P3HT (AB)**) in $CDCl_3$. Peaks at 2.8 ppm (labeled b) and 2.6 ppm (labeled b') are used to compute the regioregularity, which is found to be 93%.

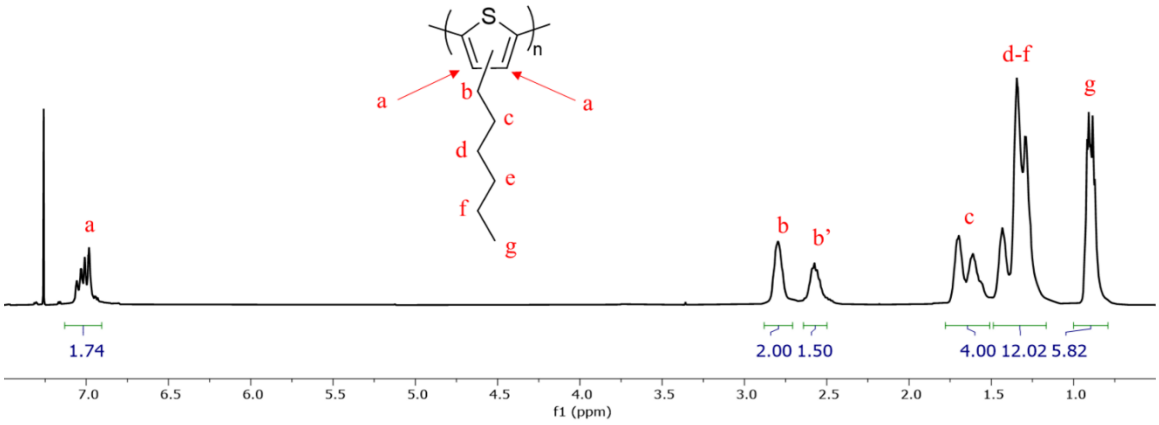

Figure A.16. ^{1}H NMR spectrum of poly(3-hexylthiophene) (AA+BB) (**P3HT (AA+BB)**) in $CDCl_3$. Peaks at 2.8 ppm (labeled b) and 2.6 ppm (labeled b') are used to compute the regioregularity, which is found to be 57%. Note the high integration for the aromatic peak is attributed to the regio-irregularity of the polymer as described by Qu et al.[130]

A.3. Polymer and Copolymer Characterizations

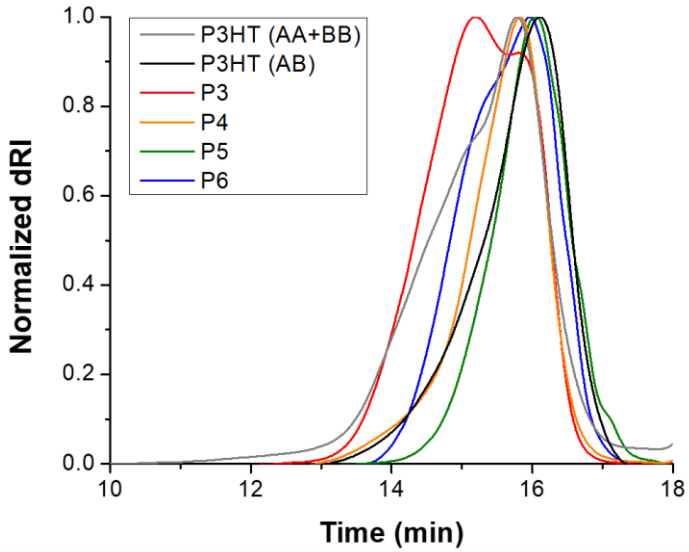

Figure A.17. GPC traces of **P3HT (AA+BB)**, **P3HT (AB)**, **P3**, **P4**, **P5**, and **P6** acquired using THF as the mobile phase at a flow rate of 1 mL/min.

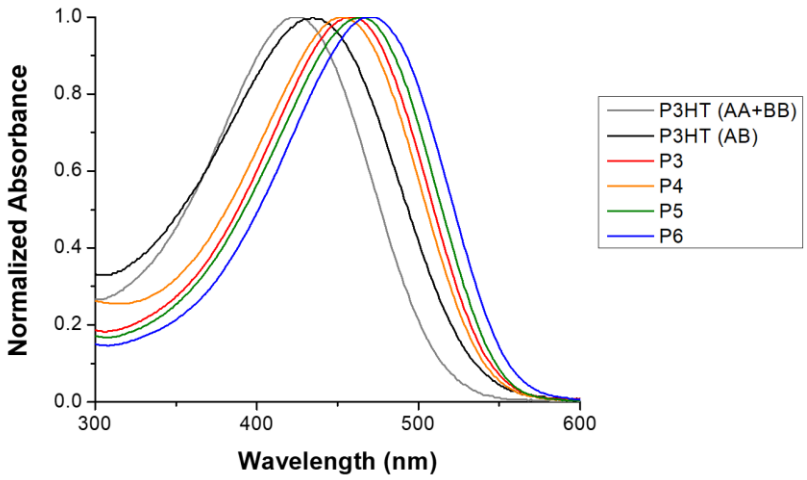

Figure A.18. Absorbance spectra of **P3HT (AA+BB)**, **P3HT (AB)**, **P3**, **P4**, **P5**, and **P6** in $CHCl_3$ (<1 mg/mL). Spectra are normalized by the absorbance measured at λ_{max} for each polymer/copolymer. A red-shift is observed as the spacing length of the expanded core increases.

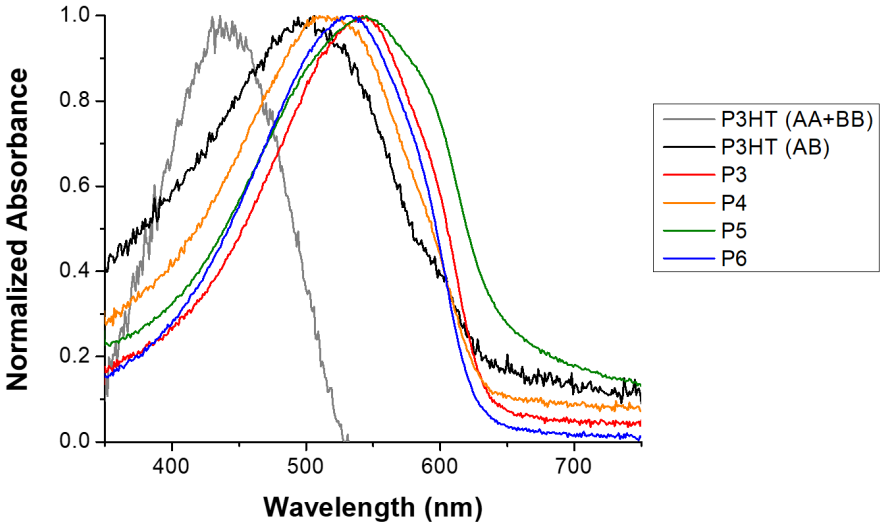

Figure A.19. Absorbance spectra of **P3HT (AA+BB)**, **P3HT (AB)**, **P3**, **P4**, **P5**, and **P6** thin films. Spectra are normalized by the absorbance measured at λ_{max}. Thin films were made by spin casting from chlorobenzene (at 2 mg/mL), and thicknesses range from 10-16 nm. A red-shift is observed compared to solution measurements and red-shifts are also observed as the spacing length increases.

Table A.1. Observed solubility of each polymer or copolymer in various solvents at a concentration of 1 mg/mL. A score of 0 indicates not soluble while a score of 1 indicates soluble.

Solvent	P3	P4	P5	P6	P3HT (AB)	P3HT (AA+BB)
Acetone	0	0	0	0	0	0
Acetonitrile	0	0	0	0	0	0
Benzene	1	1	1	1	1	1
Chloroform	1	1	1	1	1	1
Chlorobenzene	1	1	1	1	1	1
Diethyl Ether	0	0	0	0	0	0
Dimethyl Sulfoxide (DMSO)	0	0	0	0	0	0
Ethyl Acetate	0	0	0	0	0	0
Hexanes	0	0	0	0	0	1
Methanol	0	0	0	0	0	0
Methylene Chloride	1	0	1	0	1	1
N,N-Dimethyl Acetamide	0	0	0	0	0	0
N,N-Dimethyl Formamide (DMF)	0	0	0	0	0	0
2-Propanol	0	0	0	0	0	0
Tetrahydrofuran (THF)	1	1	1	1	1	1
Toluene	1	1	1	1	1	1
1,2-dichloroethane	0	0	0	0	1	1
1,1,2,2-tetrachloroethane	1	1	1	1	1	1
25:75 Hexanes:Chlorobenzene	1	1	1	1	1	1
40:60 Hexanes:Chlorobenzene	1	1	1	0	1	1
50:50 Hexanes:Chlorobenzene	1	1	1	0	1	1
60:40 Hexanes:Chlorobenzene	1	0	0	0	1	1
75:25 Hexanes:Chlorobenzene	0	0	0	0	1	1

A.4. AFM Characterization of Solution-Doped Thin Films

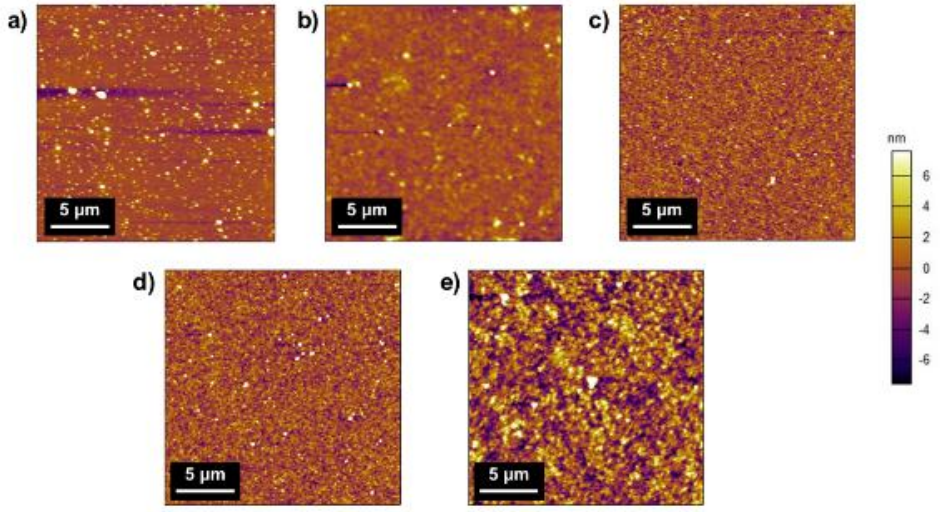

Figure A.20. Representative AFM height images of **P3** thin films solution-doped at a) 0 mol%, b) 6 mol%, c) 10 mol%, d) 17 mol%, and e) 23 mol% F4TCNQ. Each image was obtained in tapping mode over an area of 20 µm × 20 µm.

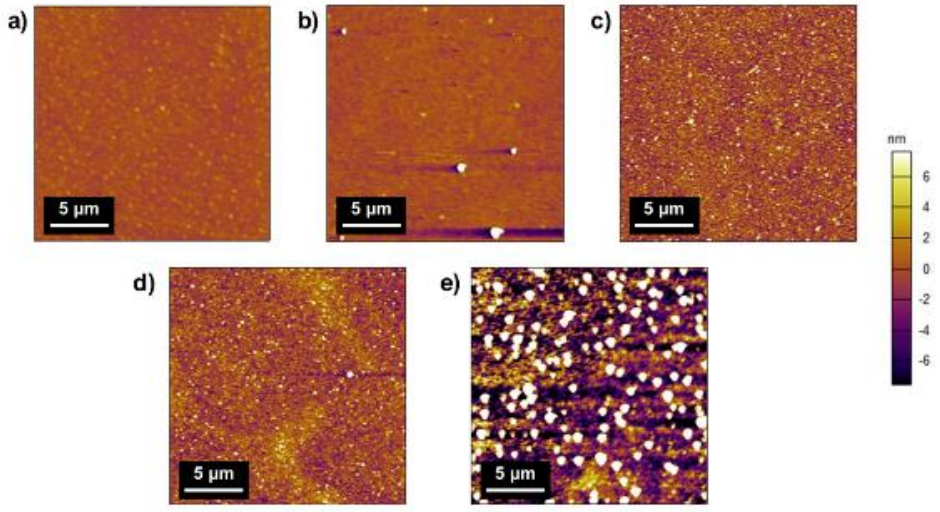

Figure A.21. Representative AFM height images of **P4** thin films solution-doped at a) 0 mol%, b) 6 mol%, c) 10 mol%, d) 17 mol%, and e) 23 mol% F4TCNQ. Each image was obtained in tapping mode over an area of 20 µm × 20 µm.

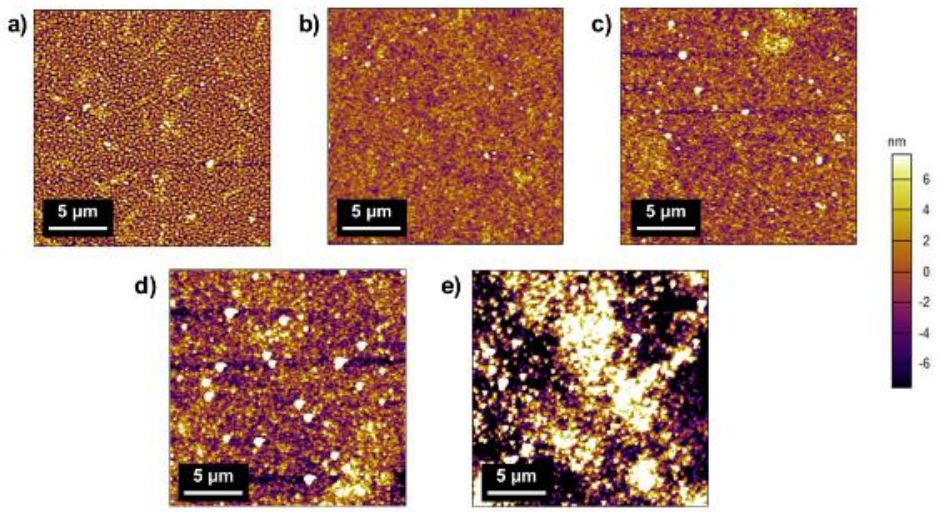

Figure A.22. Representative AFM height images of **P5** thin films solution-doped at a) 0 mol%, b) 6 mol%, c) 10 mol%, d) 17 mol%, and e) 23 mol% F4TCNQ. Each image was obtained in tapping mode over an area of 20 µm × 20 µm.

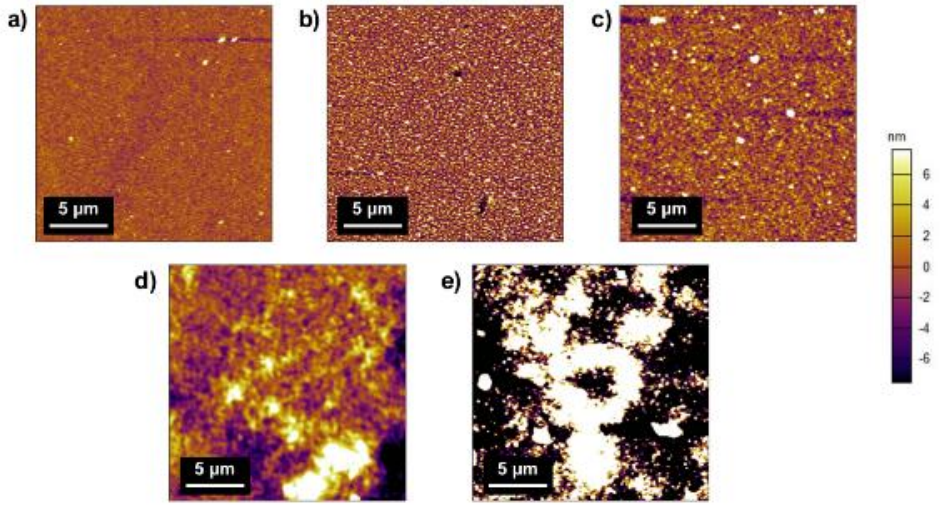

Figure A.23. Representative AFM height images of **P6** thin films solution-doped at a) 0 mol%, b) 6 mol%, c) 10 mol%, d) 17 mol%, and e) 23 mol% F4TCNQ. Each image was obtained in tapping mode over an area of 20 µm × 20 µm.

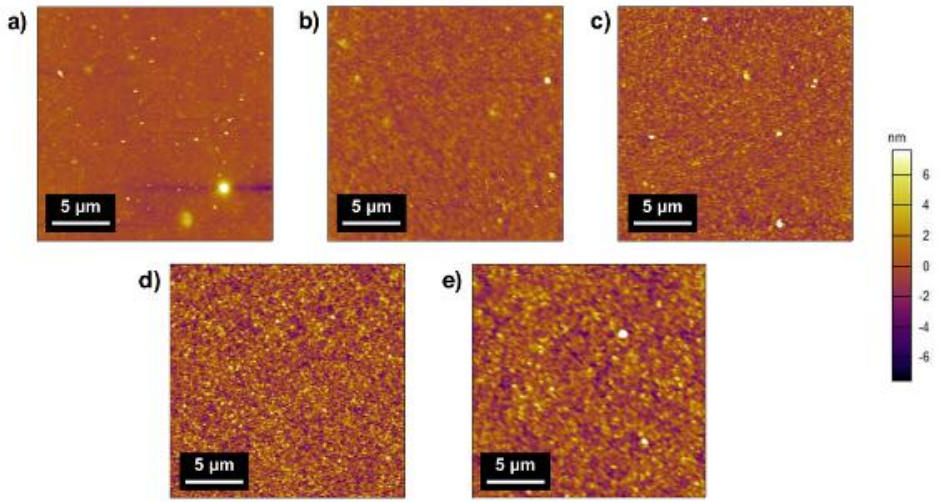

Figure A.24. Representative AFM height images of **P3HT (AB)** thin films solution-doped at a) 0 mol%, b) 6 mol%, c) 10 mol%, d) 17 mol%, and e) 23 mol% F4TCNQ. Each image was obtained in tapping mode over an area of 20 µm × 20 µm.

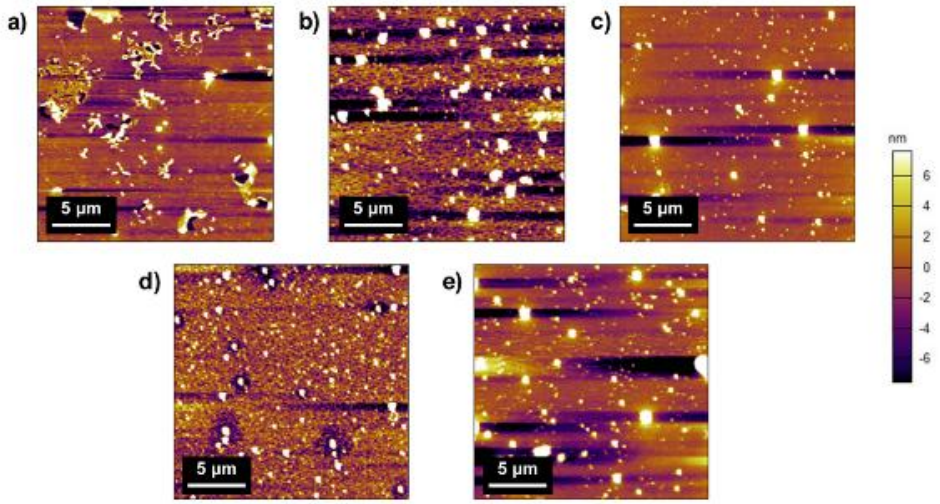

Figure A.25. Representative AFM height images of **P3HT (AA+BB)** thin films solution-doped at a) 0 mol%, b) 6 mol%, c) 10 mol%, d) 17 mol%, and e) 23 mol% F4TCNQ. Each image was obtained in tapping mode over an area of 20 µm × 20 µm.

Table A.2. Film thicknesses of solution-doped thin films as a function of doping level, as determined from AFM scratch tests.

	Film Thickness (nm)				
Polymer	**0 mol%**	**6 mol%**	**10 mol%**	**17 mol%**	**23 mol%**
P3	14.9 ± 4.0	14.6 ± 3.8	16.9 ± 3.9	20.5 ± 3.0	17.9 ± 2.4
P4	10.1 ± 2.5	14.0 ± 4.4	13.6 ± 2.5	15.4 ± 5.3	13.4 ± 4.5
P5	11.0 ± 2.1	22.1 ± 8.3	23.5 ± 9.3	16.4 ± 5.6	16.1 ± 4.2
P6	10.0 ± 2.4	10.6 ± 3.2	12.1 ± 3.0	12.1 ± 3.0	11.9 ± 3.1
P3HT (AB)	11.8 ± 4.3	14.3 ± 8.7	15.8 ± 4.8	19.5 ± 7.8	16.4 ± 1.4
P3HT (AA+BB)	16.0 ± 0.7	9.2 ± 1.6	14.6 ± 4.1	13.1 ± 1.9	10.9 ± 4.2

A.5. UV-Vis-NIR Characterization of Solution-Doped Thin Films

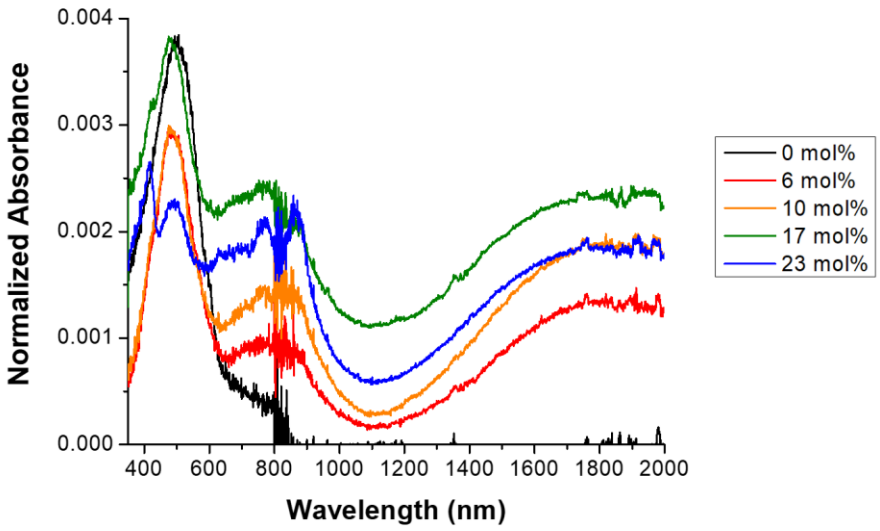

Figure A.26. UV-Vis-NIR spectra of solution-doped **P3HT (AB)** thin films. The absorbance is normalized by film thickness, and thicknesses range from 11 to 20 nm.

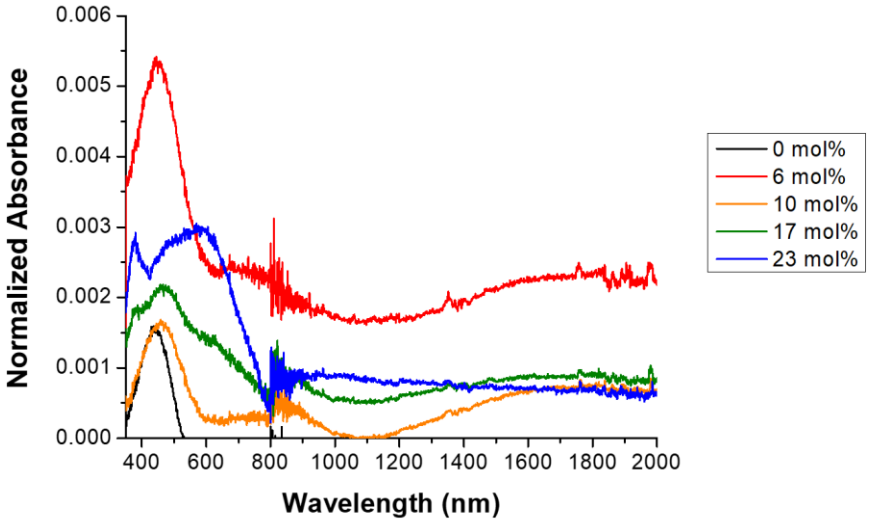

Figure A.27. UV-Vis-NIR spectra of solution-doped **P3HT (AA+BB)** thin films. The absorbance is normalized by film thickness, and thicknesses range from 9 to 16 nm.

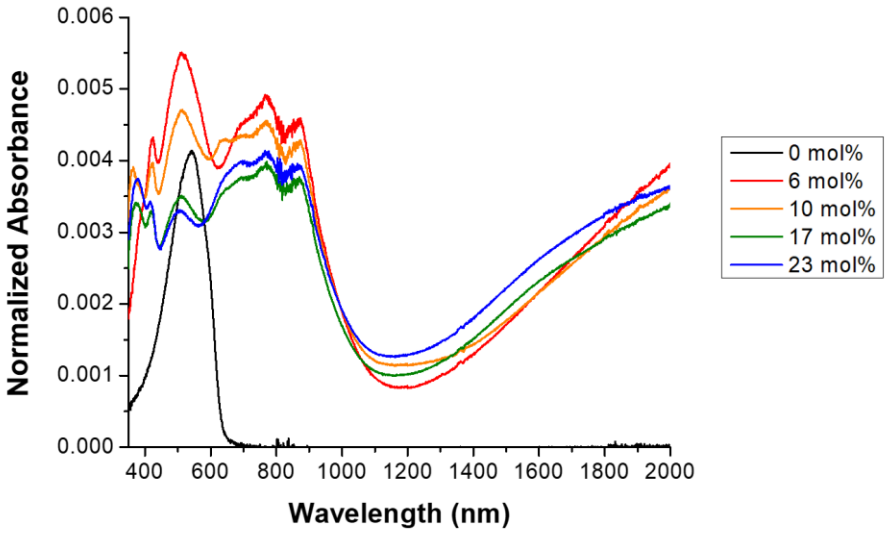

Figure A.28. UV-Vis-NIR spectra of solution-doped **P3** thin films. The absorbance is normalized by film thickness, and thicknesses range from 14 to 21 nm.

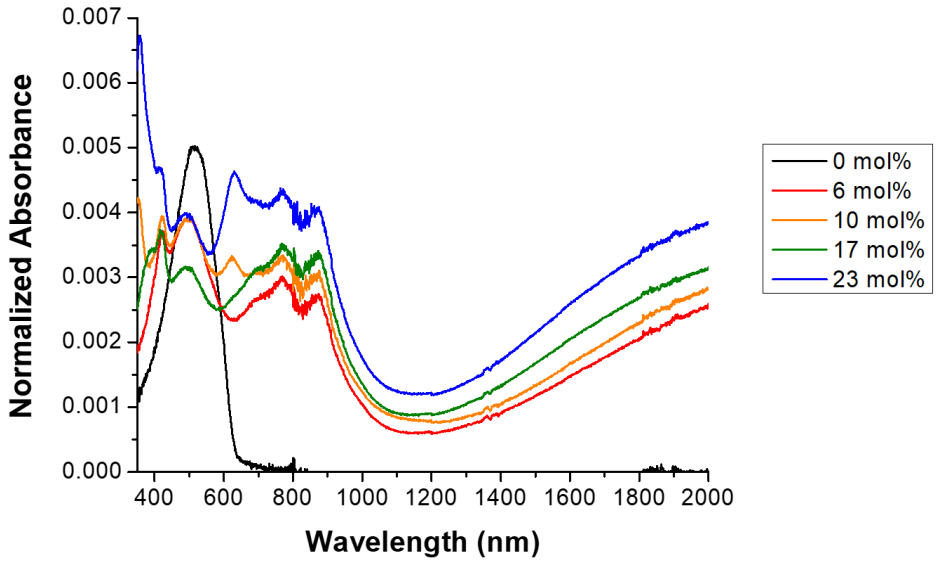

Figure A.29. UV-Vis-NIR spectra of solution-doped **P4** thin films. The absorbance is normalized by film thickness, and thicknesses range from 10 to 16 nm.

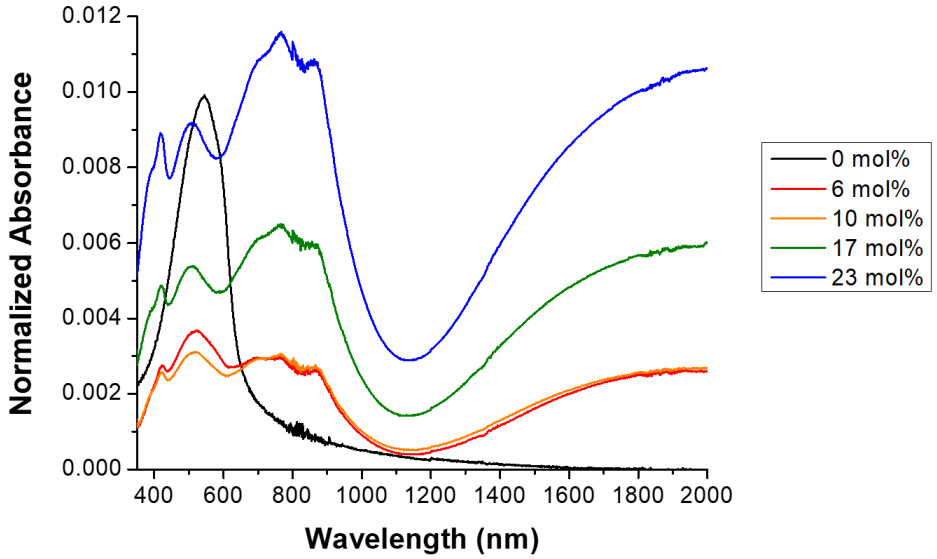

Figure A.30. UV-Vis-NIR spectra of solution-doped **P5** thin films. The absorbance is normalized by film thickness, and thicknesses range from 11 to 24 nm.

A.6. AFM Characterization of Sequentially-Doped Thin Films

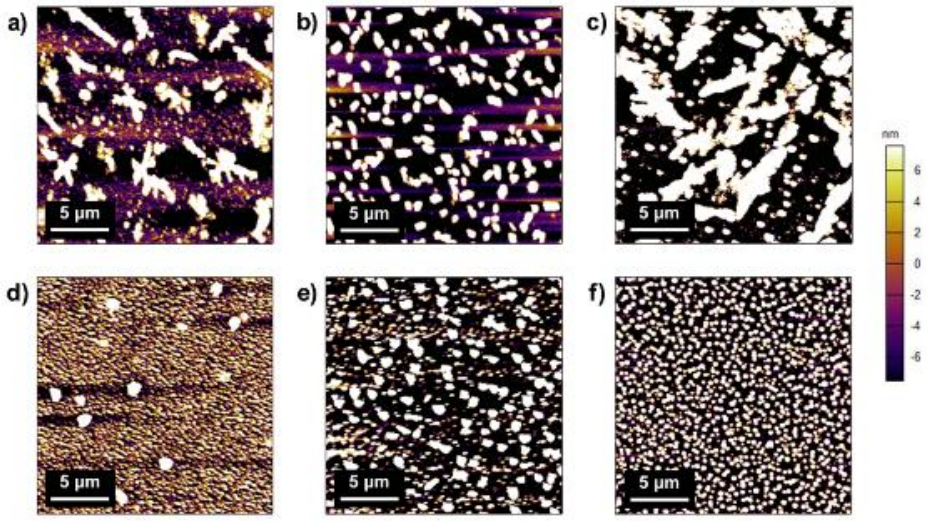

Figure A.31. Representative AFM height images of **P3** thin films sequentially-doped with F4TCNQ dissolved at 1 mg/mL in a) THF, b) DCM, c) 50:50 acetone:DCM, d) 75:25 acetone:DCM, e) acetone and f) DMF. Each image was obtained in tapping mode over an area of 20 µm × 20 µm.

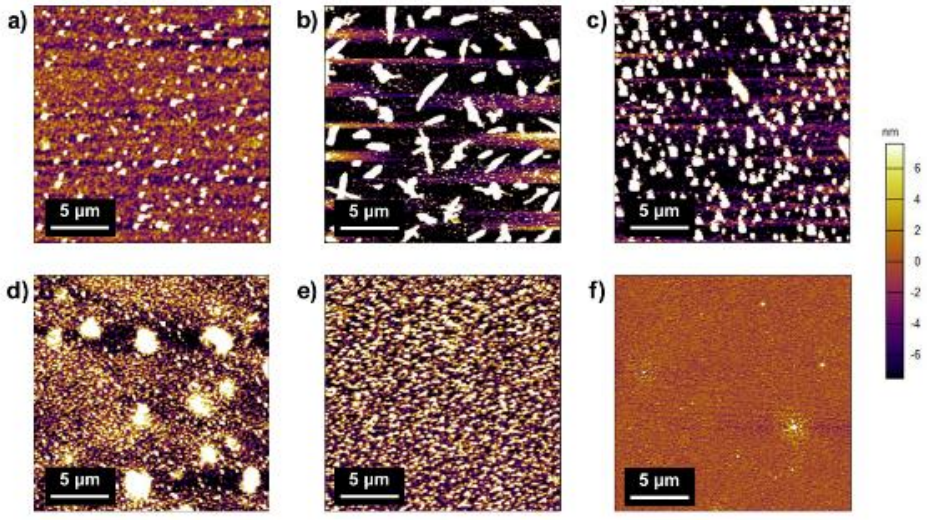

Figure A.32. Representative AFM height images of **P4** thin films sequentially-doped with F4TCNQ dissolved at 1 mg/mL in a) THF, b) DCM, c) 50:50 acetone:DCM, d) 75:25 acetone:DCM, e) acetone and f) DMF. Each image was obtained in tapping mode over an area of 20 µm × 20 µm.

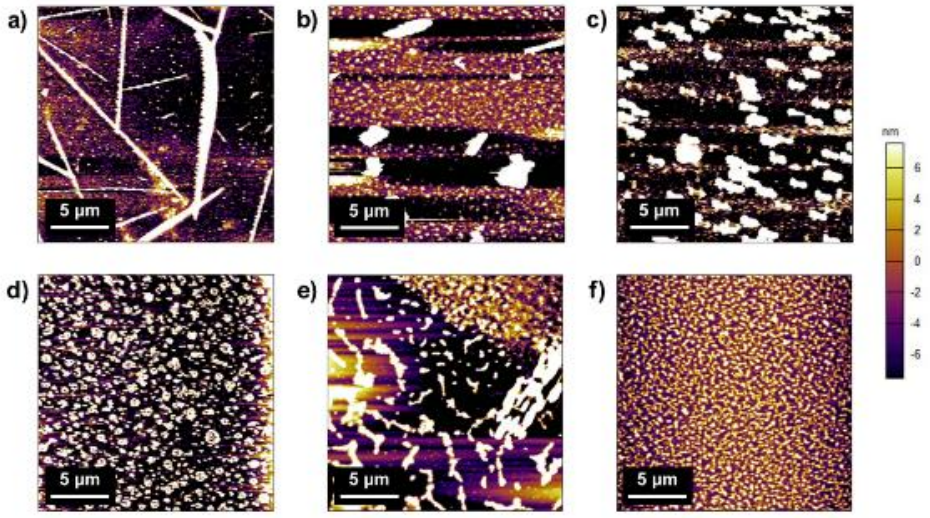

Figure A.33. Representative AFM height images of **P5** thin films sequentially-doped with F4TCNQ dissolved at 1 mg/mL in a) THF, b) DCM, c) 50:50 acetone:DCM, d) 75:25 acetone:DCM, e) acetone and f) DMF. Each image was obtained in tapping mode over area of 20 µm × 20 µm.

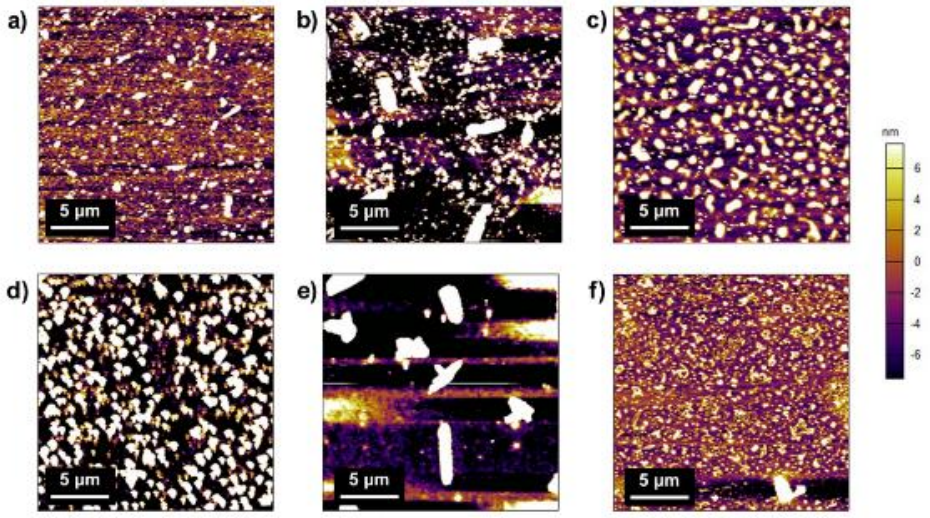

Figure A.34. Representative AFM height images of **P6** thin films sequentially-doped with F4TCNQ dissolved at 1 mg/mL in a) THF, b) DCM, c) 50:50 acetone:DCM, d) 75:25 acetone:DCM, e) acetone and f) DMF. Each image was obtained in tapping mode over an area of 20 × 20 µm.

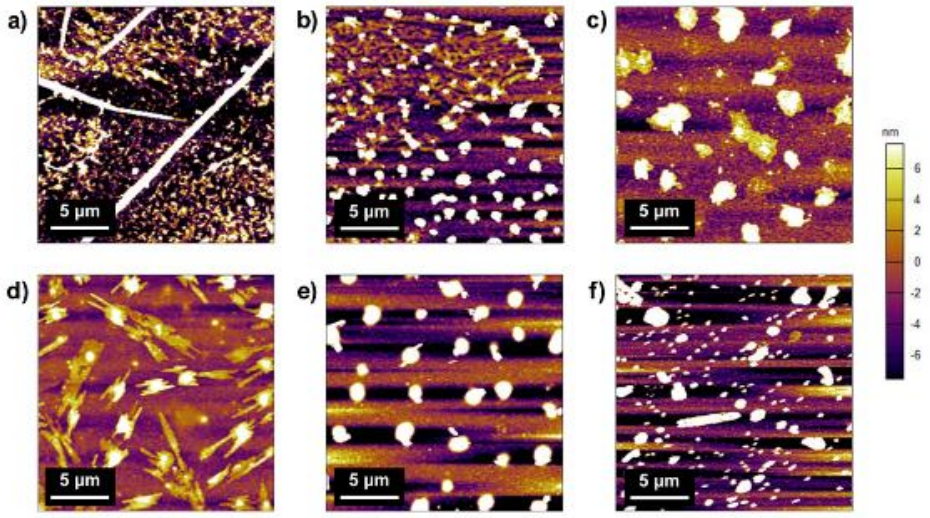

Figure A.35. Representative AFM height images of **P3HT (AB)** thin films sequentially-doped with F4TCNQ dissolved at 1 mg/mL in a) THF, b) DCM, c) 50:50 acetone:DCM, d) 75:25 acetone:DCM, e) acetone and f) DMF. Each image was obtained in tapping mode over an area of 20 µm × 20 µm.

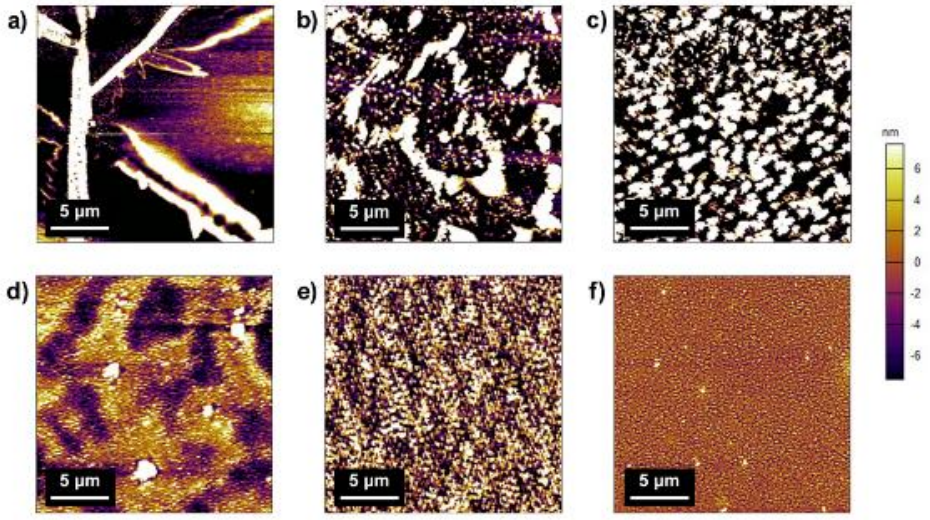

Figure A.36. Representative AFM height images of **P3HT (AA+BB)** thin films sequentially-doped with F4TCNQ dissolved at 1 mg/mL in a) THF, b) DCM, c) 50:50 acetone:DCM, d) 75:25 acetone:DCM, e) acetone and f) DMF. Each image was obtained in tapping mode over an area of 20 µm × 20 µm.

As mentioned in *Chapter 2*, the surface roughnesses of sequentially-doped films shown in Table 2.6 are high and display high variation. This is attributed to excess dopant on the surface of the polymer film. It should be noted that these aggregates of excess F4TCNQ do not contribute to the film thicknesses reported in Table A.3. Rather, film thickness is defined as the height difference between the polymer film and glass substrate; and care was taken to avoid aggregates during this measurement to prevent overestimation of film thickness. As a result and as seen in some cases, surface roughnesses measured for the sequentially-doped thin films are greater than or equal to the film thickness.

Table A.3. Film thicknesses of sequentially-doped thin films obtained from AFM scratch tests.

	Film Thickness (nm)					
Polymer	**THF**	**DCM**	**50:50 Act:DCM**	**75:25 Act:DCM**	**Acetone**	**DMF**
P3	16.2 ± 4.1	14.9 ± 4.8	27.6 ± 8.0	17.4 ± 5.4	16.6 ± 2.8	16.7 ± 7.2
P4	9.8 ± 4.0	14.7 ± 8.0	17.6 ± 6.6	12.4 ± 3.5	18.8 ± 3.7	9.6 ± 4.9
P5	8.5 ± 3.4	21.6 ± 9.5	14.2 ± 7.7	17.5 ± 6.7	17.2 ± 4.6	12.0 ± 3.5
P6	14.5 ± 4.7	24.9 ± 5.7	14.7 ± 6.3	29.0 ± 11.9	15.9 ± 5.4	20.2 ± 8.0
P3HT (AB)	14.0 ± 3.2	12.3 ± 2.2	16.8 ± 5.6	14.4 ± 6.1	10.1 ± 4.7	10.2 ± 5.3
P3HT (AA+BB)	23.9 ± 7.8	17.1 ± 7.2	14.2 ± 2.9	19.7 ± 8.0	17.5 ± 4.4	10.9 ± 2.9

A.7. UV-Vis-NIR Characterization of Sequentially-Doped Thin Films

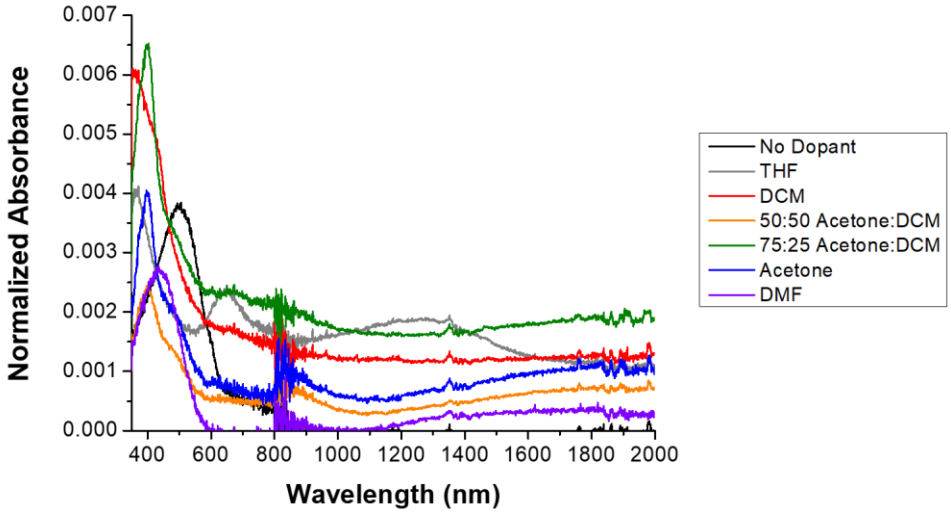

Figure A.37. UV-Vis-NIR spectra of sequentially-doped **P3HT (AB)** thin films. The absorbance is normalized by film thickness, and thicknesses range from 10 to 17 nm. All films were doped using solutions at 1 mg F4TCNQ /mL.

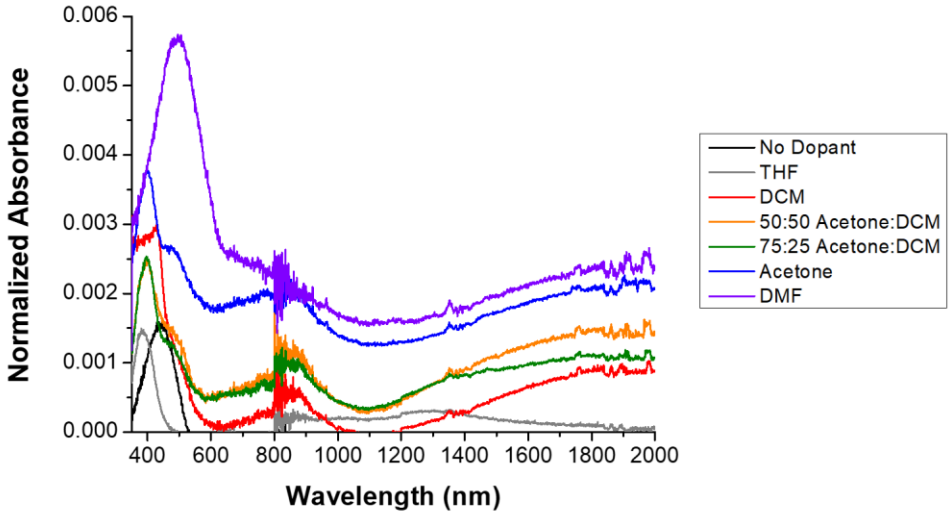

Figure A.38. UV-Vis-NIR spectra of sequentially-doped **P3HT (AA+BB)** thin films. The absorbance is normalized by film thickness, and thicknesses range from 10 to 24 nm. All films were doped using solutions at 1 mg F4TCNQ /mL.

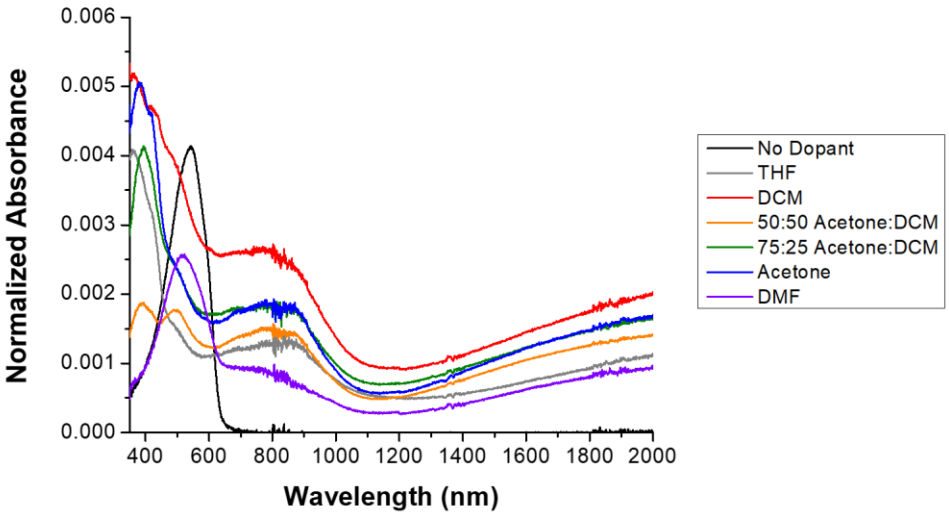

Figure A.39. UV-Vis-NIR spectra of sequentially-doped **P3** thin films. The absorbance is normalized by film thickness, and thicknesses range from 14 to 28 nm. All films were doped using solutions at 1 mg F4TCNQ /mL

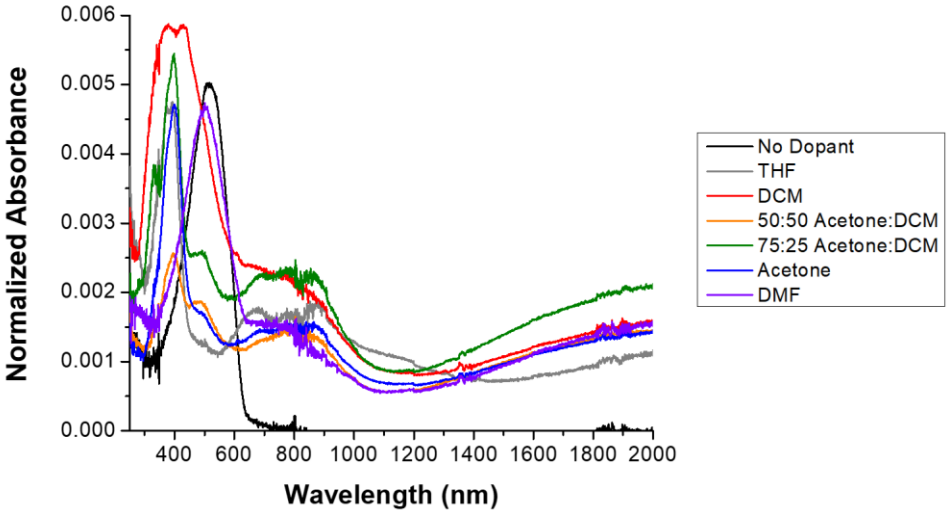

Figure A.40. UV-Vis-NIR spectra of sequentially-doped **P4** thin films. The absorbance is normalized by film thickness, and thicknesses range from 9 to 19 nm. All films were doped using solutions at 1 mg F4TCNQ /mL.

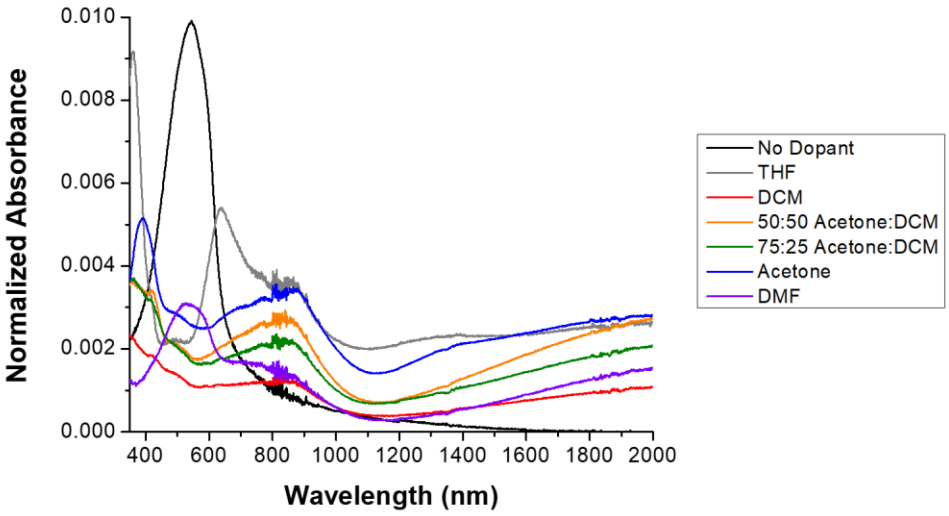

Figure A.41. UV-Vis-NIR spectra of sequentially-doped **P5** thin films. The absorbance is normalized by film thickness, and thicknesses range from 8 to 22 nm. All films were doped using solutions at 1 mg F4TCNQ /mL.

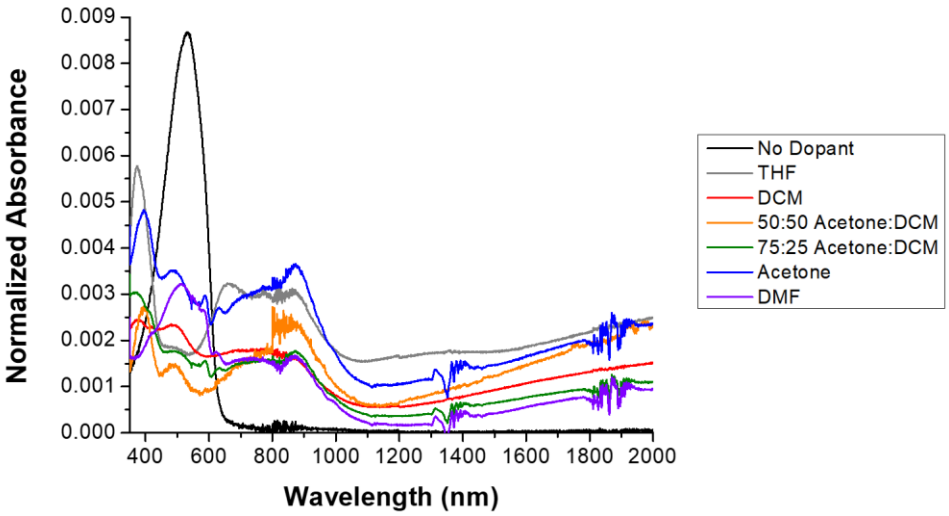

Figure A.42. UV-Vis-NIR spectra of sequentially-doped **P6** thin films. The absorbance is normalized by film thickness, and thicknesses range from 14 to 29 nm. All films were doped using solutions at 1 mg F4TCNQ /mL.

Appendix B. Supplementary Information for Chapter 3

B.1. ^{1}H NMR Spectra of P3HT and Expanded Core Copolymers

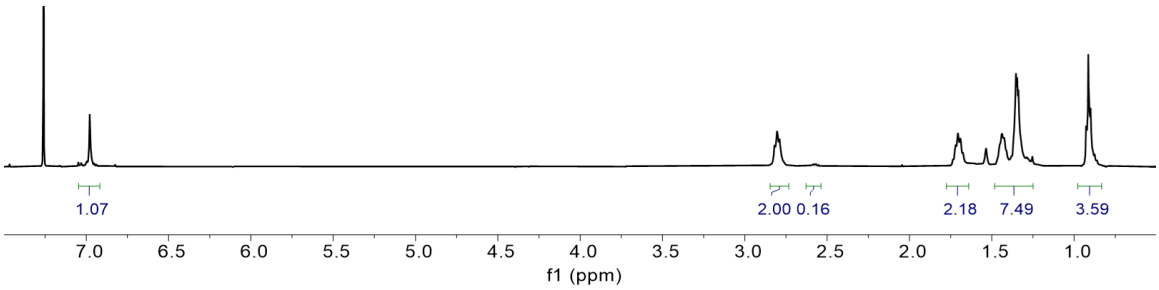

Figure B.1. ^{1}H NMR spectra of poly(3-hexylthiophene) (**P3HT**) in $CDCl_3$. Peaks at 2.8 ppm and 2.6 ppm were used to calculate the regioregularity of 93%.

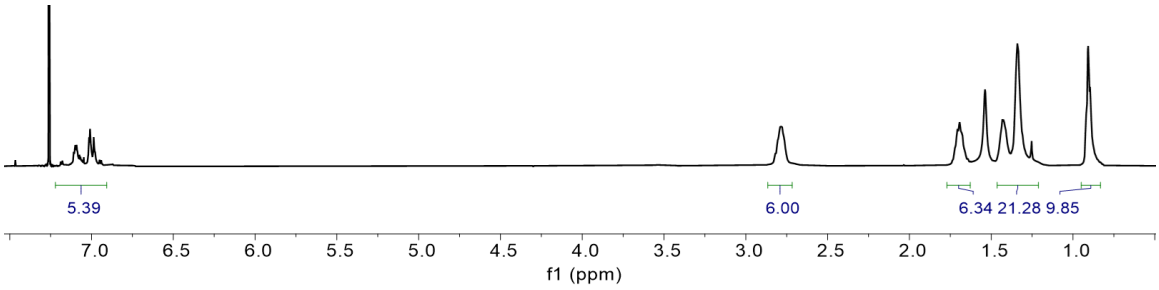

Figure B.2. ^{1}H NMR spectrum of poly(3,3"',4"'-trihexyl-2,2':5',2":5",2"'-quaterthiophene) (**P3**) in $CDCl_3$.

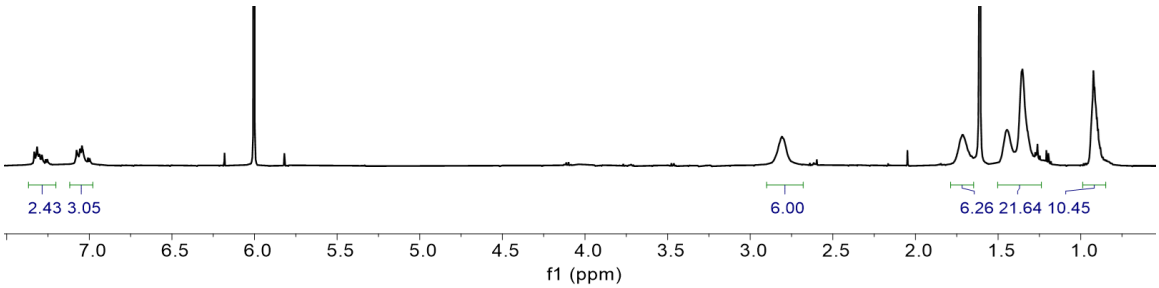

Figure B.3. ^{1}H NMR spectrum of poly(2-(4,4'-dihexyl-[2,2'-bithiophen]-5-yl)-5-(3-hexyl-thiophen-2-yl)thieno[3,2-*b*]thiophene) (**P4**) in $C_2D_2Cl_4$.

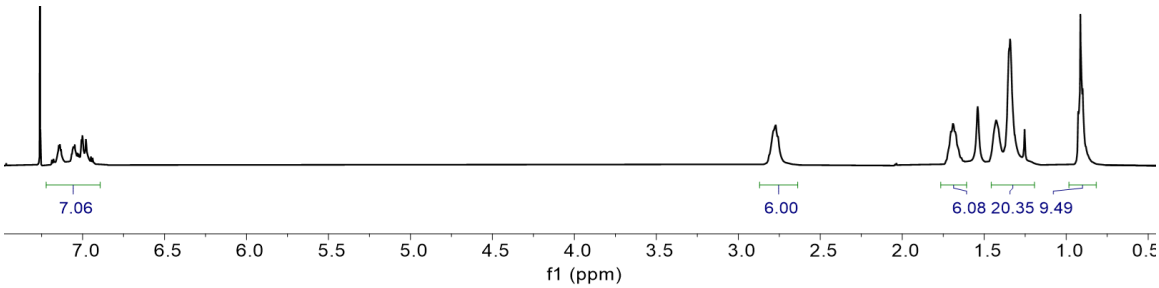

Figure B.4. ^{1}H NMR spectrum of poly(3,3'''',4''''-trihexyl-2,2':5',2'':5'',2''':5''',2''''-quinque-thiophene) (**P5**) in $CDCl_3$.

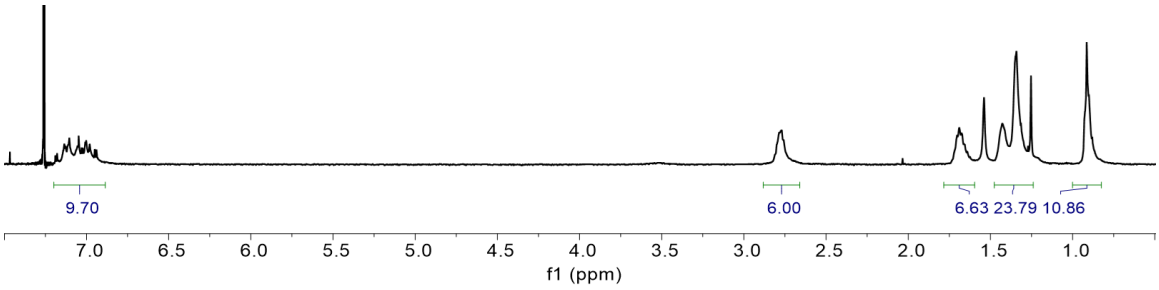

Figure B.5. ^{1}H NMR spectrum of poly(3,3'''',4''''-trihexyl-2,2':5',2'':5'',2''':5''',2'''':5'''',2''''-sexi-thiophene) (**P6**) in $CDCl_3$.

B.2. GPC Characterization of P3HT and Expanded Core Copolymers

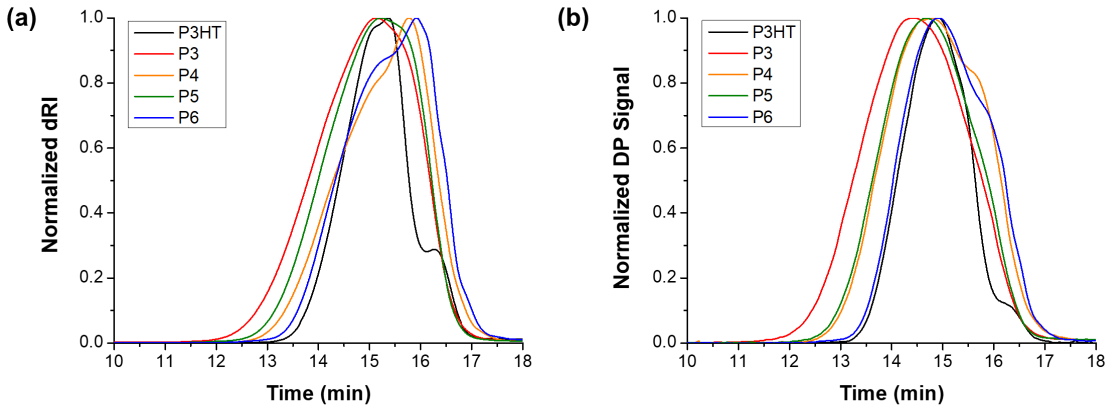

Figure B.6. GPC traces of (a) differential refractive index and (b) differential pressure (viscosity detector) for each copolymer, which were used to determine molecular weight based on universal analysis.

Table B.1. Molecular weight characterization of each copolymer based on universal analysis.

Polymer	M_n (kg/mol)	M_w (kg/mol)	Đ
P3HT	15.4	26.7	1.7
P3	11.0	49.4	4.5
P4	9.4	28.2	3.0
P5	9.1	33.5	3.7
P6	6.6	22.1	3.4

B.3. AFM Film Thickness Measurements

An Asylum Atomic Force Microscope was used in tapping mode fitted with an AC200TS tip (spring constant of 9 N/m and resonance frequency of 150 kHz) to acquire images of 20 μm × 20 μm. To measure the thickness of each film, a scratch test was performed. Specifically, a razor was used to scratch the film, thereby displacing the

polymer film and exposing the glass substrate. Images were then acquired at the scratch interface and film thickness was taken as the height difference between the polymer film and glass substrate. Thicknesses are used to calculate film conductivity and to normalize the absorbance measured by UV-Vis-NIR spectroscopy. This thickness normalization makes the absorbance across the entire spectra proportional to concentration.

Table B.2. Film thickness of as-cast films and those created using solution, sequential, and serial doping, as determined by AFM measurements.

Polymer	As-Cast	Solution	Sequential	Serial
P3HT	62.1 ± 11.2	67.7 ± 23.2	105.2 ± 33.3	134.7 ± 21.0
P3	163.0 ± 44.8	131.1 ± 35.8	123.9 ± 26.9	168.4 ± 19.2
P4	92.5 ± 13.4	150.5 ± 64.3	99.3 ± 12.0	237.1 ± 80.6
P5	93.9 ± 26.9	103.2 ± 18.0	132.9 ± 17.5	141.8 ± 15.5
P6	85.2 ± 38.3	271.7 ± 36.9	150.4 ± 84.2	299.3 ± 26.6

B.4. DSC Thermograms of P3HT and Expanded Core Copolymers

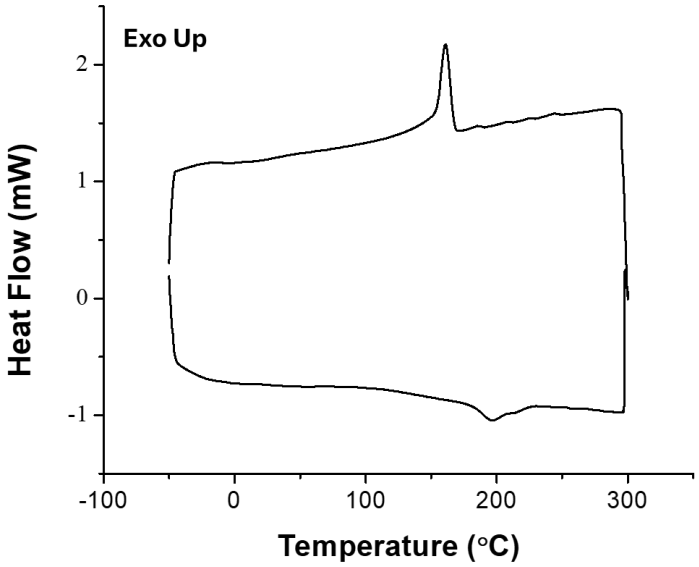

Figure B.7. DSC thermogram of **P3HT**. Measurement was performed from −50-300 °C at a rate of 10 °C/min and the 2nd cycle, shown here, was used for analysis.

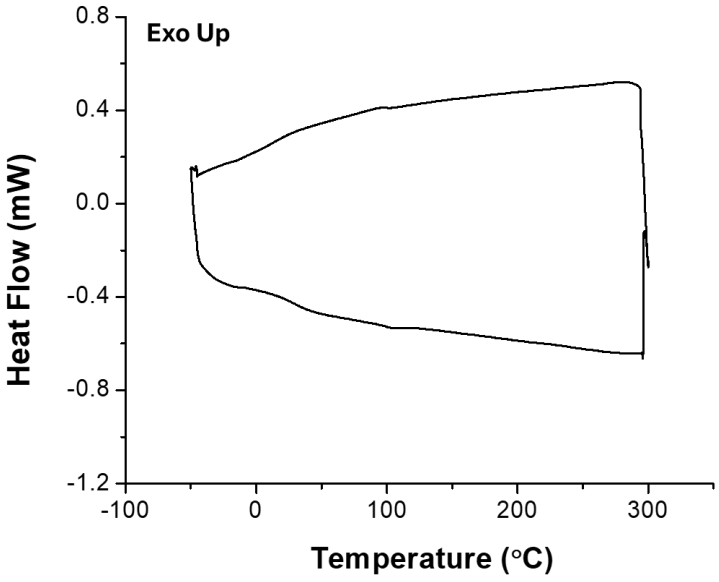

Figure B.8. DSC thermogram of **P3**. Measurement was performed from −50-300 °C at a rate of 10 °C/min and the 2nd cycle, shown here, was used for analysis.

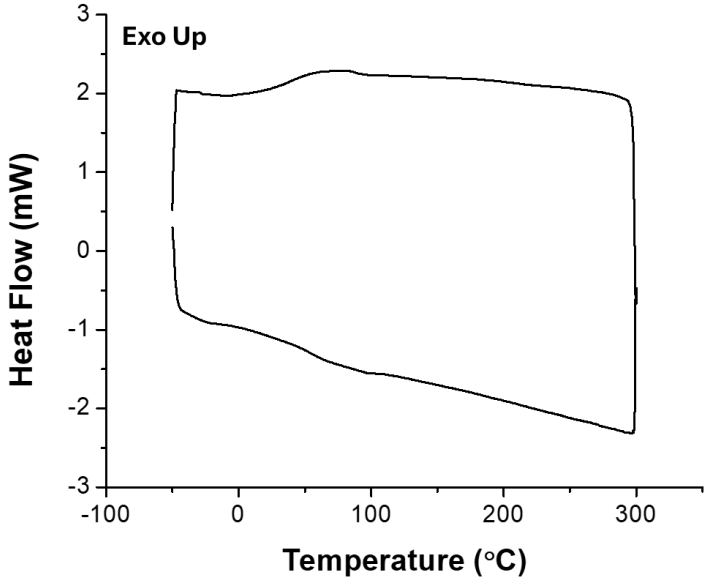

Figure B.9. DSC thermogram of **P4**. Measurement was performed from −50-300 °C at a rate of 10 °C/min and the 2nd cycle, shown here, was used for analysis.

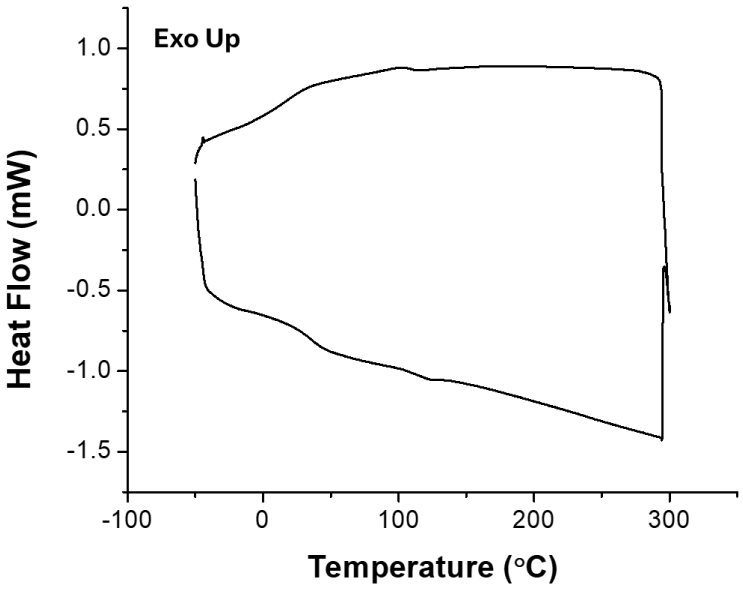

Figure B.10. DSC thermogram of **P5**. Measurement was performed from −50-300 °C at a rate of 10 °C/min and the 2nd cycle, shown here, was used for analysis.

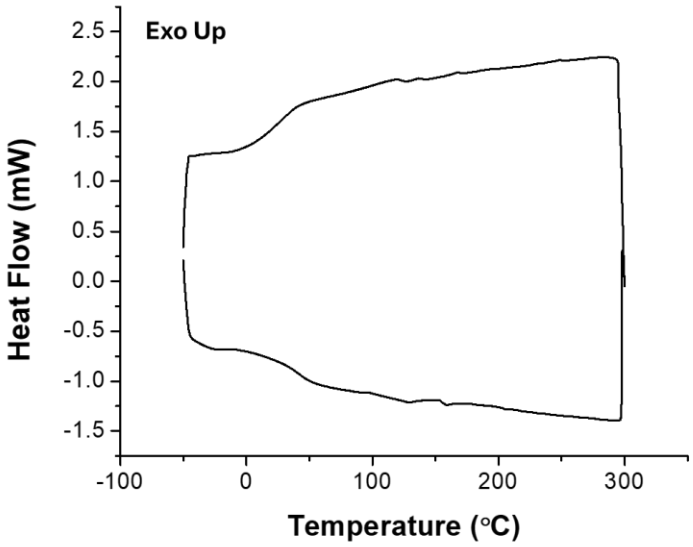

Figure B.11. DSC thermogram of **P6**. Measurement was performed from −50-300 °C at a rate of 10 °C/min and the 2nd cycle, shown here, was used for analysis.

Appendix C. Supplementary Information for Chapter 4

C.1. GPC Traces of PS, P3HT, and Expanded Core Copolymers

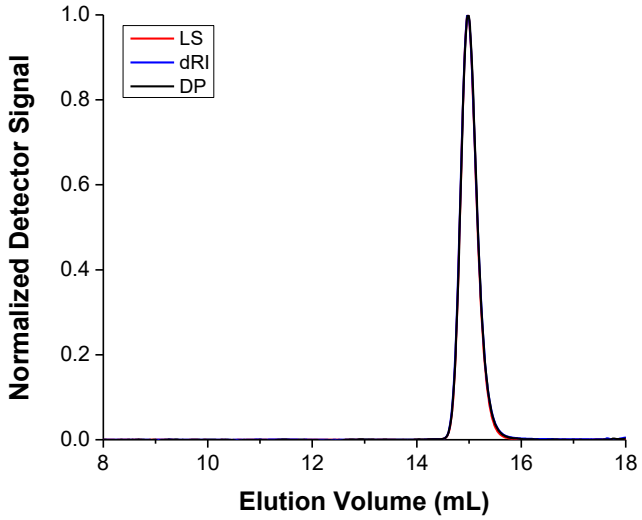

Figure C.1. GPC traces of PS corresponding to the light scattering (LS) signal, refractive index (dRI) signal, and differential pressure (DP) signal.

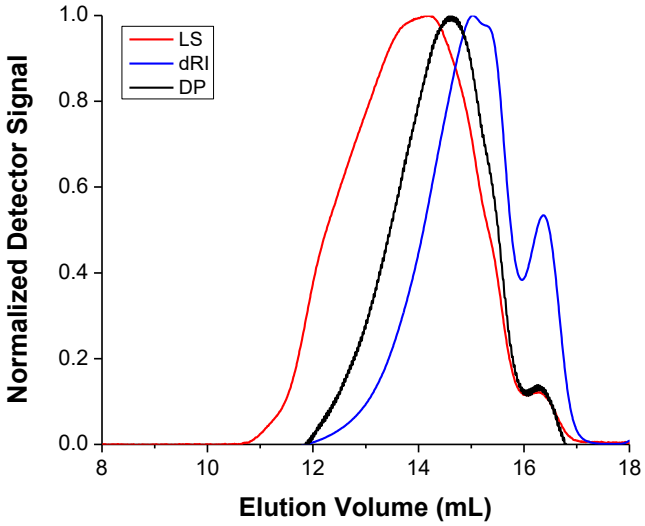

Figure C.2. GPC traces of **P3HT** corresponding to the light scattering (LS) signal, refractive index (dRI) signal, and differential pressure (DP) signal.

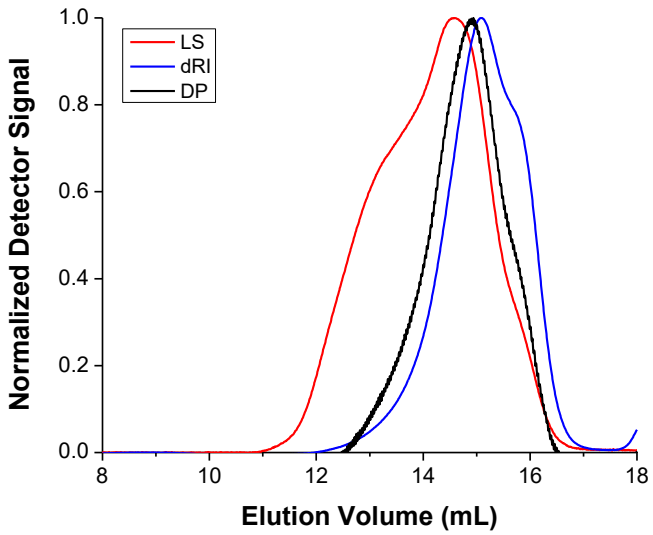

Figure C.3. GPC traces of **P3** corresponding to the light scattering (LS) signal, refractive index (dRI) signal, and differential pressure (DP) signal.

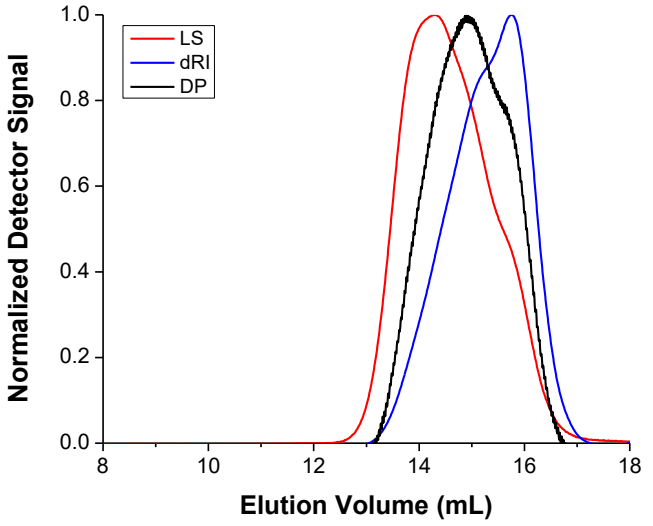

Figure C.4. GPC traces of **P4** corresponding to the light scattering (LS) signal, refractive index (dRI) signal, and differential pressure (DP) signal.

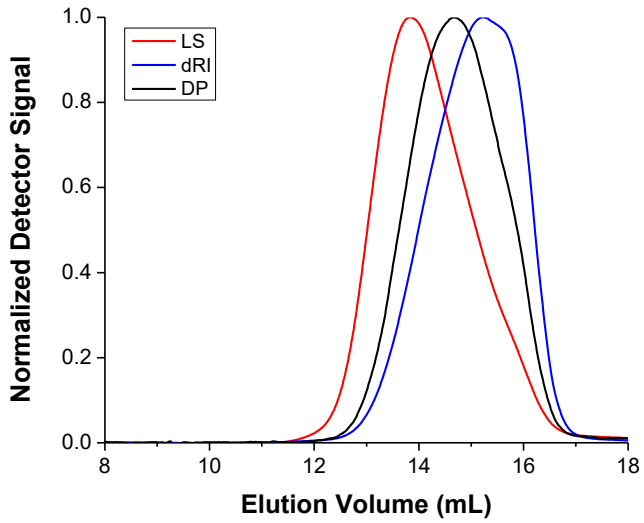

Figure C.5. GPC traces of **P5** corresponding to the light scattering (LS) signal, refractive index (dRI) signal, and differential pressure (DP) signal.

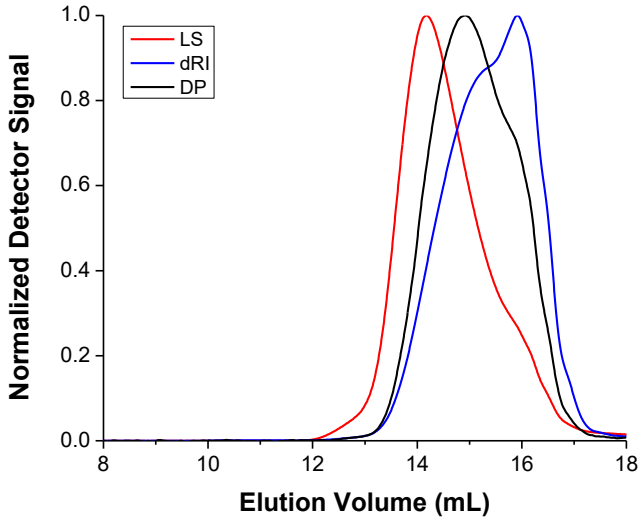

Figure C.6. GPC traces of **P6** corresponding to the light scattering (LS) signal, refractive index (dRI) signal, and differential pressure (DP) signal.

C.2. Mark-Houwink Plots

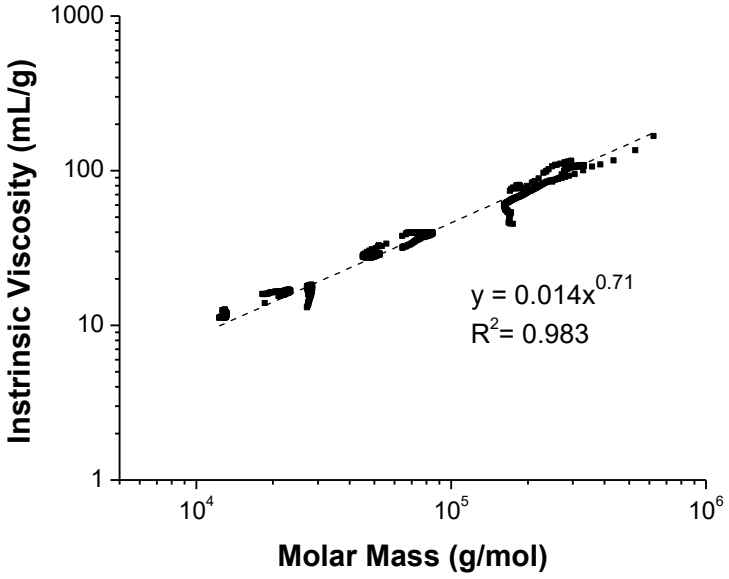

Figure C.7. Mark-Houwink plot of PS. Calibration standards of different molecular weights were used to obtain the plot.

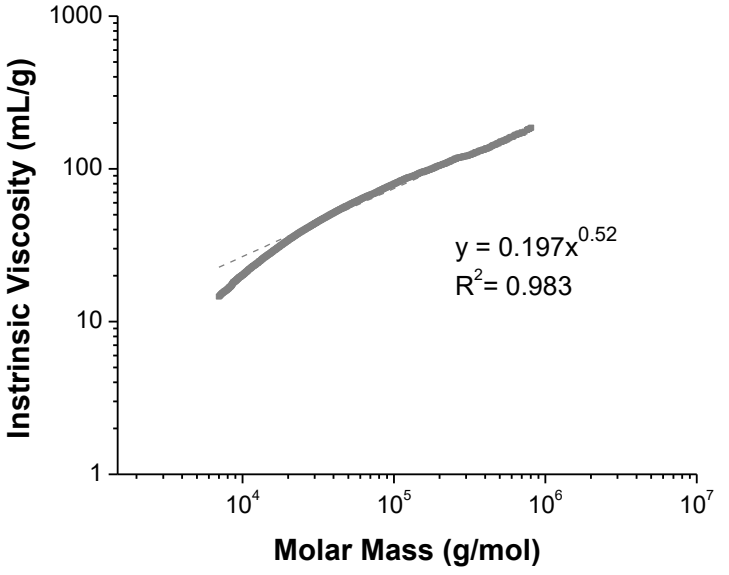

Figure C.8. Mark-Houwink plot of **P3HT**.

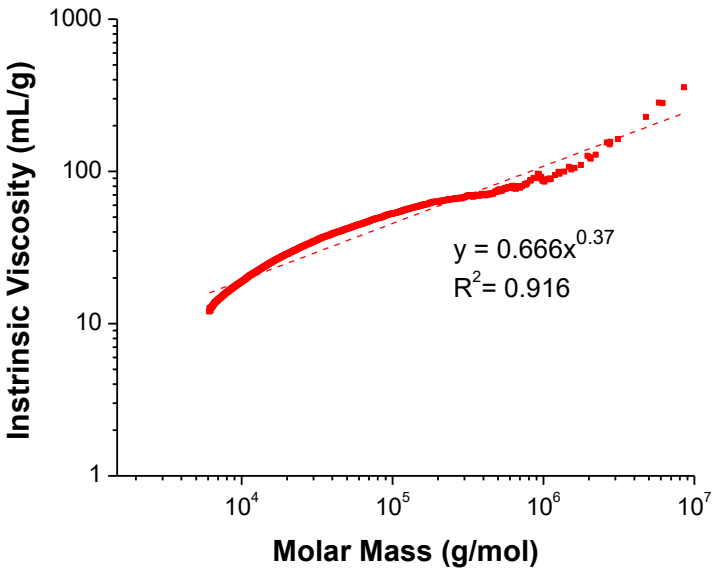

Figure C.9. Mark-Houwink plot of **P3**.

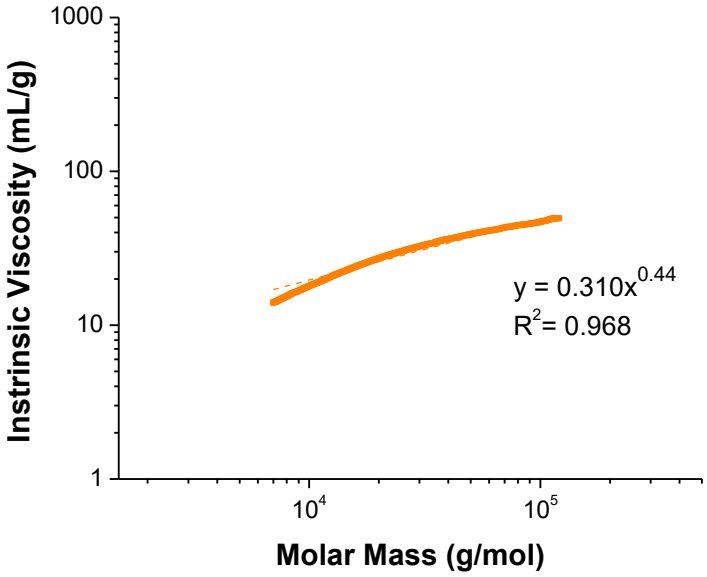

Figure C.10. Mark-Houwink plot of **P4**.

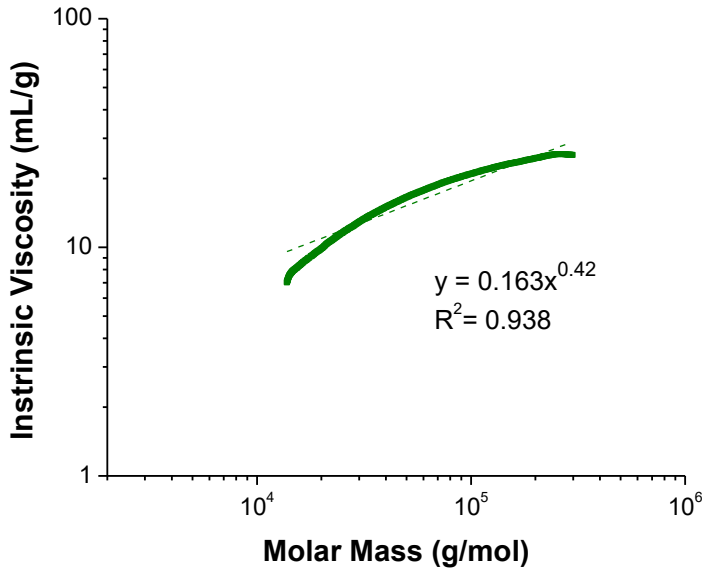

Figure C.11. Mark-Houwink plot of **P5**.

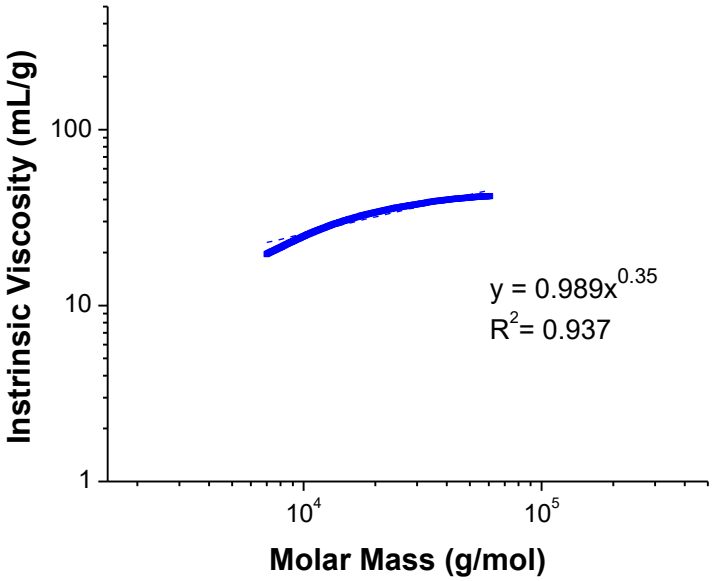

Figure C.12. Mark-Houwink plot of **P6**.

Appendix D. Supplementary Information for Chapter 5

D.1. ^{1}H NMR of P3HT and Copolymers

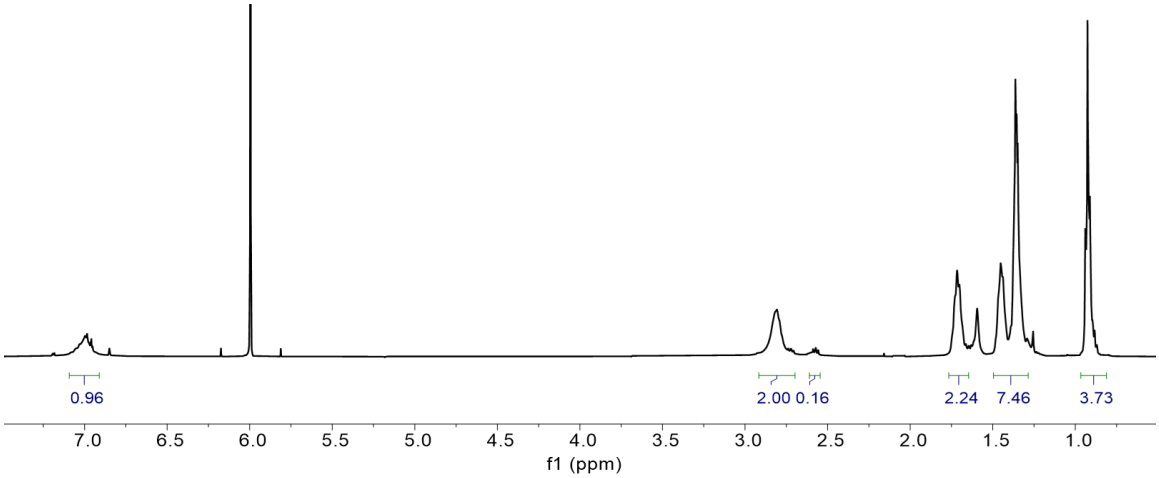

Figure D.1. ^{1}H NMR spectra of **P3HT** obtained in $C_2D_2Cl_4$. Peaks at 2.8 ppm and 2.6 ppm were used to calculate the regioregularity of 93%.

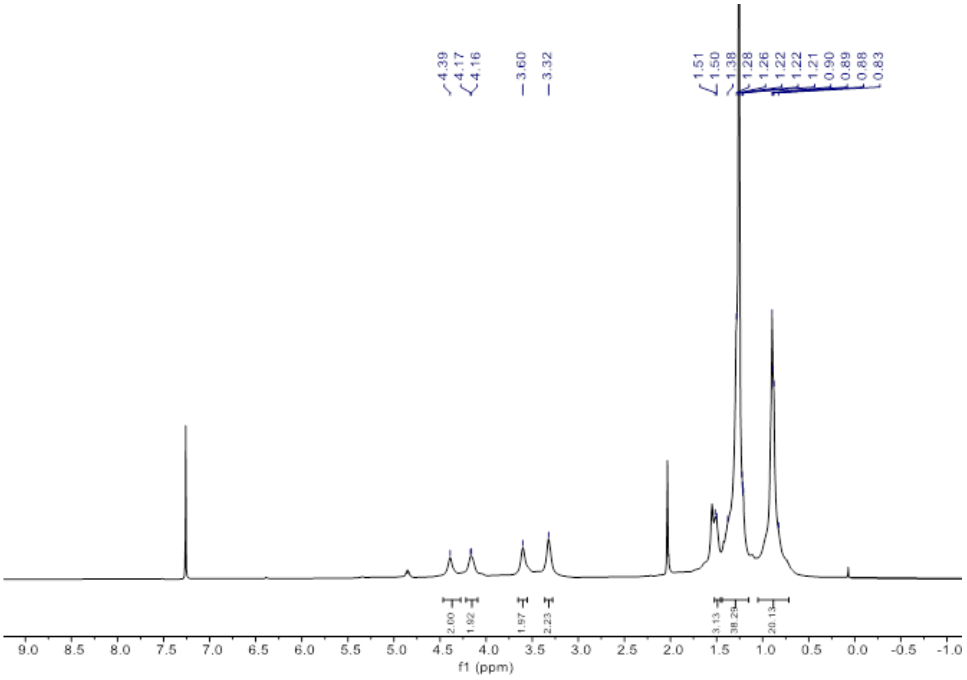

Figure D.2. ^{1}H NMR spectrum **P(EDOT-*co*-ProDOT)**.

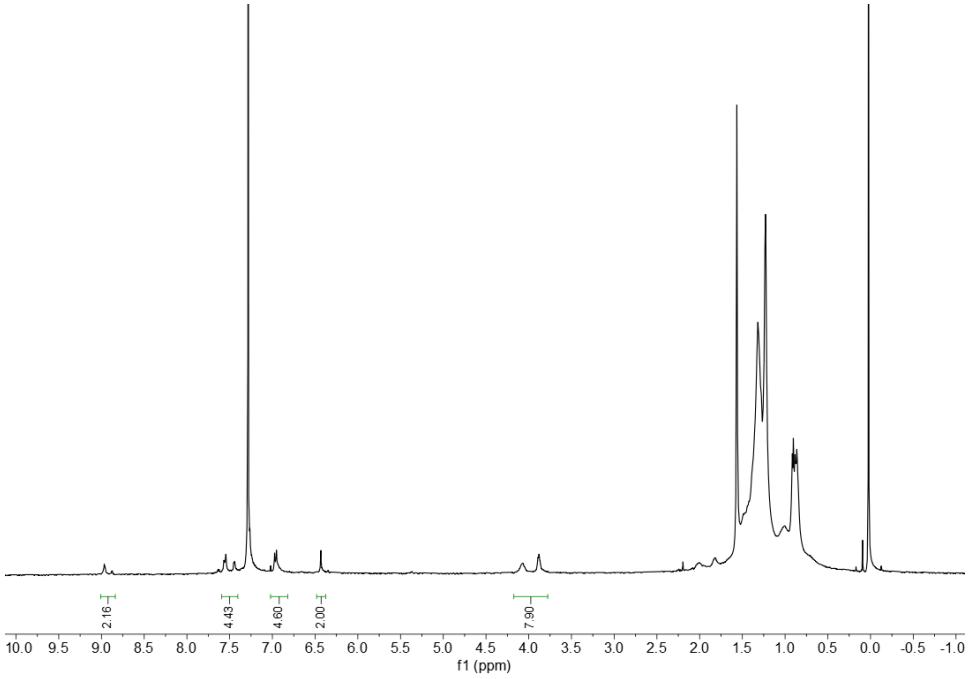

Figure D.3. ^{1}H NMR spectrum of **P(DHPP-*co*-DPP)**.

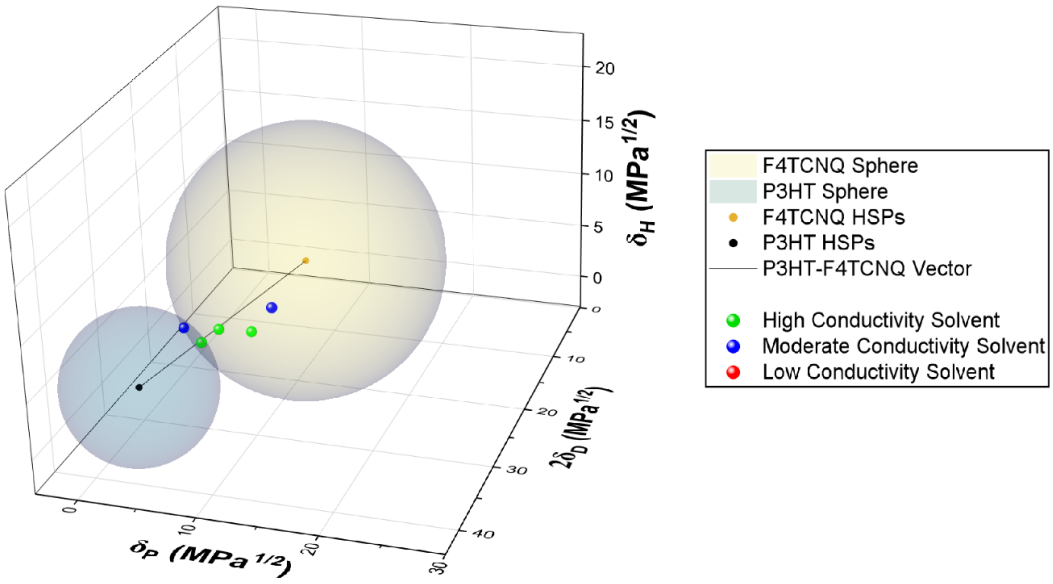

Figure D.4. Hansen solubility spheres of F4TCNQ and **P3HT**. The overlap volume is 145.1 $(MPa^{1/2})^3$.

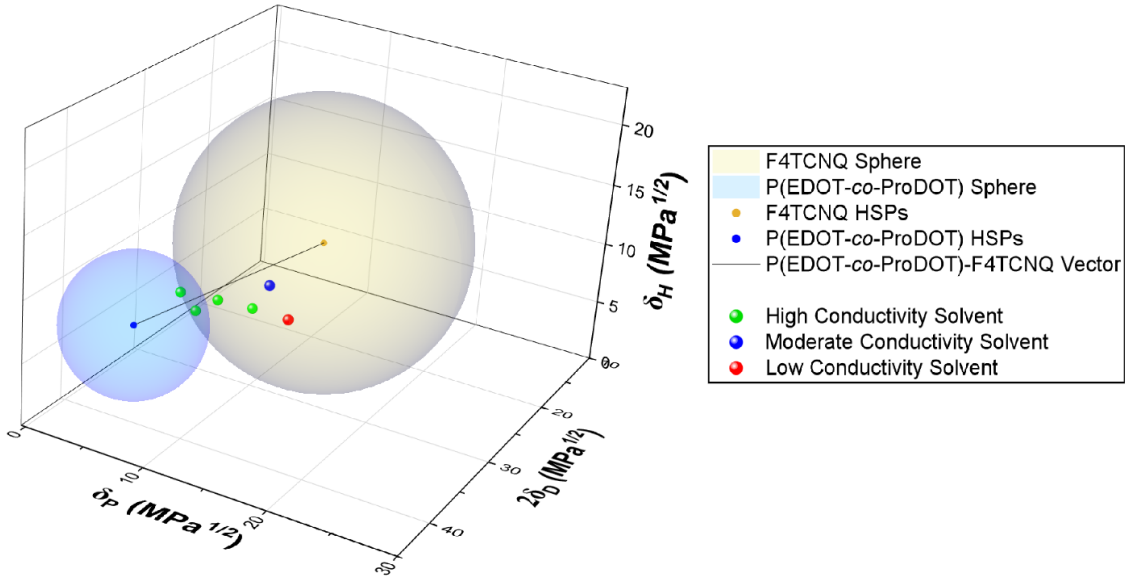

Figure D.5. Hansen solubility spheres of F4TCNQ and **P(EDOT-*co*-ProDOT)**. The overlap volume is 275.8 $(MPa^{1/2})^3$.

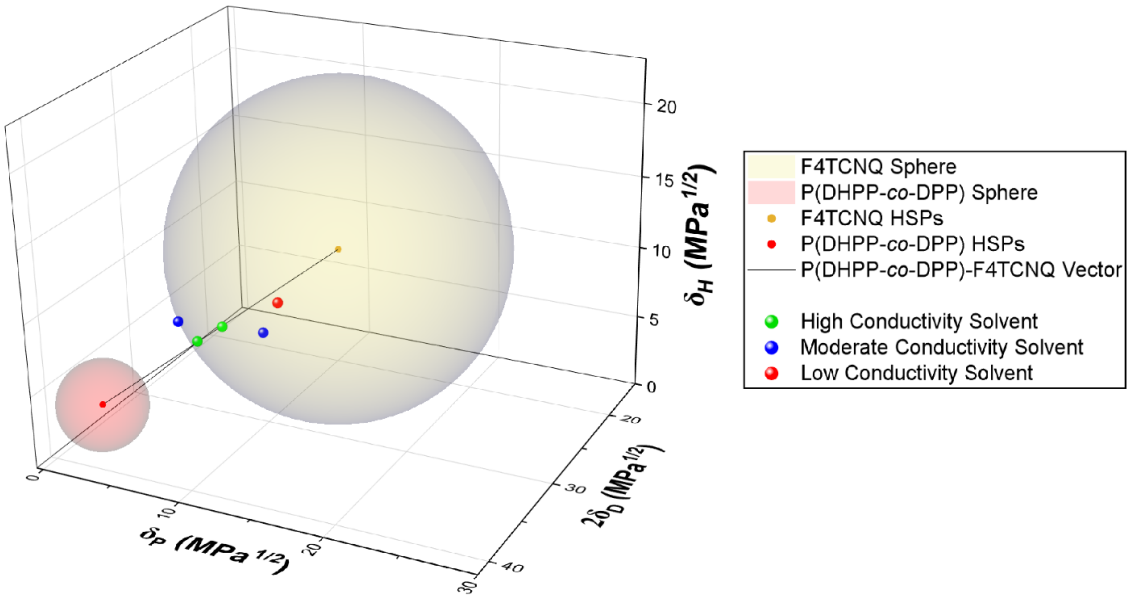

Figure D.6. Hansen solubility spheres of F4TCNQ and **P(DHPP-*co*-DPP)**. The overlap volume is 0 $(MPa^{1/2})^3$.

D.2. Molecular Weight Characterization of P3HT and Copolymers

Table D.1. Molecular weight characterization of **P3HT**, **P(EDOT-*co*-ProDOT)**, and **P(DHPP-*co*-DPP)**.

Polymer	M_n (kg/mol)	Đ
P3HT	15.5	1.5
P(EDOT-*co*-ProDOT)	64.5	1.5
P(DHPP-*co*-DPP)	30.5	2.5

D.3. Film Thickness of As-Cast and Sequentially-Doped Thin Films

Table D.2. Film thickness of as-cast and doped thin films for each polymer-solvent pair as determined by AFM measurements.

	Film Thickness (nm)						
Polymer	**As-cast**	**THF**	**DCM**	**50:50 Acetone:THF**	**Acetone**	**DMF**	**DMSO**
P3HT	45.2 ± 8.0	24.6 ± 6.9	48.1 ± 4.2	50.1 ± 18.2	43.6 ± 6.7	48.5 ± 14.5	–
P(EDOT-*co*-ProDOT)	50.3 ± 10.4	47.5 ± 5.4	54.9 ± 16.7	54.8 ± 10.1	59.4 ± 17.7	64.5 ± 14.8	87.3 ± 34.9
P(DHPP-*co*-DPP)	246.4 ± 22.3	261.8 ± 30.3	394.2 ± 41.8	280.2 ± 56.9	269.1 ± 43.5	264.3 ± 19.3	–

D.4. Thin Film UV-Vis Measurements

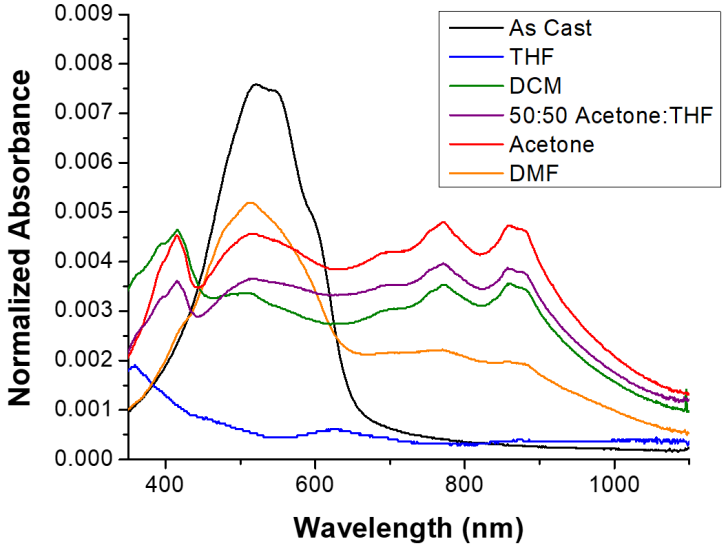

Figure D.7. UV-Vis spectra of as-cast and doped thin films made from **P3HT**. The spectra are normalized by film thickness. The λ_{max} obtained from the as-cast spectrum is 521 nm.

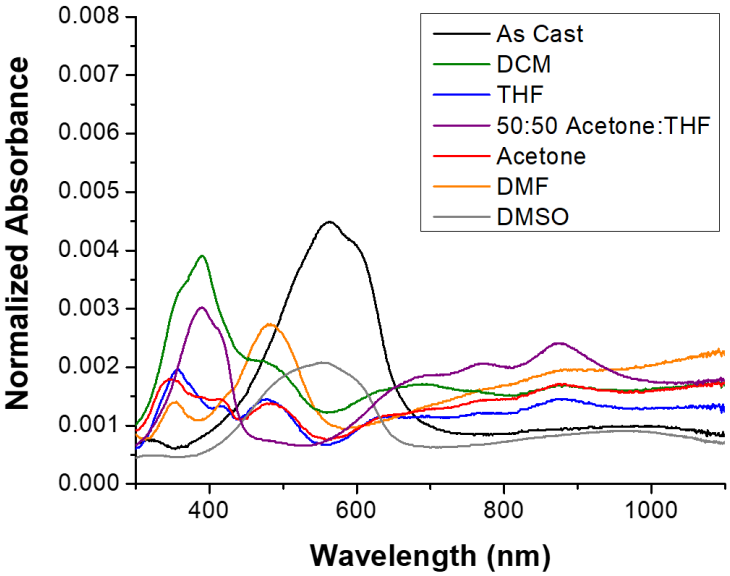

Figure D.8. UV-Vis spectra of as-cast and doped thin films made from **P(EDOT-*co*-ProDOT)**. The spectra are normalized by film thickness. The λ_{max} obtained from the as-cast spectrum is 563 nm.

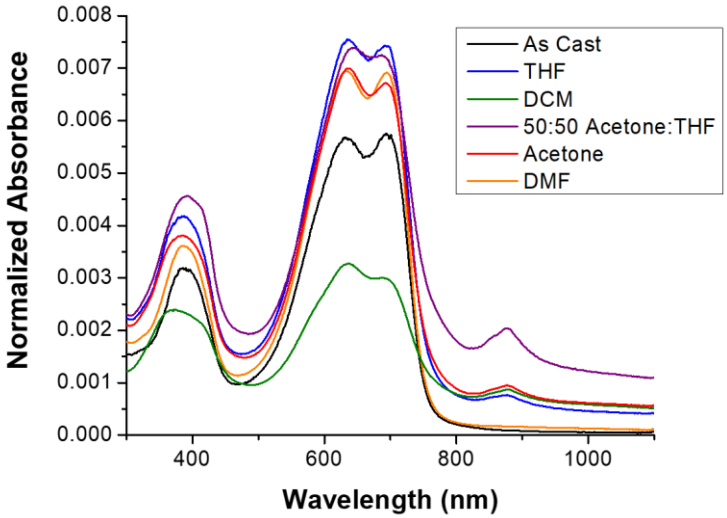

Figure D.9. UV-Vis spectra of as-cast and doped thin films made from **P(DHPP-*co*-DPP)**. The spectra are normalized by film thickness. The λ_{max} obtained from the as-cast spectrum is 693 nm.

Vita

Abigail N. Linhart was born and raised in Harvard, IL. In 2018, Abigail graduated with a Bachelor of Science degree in Chemistry from Lewis University. She then continued her academic career at Lewis University and earned Master of Science degrees in Chemistry and in Physics in 2021. Her research focused on the strategic design and characterization of stimuli-responsive nanocomposite systems. Abigail then moved to Knoxville, TN to pursue a PhD in Polymer Chemistry at the University of Tennessee - Knoxville. She joined the group of Prof. S. Michael Kilbey II, where her research focused on elucidating relationships between molecular design, organization, and electrical properties of conjugated polymers. During her PhD studies Abigail was awarded a National Defense and Science and Engineering Graduate (NDSEG) fellowship and the Burchfield Burridge Warner Fellowship in Polymer Chemistry.